von Karman Institute for Fluid Dynamics
Chaussée de Waterloo, 72
B - 1640 Rhode Saint Genèse - Belgium

CONTRACT REPORT 2003-08 December 2002

LES INVESTIGATION OF COHERENT STRUCTURES IN BOUNDARY LAYERS AND WAKES
VOLUME II: WAKE AROUND SQUARE CYLINDER

GRANT N00014-99-1-0834

R. Giammanco & C. Benocci

Abstract

Purpose of the present investigation is to assess the feasibility of simulating and studying coherent structures in turbulent shear layers, making use of Large Eddy Simulations (LES).

Volume I of present report has described the general background, the main development and the results obtained for wall bounded turbulent flow, particularly the turbulent channel flow at equilibrium.

The present Volume II is devoted to the study of the flow around an obstacle, in particular a cylinder with square cross section and infinite length in span-wise direction. This test case belongs to a completely different class of flow respect the one analyzed in Volume I, and it is a rather severe test case for the LES code.

Most of the advanced features of the code were exploited, and different simulations were performed, to collect, whenever possible, sufficient data to draw conclusions and remarks.

Differently from the case of channel flow, were the code has been extensively validated and analyzed in detail, down to the level of turbulent kinetic energy budget, the present flow constitutes a still active area of basic research.

The higher complexity of the flow, the absence of a second direction of homogeneity, beside the span-wise direction, the existence of a dominant frequency in the flow, the necessity of employing upwinding discretization for advection terms and other numerical difficulties have led to such complexities of execution that only the very basic set of statistics (statistical moments of first and second order) were obtained. At the same time, limits and draw-backs for current LES code implementation have been outlined.

Most of the efforts were devoted to reach a sufficient similarity in behavior between LES simulation and reference experimental data; this attempt has led to build grids not perfectly suited to analyze structures applying the criteria based on the gradient of velocity tensor introduced in Volume I.

This fact, together with intrinsic difficulty of dealing with a wide range of structures of different sizes and dimensions, has limited the possibility to obtain a through and complete description of vortical behavior for this class of flow.

However, it was possible to find useful global statistics for organized turbulence and to show that a very important part of the entire turbulent field lies within very active structures, which cover a very small part of the entire flow field. It can be moreover suggested that these characteristics of these structures are the ones which define and control the wake behavior, and their identification could be key of understand and possibile identify and regcognize specific wakes.

Possible avenues for future investigations starting from present study are also suggested.

Acknowledgements

Present research has been funded by the by Office Naval Research under Grant N00014-99-1-0834, under supervision of Program Officers Dr. Candace Wark and Dr. Patrick Purtell.

Table of Contents

List of Tables

List of Figures

1. INTRODUCTION

Since it was first recognized, turbulence has defied any complete definition:

Observe the motion of the water surface, which resembles that of hair, that has two motions: one due to the weight of the shaft, the other to the shape of the curls; thus, water has eddying motions, one part of which is due to the principal current, the other to the random and reverse motion. (Leonardo da Vinci 1510)

Under the practical point of view, the most visible and striking feature of turbulent flows would appear their exhibited unsteadiness and irregularity, leading to consider the details of their behavior random and unpredictable.

However, starting from the experiments of Brown and Roshko in 1975 (Brown and Roshko, 1975), the idea that there could be an underlying order in the chaos of the turbulence has gained momentum; the difficulty in the matter lying with its mix of deterministic organization together with chaotic features.

...frustration results largely from the mixture of chaos and order and the wide range of length and time scales that turbulent flows possess. (Moin and Mahesh, 1998)

The concept of an underlying deterministic structure of turbulent flow has been expressed by the definition of coherent structure, originally given by Hussain (Hussain, 1983, 1986):

> *A coherent structure is a connected turbulent fluid mass with instantaneously phase correlated vorticity over its spatial extend. ... We choose to designate the instantaneously space and phase-correlated vorticity as* <u>*coherent vorticity*</u>*. Thus, coherent vorticity is the primary identifier of coherent structures, which have distinct boundaries and independent territories.*

Therefore, the understanding of the physics of the coherent structures and their interaction with the background motion is of paramount interest in turbulence research. Indeed, recently had been suggested by Farge (Farge et al., 1996) that separating and understanding the different physical behavior of coherent structures and un-coherent background might be the key to understand and predict the turbulence behavior.

Most previous studies on the topic followed the experimental approach: detection of coherent structures and deduction of their behavior alongside their physics are obtained by velocity measurements of the flow, applying point measurements as such Laser Doppler Velocimetry (LDV) (Lyn et al., 1995); multi-point point measurements such as a rack of Hot Wire (HW) probes (Hussain and Hayakawa, 1987); in plane measurements as such as Particle Image Velocimetry (PIV) (Scarano et al., 1999). Of course, in all the cases previously

considered, it is impossible to have simultaneous three-dimensional data to take into account the inherited three-dimensional nature of turbulent processes.

The fundamental advantage of the numerical approach, in the present case, is its capability to produce instantaneous, three-dimensional flow-fields. The tremendous potential of this approach was demonstrate by pioneering work of Robinson & al. (Robinson et al., 1990) who visualized the coherent structures in boundary layer flow over a flat plate.

This study was performed using flow-fields created by Direct Numerical Simulation (DNS) (Spalart, 1988) where all the turbulent scales down to the Kolmogorov scale are resolved.

While the advantages of DNS are evident and well know (Moin and Mahesh, 1998), its numerical costs are likely to confine its applications to Reynolds numbers (*Re*) and simple geometry for next future.

Simulation of flows at higher *Re* and complex geometry could be feasible applying Large Eddy Simulation (LES) (Rodi et al., 1997; Piomelli, 1997).

The basis of LES approach is the application of a filter operation to the Navier-Stokes equations to obtain the corresponding transport equation for filtered scales: scales larger than width of filter (grid scales) are resolved by numerical solution. Scales than smaller width of filter (sub-grid scales) are cut-off by filtering operation; effect sub-grid scales on the grid ones takes the form of stresses (sub grid stresses: SGS) and are modeled with an ad hoc model (sub-grid model). Under the physical point of view, the concept is to reproduce the different behavior of large eddies and small eddies in the transfer of turbulent kinetic energy (Tennekes and Lumley, 1983): assuming the spectrum of energy to have an equilibrium range, it can be supposed that smaller scales in this range are nearly isotropic in their behavior, and therefore easier to be modeled than the full turbulent field.

Available understanding of coherent structures shows that their size is considerably larger than the turbulent macro-scale, making permissible the application of LES to their simulation and study, with the advantage to be able to study their behavior at higher *Re* and complex geometry.

Purpose of the present study is to validate the use of LES to the study of coherent structures in shear layer and apply it to different flow cases at high *Re*.

As previous studies have shown that structures characteristics are quite different for different classes of flow, notably between wall-bounded and free flows, three different cases will considered, namely:

1. Attached wall-flows, for which plane channel at equilibrium will be adopted as test case
2. Free flows, for which case plane mixing layer will be studied

3. Separated flows; which will be represented by flow around a bluff body

All these three types of flow are investigated in order to find out the general and universal characteristics of the coherent structures.

The initial point of the present work is the Large Eddy Simulation code developed at the von Karman Institute (Simons, 2000).

Its fundamental features are:

- Finite differences
- Cartesian coordinates
- Staggered Grid Approach
- Second order accurate in space and time
- Filtering implicitly performed from finite differences
- Multi-Domain approach for not trivial geometries

In order to apply this code the study of the coherent structures the main task to be performed will the development of:

- Algorithms for detection for the coherent structures in three-dimensional fields
- Statistical tool for analysis of the structures

These capabilities are implemented in a code treating structures defined on structured, Cartesian grids.

In order to assess the capability of LES to the study of coherent structures in general flows which cannot well be represented over Cartesian grids, a code which solves large-eddy equations in un-structured frame has been developed.

Present report is the subdivided in 3 volumes, each for the basic topics of the study.

Volume I Is devoted to the discussion of the structured code, the development of algorithm for detection and classification of the coherent structures and assess the result of its application to simulation of attached wall flow.

Volume II Covers the simulation of flow and coherent structures around the cylinder of square cross-section, and assess the performances of the present algorithms for wake flows.

Volume III Discusses the development and the performances of unstructured LES code.

Present Volume II, is devoted to the investigation of flow around a cylinder of square cross-section and the analysis of organized turbulence within its wake.

The Volume is organized as:

- Selected test-case description and its importance in the frame of present investigation in § 2
- Description and discussion on the flow field generated by LES and corresponding basic eulerian statistics in § 2.4 and § 2.5
- Description and discussion on the results of identification and analysis of coherent structures in the wake behind the body in § 3
- Conclusions concerning the performances of present algorithms and their applicability to complex turbulent flows are offered in § 4
- Additional simulations presented in the appendices, § B- § C

2. DESCRIPTION AND DEFINITION OF TEST-CASE

2.1 Introduction

As stated in § 1, present volume is devoted to assess the capability of LES, and of present code, to reproduce, recognize and study the coherent structures present within a complex turbulent flow.

In this optics, flow around an cylinder of square cross-section with infinite extension along its axis (Fig. 2.1) represents a very challenging test for both LES code and algorithm for identification and analysis of coherent structures (see Volume I).

Fig. 2.1: Overview of instantaneous flow-field around a cylinder of square cross-section. 3D-streamlines and pressure isolines; LES ($Re = 22,000$)

Flow around this body is characterized by multiple separated and re-developed regions, as it is shown by the streamlines of the averaged flow field (Fig. 2.3); all complexity is concentrated within the region close the body, while the rest of the flow, just a couple of diameters (or obstacle's edges) away the centerline, looks almost unperturbed (see Fig. 2.2).

As it can be there seen in Fig. 2.2, incoming flow separates itself on the upstream corners, to give birth to two symmetric re-circulation regions over the two faces parallel to main flow; these separated regions interact and merge with the separation region on downstream base face of the body.

Downstream of the base separated region, flow re-organizes itself in an unsteady wake, dominated by vortex-shedding from the two trailing edges (Fig. 2.4).

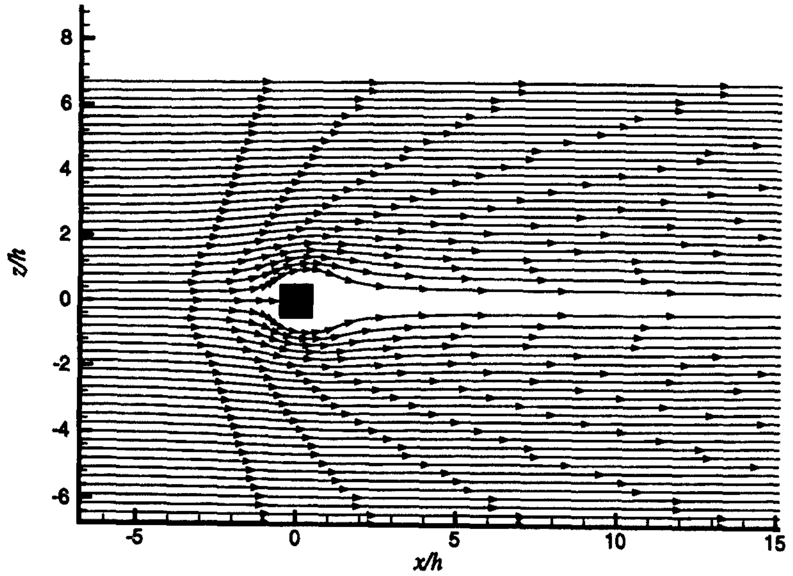

Fig. 2.2: Time averaged stream-lines around square cylinder; LES ($Re = 22,000$)

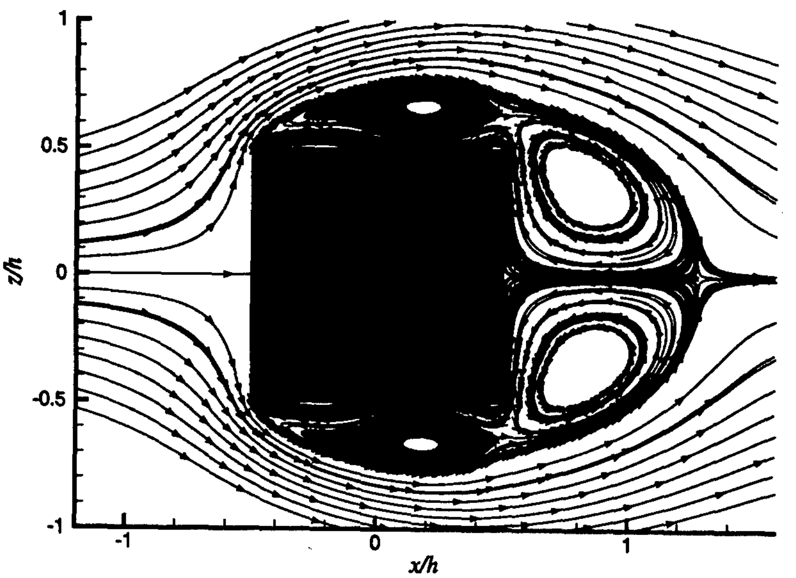

Fig. 2.3: Time averaged stream-lines around square cylinder, close-up; LES ($Re = 22,000$)

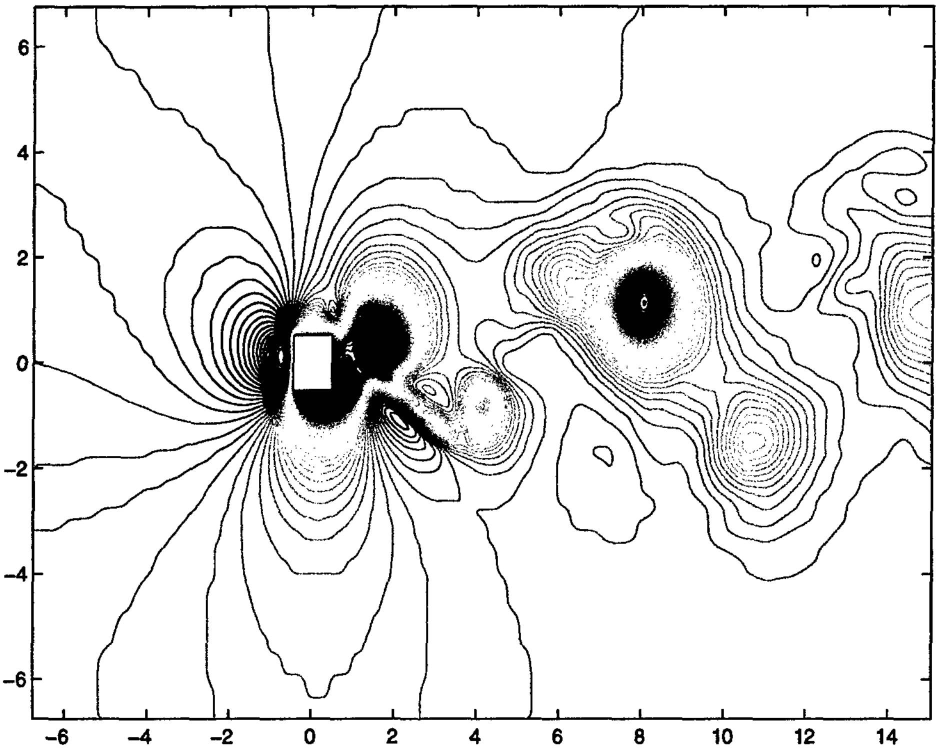

Fig. 2.4: Vortex shedding from cylinder of square cross section; instantaneous pressure isolines; LES ($Re = 22,000$)

Of course, dynamic behavior of separation over the body, vortex shedding and wake development is a much more complex process, as it can be observed by the visualization of iso-surfaces of span-wise vorticity over the body (Fig. 2.5).

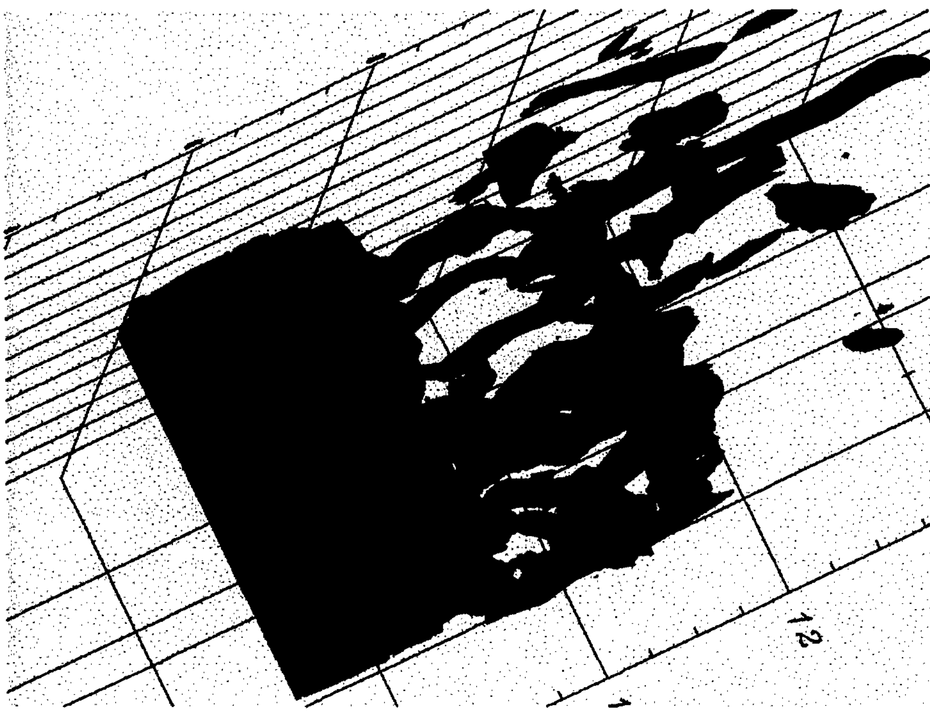

Fig. 2.5: Instantaneous iso-surfaces of span-wise vorticity around the cylinder; LES(Re = 22,000)

Separation of the flow at the upstream corner gives birth to a two-dimensional vorticity sheet, which is destabilized by the Kelvin-Helmholtz effect, leading to the formation of complex three-dimensional structures.

Downstream of the cylinder, vorticity field re-arranges itself in span-wise rolls and stream-wise oriented structures (Fig. 2.6).

These stream-wise oriented structures ("braids", or "ribs"), are considered (Hussain and Hayakawa, 1987) to be the main mean by turbulent kinetic energy is transported and fed to the rolls(Fig. 2.7).

2.2 Challenges to be faced

This general overview put in evidence, well enough, the difficulties to be faced to simulate eulerian flow-field and dynamics of organized entities moving through it.

Considering the eulerian point of view, the difficulty lies with the need to resolve the very steep gradients of velocity and turbulence which develop themselves in the near neighborhood

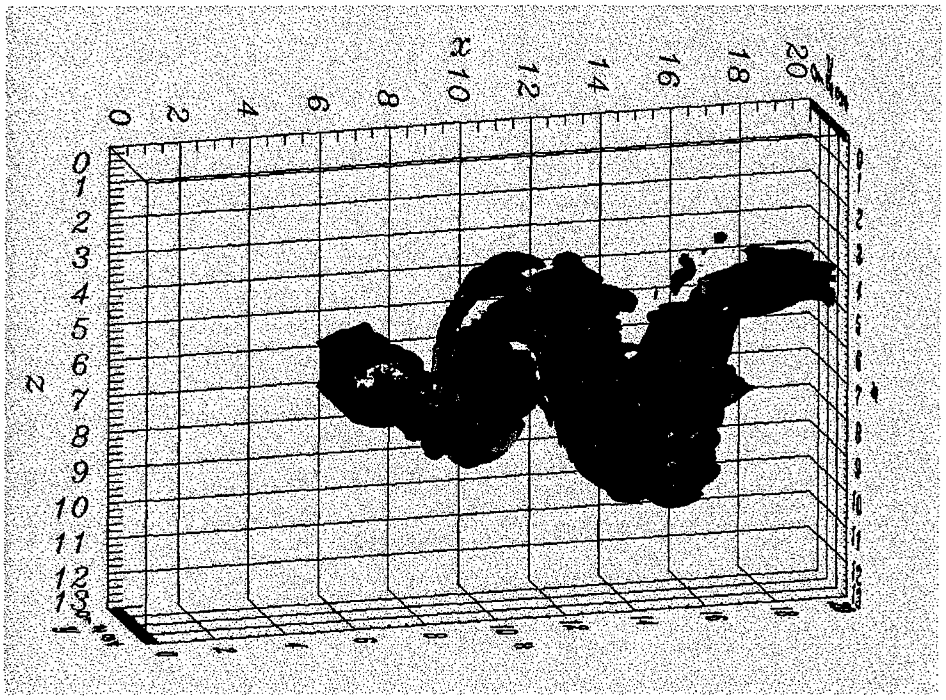

Fig. 2.6: Instantaneous iso-surfaces of modulus of vorticity around the cylinder; overview of wake development, LES($Re = 22,000$)

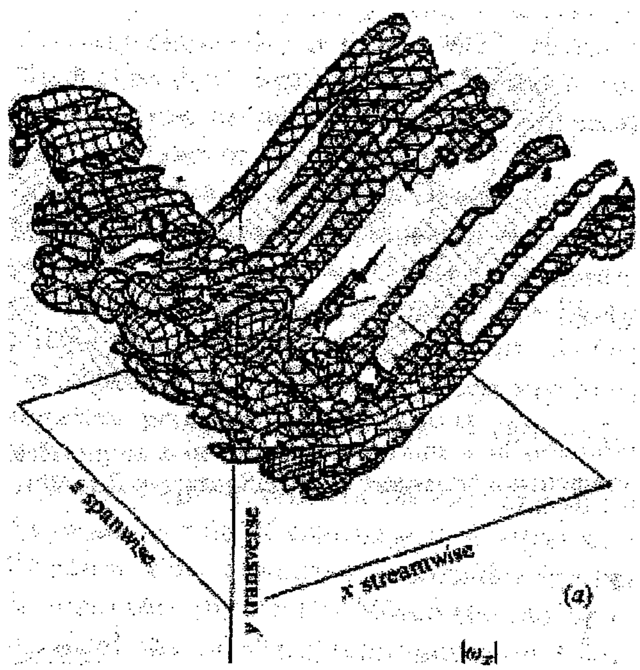

Fig. 2.7: Conceptual model of rib-roll mechanism in wakes

of the body, as well the need to assure the correct development of the wake.

The importance and difficulty to simulate these behaviors by LES was long recognized: in the frame of a recent workshop (Rodi et al., 1997) dedicated to LES, flow around cylinder of square cross-section at Reynolds number $Re = 22,000$ (Reynolds number based upon uniform inlet velocity U, and height H of the square) was one of the two benchmark cases, and this case is now widely accepted as standard benchmark test for LES applications (AGARD, 1998).

Concerning the study of dynamics of the wake, the difficulty can well be appreciated examining Fig. 2.7: differences of scales between rolls aligned along the span-wise direction y and braids lying in $x - z$ plane are evident. An algorithm for detection and definition of organized structures should be able, given sufficient resolution, to define these different structures configurations and their interactions, especially, the mechanism by braids feed turbulent energy to the rolls (Fig. 2.8). The objectives actually met and technical difficulties which made impossible to reach a satisfactory analysis of the structures, will be discussed in detail in current chapter and in § 3.

From above presentation, it can well be appreciated that present task is more difficult, by one order of magnitude, than the one associated with simulation of plane channel at equilibrium (see Volume I), when a single class of structures was present.

2.3 Numerical set-up of LES

Current section provides all the information concerning the setting-up, computing and processing of the LES simulations. It must kept in mind that, during the whole study of the square cylinder, the initial choices of parameters, dimensions and grid-resolution have been made in order to produce a simulation close, as much as possible, to the reference data provided by Lyn et al. (1995) and AGARD (1998). This choice has led to discretize the wake region with the minimum resolution necessary to resolve the flow-field, which has been found, at posteriori, to be not fine to enough provide a sufficiently good structure analysis.

2.3.1 Computational domain

The topology of the present flow is relatively simple (Fig. 2.9): an obstacle is invested by a flow of uniform velocity; beside the dynamics of flow field around the obstacle, the important macroscopic quantities to be reproduced are the lift coefficient and the drag coefficient for the body, as well the Strouhal number of the flow, in the case a predominant frequency exists and it can be determined.

Boundary conditions for the simulation are resumed in Fig. 2.9 and are below discussed in detail; as stated above, the are chosen in order to match the experiments of Lyn et al.

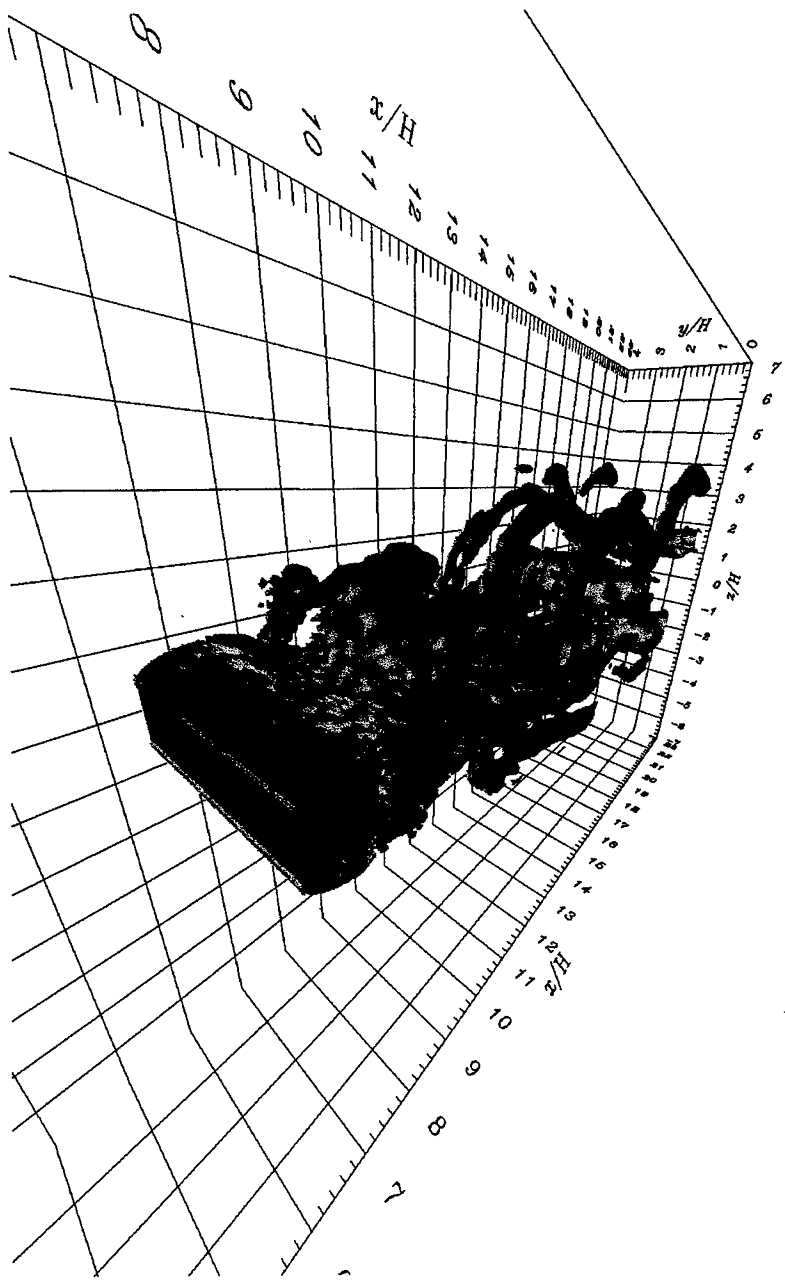

Fig. 2.8: Interaction between braid and roll. Q identification criterion, LES($Re = 22,000$)

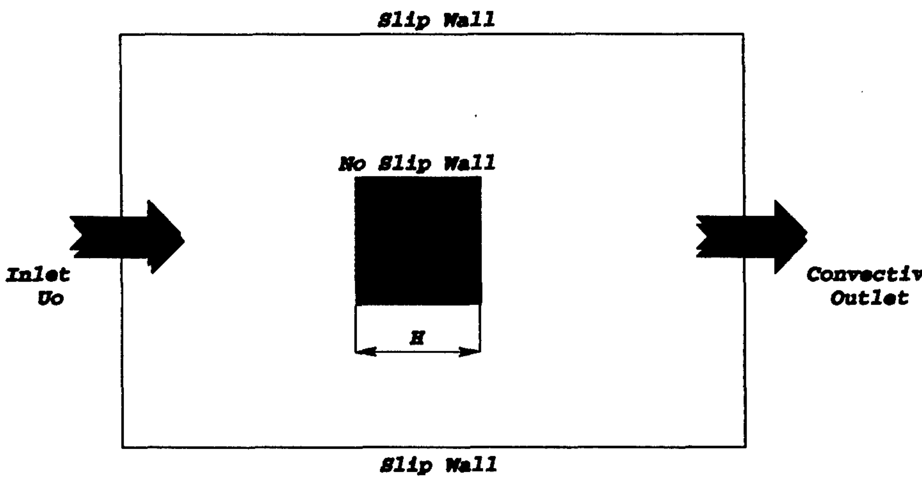

Fig. 2.9: Layout of simulation

(1995).

Inlet boundary In reference experiments, the incoming flow is made by an unperturbed uniform flow with free stream turbulence (Lyn et al., 1995); the estimation of its level is found to depend of the experimental set-up used to gather the data. In the optics of numerical simulation, however, it is not easy to produce a inlet turbulence which is realistic in terms of spectral behavior, energy contents, etc. etc. The simplest approach to the problem would then be to neglect inlet turbulence altogether, and impose a laminar inlet. This approach has been adopted by different groups participating to the above-quoted work-shop on the topic (Rodi et al., 1997), and can be supported by two considerations.

1. First In present geometrical configuration of obstacle, the determining feature of flow development is the formation of a shear layer which detaches itself at the leading edges and, down-stream, generates vortices shedding from the trailing edges. The influence of a low level inlet turbulence can be assumed to be of little consequence on the this process and, therefore, on the overall outcome of the simulation.
2. Second Considering the simulation in itself, it was found that complex and visible differences exist among results obtained with different numerical codes which, all, impose a laminar inlet, but apply different grids sizes, discretization schemes and SGS models. Therefore it was felt that, introducing an arbitrariness in the simulation of the free stream turbulence, it would become even more difficult to compare different results, assuming the inlet turbulence to have a significant impact on the simulation.

In consequence, an imposed uniform velocity Uo is imposed for the inlet and its value

is used to define the Reynolds number of the flow.

Top and Bottom boundaries The reference experiments were taken with a water tunnel of blockage ratio ($\frac{1}{14}$ relative to the physical dimensions of the cylinder of square cross section, and this ratio was reproduced in computational field for all present simulations). Boundary layers developing on top and bottom walls of the test section are usually disregarded in the simulations where slip (or symmetry) conditions are generally applied. The present analysis for the basic LES computations follows a similar approach[1].

Outlet Boundary At the outlet, a simple convective condition has been applied, coupled with a mass correction mechanism, which enforces equality of incoming and exiting fluxes [2].

Transversal boundaries The set-up was for reference experiment is characterized by a span-wise size equal to 9.8 times the size (or diameter, as will be convenient to call it from now on) of the cross-section, so that data gathered in the middle of the section (around 5 diameters from each side) could be considered representative of a cylinder of infinite length. This assumption greatly simplifies the task of numerical simulation since periodic boundary conditions can be used for the span-wise direction.

Wall boundary Flow over the surface of the obstacle is resolved numerically: no wall function or other approximations are used. This choice is made necessary by to the nature of the flow, namely by the need to well capture detachment and re-attachment points.

Full advantage was taken of the multi-domain framework (see Volume I, §3) to sub-divide the actual computational field in 24 sub-domains (Fig. 2.10).

Computational field is discretized over a cartesian grid of $197\times32\times178 \cong 1.1\times10^6$ points. Different stretching ratios are applied for different sub-domains in order to ensure maximum resolution on the most critical zones of the flow from the flow simulation stand-point; the grid is most refined close to the surface, while, further away, it is progressively coarsened. The distance of the first pressure node from the wall is $\cong 0.002H$, (H the side of the square cylinder); a close-up for the grid around the obstacle is shown in Fig. 2.11, while full description of the grid is shown in to Fig. 2.10 and detailed in Tab. 2.1. Tab. 2.1 indicates the parameter of grid-stretching, which is made by power stretching, namely, the ratio between cell sizes is constant and equal to the aforementioned parameter. In other words, considering

[1] Regardless of the experimental set-up of the reference simulation, it would be logical to use a free stream condition, namely to allow the flow to go out or in from top and down boundaries. Steps in this direction have been taken (see § A, but the effect of these boundary conditions seems not to affect the main wake, close to the centerline of the domain, where our attention is focused.

[2] Whenever the top and bottom boundaries allow flow to pass through them, the mass mechanism is modified in order to take into account these additional, even if relatively small, fluxes.

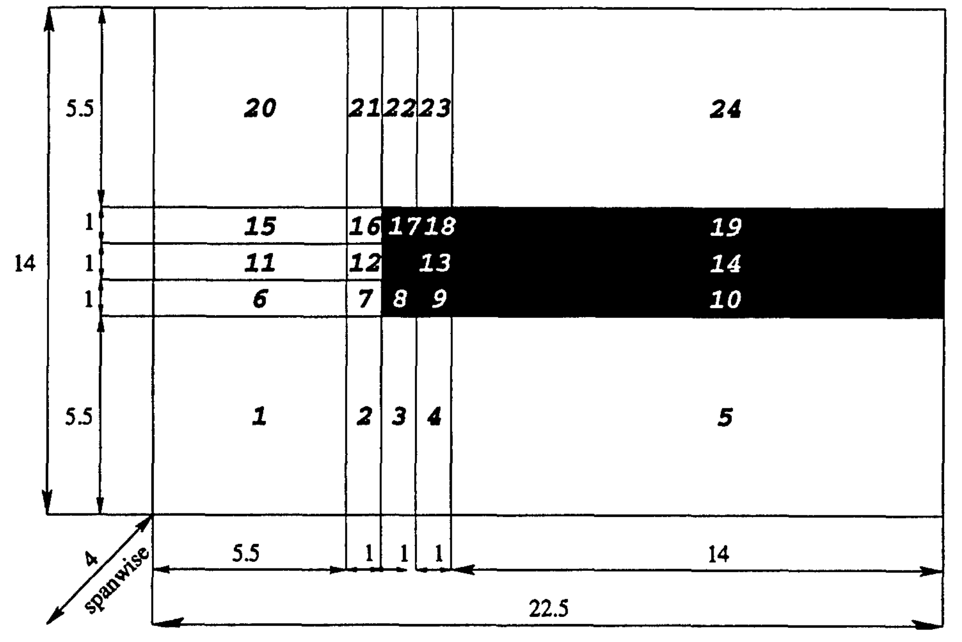

Fig. 2.10: Multi-domain set-up for computational field. No coloring: 3^{rd} order, upwind treatment of advective term; coloring: 4^{th}order central treatment of advective term.

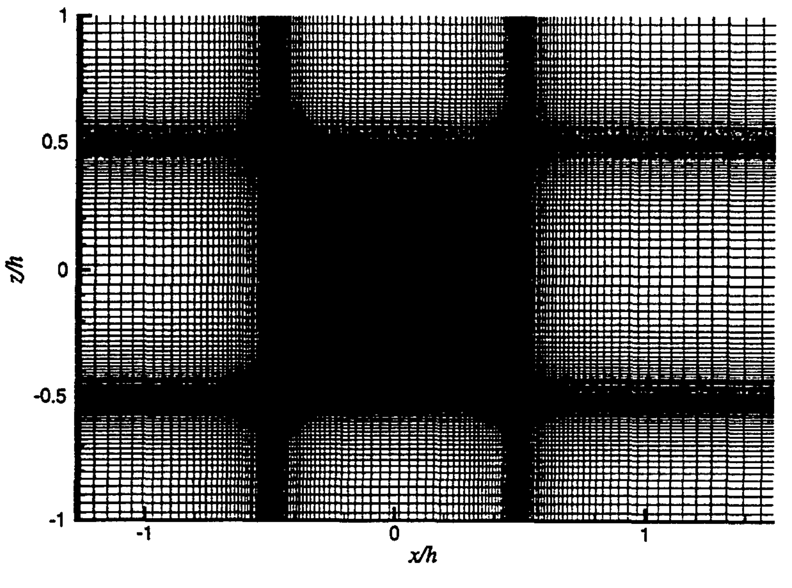

Fig. 2.11: Close-up of grid around obstacle.

cell i, being its size in stream-wise ${\Delta_x}^i$, the next cell $i+1$ has a size ${\Delta_x}^{i+1} = {\Delta_x}^i \times c$, where c is the stretching parameter.

Table 2.1: Number grid points and stretching ratios for individual sub-domains. Number of points in span-wise : 32; L, extension, N number of points, c stretching parameter, x stream-wise, z vertical direction.

Domain	L_x	L_z	N_x	N_z	c_x	c_z
1	5.5	5.5	21	21	1.075	1.075
2	1.0	5.5	38	21	1.075	1.075
3	1.0	5.5	60	21	1.075	1.075
4	1.0	5.5	38	21	1.075	1.075
5	14.0	5.5	40	21	1.05	1.075
6	5.5	1.0	21	38	1.075	1.075
7	1.0	1.0	38	38	1.075	1.075
8	1.0	1.0	60	38	1.075	1.075
9	1.0	1.0	38	38	1.075	1.075
10	14.0	1.0	40	38	1.05	1.075
11	5.5	1.0	21	60	1.075	1.075
12	1.0	1.0	38	60	1.075	1.075
13	1.0	1.0	38	60	1.075	1.075
14	14.0	1.0	40	60	1.05	1.075
15	5.5	1.0	21	38	1.075	1.075
16	1.0	1.0	38	38	1.075	1.075
17	1.0	1.0	60	38	1.075	1.075
18	1.0	1.0	38	38	1.075	1.075
19	14.0	1.0	40	38	1.05	1.075
20	5.5	5.5	21	21	1.075	1.075
21	1.0	5.5	38	21	1.075	1.075
22	1.0	5.5	60	21	1.075	1.075
23	1.0	5.5	38	21	1.075	1.075
24	14.0	5.5	40	21	1.05	1.075

It is obvious that the main influence on the quality of the simulation is the one of the numerical accuracy of the discretization, and, in particular, the discretization of the advective term; account must taken that, when an upwind discretization is applied made, an artificial dissipation is introduced which makes difficult to assess the effect of SGS model, whose main purpose is to simulate the physical dissipation of kinetic energy transported by the biggest scales.

Need of applying upwind discretization was suggested from preliminary simulations;

however, full advantage was taken of the multi-domain frame to apply different formulations of the advective term to different sub-domains. Therefore, 4^{th} order central discretization was applied to the sub-domains near the cylinder and the to ones corresponding to the core of the wake, while 3^{rd} upwind discretization was adopted for the outer sub-domains, where the biggest scales were expected to be present and where upwinding and SGS modeling could be expected to not play a major role[3].

The ability of this approach to control the aliasing of the solution in advection-dominated regions is demonstrated by the absence of spurious oscillations in the velocity field, in comparison with preliminary computations with central schemes for the advection term, which showed the presence of aliasing behavior. A contour plot of the vertical velocity field is shown in Fig. 2.12 for an instantaneous realization: the lack of spurious oscillation is visible in the smooth behavior of the velocity isolines. Only minor influence of the aliasing effect can be observed, in a zoom of the region of Fig. 2.12 shown in Fig. 2.13.

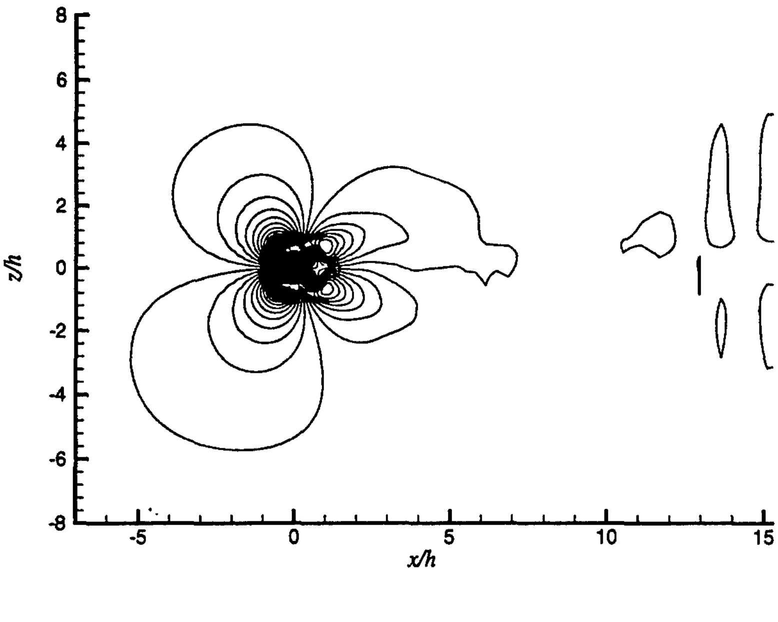

Fig. 2.12: Instantaneous vertical velocity isolines. Smooth behavior insure that aliasing effects have been taken care of.

The SGS model applied for present simulation (to be denoted as "reference simulation" in the following) is the filtered structure function ('FSF') model (Compte et al., 1994), however the effects of other a SGS model and a different grid resolution on the computed flow field have been tested and the corresponding results are briefly outlined in § A. Main reason to adopt the filtered structure function model lies with the higher dissipation provided by this

[3]Dissipation provided from upwinding and SGS model affect, indeed, only high frequencies associated to the smallest structures resolved by the grid, <u>if they are present</u>.

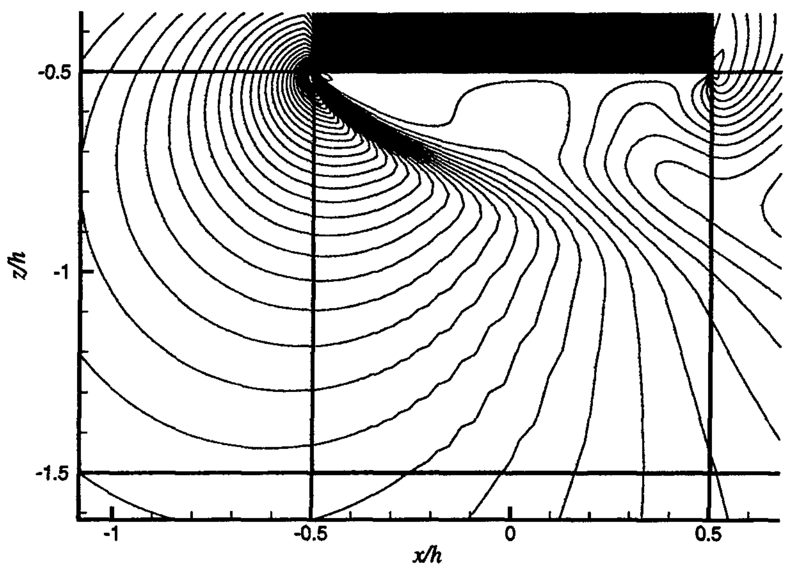

Fig. 2.13: Instantaneous vertical velocity isolines, magnified region close to the obstacle. Crossing domain boundaries from domains with upwinding toward domain without upwinding, the aliasing effect has jut time to start before being damped out from the SGS model.

SGS model, even if some other available results seemed to suggest Smagorinsky model could yield better results. The main drawback of both Smagorinsky and FSF model, is they need to introduce a coefficient, fixed a priori, to quantify the resulting sub-grid viscosity (Volume I). This drawback could be avoided applying the dynamic procedure (Germano et al., 1991), which would allow the coefficient(s) of the SGS model be function of time and space, self-adjusting to the actual flow development However, application of the dynamic procedure would have introduced additional complications and would be very costly when applied to a flow having only one direction of homogeneity (the span-wise direction for the present case) and was, therefore, left aside for the present investigation.

A major problem in the application a SGS model to wall-bounded flows lies with the need to ensure the proper scaling of the SGS viscosity close to the wall: if the LES is resolved, or no wall functions or approximate boundaries are used, the SGS viscosity should go to zero at the wall surface with a very well defined behavior (Pope, 2000); this behavior can be approximated by Smagorinsky model only if a damping function, such as van Driest damping function (see Volume I, §2.3.1.1), is applied. The formulation of van Driest damping function is briefly recalled here for simplicity sake.

$$\nu_t = C\overline{\Delta}^2 \left(1 - e^{-z^+/A^+}\right)^3 |\overline{S}| \tag{2.1}$$

where

$$z^+ = \frac{u_\tau z}{\nu}, \quad u_\tau = \sqrt{\frac{\tau_w}{\rho}}, \quad A^+ = 25 \tag{2.2}$$

The main difficulty of this approach, when applied to complex flows, lies with the need to compute dynamically and locally the distance in wall-units; in present application this parameter is set to a constant, for all the computational domain, and this could undermine the validity of the Smagorinsky model close to the wall; however, it is reasonable to assume that in present flow a not perfect evaluation of the distance in wall units it is not of paramount importance, since the major contribution to turbulent production is not due to the interaction with the wall, but to the flapping shear layer separating from the leading edges of the obstacle. The resolution of the wall is not, therefore, of primary importance, even because the resolutions achievable do not allow to comfortably speak of <u>resolved LES</u> for such a class of flows.

The approach just described is applied, in present work, to simulation with Smagorinsky model; FSF model does not allow for such correction and an overestimation of sub-grid viscosity close the wall had to be accepted.

2.4 Results for flow over the cylinder

The complexity of flow in the immediate neighborhood of the cylinder was shown in Fig. 2.4; this complexity is reflected in the time evolution of the forces acting on the obstacle.

The square cylinder is subjected to viscous forces and pressure forces, whose relative weights depend of the Reynolds number of the flow. As soon Reynolds number is high enough for shedding of vortices to happen, pressure in the base region of the square cylinder (in other words, the region immediately behind the obstacle) becomes significantly lower than the one of the opposite side, where pressure at the centerline becomes equal to the total pressure of the flow. A net pressure unbalance is then created which is translated into pressure drag.

It must be kept in mind that viscous terms have not been taken into consideration in the current analysis , since they have been considered to be small, compared to pressure terms; another source of inaccuracy present in current analysis lies with the fact that the pressure distribution on the obstacle surfaces is influenced from the SGS model adopted; matter of fact, in the filtered Navier stokes equations (see Volume I §3) the computed pressure is a modified pressure which contains the isotropic part of the SGS tensor[4]; if the SGS model, or the grid resolution close to the wall, do not allow the SGS tensor to fall to zero at the wall or, more practically, at the first cell close to the wall, a biasing could be introduced in the assessment of pressure forces.

A more precise approach has been considered but it was impossible to implement within time constraints of present investigation, and is, therefore, left out of current discussion. The concept of this possible alternative approach was based on a macroscopic balance for a region of the flow including the square cylinder, taking into account viscous effects, pressure effects and SGS effects. The main difficulties in application this procedure lies with the necessity to perform volume and surface integrals across multiple domains. In spite of the difficulties linked to such method, it was recognized that this could lead to a more precise and accurate procedure to compute lift and drag on the square cylinder, and should be, possibly, implemented, if further work on this subject should be considered.

Returning to present results, it must then be recognized that neglecting viscous effects and SGS effects could affect the accuracy of computed lift and drag coefficient, but, since the main objective of the simulation is to provide a realistic simulation of wake flow to use to assess the capabilities and limitations of present algorithm of structures identification, their impact can be considered minor for performance evaluation of the task at hand.

This put in evidence, it is possible to analyze the pressure distribution around the obstacle and extract the relevant information; at this point, it would be useful to remember that pressure computed by present simulation is not the physical quantity, but the result

[4]We limit ourselves for simplicity to eddy viscosity models

of the mathematical constraint which insures divergence-free flow field through the mean of the predictor-corrector scheme (see Volume I, §3). It is therefore necessary to interpret this value through an non-dimensional parameter, independent of particular aspects of definition of numerical pressure and related solver; in this optic, it is convenient to make use of the classical definition of pressure coefficient:

$$c_p = \frac{p - p_\infty}{\frac{1}{2}\rho {U_\infty}^2} \tag{2.3}$$

In present code is not possible to define a reference pressure which is constant in time, since the pressure field fluctuates time-step by time-step accordingly to the results of the pressure solver; it was considered reasonable to average, at each time-step, the pressure field at the inlet of the computational domain and define this value as the p_∞ of the simulation; in above definition U_∞ is the free stream velocity and c_p is computed in terms variables of the filtered Navier stokes equations (See Volume I §3). The result is a pressure coefficient consistent with the physical stand-point, in so far as it taken the correct value 1 at the stagnation point at the centerline of upstream face of the square cylinder.

Average c_p distribution is presented in Fig. 2.14, where the arrow convection has been used for the sign of c_p: a positive c_p corresponds to an arrow pointing against the obstacle, while a negative c_p corresponds to an arrow pointing in the opposite direction.

A different representation of the quantity of interest is presented Fig. 2.15 in order to allow a comparison with some of the experimental data available in literature. Dispersion of available experimental data concerning macroscopic quantities such as drag coefficient will be addressed in the following, but it is already evident in present Fig. 2.15, looking to experimental data taken from Rodi et al. (1997).

It is now possible to extract lift coefficient c_l and drag coefficient c_d from the instantaneous c_p distribution; these values can be processed to provide other macroscopic quantities of practical interest, namely:

- The non-dimensional frequency associated to time-evolution of c_l .
- The RMS value of the lift coefficient ($c_{l_{rms}}$).
- The mean drag coefficient ($\langle c_d \rangle$).
- The RMS value of the drag coefficient ($c_{d_{rms}}$).

It is important also to evaluate the length of recirculation behind the obstacle, because this parameter is linked to the behavior of average and RMS velocity along the wake centerline and, therefore, it can offer a first global indication of the quality of the present simulation.

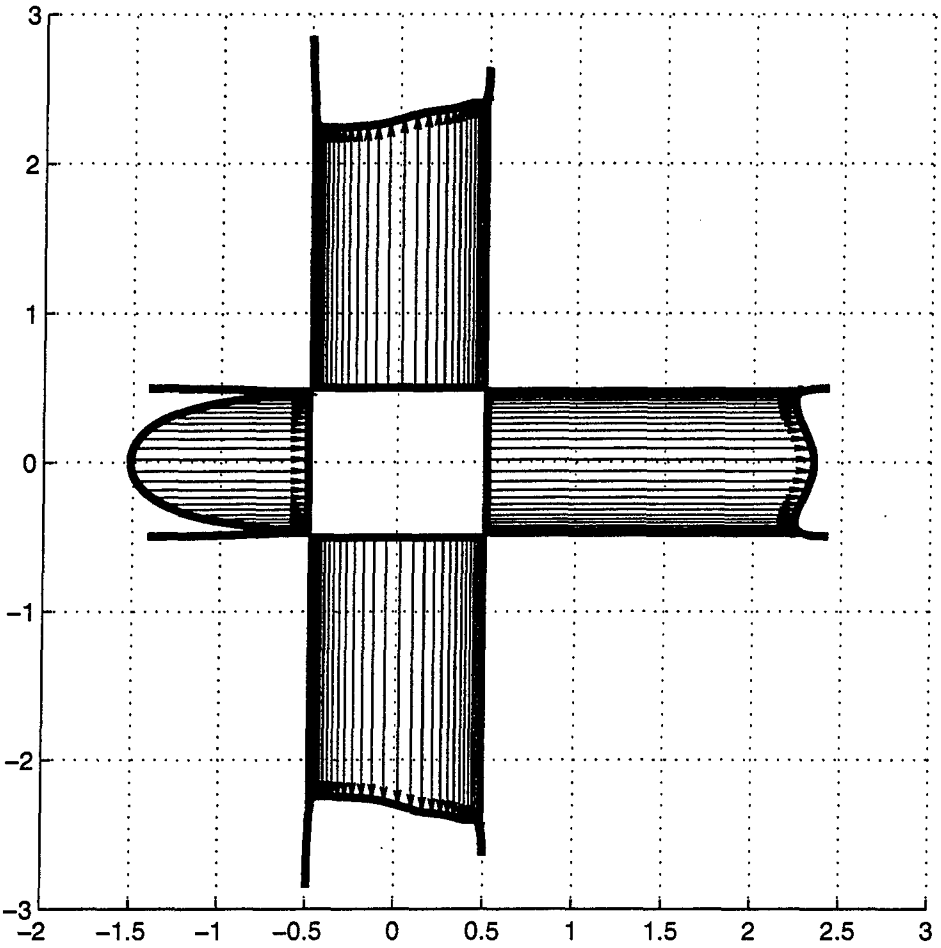

Fig. 2.14: Diagram of averaged c_p distribution around the square cylinder. Average in time and in span-wise direction.

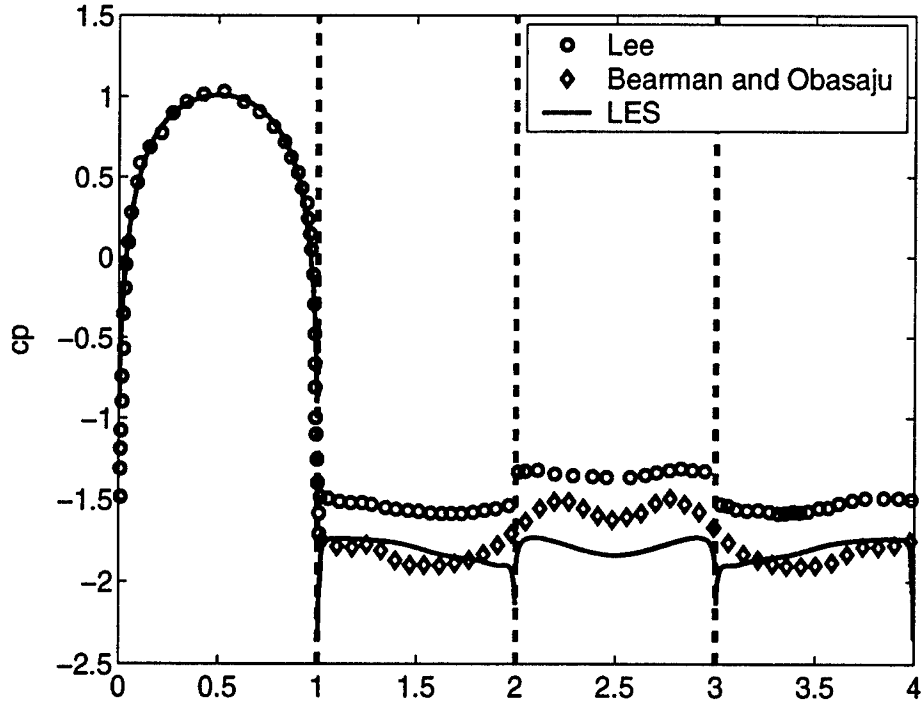

Fig. 2.15: Plot of averaged c_p distribution around the square cylinder. Average in item and in span-wise direction.

In many investigations, referred by the literature, the quality of simulation is assessed on the single basis of values of average and RMS velocity on the wake centerline.

The experimental values for the aforementioned quantities were taken from Rodi et al. (1997), which reviews a collection of different experiments; the extrema of this collection of data are presented in Tab. 2.2, together with corresponding values from present reference simulation.

Table 2.2: Macroscopic quantities of interest: experimental range of admissible values and computed ones.

	St	$c_{l_{rms}}$	c_d	$c_{d_{rms}}$	lr
EXP	0.133	0.1-1.4	1.9-2.1	0.1-0.23	1.38
LES	0.1284	1.58	2.5	0.31	0.56

To understand the problems related to extraction of these numerical values from present simulation, it must be kept in mind that present solver is explicit with respect to both advective and viscous operators (Volume I) and there are, therefore, two requirements which the time-step must satisfy for the calculation be stable and bounded; in the present implementation the time-step is computed dynamically during execution in order to satisfy both two constraints at each time-step, and, therefore, its value is different step by step.

This procedure makes more difficult the evaluation of some parameters and, in particular, of the Strouhal number; the correct procedure would be to choose a constant time step for the simulation, sufficiently small to ensure that the two constraints are always met. In this case it would be possible to compute directly the power spectra of lift coefficient from the raw data provided from the simulation. Under practical point of view, however, adoption of a constant, minimum, time step would further slow down the computations; therefore, the procedure actually adopted is to re-sample the lift signal at uniform intervals. Re-sampling, or filtering, of the raw signal does not alter its frequency content, with the exception of the highest frequencies: since the macroscopic time scale, namely the shedding period, is very big in comparison to the average time-step of the computation, re-sampling the signal, at an uniform time intervals, will hardly affect the value of the Strouhal number, computed from the filtered lift signal. In Fig. 2.16(a), the recorded history for the lift coefficient for the reference LES is shown, in terms of turnover times[5], while the corresponding history for the drag coefficient is presented in Fig. 2.16(b) . It is possible to observe that a dominant frequency exists, which is related to the shedding of the von Karman street of vortices, but other frequencies, either higher ones, related to turbulence phenomena, or lower ones, related to some modulation of the shedding, are present as well.

The Strouhal number can be then computed from the power spectra of the re-sampled lift coefficient, or could be estimated from the average shedding period T, the former being the preferred method. Present statistics are based on around 20 shedding periods.

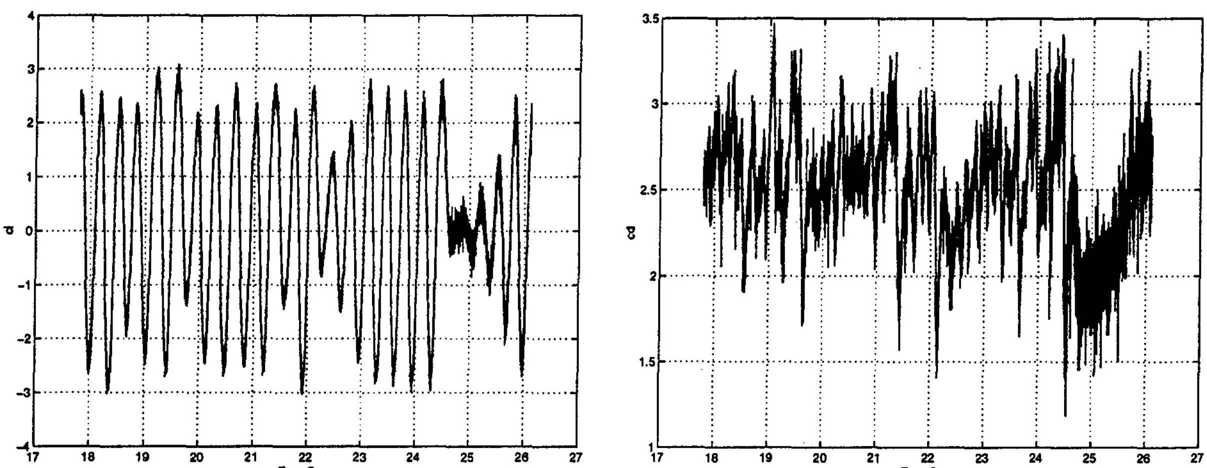

(a) Lift Coefficient

(b) Drag Coefficient

Fig. 2.16: Time history of lift and drag coefficients.

[5]A turnover time is defined as the time a particle would need to cross the complete flow field. In this case it is simply computed assuming an average velocity equal to the bulk velocity of the flow, which does not change with time, since there are no fluxes from the top or bottom boundaries.

The Strouhal number, St, associated with vortex shedding is estimated as 0.1284; this value is close enough to the experimental value, and is within the range of similar simulations Rodi et al. (1997); in a previous simulation, the value of 0.1327 was found, which would be extremely close to the experimental value, without apparent significant changes in the parameters of the simulation. This relative scattering of results suggests that low frequency effects could affect the outcomes of the simulations and a very long observation time would be necessary to ensure full convergence for this parameter.

Beside the afore-discussed macroscopic quantities, Lyn et al. (1995) provides sufficient experimental data to compare simulated and measured profiles of average velocities and turbulent quantities at different stream-wise (x) positions, over and behind the obstacle. In the present section a comparison is presented for stream-wise locations over the surface of the obstacle; for ease of representation, the data are presented in a local frame whose origin point $x = 0$ is taken at the center of the obstacle (see Fig. 2.17).

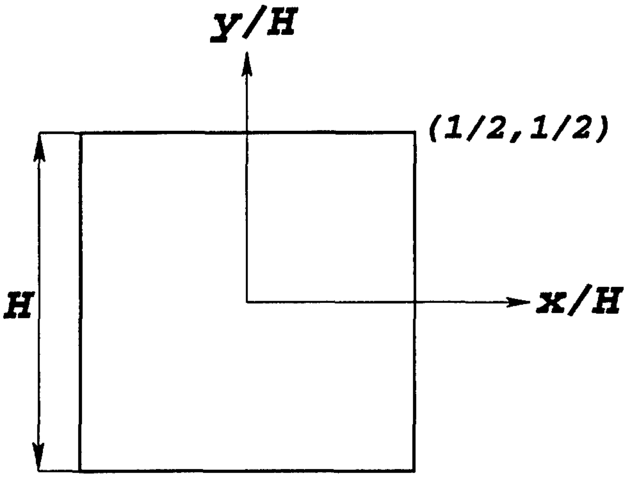

Fig. 2.17: Axis disposition for the cylinder of square cross section.

Fig. 2.18 to Fig. 2.23 present average and RMS stream-wise and vertical velocities over the obstacle at 9 different x locations; it must be stressed that comparison between present RMS, computed on the filtered velocity, and experimental RMS (as already noted in Volume I for the case the channel flow) is not fully consistent. Matter of fact, when an eddy viscosity model is applied, then the simulated Reynolds stress tensor (see Eq. 2.4 and 2.5), and the true one are only related through their anisotropic part; as the experiments do not provide measured RMS of the three velocity components (namely, the isotropic part of the Reynolds stress tensor), the compared quantities are not fully equivalent, although this comparison remains useful to clear and assess the general shape of the profile the simulated RMS and its evolution.

$$u(\vec{x}, t) = \langle u(\vec{x}, t) \rangle + u'(\vec{x}, t) \tag{2.4}$$

$$R_{ij} = -\left\langle u'_i u'_j \right\rangle \tag{2.5}$$

On the other hand, comparison between simulated and experimental turbulent stresses (the off-diagonal terms of the Reynolds tensor, Eq. 2.5) is consistent and it can be rightfully used in order to assess the quality of the simulation. In this case, experimental data were obtained by an instantaneous measurements of two components of velocity; this task is achieved, in the experiments performed by Lyn et al. (1995), by the mean of a two components LDV; however, the short-comings of this more complex technique (compared with one component LDV) has limited the region of applicability of this technique. Namely, measurements were feasible only above a distance from the wall of the obstacle which is higher than the one feasible for one-component measurements; therefore the availability of experimental turbulent shear stress is limited to fewer number of points and at higher distances from the wall.

The available data for the region above the obstacle are presented in Fig. 2.24 to 2.25; it is possible to see how, for present grid and chosen SGS model, computed flow is consistent with with the reference data, but further improvements should be performed in order to achieve a better agreement with experimental data[6].

2.5 Results for flow of the wake

Of course, satisfactory simulation of mean and turbulent flow in the wake are of fundamental importance in the study of its dynamic and the assessment of performance of present tools for detection and definition of organized structures. This task is made difficult by both the inherent complexity of the phenomenon and the practical need to simulate the wake over a grid which is coarser than the one adopted close to the body, as it was briefly stated in the previous section.

An overview of the difficulty and the quality of present simulation can be gained by Fig. 2.26 and Fig. 2.27 which present respectively average stream-wise velocity and stream-wise and vertical RMS along the wake centerline.

The procedure applied to compute the averages presented Fig. 2.26 and successive require some further explanations: in a the case of a flow without a dominant frequency, ensemble average is equal to time averaging, and more samples are collected, more refined becomes the average. In present case, the presence of a dominant frequency (vortex shedding) makes necessary to average over an integer number of shedding periods, and, even so, the results cannot be not assured to be perfectly symmetric respect to the wake centerline; an asymmetry of this type could be eliminated averaging top and bottom halves of the wake, but this procedure might well hide true problems with the simulation. It was considered safer to

[6]See § A for further comments.

compute a penalty function[7], and perform an integral over the whole domain, searching for the particular average which minimize the error. This could mean that two or more shedding periods must be processed before finding a better candidate for a significant average. Since the particular average chosen is guaranteed to have the minimal asymmetry, upper and lower halves are averaged, and this result is applied for the figures presented in the present chapter.

The present results show an underestimation of the recirculation length and a slight over-estimation of wake velocity along the centerline. It should be noted that a better agreement was found in a previous test-case (Giammanco et al., 2001); in that case the average was performed without applying a penalty function and that different choice could have brought a different effect of the flow low frequencies.

An overview of the wake behavior can be seen in Fig. 2.28 and 2.29, while a complete overview for all the stations is presented in Fig. 2.30 through Fig. 2.48.

[7]Given $g(y)$ a supposedly even function ($g(-y) = g(y)$) a possible penalty function could be $f(y) = \frac{g(y)-g(-y)}{2}$, identically null if the function $g(y)$ is really even. This means that multiple weights could be used trying to minimize the error on the stream-wise velocity, vertical velocity and so on. Present case, this approach is applied to minimize the error on the stream-wise velocity.

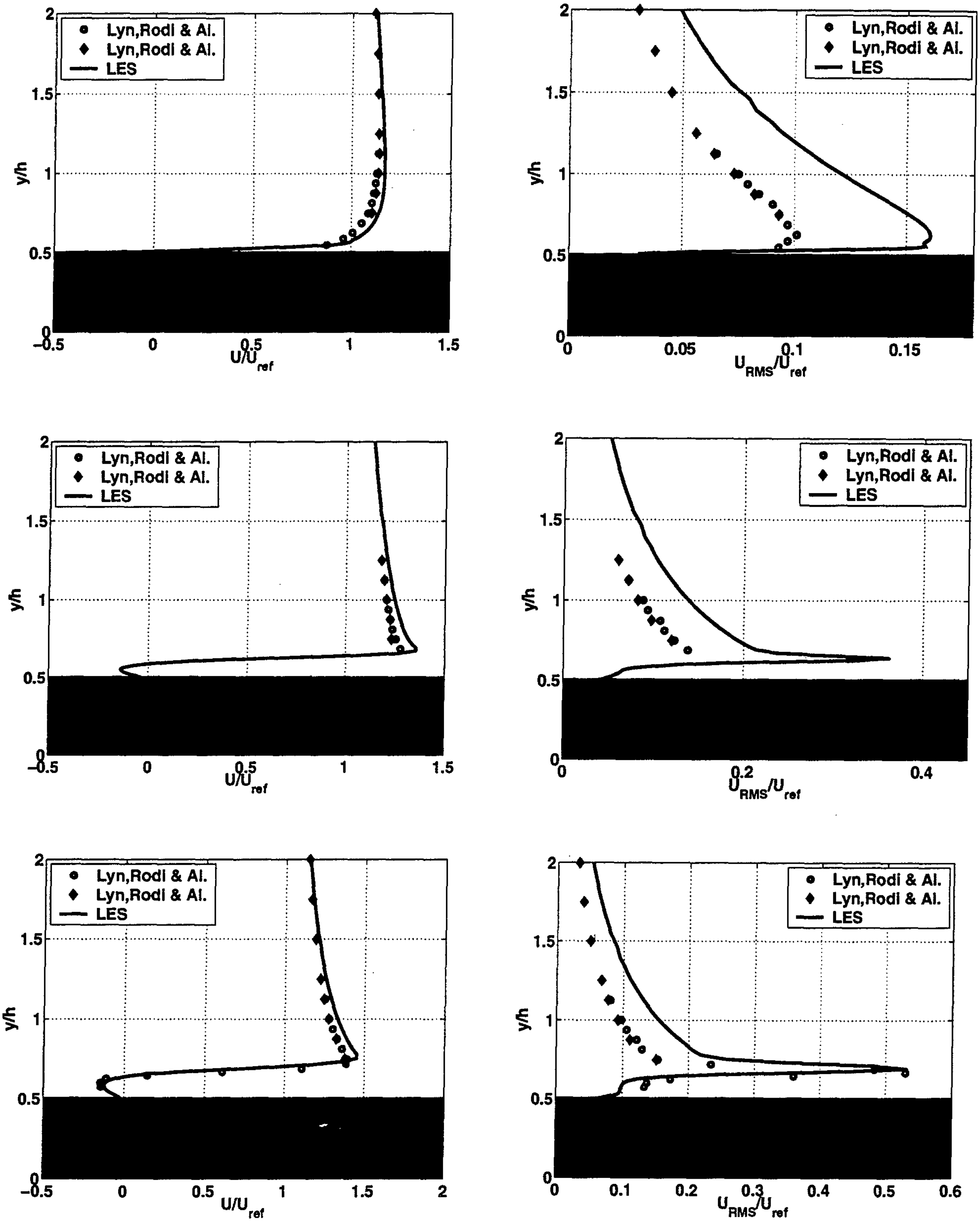

Fig. 2.18: Velocity profiles for stream-wise velocity, left and stream-wise RMS, right, at three stations, from top to bottom: $x = -\frac{1}{2H}$,$x = -\frac{3}{8H}$ and $x = -\frac{1}{4H}$.

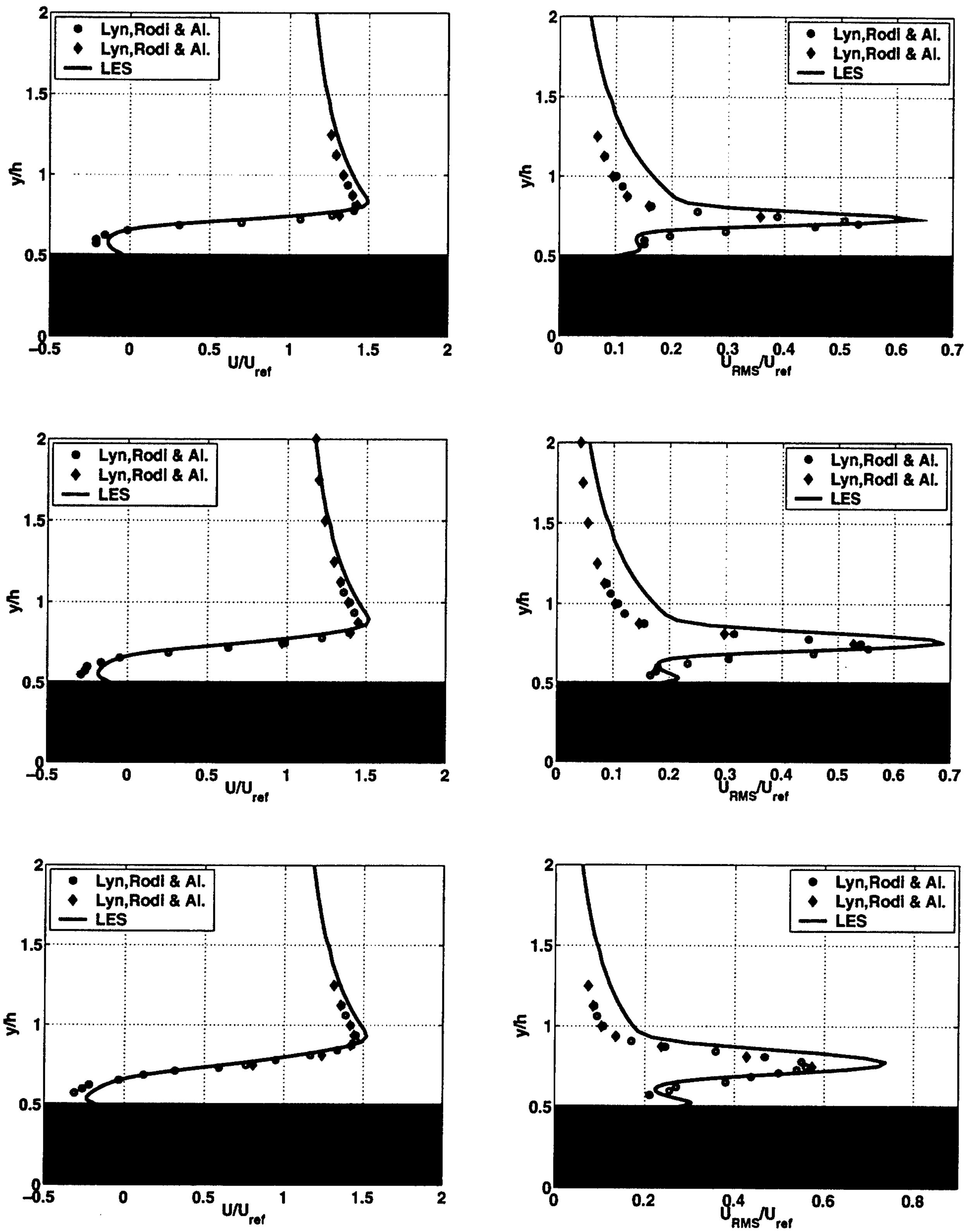

Fig. 2.19: Velocity profiles for stream-wise velocity, left and stream-wise RMS, right, at three stations, from top to bottom: $x = -\frac{1}{8H}$,$x = 0$ and $x = \frac{1}{8H}$.

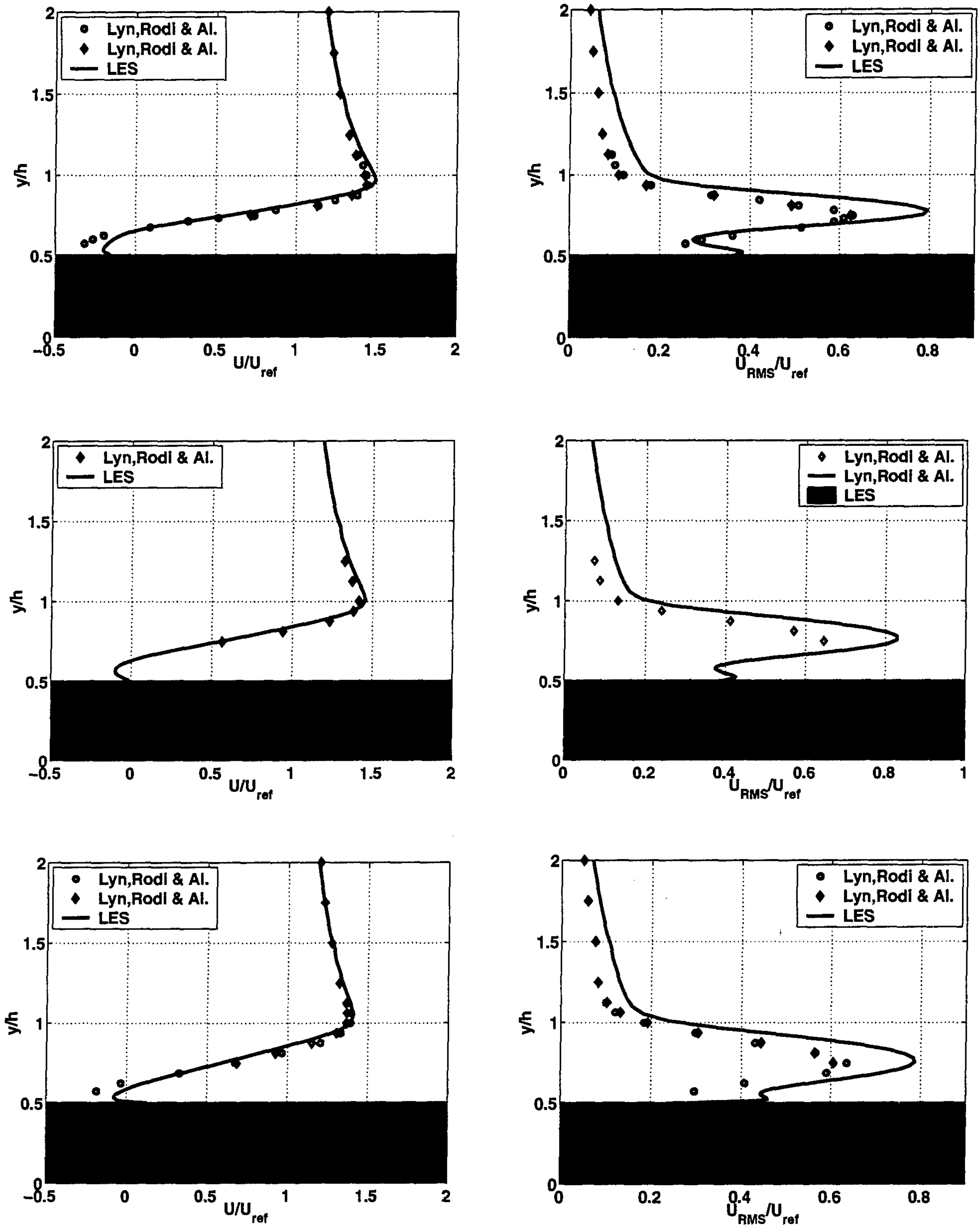

Fig. 2.20: Velocity profiles for stream-wise velocity, left and stream-wise RMS, right, at three stations, from top to bottom: $x = \frac{1}{4H}$,$x = \frac{3}{8H}$ and $x = \frac{1}{2H}$.

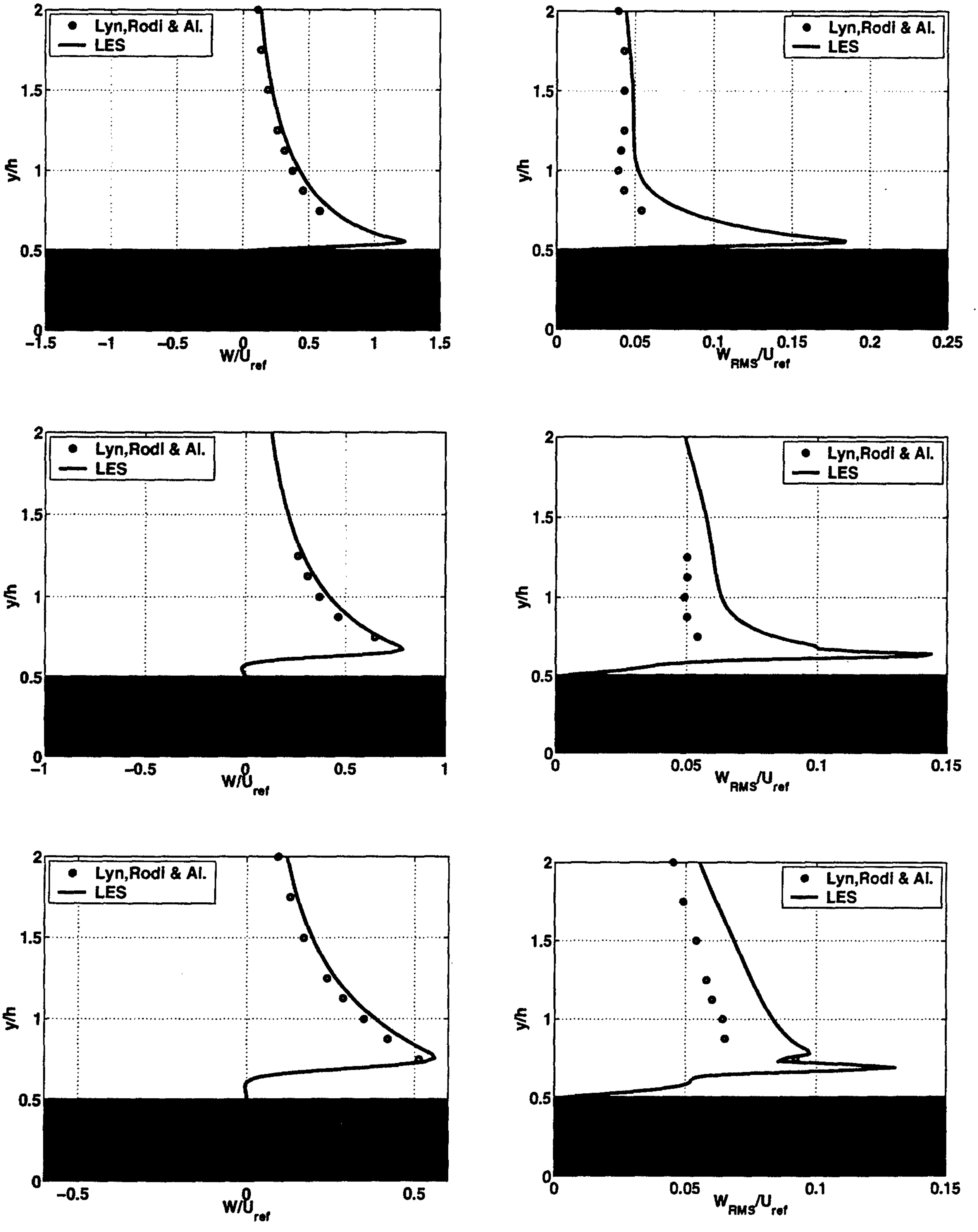

Fig. 2.21: Velocity profiles for vertical velocity, left and vertical RMS, right, at three stations, from top to bottom: $x = -\frac{1}{2H}$,$x = -\frac{3}{8H}$ and $x = -\frac{1}{4H}$.

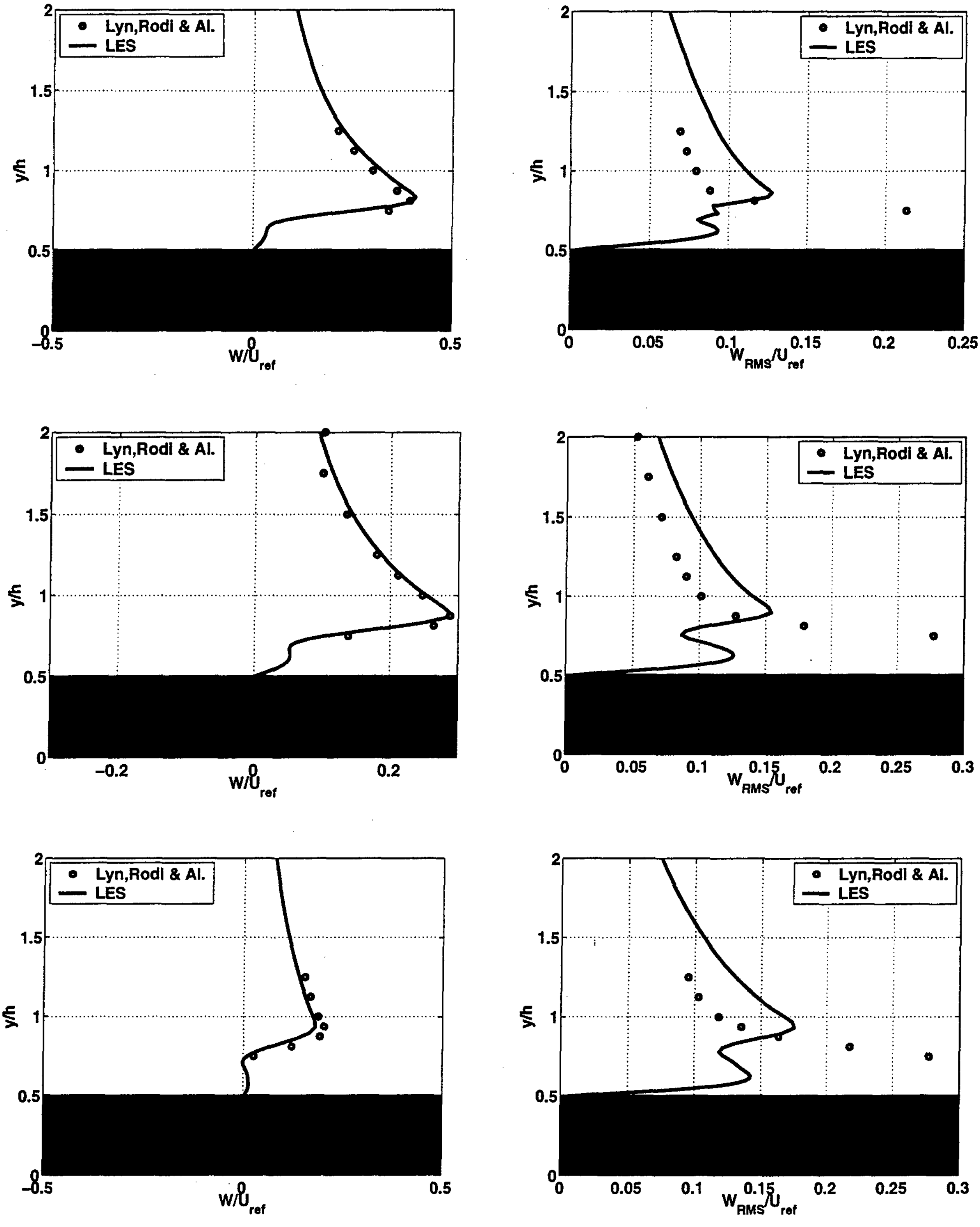

Fig. 2.22: Velocity profiles for vertical velocity, left and vertical RMS, right, at three stations, from top to bottom: $x = -\frac{1}{8H}$, $x = 0$ and $x = \frac{1}{8H}$.

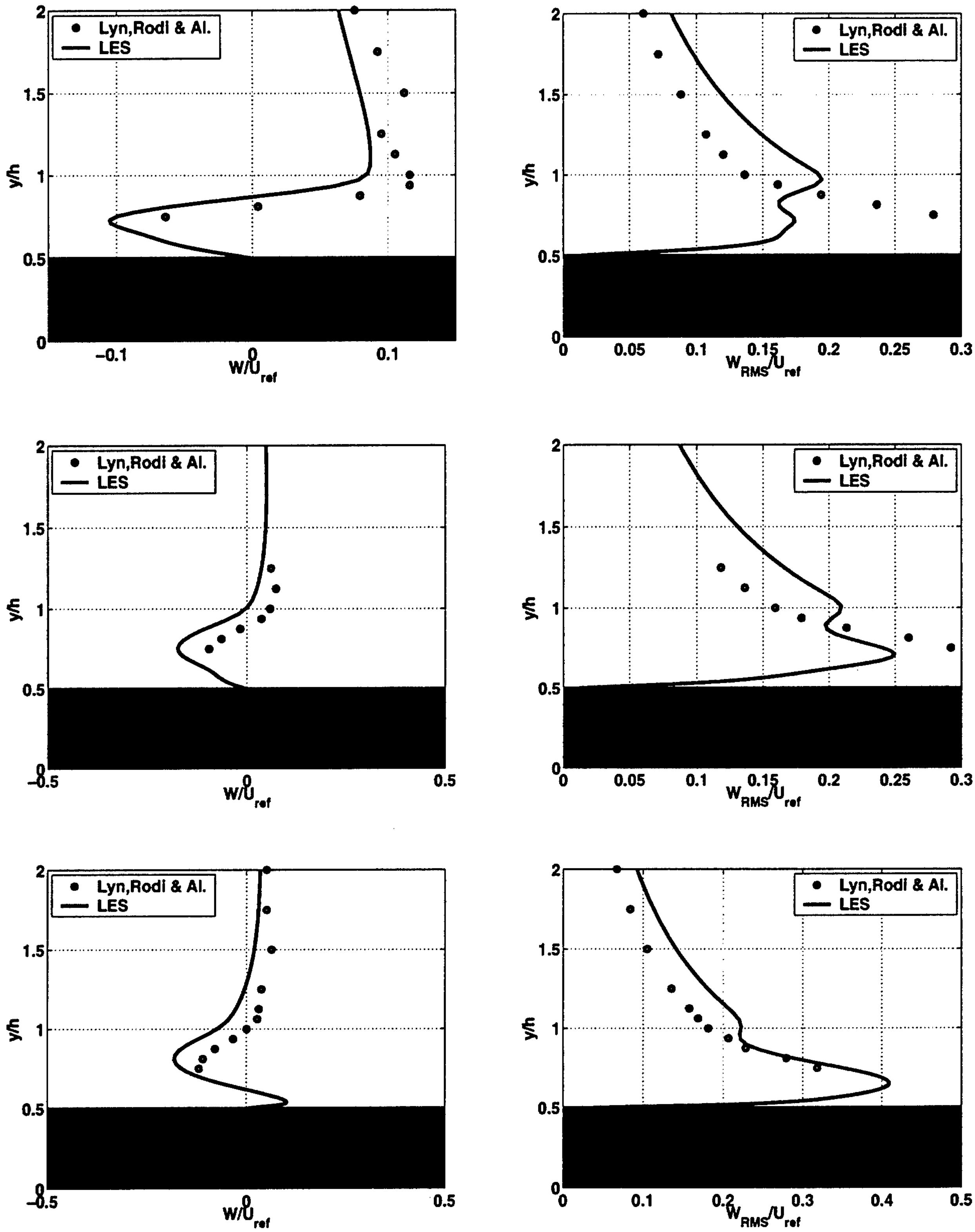

Fig. 2.23: Velocity profiles for vertical velocity, left and vertical RMS, right, at three stations, from top to bottom: $x = \frac{1}{4H}$,$x = \frac{3}{8H}$ and $x = \frac{1}{2H}$.

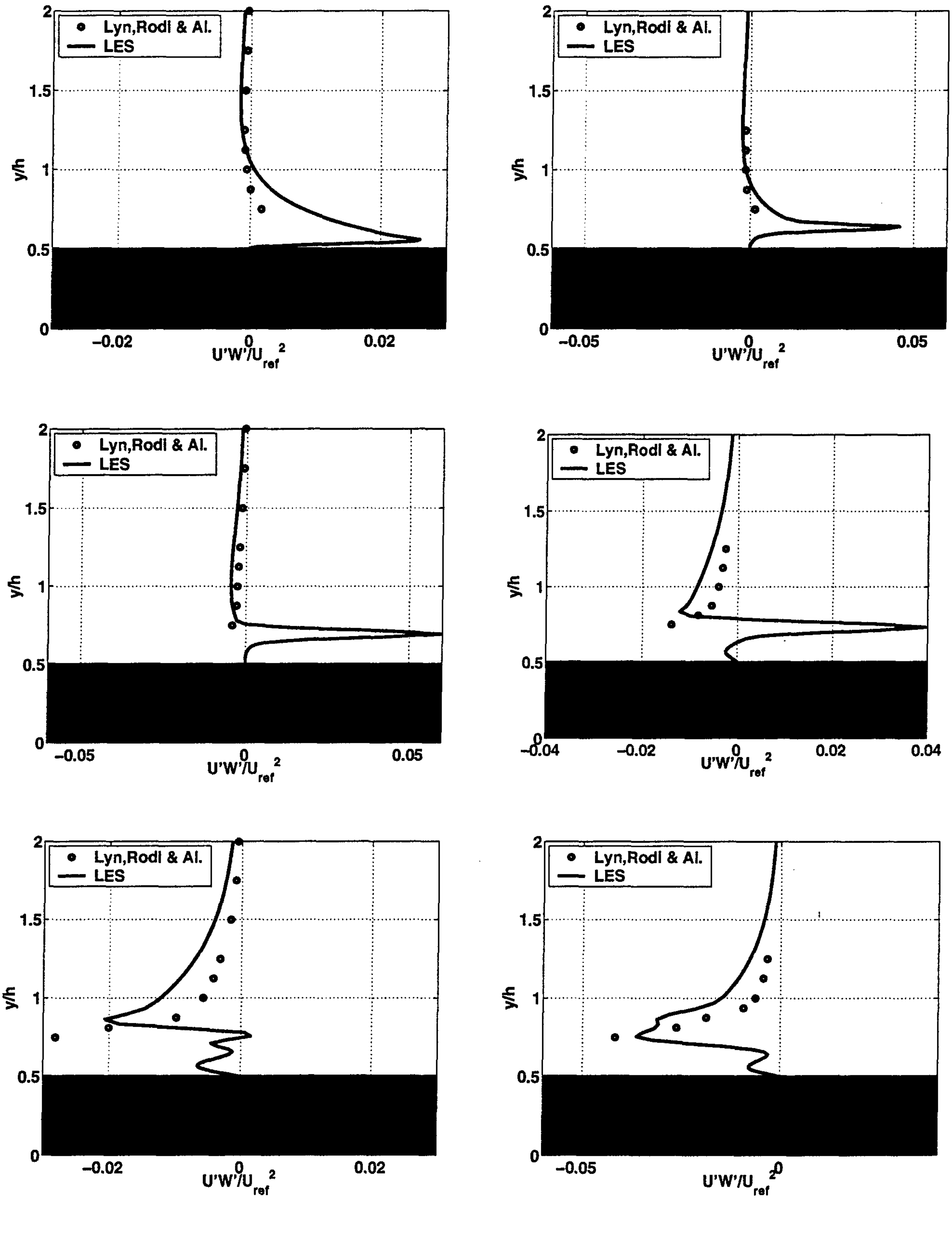

Fig. 2.24: Velocity profiles for turbulent shear stress, from top to bottom and left to right, at the stations: $x = -\frac{1}{2H}$, $x = -\frac{3}{8H}$,$x = -\frac{1}{4H}$,$x = -\frac{1}{8H}$,$x = 0$ and $x = \frac{1}{8H}$

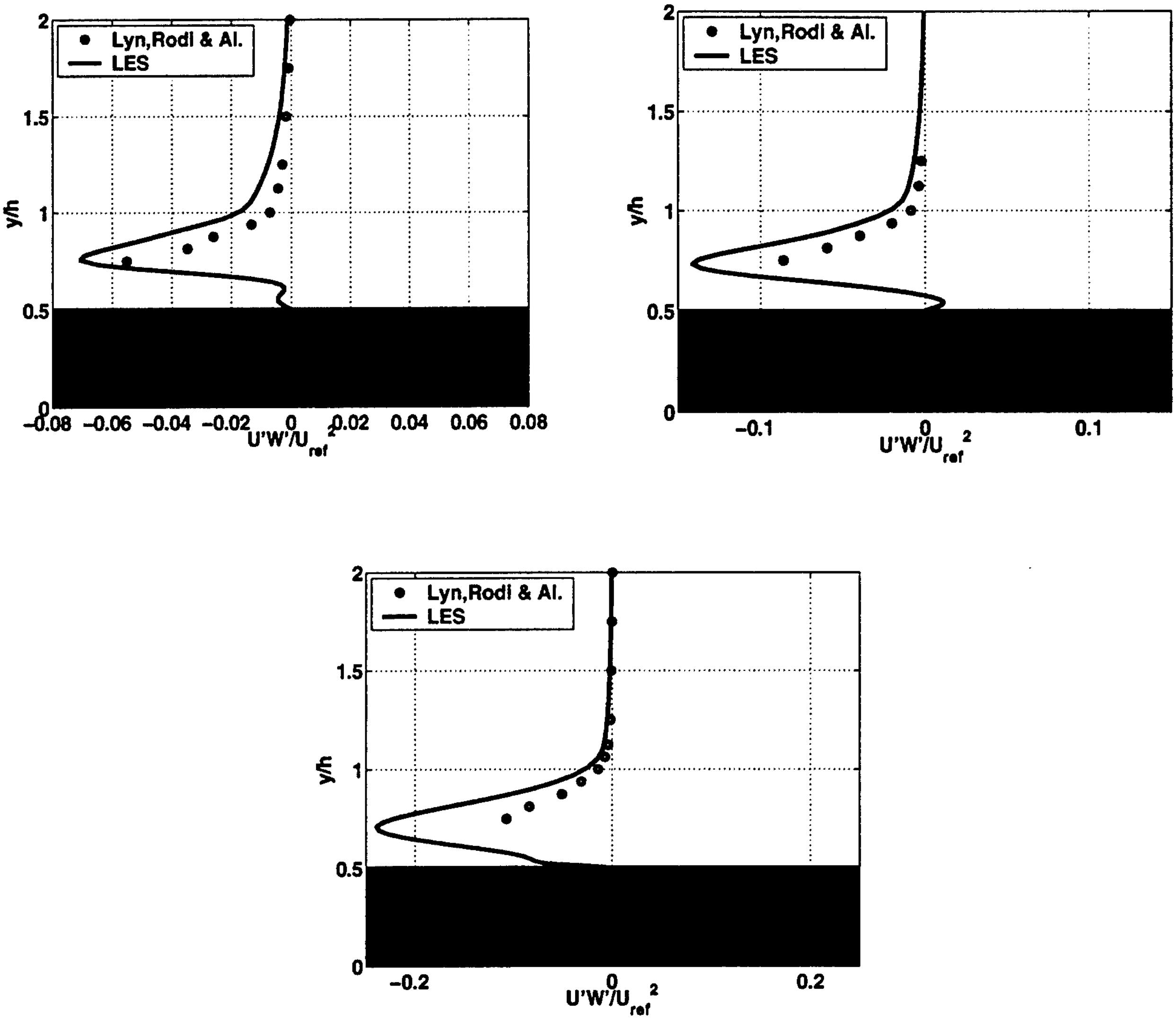

Fig. 2.25: Velocity profiles for turbulent shear stress, from top to bottom and left to right, at the stations: $x = \frac{1}{4H}$, $x = \frac{3}{8H}$ and $x = \frac{1}{2H}$

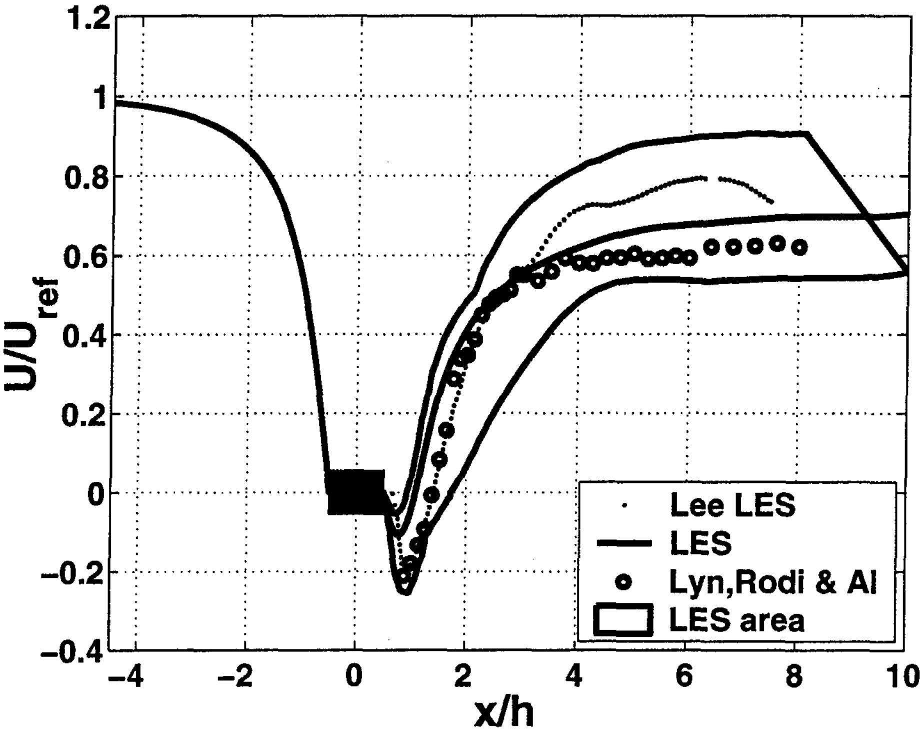

Fig. 2.26: Average stream-wise velocity at wake centerline; present simulation versus experimental data and alternative LES (Sungsu, 1998)

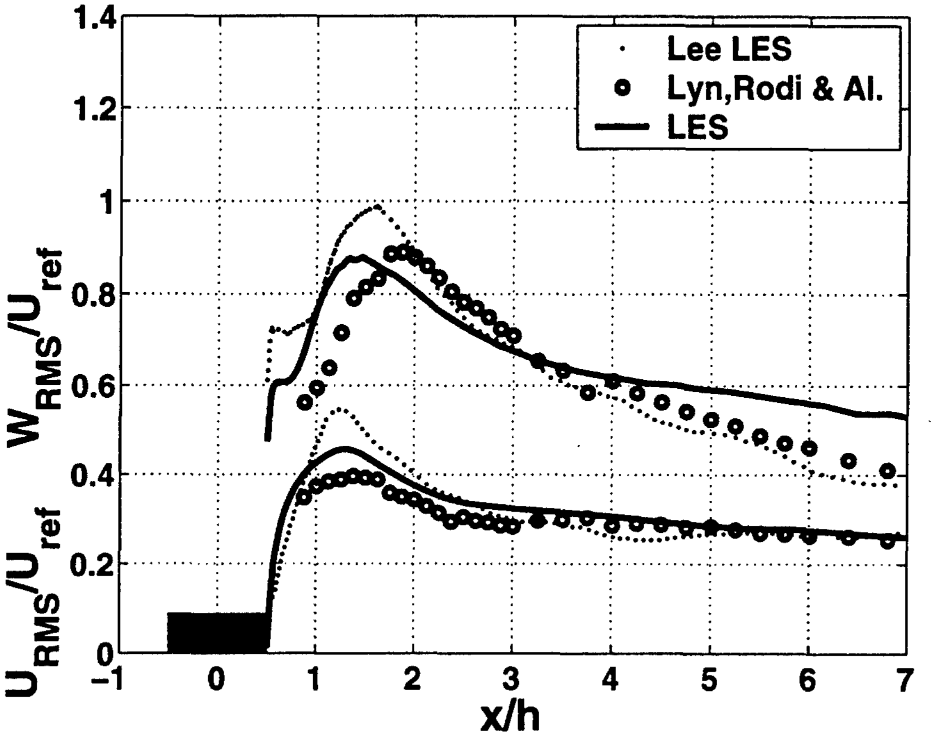

Fig. 2.27: Average stream-wise and vertical velocity RMS at wake centerline; present simulation versus experimental data and alternative LES (Sungsu, 1998)

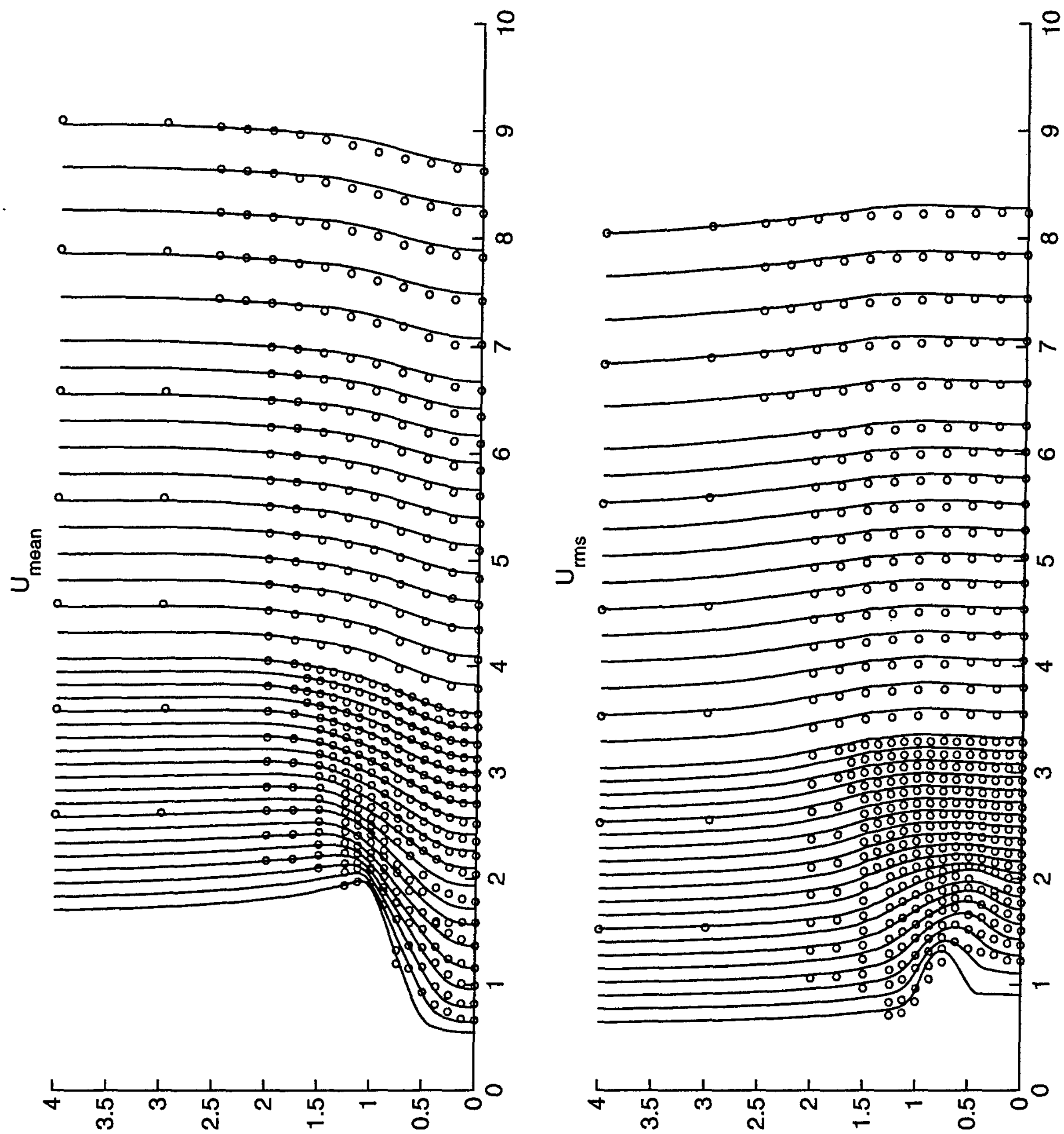

(a) Stream-wise average

(b) Stream-wise RMS

Fig. 2.28: Wake overview, stream-wise velocity comparison with experiments.

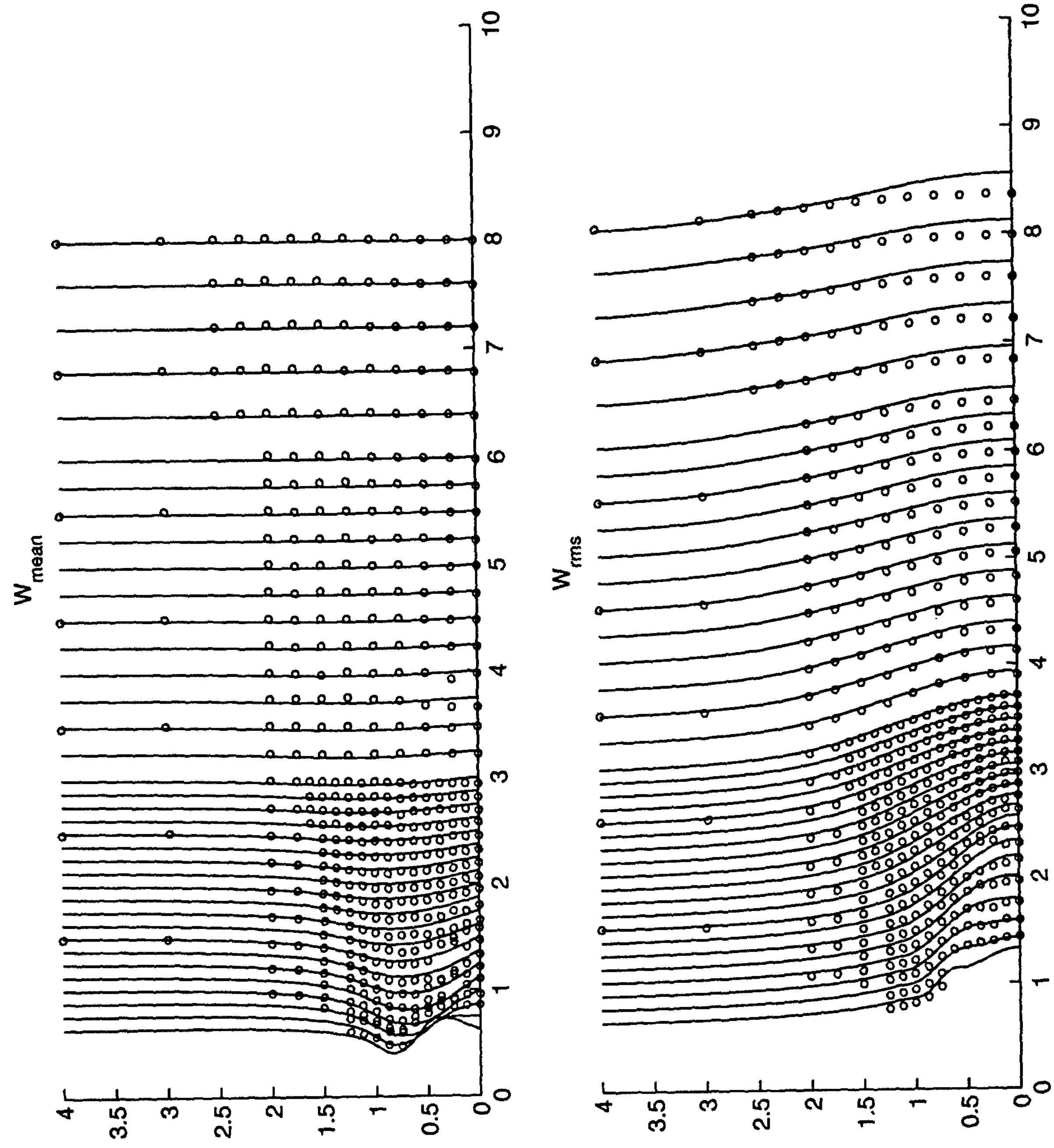

(a) Vertical average

(b) Vertical RMS

Fig. 2.29: Wake overview, vertical velocity comparison with experiments.

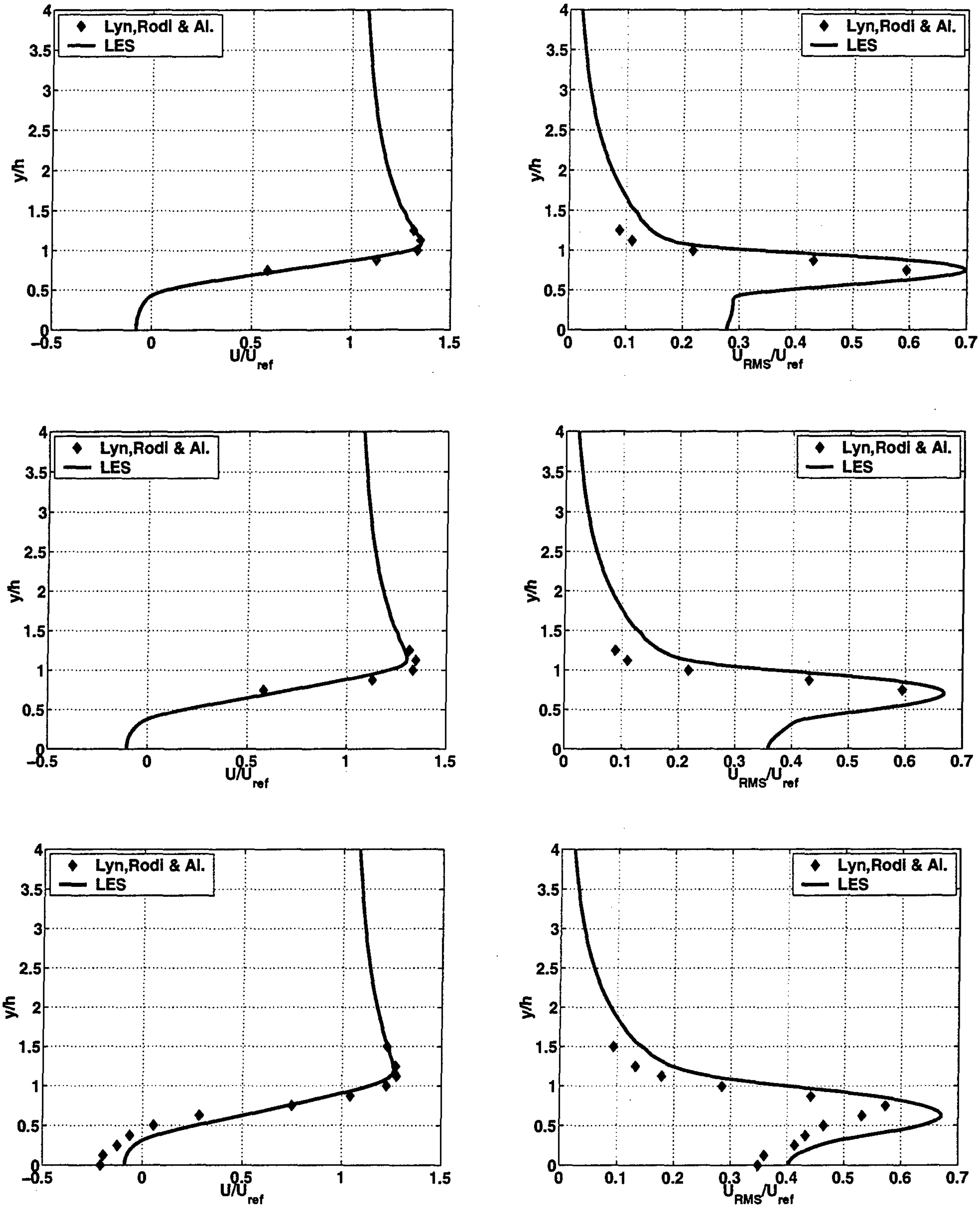

Fig. 2.30: Velocity profiles for stream-wise velocity, left and stream-wise RMS, right, at three stations, from top to bottom: $x = \frac{5}{8H}$,$x = \frac{6}{8H}$ and $x = \frac{7}{8H}$.

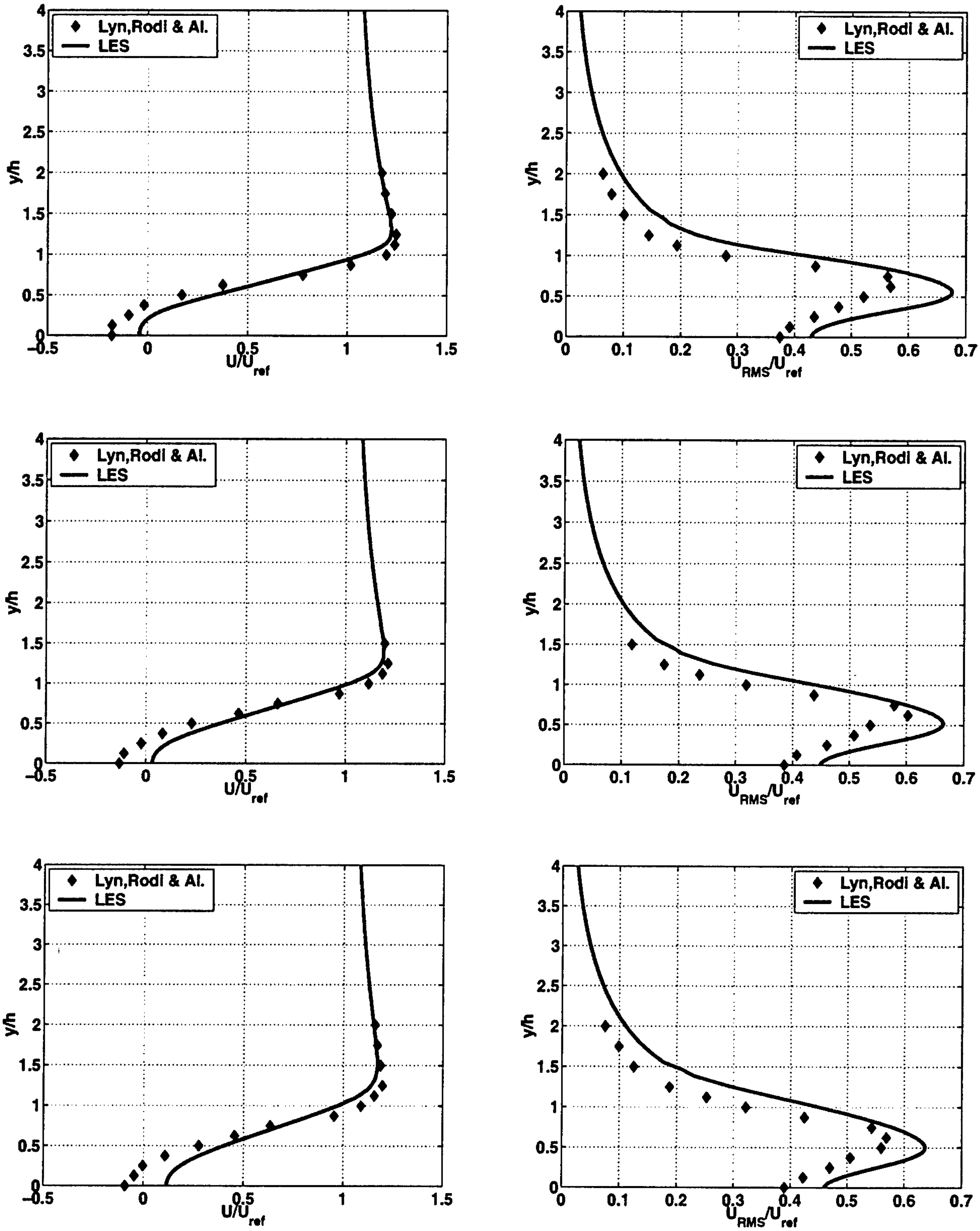

Fig. 2.31: Velocity profiles for stream-wise velocity, left and stream-wise RMS, right, at three stations, from top to bottom: $x = \frac{8}{8H}$,$x = \frac{9}{8H}$ and $x = \frac{10}{8H}$.

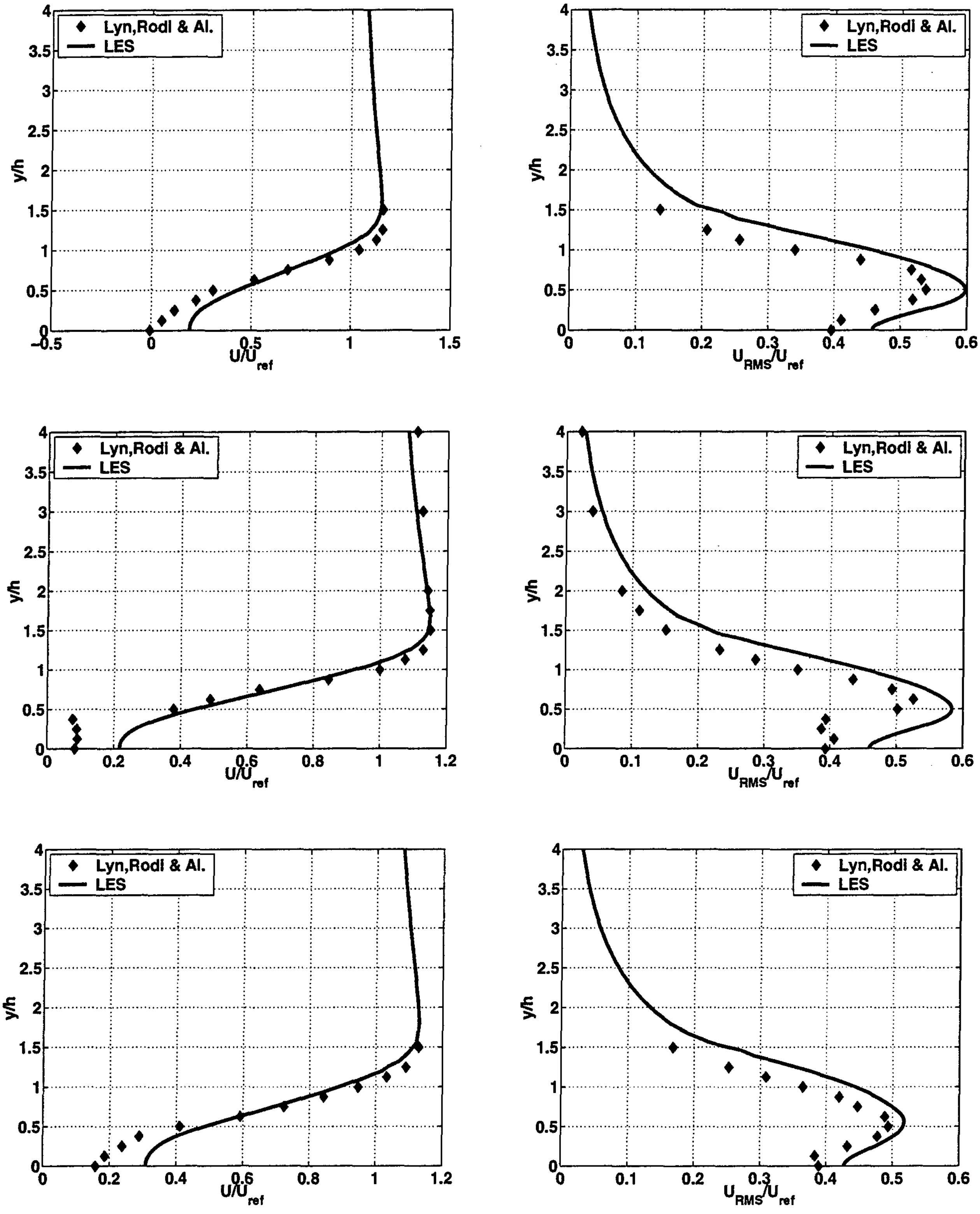

Fig. 2.32: Velocity profiles for stream-wise velocity, left and stream-wise RMS, right, at three stations, from top to bottom: $x = \frac{11}{8H}$,$x = \frac{12}{8H}$ and $x = \frac{13}{8H}$.

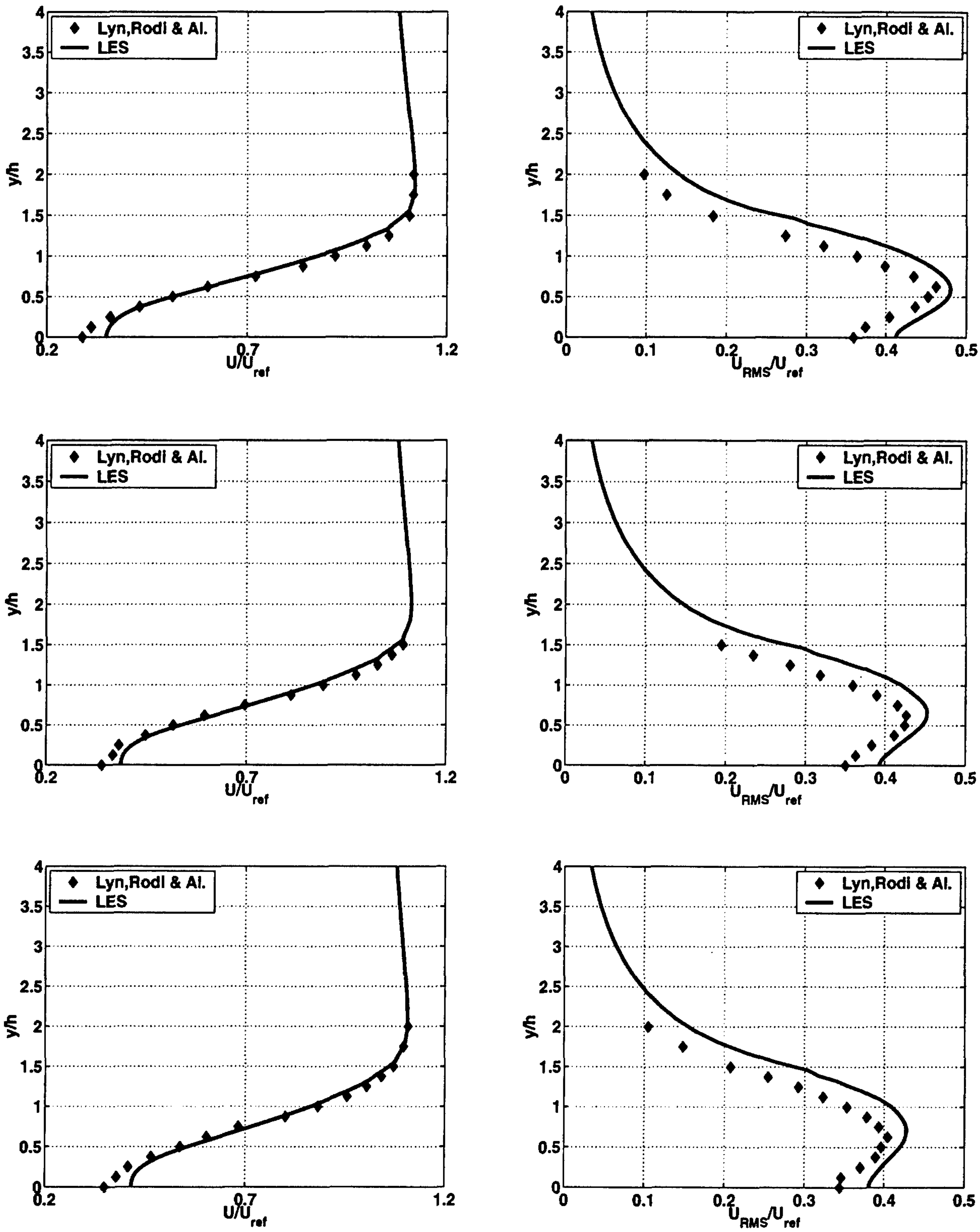

Fig. 2.33: Velocity profiles for stream-wise velocity, left and stream-wise RMS, right, at three stations, from top to bottom: $x = \frac{14}{8H}$,$x = \frac{15}{8H}$ and $x = \frac{16}{8H}$.

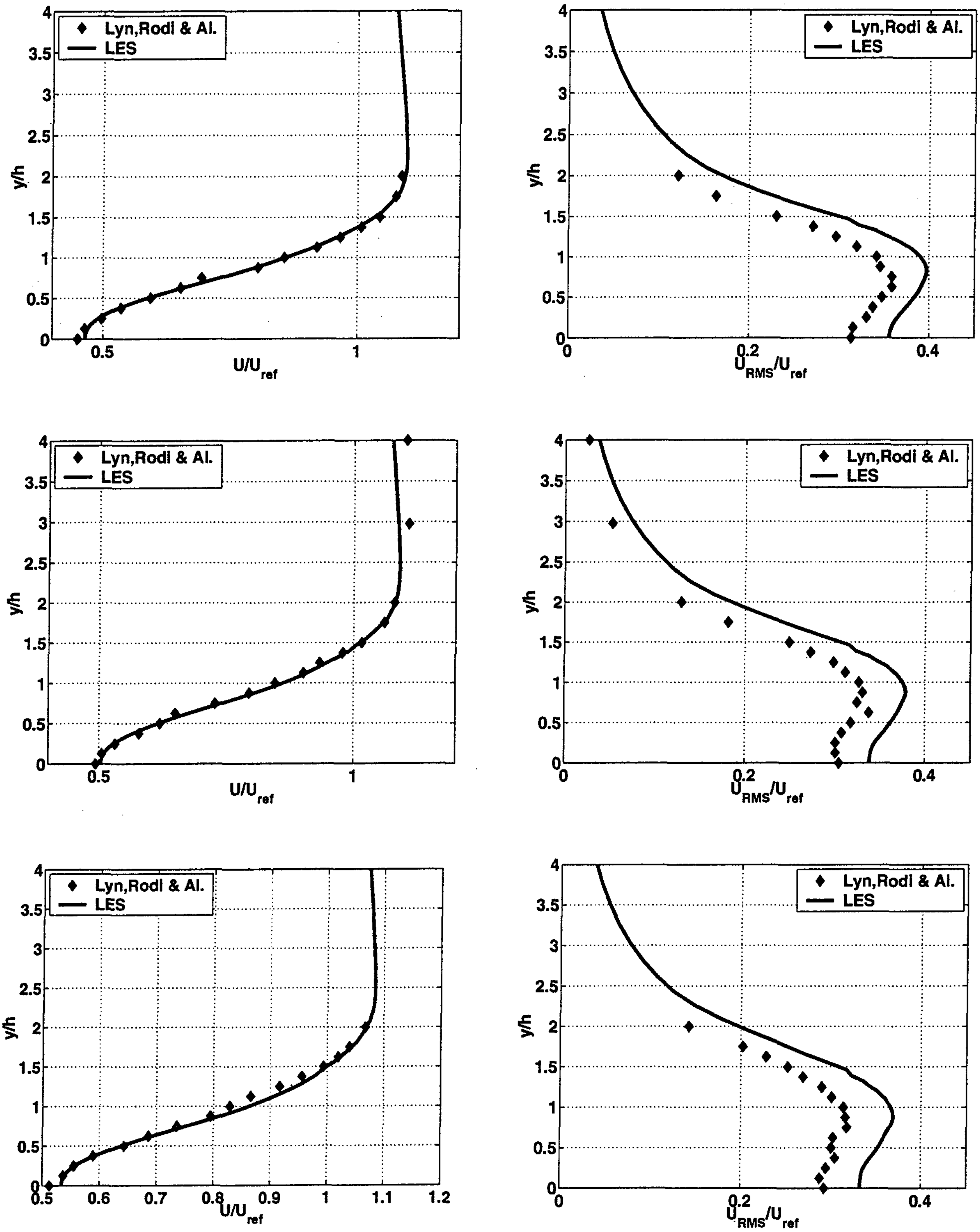

Fig. 2.34: Velocity profiles for stream-wise velocity, left and stream-wise RMS, right, at three stations, from top to bottom: $x = \frac{18}{8H}$,$x = \frac{20}{8H}$ and $x = \frac{22}{8H}$.

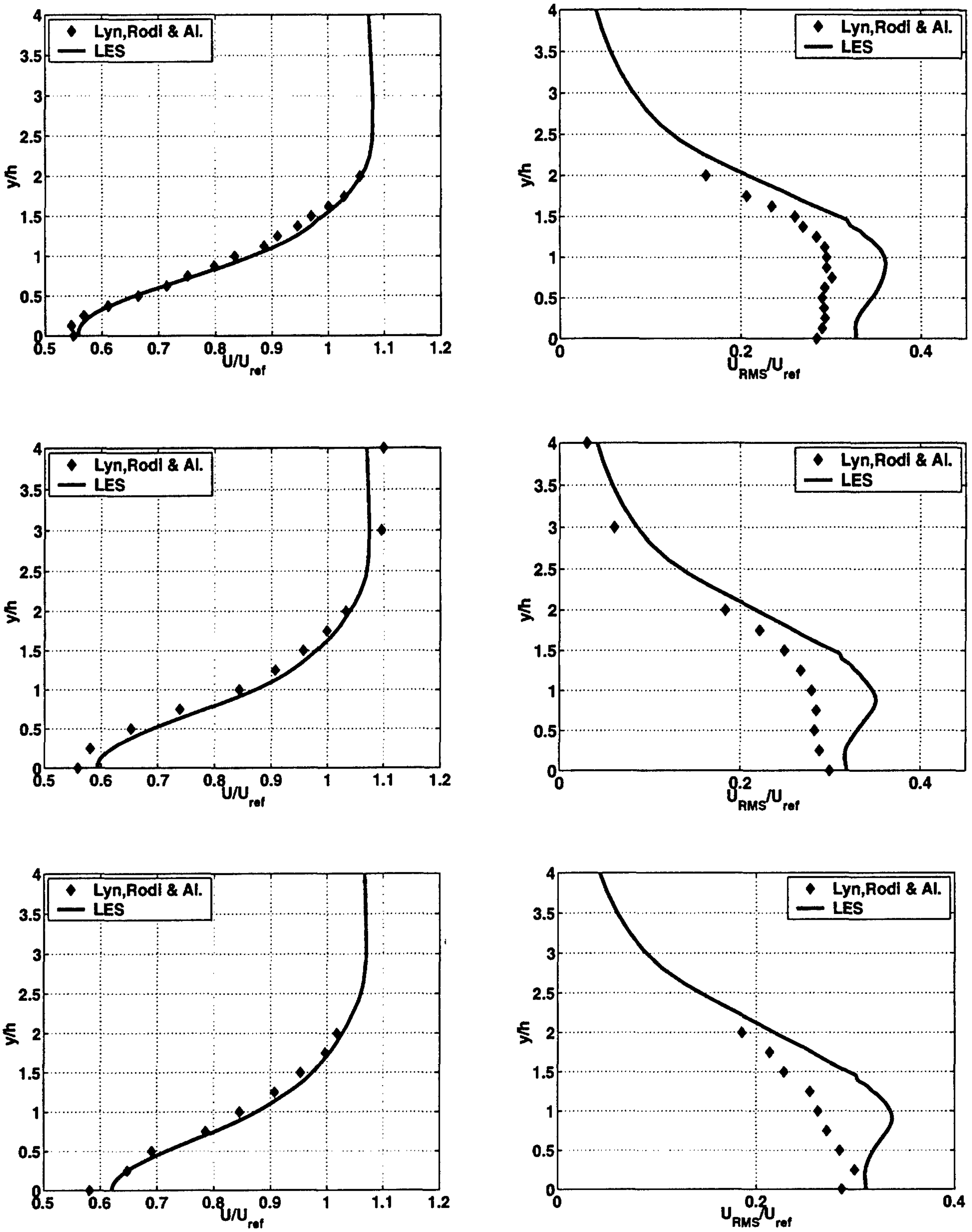

Fig. 2.35: Velocity profiles for stream-wise velocity, left and stream-wise RMS, right, at three stations, from top to bottom: $x = \frac{24}{8H}$,$x = \frac{28}{8H}$ and $x = \frac{32}{8H}$.

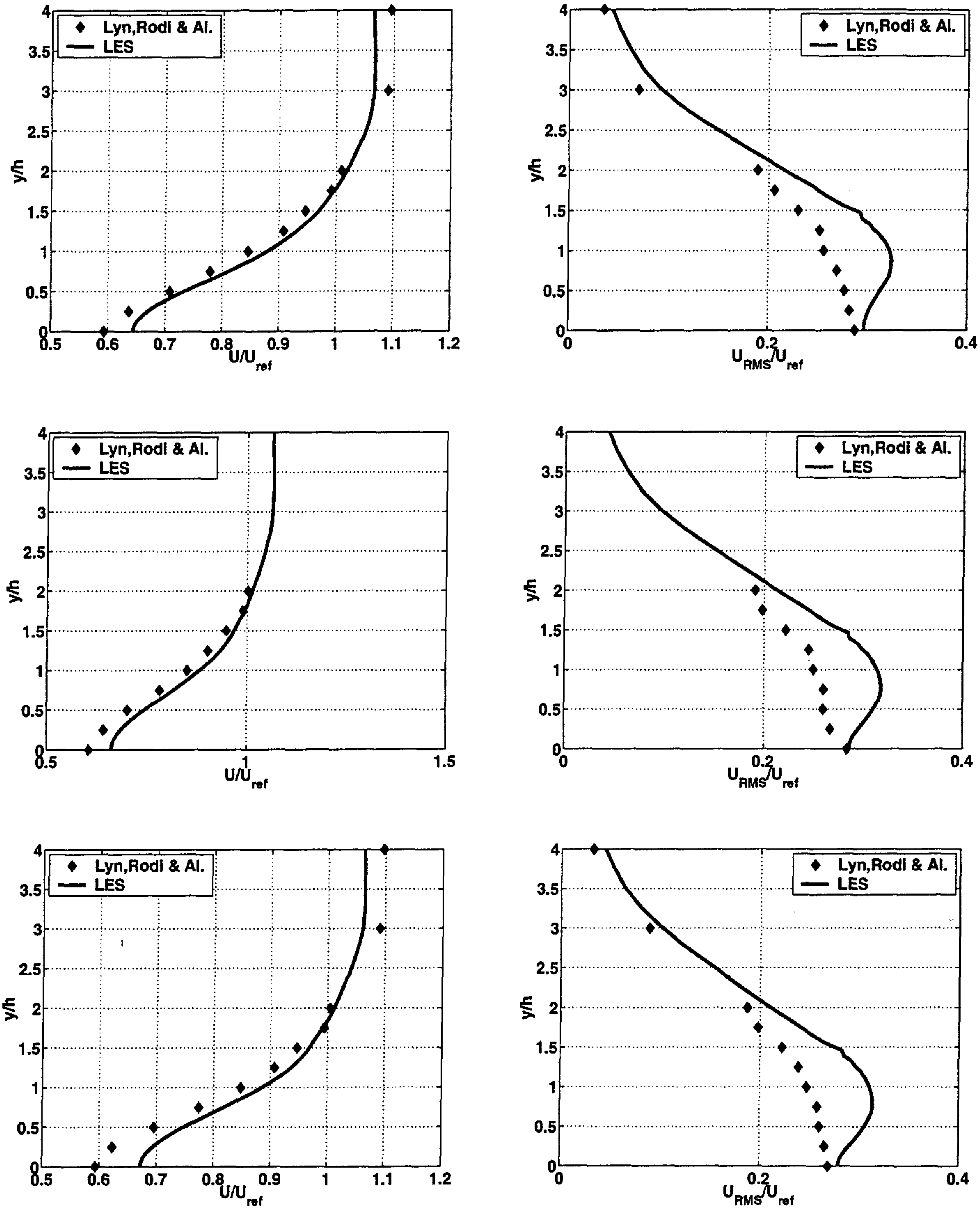

Fig. 2.36: Velocity profiles for stream-wise velocity, left and stream-wise RMS, right, at three stations, from top to bottom: $x = \frac{36}{8H}$,$x = \frac{40}{8H}$ and $x = \frac{44}{8H}$.

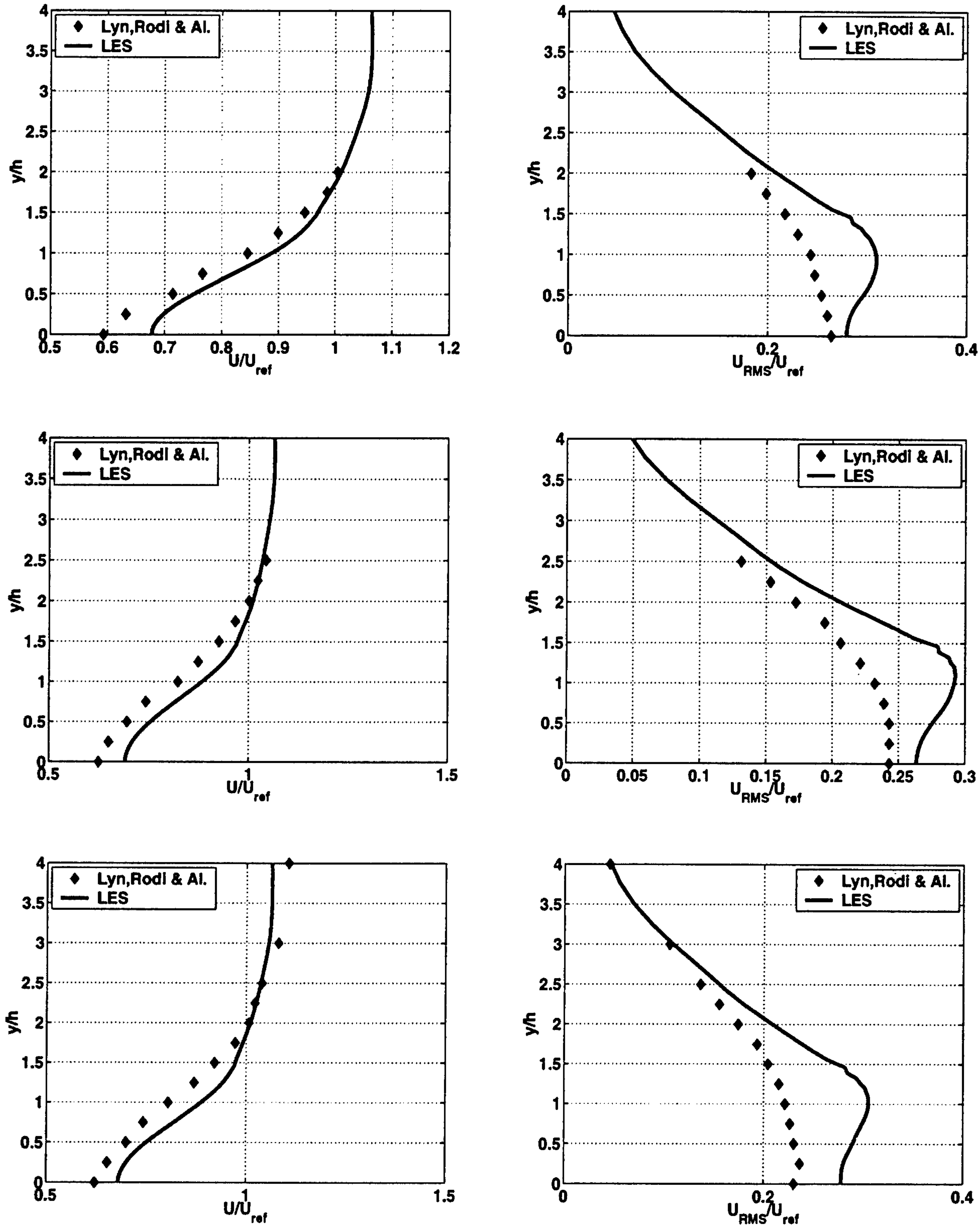

Fig. 2.37: Velocity profiles for stream-wise velocity, left and stream-wise RMS, right, at three stations, from top to bottom: $x = \frac{48}{8H}$,$x = \frac{57.6}{8H}$ and $x = \frac{64}{8H}$.

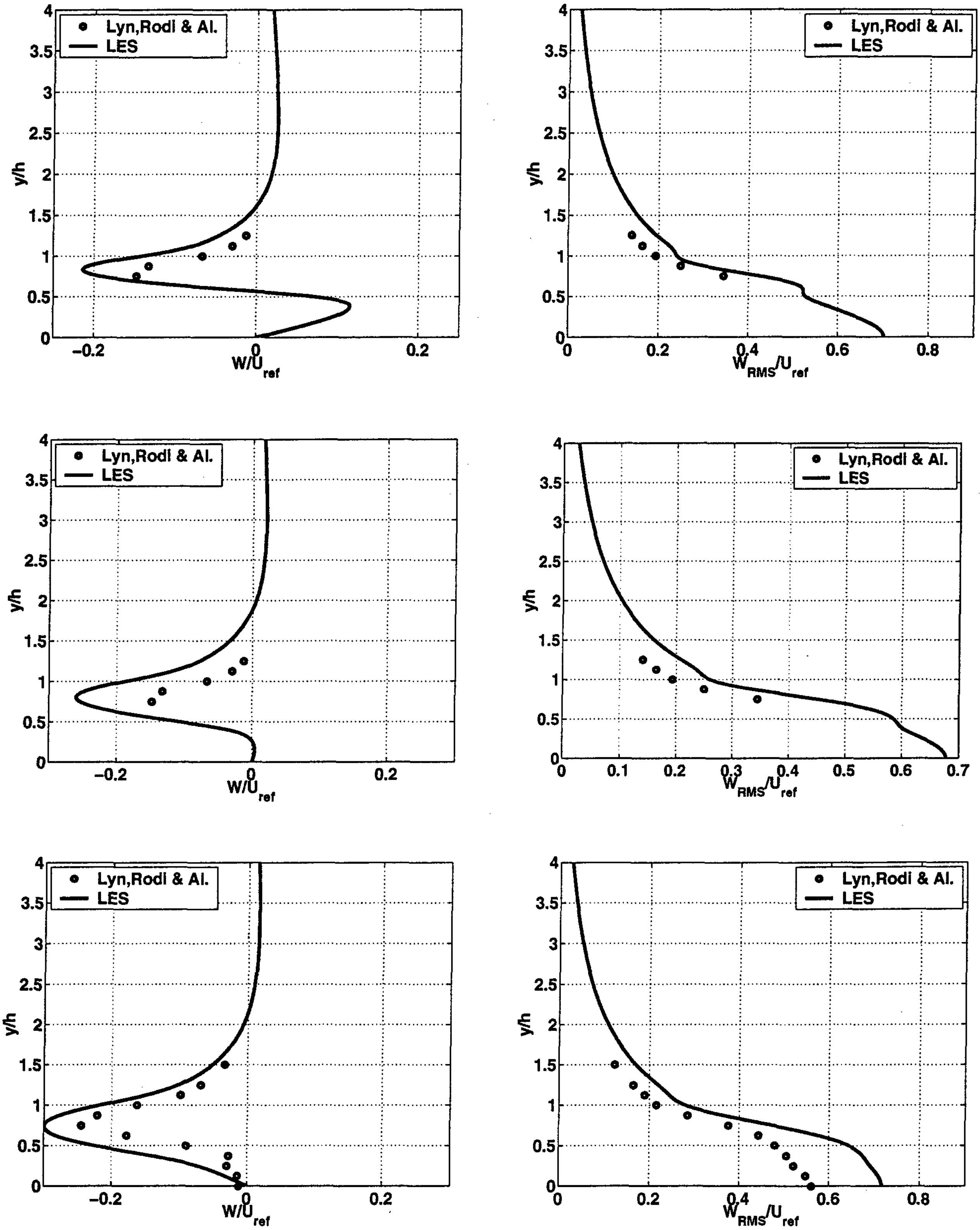

Fig. 2.38: Velocity profiles for vertical velocity, left and vertical RMS, right, at three stations, from top to bottom: $x = \frac{5}{8H}$,$x = \frac{6}{8H}$ and $x = \frac{7}{8H}$.

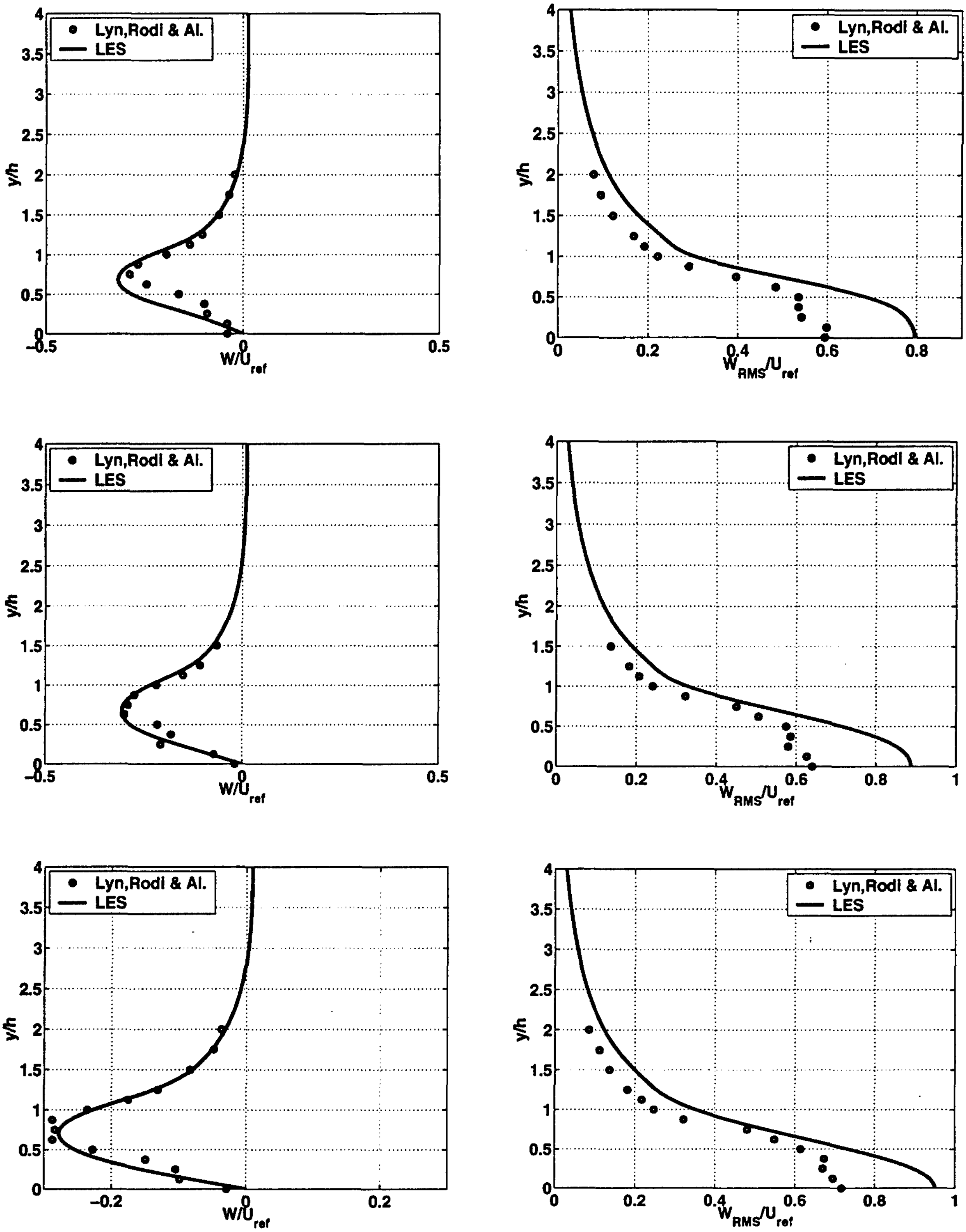

Fig. 2.39: Velocity profiles for vertical velocity, left and vertical RMS, right, at three stations, from top to bottom: $x = \frac{8}{8H}$,$x = \frac{9}{8H}$ and $x = \frac{10}{8H}$.

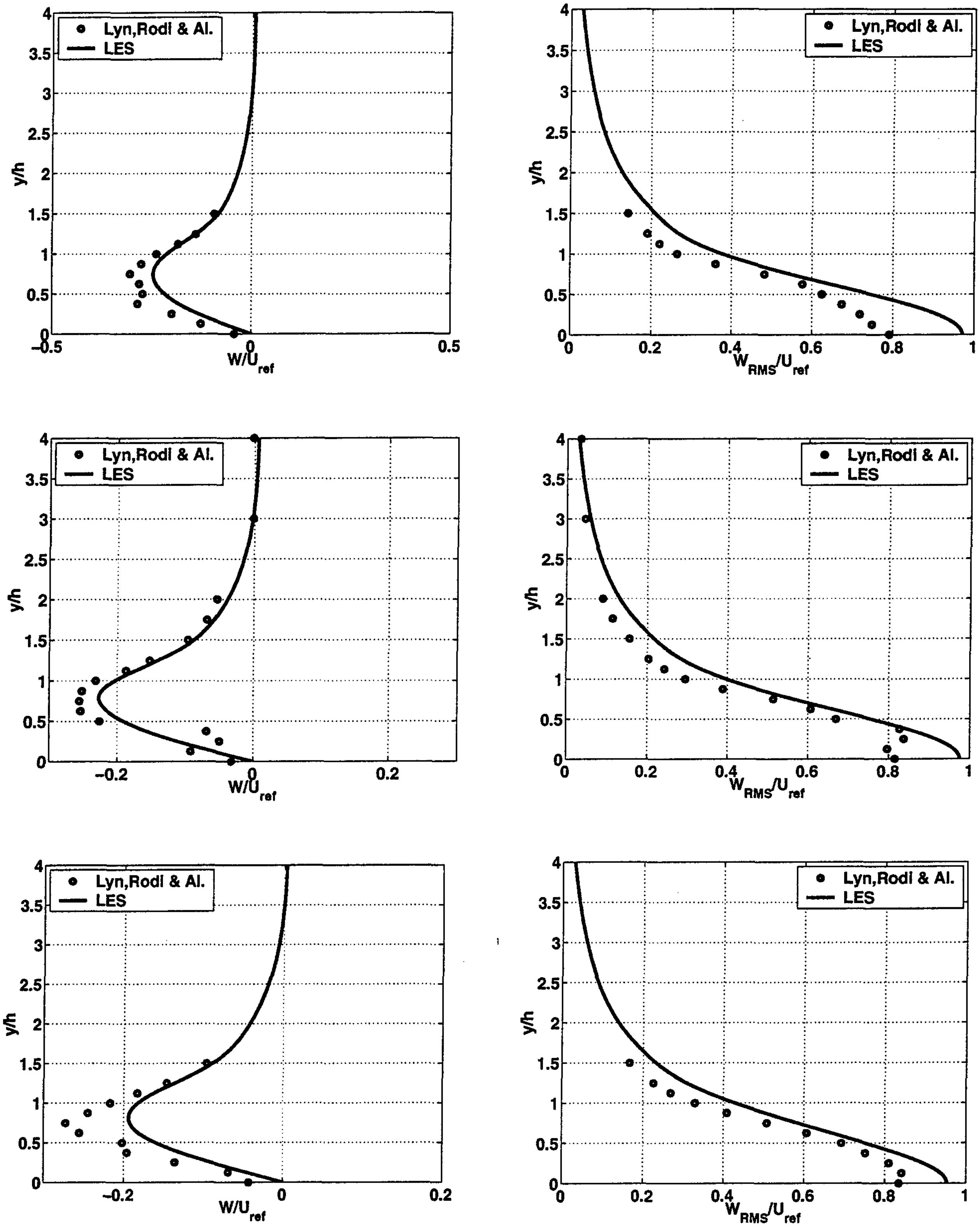

Fig. 2.40: Velocity profiles for vertical velocity, left and vertical RMS, right, at three stations, from top to bottom: $x = \frac{11}{8H}$,$x = \frac{12}{8H}$ and $x = \frac{13}{8H}$.

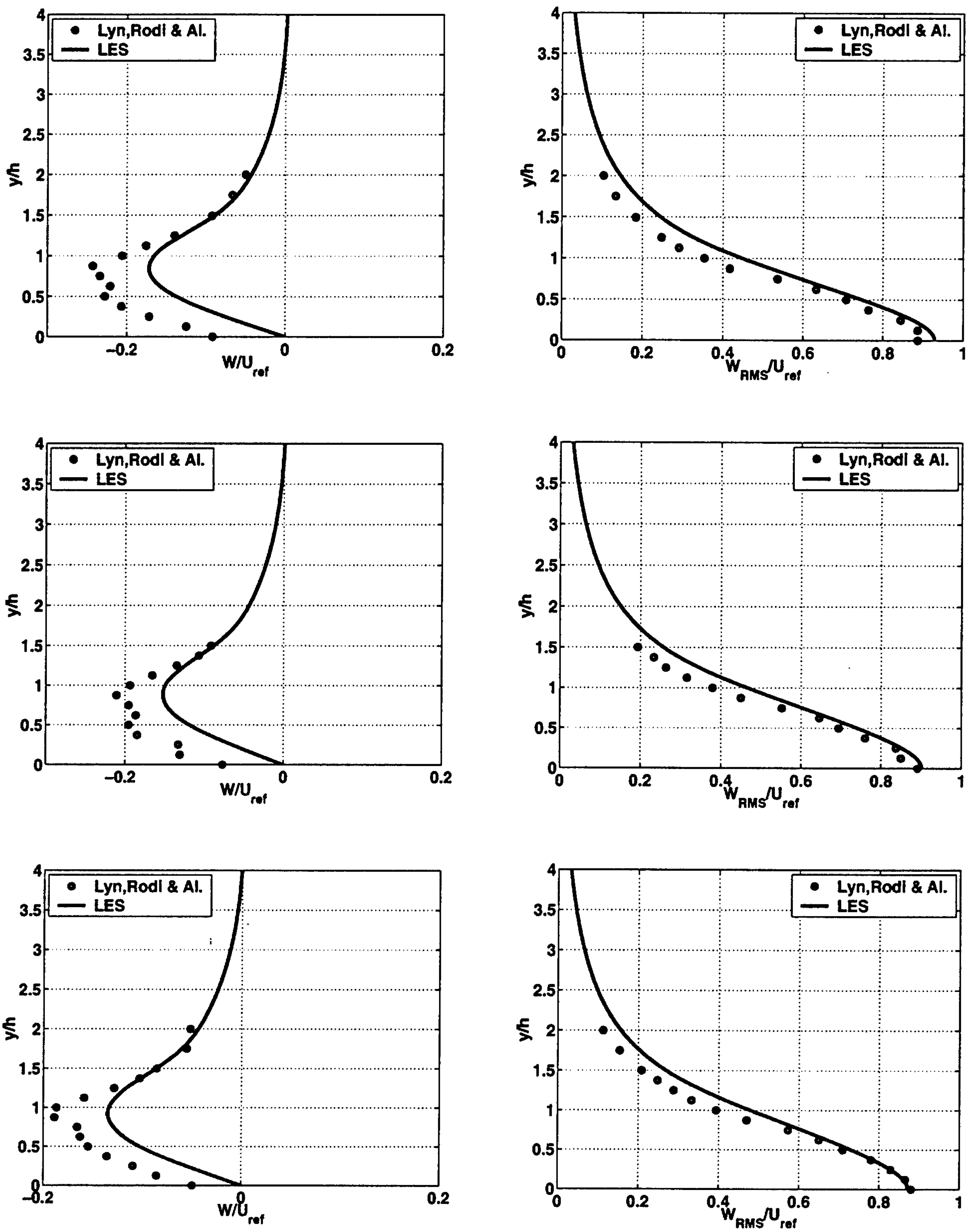

Fig. 2.41: Velocity profiles for vertical velocity, left and vertical RMS, right, at three stations, from top to bottom: $x = \frac{14}{8H}$,$x = \frac{15}{8H}$ and $x = \frac{16}{8H}$.

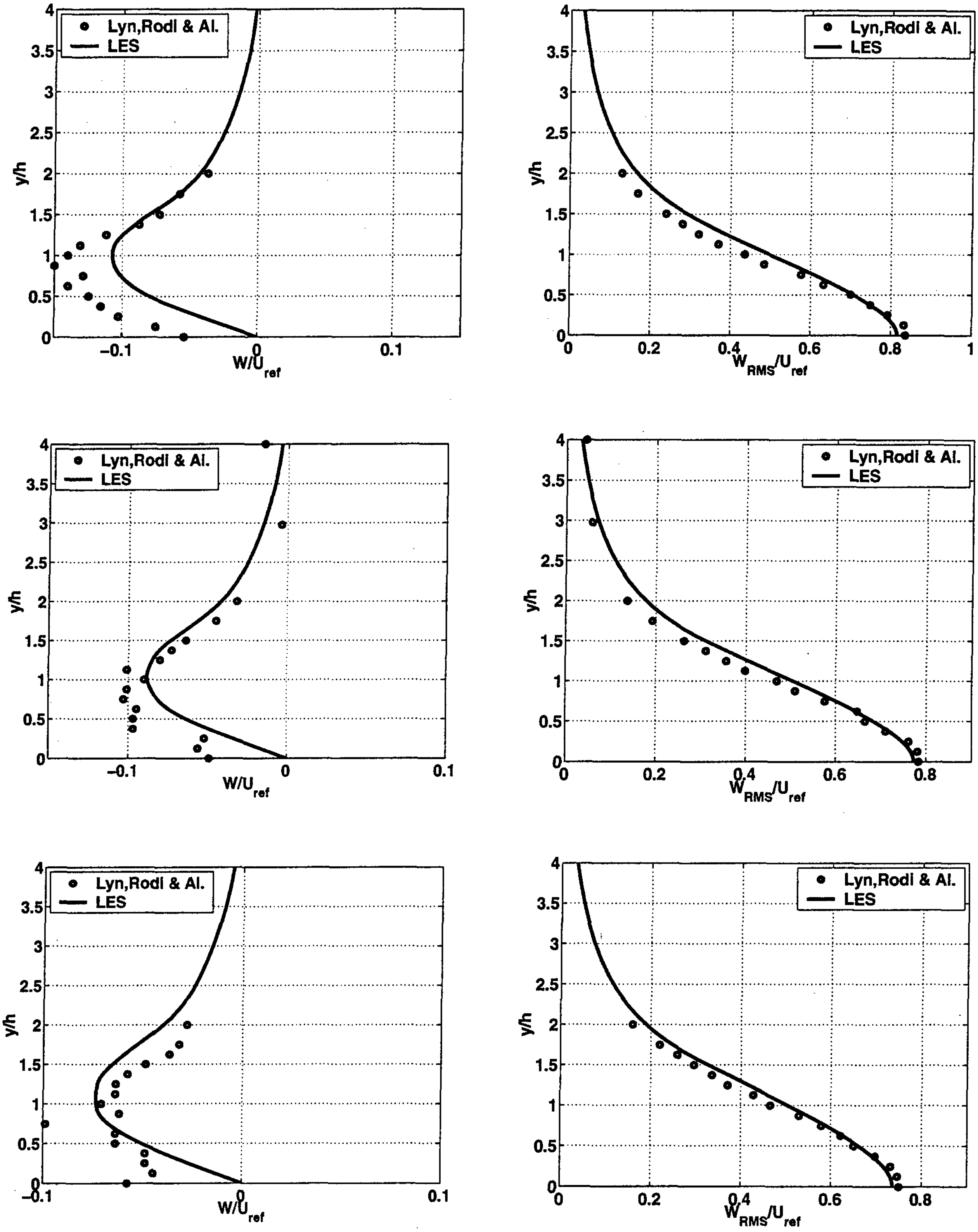

Fig. 2.42: Velocity profiles for vertical velocity, left and vertical RMS, right, at three stations, from top to bottom: $x = \frac{18}{8H}$,$x = \frac{20}{8H}$ and $x = \frac{22}{8H}$.

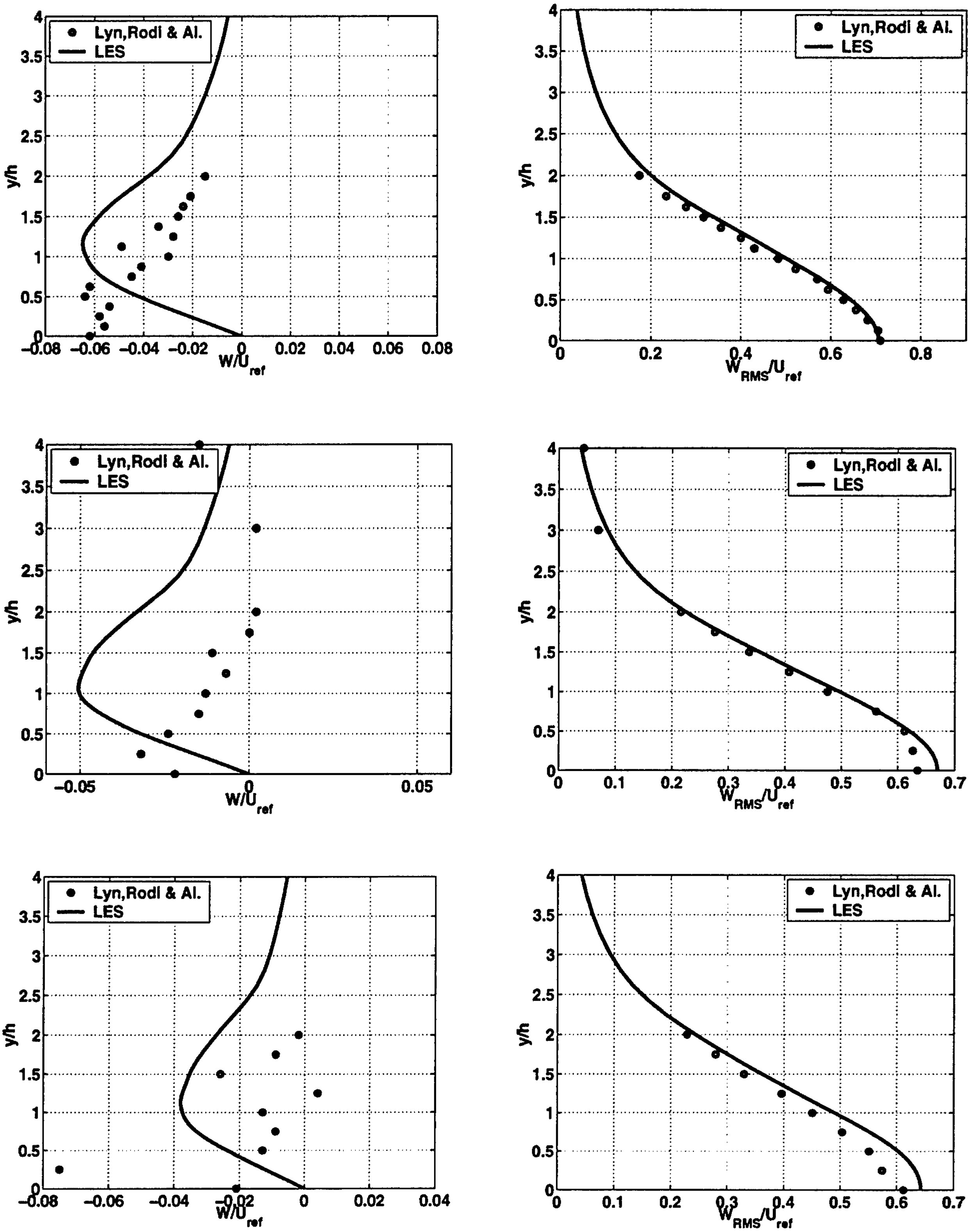

Fig. 2.43: Velocity profiles for vertical velocity, left and vertical RMS, right, at three stations, from top to bottom: $x = \frac{24}{8H}$,$x = \frac{28}{8H}$ and $x = \frac{32}{8H}$.

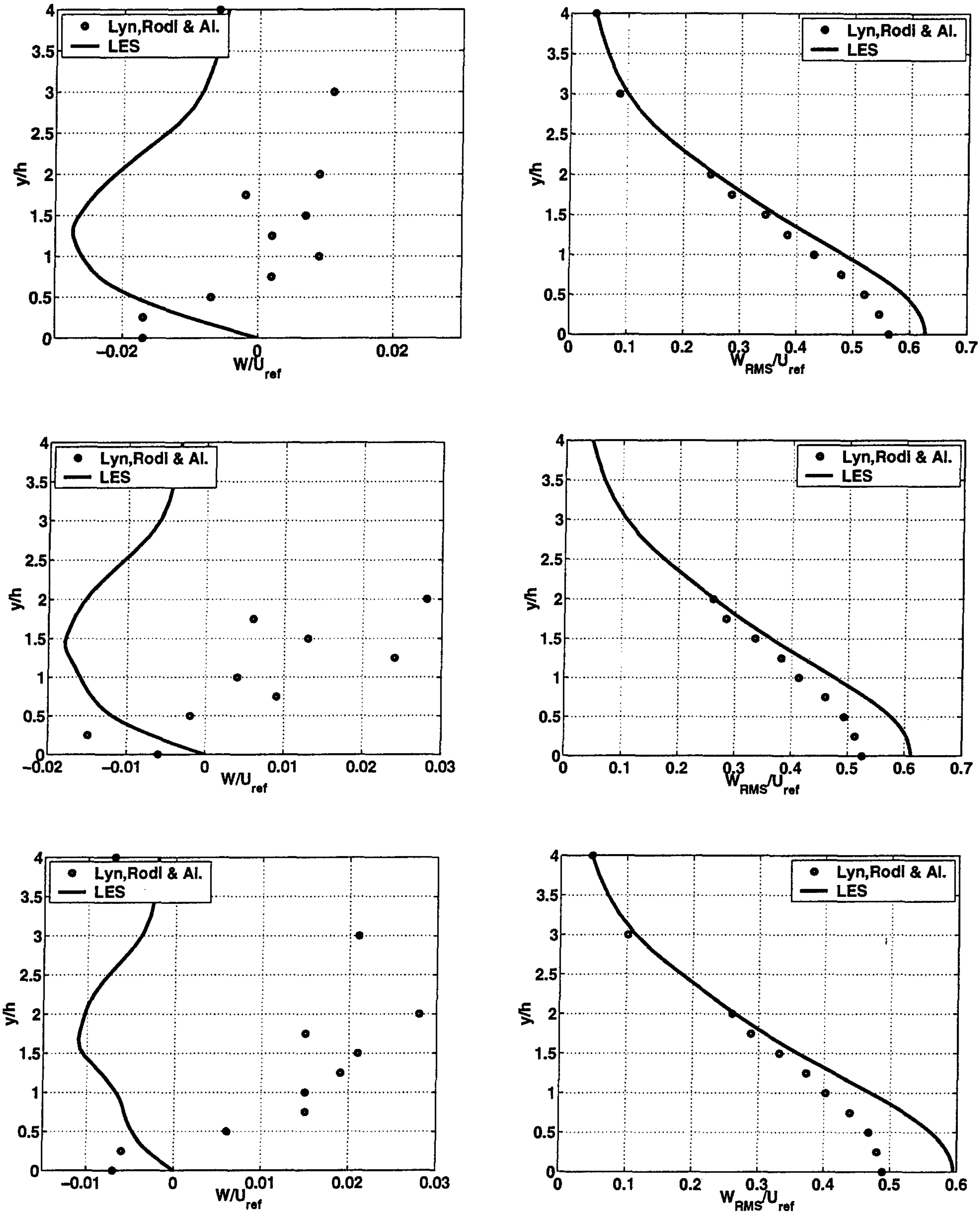

Fig. 2.44: Velocity profiles for vertical velocity, left and vertical RMS, right, at three stations, from top to bottom: $x = \frac{36}{8H}$,$x = \frac{40}{8H}$ and $x = \frac{44}{8H}$.

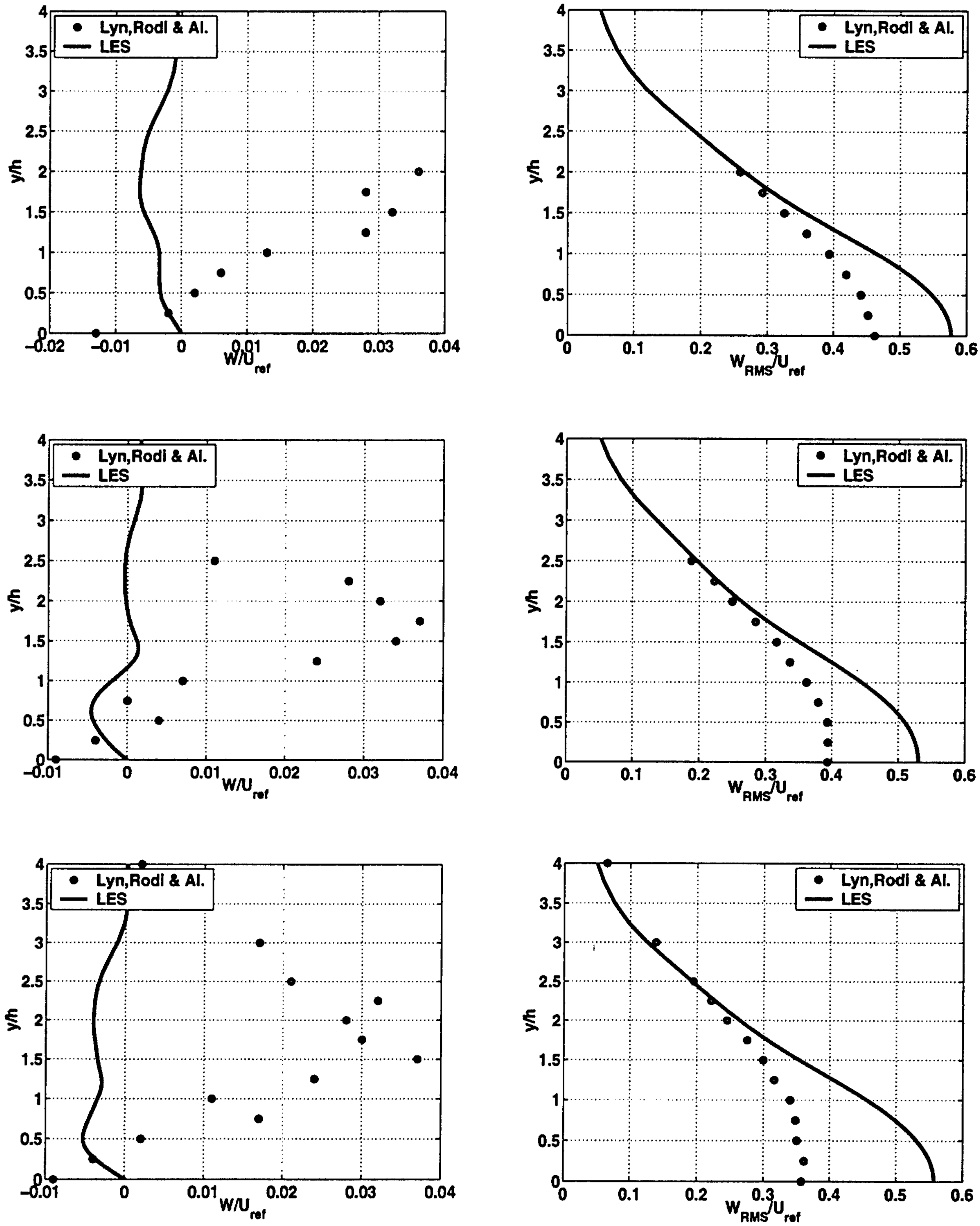

Fig. 2.45: Velocity profiles for vertical velocity, left and vertical RMS, right, at three stations, from top to bottom: $x = \frac{48}{8H}$,$x = \frac{57.6}{8H}$ and $x = \frac{64}{8H}$.

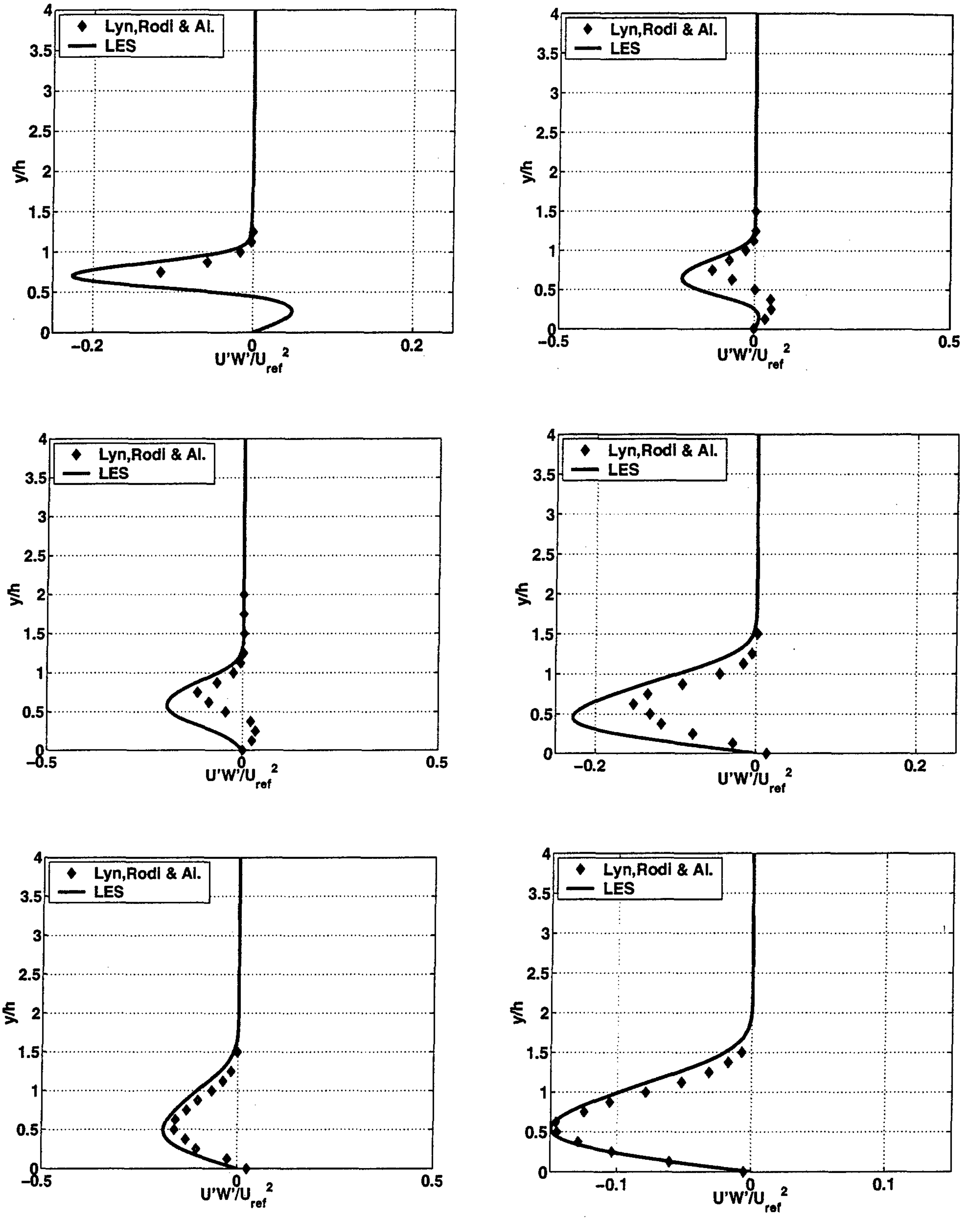

Fig. 2.46: Velocity profiles for turbulent stress from top to bottom and from left to right: $x = \frac{5}{8H}$,$x = \frac{7}{8H}$,$x = \frac{8}{8H}$, $x = \frac{11}{8H}$,$x = \frac{13}{8H}$ and $x = \frac{15}{8H}$.

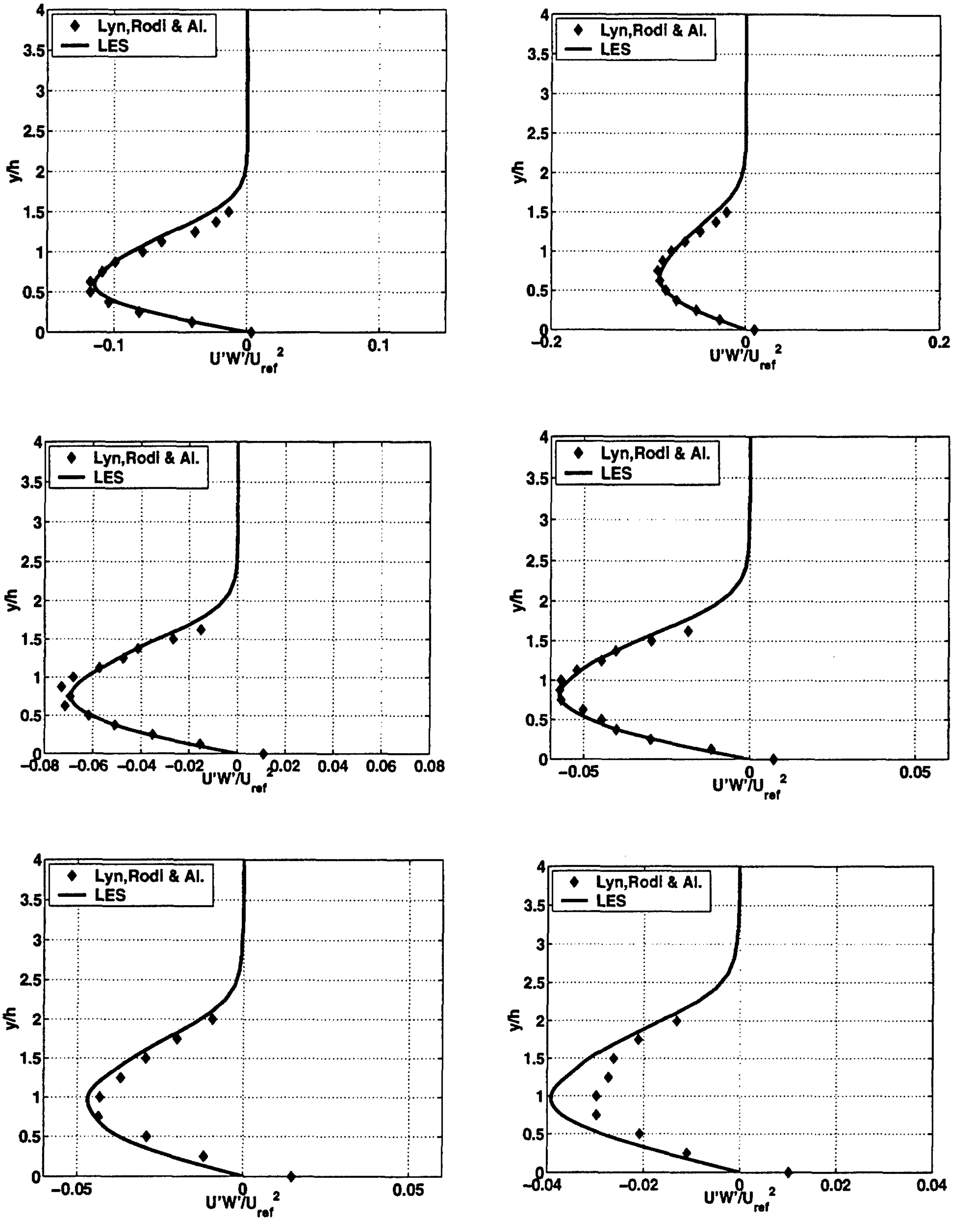

Fig. 2.47: Velocity profiles for turbulent stress from top to bottom and from left to right: $x = \frac{17}{8H}$,$x = \frac{19}{8H}$,$x = \frac{21}{8H}$, $x = \frac{23}{8H}$,$x = \frac{26}{8H}$ and $x = \frac{30}{8H}$.

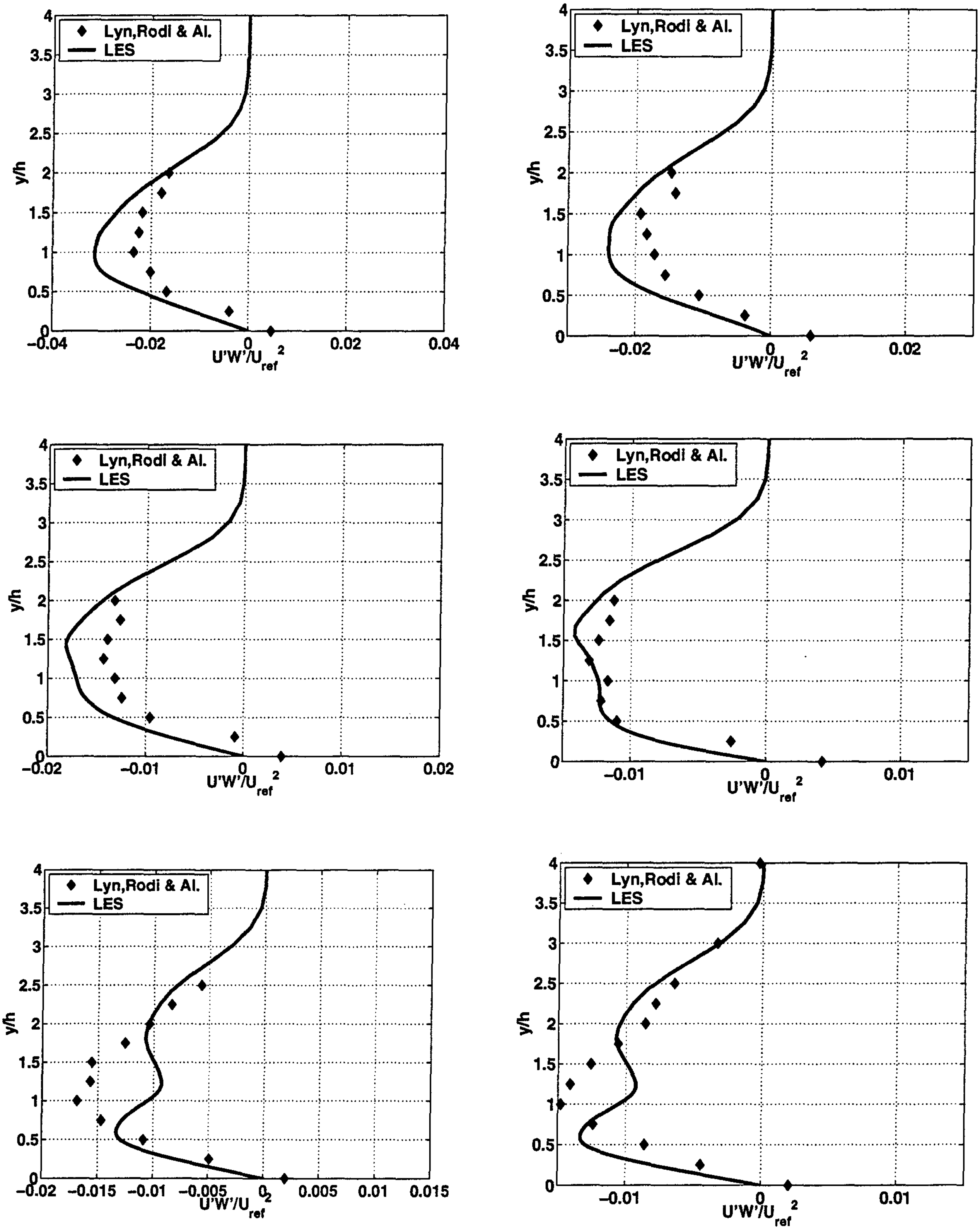

Fig. 2.48: Velocity profiles for turbulent stress from top to bottom and from left to right: $x = \frac{34}{8H}$,$x = \frac{38}{8H}$,$x = \frac{42}{8H}$, $x = \frac{46}{8H}$,$x = \frac{51.2}{8H}$ and $x = \frac{64}{8H}$.

To conclude, it is possible to observe that the agreement between simulation and experiments is acceptable within the base region and the near wake, while an important disagreement can be remarked for the far wake for what concerns higher order statistical moments (namely, RMS and turbulent shear stress): in Fig. 2.48 it can be remarked that the turbulent stress deviates significantly from the reference data, result which is understandable in view of the increasing coarsening of the grid in stream-wise direction, compared with the fact that the same resolution is kept in span-wise and in vertical direction. The RMS of stream-wise velocity and vertical velocity deviate from the experimental data in the sense that the peak of vertical velocity is too strong, while the RMS of stream-wise velocity presents two prongs corresponding to the two regions of more refined grid around the two horizontal faces of the obstacle. Simulations presented in appendix (see § A), even not completely converged, suggest that this effect could be related to the the influence of SGS model; this conclusion would understandable, considering that coarser is the grid, more significant is the contribution of the SGS model to the solution.

On more general terms, the base region (the region immediately after the cylinder) presents an over-prediction of the velocity RMS, which could be an indication of the fact the computational domain might be too small in span-wise direction. Inherently three-dimensional secondary motions are extremely active in this region and the span-wise length of domain strongly influences the flow behavior, as it stated in literature and direct experience of present authors[8]. In this optic, a value of $6H$ could be suggested in order to decrease the effects of this parameter on the computed flow[9].

[8]Through a series of computations which spanned span-wise extensions of: $2H$; the current $4H$ and $6H$, as shown in in § B and § C

[9]And apparently this is true, at least of the RMS in vertical direction, see § C.

3. STRUCTURES ANALYSIS

Present chapter discusses results obtained by the application of the identification algorithm to wake flow and their qualitative differences with respect to statistics presented in Volume I. In addition of what presented in previous volume, a very simplified attempt is made to track large span-wise rolls shedded from the obstacle; this procedure makes use of pressure as marker, instead of identification criteria introduced in Volume I; its application is discussed and justified, and results for estimation of mean convection velocity of vortices is be presented.

3.1 Flow description and related properties

In § 2 the flow has been studied only in terms of comparison with experimental data, and a more general description of the topology of the flow has not been given, even if some concepts such as the one of vortex shedding have been used. This section briefly illustrates the characteristics of the flow by the mean of flow-visualizations obtained with Open DX (the post processing and visualization meta-program from IBM)[1]. This software is applied to plot the iso-surfaces of the structure discriminant (Q identification criterion), as introduced in Volume I, for a suitable value of the trigger. A shedding period is examined, and two series of plots are shown in Fig. 3.1 and Fig. 3.2. These plots are completed by the iso-contours of pressure in the median plane of the computational domain, and confirm that the cores of vortices are associated to a local minimum of pressure.

Fig. 3.1 presents a side view of the field and puts in evidence the existence of two staggered rows of span-wise vortices (roll) of approximately diameter $D = 1H$, although this value could be influenced by the value chosen for generation of iso-surfaces.

The detected rolls are characterized by a longitudinal separation of around $5.2H$, between vortices of the same row, while the transversal separation between the two rows is estimated around $1.8 - 2H$ at a distance of $10H$ downstream the cube.

Fig. 3.2 presents, at the same relative times, the view from the top of the computational field and offers a clear vision of the development of the wake.

These figures allow a better understanding of the physics of the present flow field: separation of the flow at the upstream corner gives birth to a two-dimensional vorticity sheet, which is destabilized by secondary instabilities and soon break-down, leading to the formation of complex three-dimensional structures. Downstream of the cylinder the vorticity re-arranges itself in span-wise rolls and stream-wise structures (braids) which are considered (Hussain and Hayakawa, 1987) to be the main medium of production of turbulent kinetic energy, which is

[1] It is the case of OSS, or Open Source Software; the program is freely available at www.opendx.org. For more informations about OSS, refer to the Free Software Foundation at www.gnu.org.

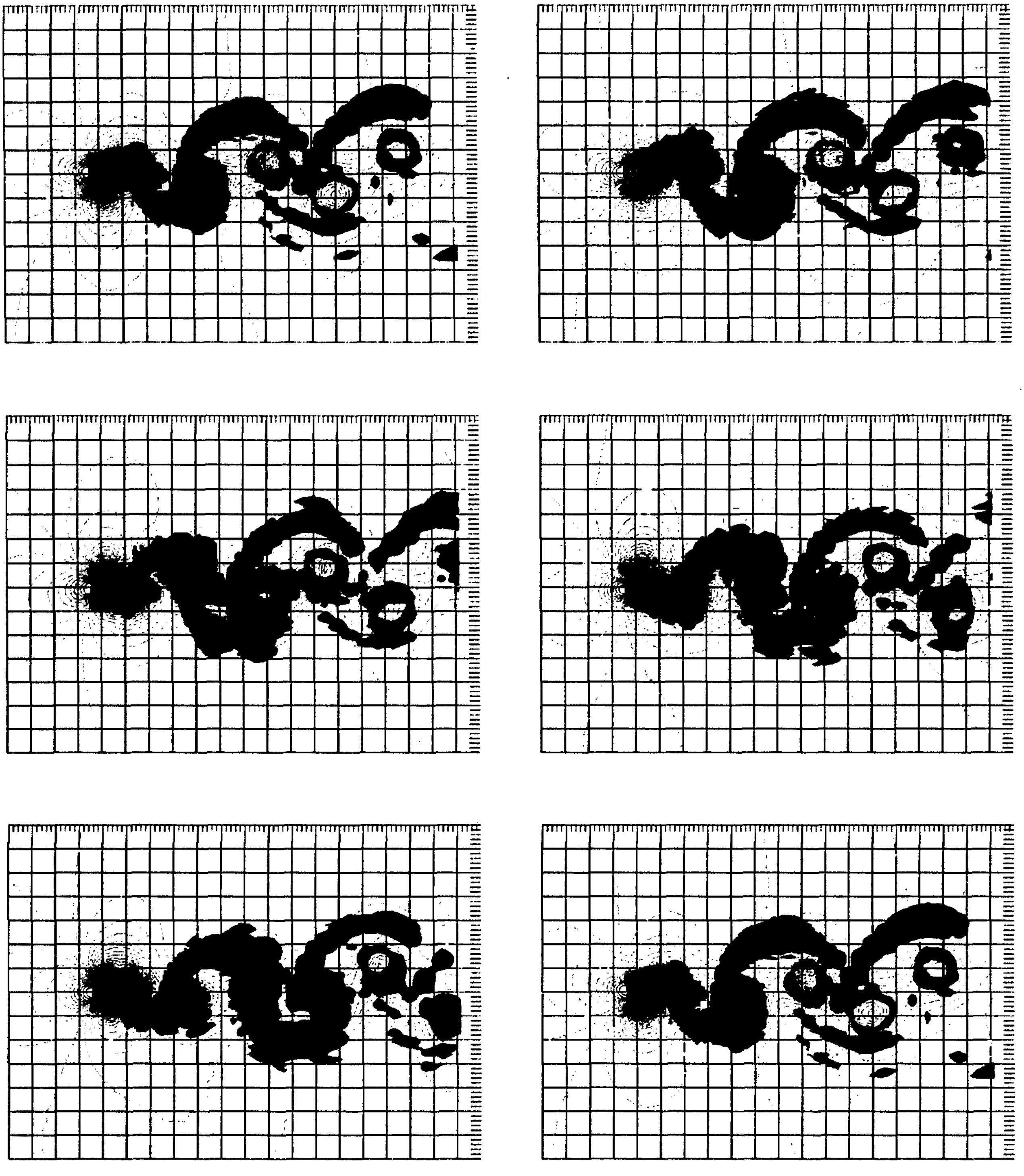

Fig. 3.1: Flow visualization: a shedding sequence in the stream-wise,vertical plane for one period is recorded, using Q criterion. Starting from top to bottom and from left to right, the images are recorded at the following times: $t = 0 \times T$, $t = \frac{1}{5} \times T$, $t = \frac{2}{5} \times T$, $t = \frac{3}{5}$, $t = \frac{4}{5}$ and the again $t = 0 \times T$ to close the loop.

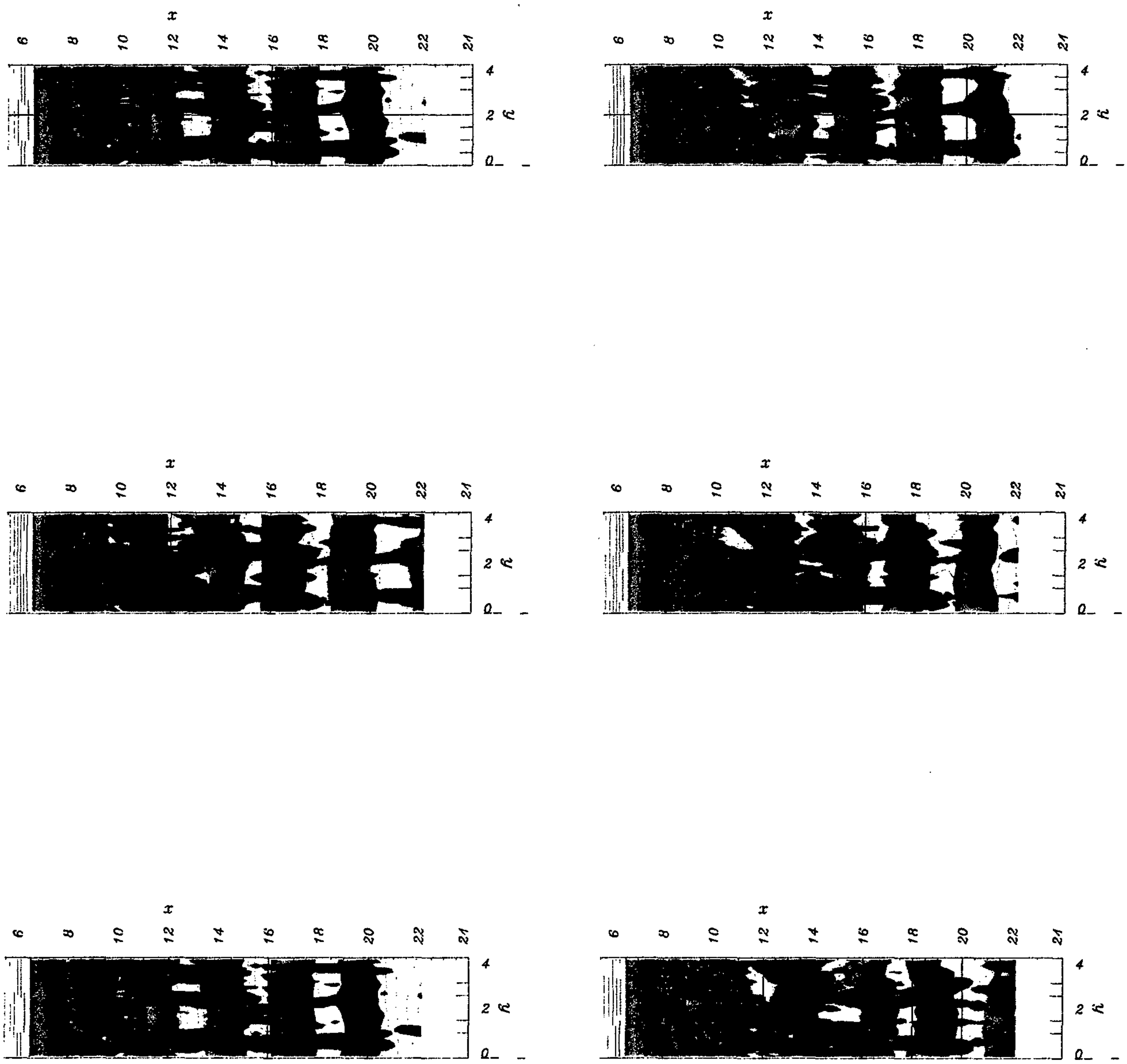

Fig. 3.2: Flow visualization: a shedding sequence in the stream-wise,span-wise plane of one period is recorded, using Q criterion. Starting from top to bottom and from left to right, the images are reordered at the following relative times: $t = 0 \times T$, $t = \frac{1}{5} \times T$, $t = \frac{2}{5} \times T$, $t = \frac{3}{5}$, $t = \frac{4}{5}$ and the again $t = 0 \times T$ to close the loop.

then fed to the rolls. The process through which braids are developed is very complex: it involves interaction and merging of intermediate structures, but, downstream of their inception the braids are established and repetitive in terms of their span-wise separation $Ly = 1.5H$ and diameter $d = 0.35H$[2].

Present analysis, of course, is quite qualitative and strongly influenced from detection algorithm and trigger level chosen. The values here given must be considered a very rough estimations based on flow-visualization techniques. But, it can already be remarked that most of the mechanisms of wake formation proposed by Hussain and Hayakawa (1987) for the case of plane wake, also apply to the present case.

3.2 Alternative approach to structure identification

In Volume I, §4, different criteria have been examined in order to detect coherent structures; independently from the particular criterion chosen, all of them had in common the fact that they were based on manipulations of the gradients of velocity tensor and share the underlining assumption that the vortex core is a connected region corresponding to a local minimum of pressure (Hunt et al., 1988). This fundamental fact cannot always be exploited, depending of the class of flow and, within the same flow, of the particular class of structures which must be studied; nevertheless, the minimum pressure concept can be sometimes applied and full advantage can be taken of simplicity and efficiency of this concept.

Considering Fig. 3.1, observation of span-wise rolls allows to confirm that the pressure iso-lines indeed conform to the patterns described by Q iso-surfaces chosen for that particular flow visualization; as the only median plane is plotted, local minima of the pressure correspond to extrema of the particular detection criterion chosen. This observation suggests that it could be possible to disregard, altogether, the detection criterion (which is costly in computer memory and time) to base a sub-set of analysis on the pressure field alone.

3.2.1 Technique Description

Since the span-wise rolls are quasi bi-dimensional, that is, their span-wise size corresponds to the one of entire computational field in y direction, it is possible to consider the single median plane and it is only necessary to store the corresponding pressure field for further processing. A series of such planes is stored, at constant sampling frequency equal to $\frac{1}{72}^{th}$ of shedding period; as the time step for LES simulation is orders of magnitude smaller than such value, it can be safely assumed that the data are sampled at regular constant intervals.

[2]Considering present span-wise resolution of the domain, this means that the ribs generally span less of 3 nodes in span-wise direction, which will turn out to be a crucial point for their detection, as it will discussed later on in § 3.3.

The pressure distribution along the wall of the obstacle can then be extracted from this pressure field together with a local lift and drag coefficient, and, at the same time, the finger-prints of the span-wise rolls and, occasionally, of the longitudinal ribs.

A relatively high number (around six hundreds) of samples has been gathered, corresponding to about eight shedding periods. A MATLAB© [3] program reads the data for each single realization, computes the local c_l and c_d and, finally, identifies and tracks the span-wise rolls.

An intermediate step of the process is shown in Fig. 3.3; the program is interactive in the sense that it not able to independently identify a single vortex and it needs an input from the user. It is sufficient to feed to the program the two opposite corners of an interrogation area shown on screen (for example Fig. 3.3(a)) and the program will take care of the rest; the detail of implementation will be discussed further on. Present program can track multiple vortices at the same time, but the maximum number to be processed depends from actual presence of vortices to track; on the basis of analysis of the raw data, the number of vortices to be followed at the same time was set to three (for example Fig. 3.3(d) the three tracked vortices are clearly shown). The process is then semi-autonomous: to process the first field the program requests as inputs the locations of the first three vortices and then automatically track them; the tracking operation is legitimate because successive fields differ only for a $\frac{1}{72}^{th}$ of shedding period, so that the interrogation area set for the previous field is large enough to contain also the new center of the structure. Once the latter is again found, the new interrogation area in centered on it and the procedure continues, until the vortex reaches the end of the computed wake.

At that point, the user is requested to input a new interrogation area for next vortex. Once all the available fields are processed, is it possible to build an animation linking together the four images shown in Fig. 3.3; this visualization allows to observe how the shedding of vortices affects local lift and drag coefficients and to remark that the shedding pattern is not fully regular.

It is now necessary to describe in more detail the practical implementation of the procedure. First of all, it must kept in mind that only the wake region is taken in consideration; furthermore, account must be taken of the fact that the numerical pressure field corresponds to the grid on which it was computed, meaning that locations where pressure values are available are irregularly spaced in both stream-wise and vertical direction. To simplify detection and tracking procedure, the pressure field is interpolated into an uniformly equal-spaced grid, whose spacing is smaller than the smallest cell of the original grid in the stream-wise direction. However, due to grid stretching in vertical direction, it was not possible to build a grid fine enough to capture all small movements in vertical direction too. This drawback of the technique will be illustrated and discussed in § 3.2.2. This interpolation is needed to simplify

[3] www.mathworks.com

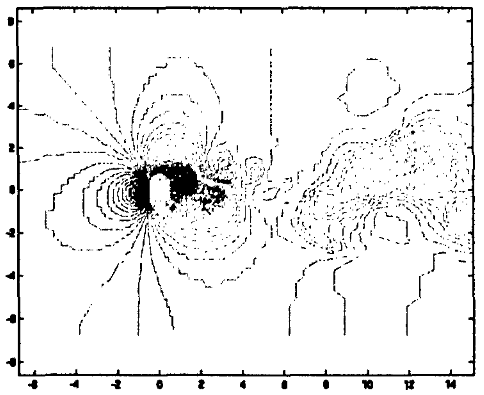

(a) Original pressure field

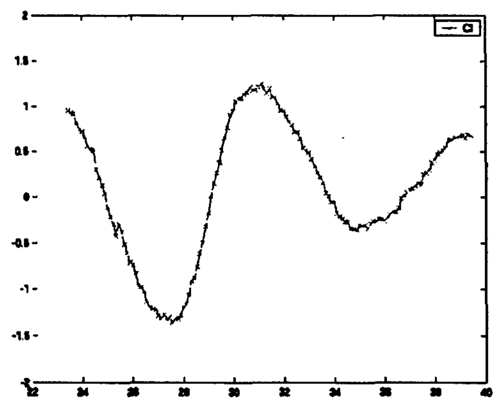

(b) Partial time history of c_l

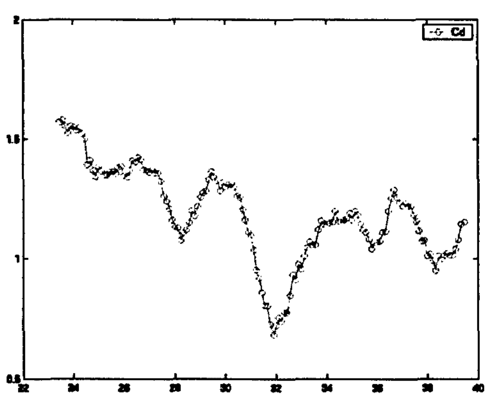

(c) Partial time history of c_d

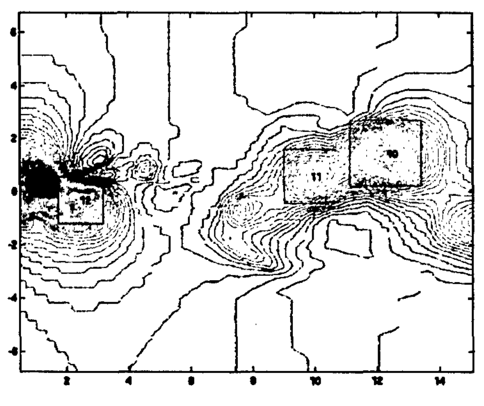

(d) Wake magnified and bounding box of tracked structures

Fig. 3.3: Intermediate step in the span-wise rolls identification and tracking; Sample N. 356.

the management of interrogation area, and final results are found to be relatively unmodified by this manipulation, in what regards evolution of vortex in the stream-wise direction, where more data are available.

The last point to be stated is the criterion applied for the identification of the center of vortex itself. A simple procedure is adopted: the pattern $f(x,y) = -e^{-\frac{x^2+y^2}{100}}$ (see Fig. 3.4) is cross-correlated with the interrogation area, and the the peak of correlation is assumed to indicate the center of the structure.

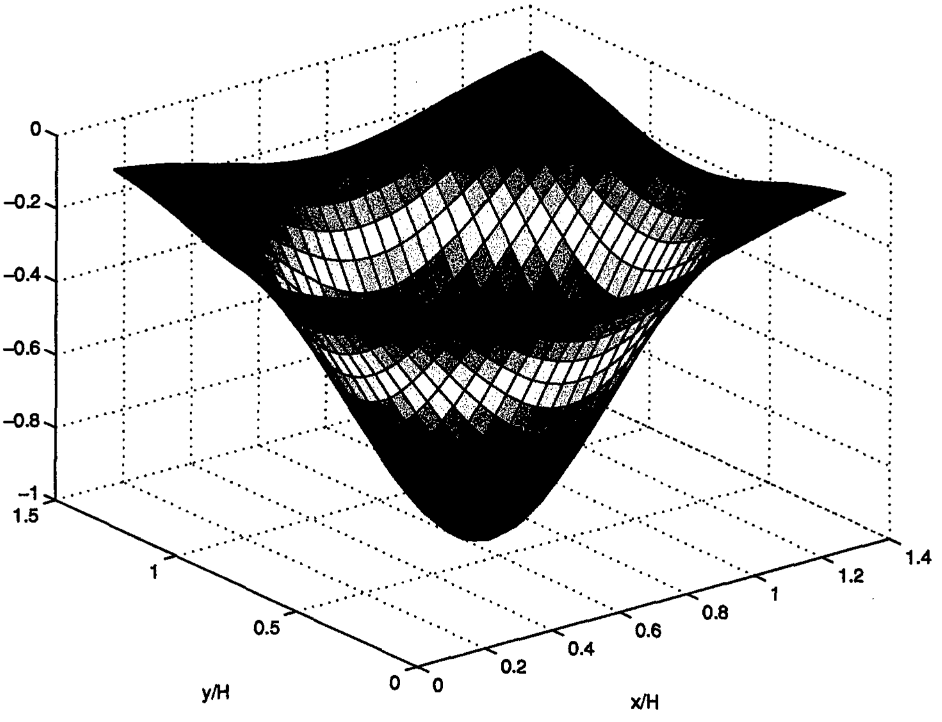

Fig. 3.4: Structure identification: reference pattern for cross correlation.

The resulting pattern is isotropic, but this set-up was deemed appropriate for the level of present investigation and for type of data to be processed.

3.2.2 Technique Results

As stated in § 3.2.1, about eight shedding periods have been sampled and about six hundreds pressure fields have been processed; this sample yielded nineteen structures totally or partially processed, meaning that some of them have been identified near to the origin of the wake and their entire evolution has been recorded. The corresponding paths have been plotted in Fig. 3.5 to 3.7; in this plot only of one each three positions has been plotted, to avoid unnecessarily to clutter the plot.

It is possible to see that, with the possible exception of maybe Fig. 3.7, the structures

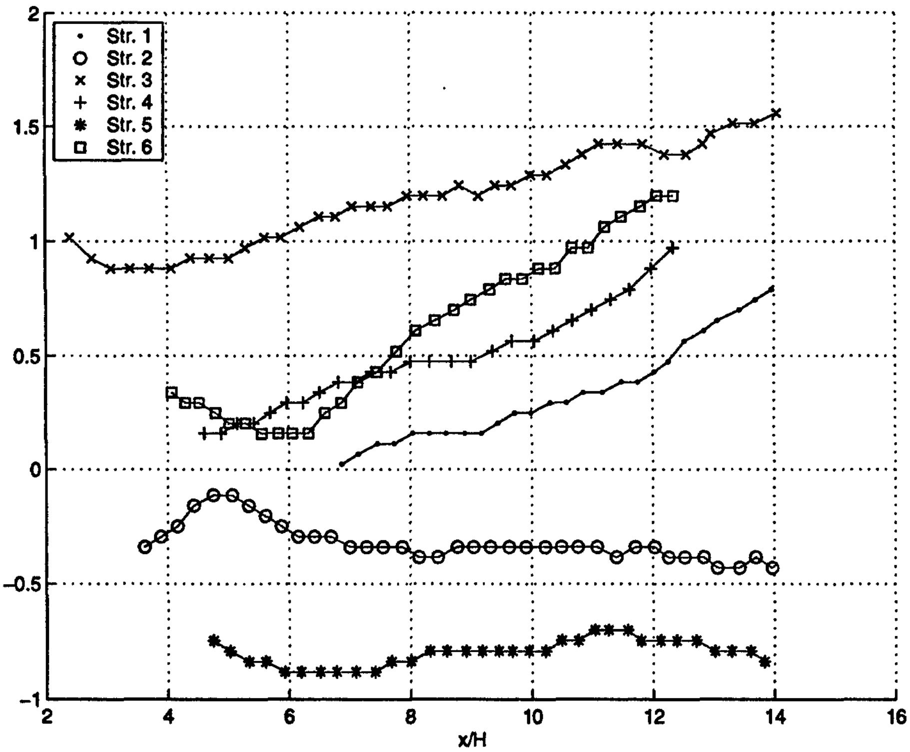

Fig. 3.5: Structure identification: Structures from 1 to 6.

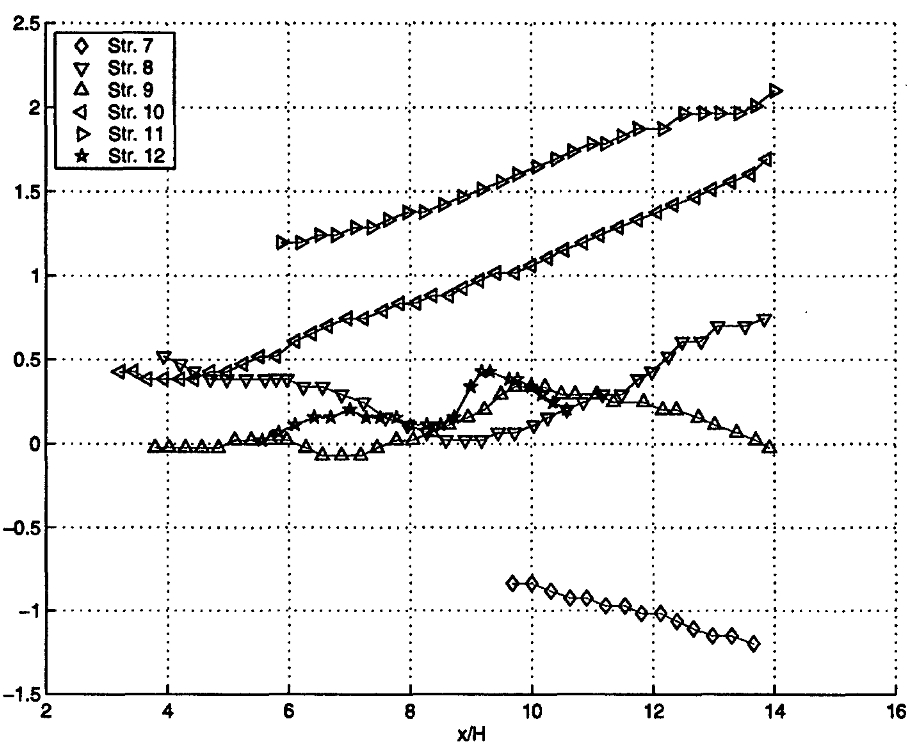

Fig. 3.6: Structure identification: Structures from 7 to 12.

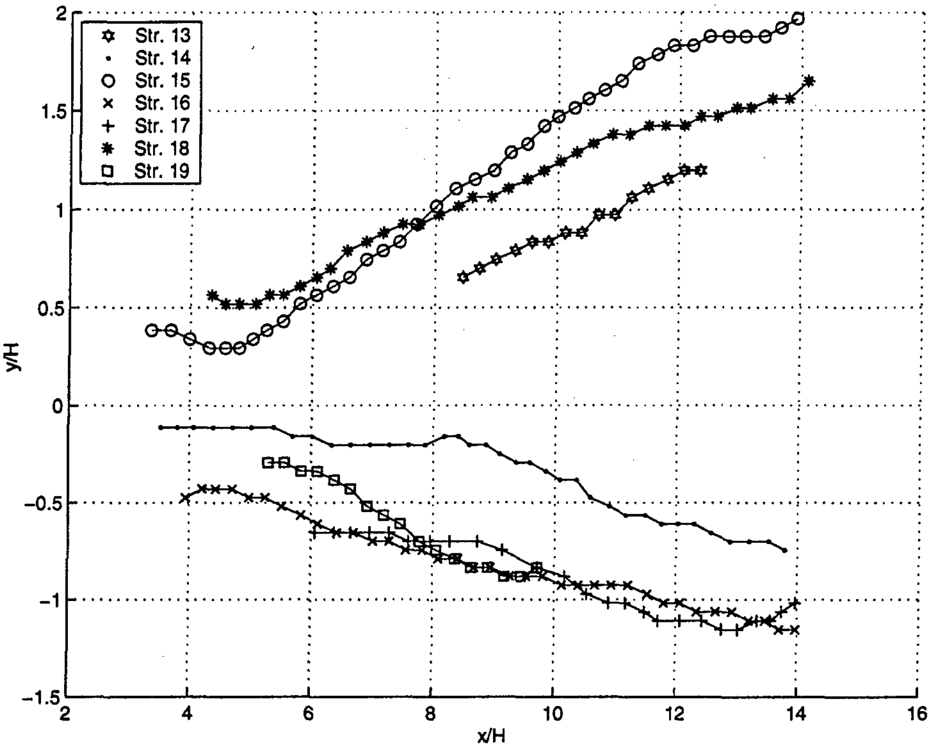

Fig. 3.7: Structure identification: Structures from 13 to 19.

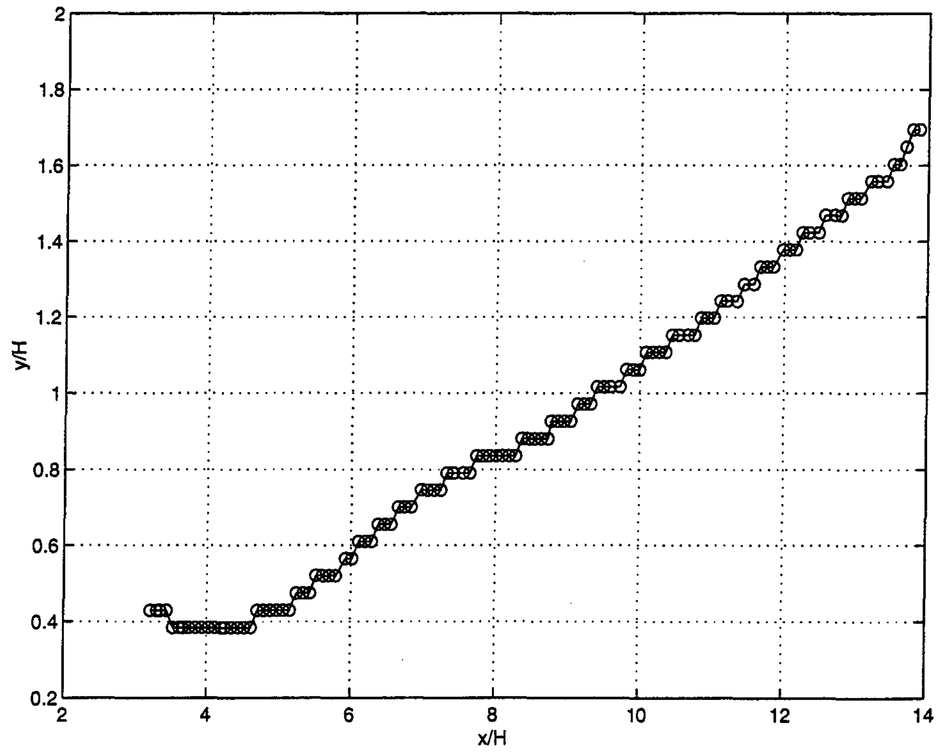

Fig. 3.8: Structure identification: Structure number 19.

generally follow different types of trajectory, and their behavior can be linked to the upstream evolution of the flapping shear layer.

A clear effect of the interpolating grid is visible when all the recorded positions are plotted, for example for structure number 19, Fig. 3.8; here it is possible to see how the structure moves in the vertical direction in a discontinuous way, and it can be recognized that the discontinuous movements in vertical direction are regularly spaced. This behavior appears to be a design flaw of present technique, which does not consider properly the effect of the grid in the vertical direction; however it would be rather easy to modify the MATLAB©program to take into account this conclusion for future studies. While it is necessary to be careful when assessing data relative to the motion in vertical direction, the information for the motion and velocity along the stream-wise direction can be considered sufficiently reliable.

The velocity associated with a structure is computed simply dividing the distance traveled by the known separation in time between two realizations (see § 3.2.1); it is a coarse approximation, but it was found to yield sufficiently reliable results. The histograms for the convection velocities in stream-wise and vertical direction are presented in Fig. 3.9.

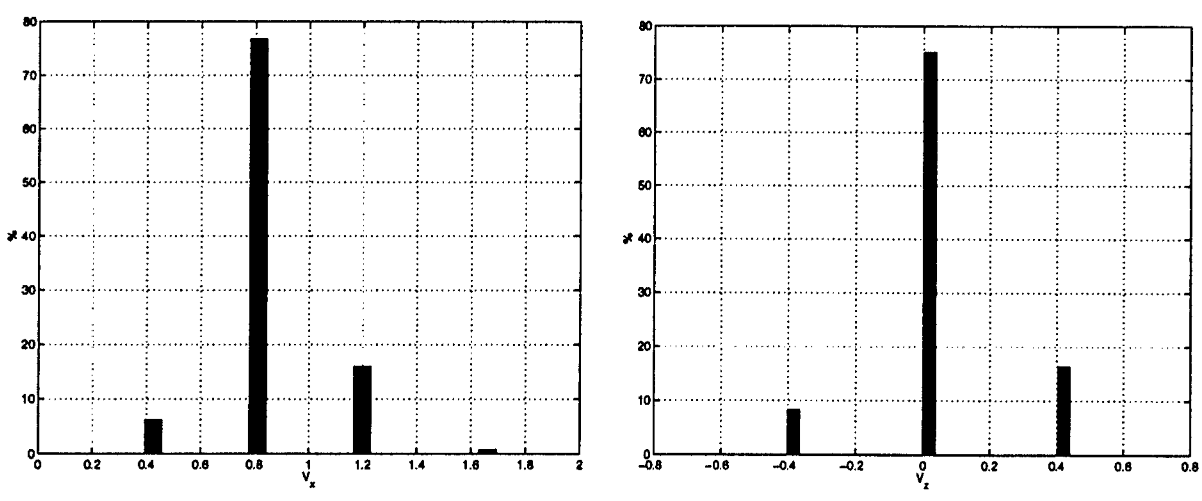

(a) Stream-wise velocity

(b) Vertical velocity

Fig. 3.9: Structure identification: convection velocity histograms.

Advection velocity for the rolls is estimated to be 0.81 times the free stream velocity (see Fig. 3.9(a)), against the experimental values of 0.78 for the square cylinder (AGARD, 1998) and the corresponding value 0.83 for the circular cylinder, which can be considered a satisfactory agreement.

Concerning the vertical velocity, it seems to appear that many of structures have negligible velocity in this direction, but it must again be stressed that this might be just an

artifact of the interpolating grid as discussed above: in Fig. 3.8 the tracked structure moves in vertical direction, but discontinuously, often keeping the same ordinate (no velocity in Fig. 3.9(b)) and sometimes moving of one cell in vertical direction (next allowed value, positive or negative, in Fig. 3.9(b)); this suggests an averaged vertical velocity equal to about 0.4 times the free stream velocity; it could have been possible to extract the vertical velocity applying a more accurate interpolation technique, but it would not have been proper to further manipulate data which already are flawed in origin.

Even in the case of convection velocity it could be argued that measured velocities are discretized on the base of grid spacing, which might be suspected considering Fig. 3.9(a).

Considering the aforementioned arguments, future implementations should consider, the idea of computing the translation velocity of the structures starting directly from the flow field itself. This option has been disregarded in this analysis for reason of simplicity of data retrieval and manipulation.

3.3 Normal approach to structure identification

The strategies developed in Volume I in order to detect and identify the coherent structures proved themselves to be not fully suitable for current case; a new approaches should be developed, but time constrains did not allow to pursue this avenue of development. In present case it was found that, not only the completely different class of flow requires a different treatment, but the resolution employed in span-wise direction was insufficiently refined to properly resolve the longitudinal braids or ribs.

The researchers had always been conscious, from their experience on the channel flow (Volume I), that the span-wise resolution was a critical issue; nevertheless, the complexity of the problem brought in the need to make use of so many grid points on the $x - z$ plane that it was unfeasible, in term of available computational resources, to use more than 32 nodes in span-wise direction.

In an attempt to ensure an acceptable resolution, the first simulations were performed on a span-wise dimension of only $2H$, as it is remembered in § 2.5, but it was found that, in this case, the flow auto excites itself due to limited extension of the domain. These simulations were therefore discarded and the span-wise dimension of the computational domain was doubled, but it was necessary to keep the value of 32 nodes for this axis, which value was then the standard for the simulations presented in § 2.

This standard is also kept for simulations presented in the appendices § B and § C: the calculations there discussed were always performed for 32 nodes in span-wise, while it was the size of the domain in this direction which was increased up to $6H$, but to the further worsening of quality of detection of structures.

Therefore, it must be admitted that current analysis was seriously undermined by lack of resolution in span-wise direction, despite the fact flow visualizations (Fig. 3.1 and Fig. 3.2) could suggest that all important structures are present in flow field and could then be identified and classified; but, in practical terms, the presence of braids hinted by iso-surfaces does not necessarily translate in automatic ability of current technique to detect and define them. In Volume I, §4.4 is shown that the minimum accepted size for a structure was chosen to be an octahedron, occupying minimum 3 nodes in span-wise; in present simulation and considering the number of points available in span-wise, this minimum became a quite severe requirement which is not often met: the grid is simply possibly too coarse to successfully retrieve this class of structures, and even testing with different trigger levels, as it will be shown below, does not provide a solution to this problem.

3.3.1 Detection algorithm and trigger choice

As stated, the procedure presented in Volume I was tested; on basis of previous experiences Q detection criterion (described in Volume I in §4.2.1) was applied; following again the procedure presented in §4.3, the histograms of Q are plotted to extract from them a suitable value of the trigger. The histograms for the individual domains numbered according to Fig. 2.10 are presented in Fig. 3.10 trough Fig. 3.13.

Referring to the Multi-domain set-up, shown in Fig. 2.10, it is evident that sub-domains 1, 6, 11, 15 and 20 should contain almost no structures, since they are located far up-stream of the obstacle. Sub-domains 2, 3 and 4 are also free of structures because they are sufficiently far away from the obstacle to be not affected from its presence; it, likewise, apply for domains 21, 22 and 23 on the other side.

Sub-domains closer to the obstacle, namely: 7, 8, 9, 12, 13, 16, 17 and 18 show, on the contrary, a presence of structures,of importance comparable to the one of the incoherent background. Structures presence is, obviously, high in sub-domains directly affected by the wake, while only the onsetting of the flapping shear layer can be observed in other sub-domains.

Sub-domains located within the wake are obviously affected by presence and effects of organized turbulence; in consequence, sub-domains 10, 14 and 19 are characterized by similar histograms which show presence of structures against the incoherent background. Downstream, the wake spreads to sub-domains 5 and 24 as well.

Following the procedure outlined in Volume I, trigger value could be chosen independently for each sub-domain which would lead to a wide range of possible triggers, from 1×10^{-1} to $1 \times 10^{+1}$, depending on the physics involved in the different domains. At title of example, it could be remarked that it is the sub-domain 13, which is located in the base region, the one where turbulent activity is the strongest (see Fig. 2.27); it was found that the trigger which could be extracted from the corresponding data was found too strict for the rest of the

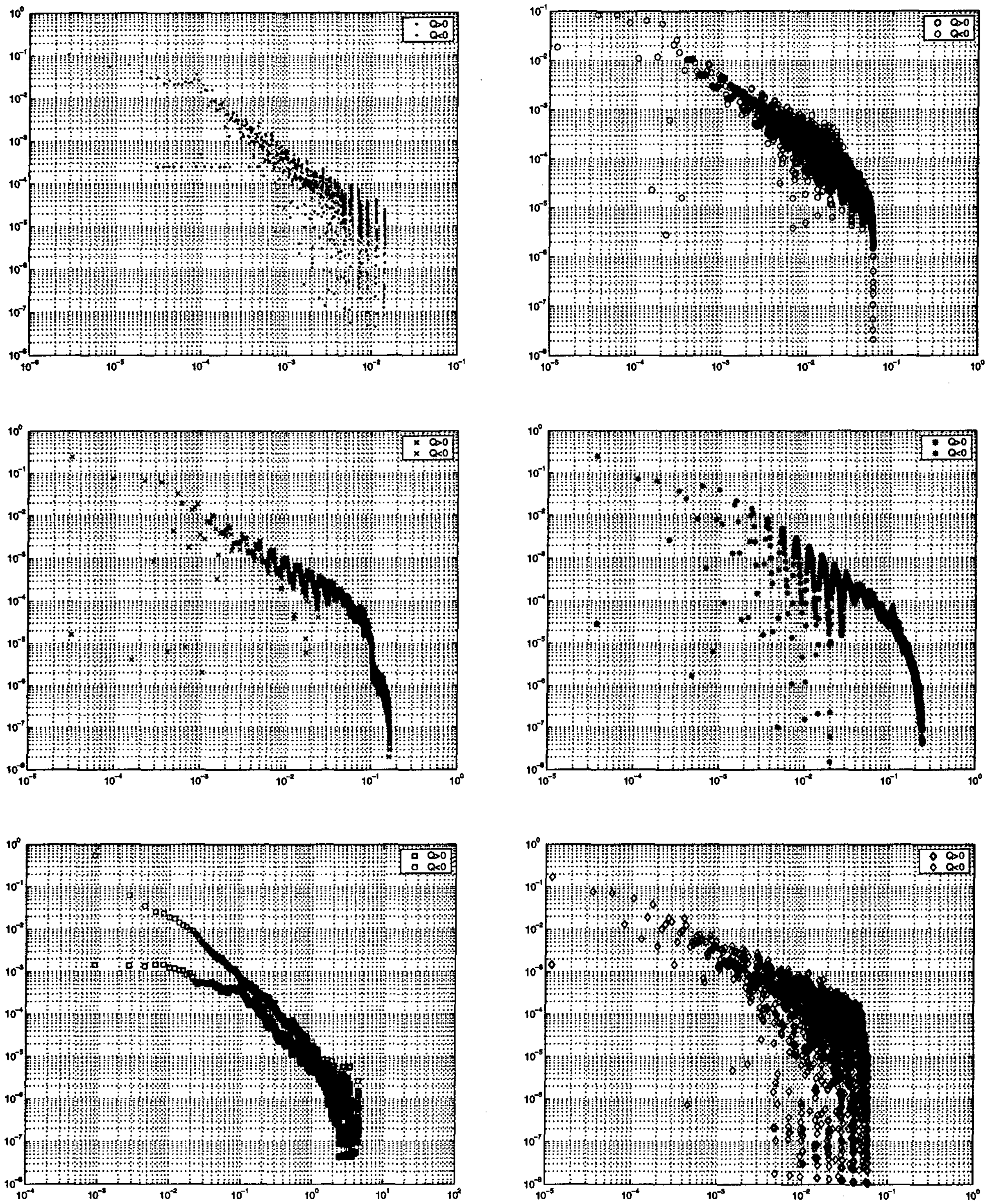

Fig. 3.10: Structures identification: histograms of Q for domains, from top left to bottom right, 1 to 6. $Q > 0$ signals presence of structures.

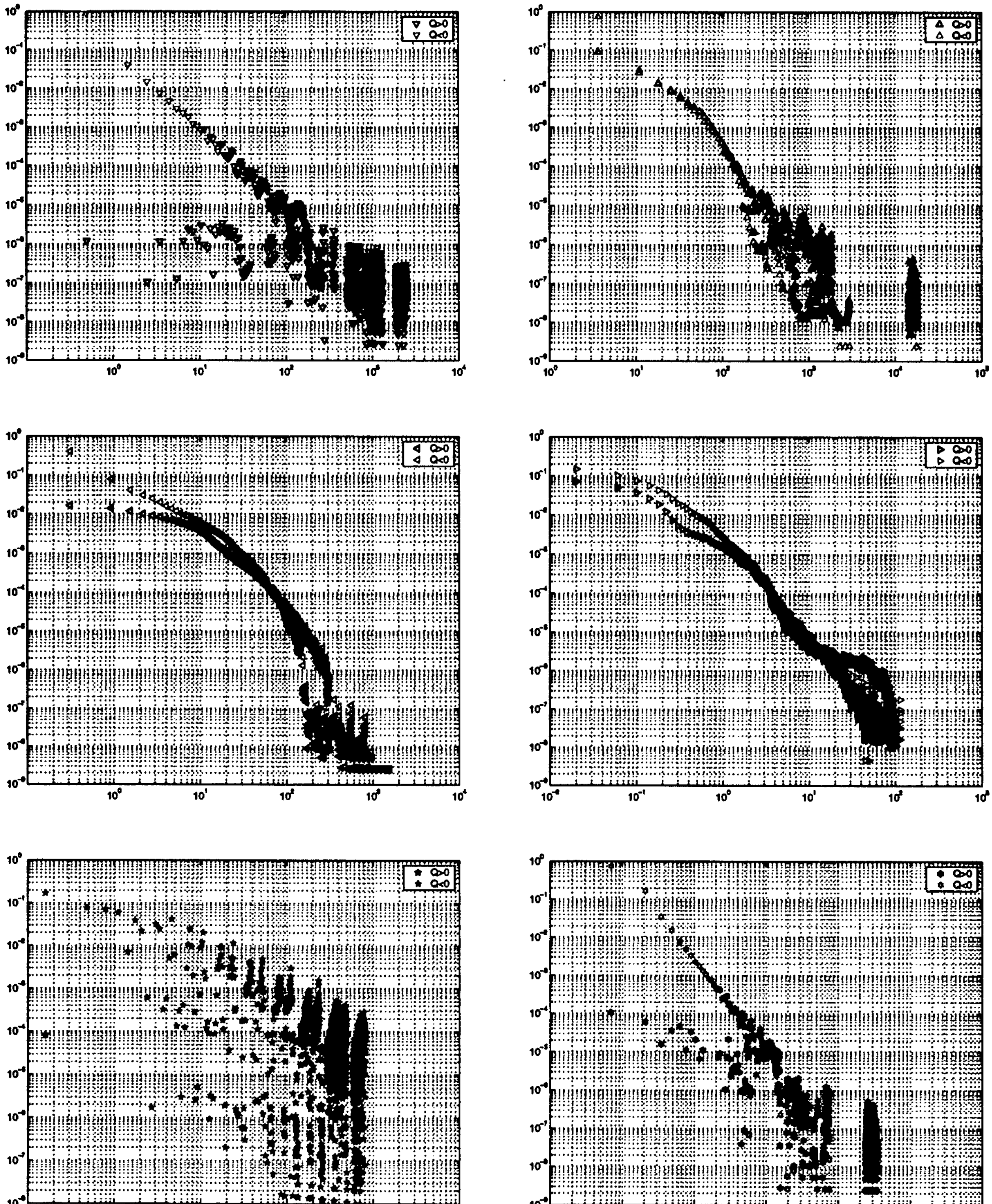

Fig. 3.11: Structures identification: histograms of Q for domains, from top left to bottom right, 7 to 12. $Q > 0$ signals presence of structures.

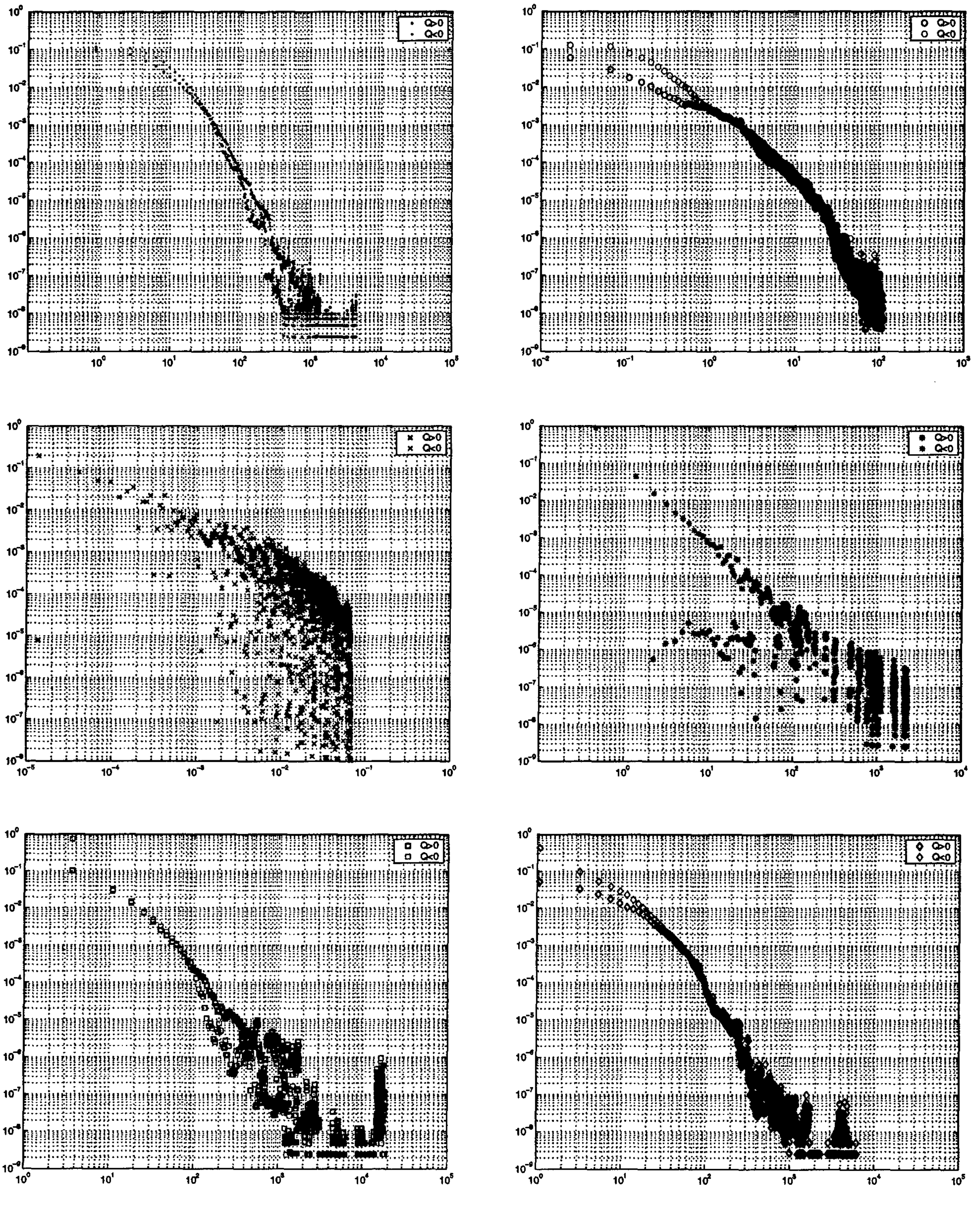

Fig. 3.12: Structures identification: histograms of Q for domains, from top left to bottom right, 13 to 18. $Q > 0$ signals presence of structures.

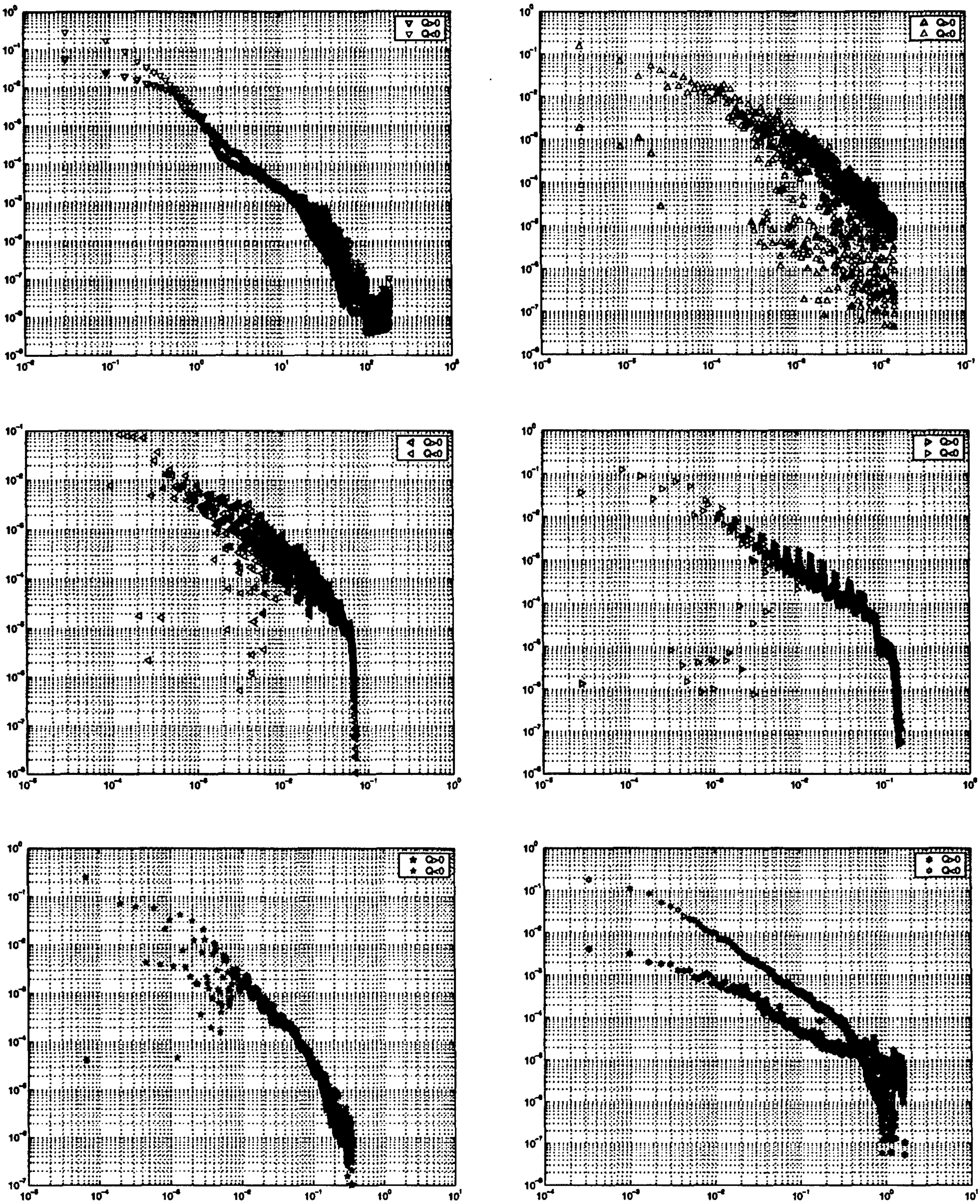

Fig. 3.13: Structures identification: histograms of Q for domains, from top left to bottom right, 19 to 24. $Q > 0$ signals presence of structures.

domains and vice versa.

The idea to choose trigger level by sub-domain by sub-domain-wise might be, by itself, considered possible, under the conceptual point of view, since already a sub-domain-wise repartition has been already made (see treatment of advective term in § 2.3.1) for other algorithms; however, under the practical point of view, it was assesses that results of this approach might turn out to be too much arbitrary.

In consequence, a single trigger was chosen for the whole domain , and it was decided to process the entire flow-field through a single sweep. The trigger level from sub-domain 14 was chosen, considering that this sub-domain was wide enough to include regions of different behavior, namely, base region, near wake and far wake; the trigger level so chosen could then be a good trade-off for the identification of the structures in the entire domain; the corresponding value of $Q = 0.4$ was applied.

The identification algorithm was applied on the mask generated from Q criterion, as described in Volume I, but it was found that the procedure was not converging at an acceptable rate and it became evident it was not going to produce acceptable results in acceptable time; the advanced conflict management described in Volume I §4.4 was now found to be more of a liability than of an advantage in the process. The main problem lies with the base region and the flapping shear layer: in these regions the flow behavior is so chaotic and complex that the list of possible structures to be considered for the algorithm grows and grows. Since the conflict management algorithm should take into account all the possible configurations of structures and then merge the connected regions, the process stalled, without being able, to identify the stream-wise ribs. The mean reason of this unsatisfactory behavior lies with the coarse resolution in span-wise direction, as it was remarked in § 3.1: size of ribs in span-wise direction seldom covers 3 connected cells, which is the minimum criterion for the size of a structure be accepted.

As available computer power made impossible to enforce the high resolution necessary for definition of the ribs, it was found logical to relax the algorithm in order to capture at least other structures of interest which are sufficiently resolved by the grid, such as the span-wise rolls.

In consequence, only the first step of the procedure described in Volume I, §4.4 is performed; in other words, only the structure cores are considered; since only strongly connected nodes are taken into consideration, and no iterative procedure is adopted to build up to bigger structures and resolve possible conflicts, the procedure remains fast enough to process the entire flow-field. The choice of the trigger then becomes of secondary importance and since only vortex cores are considered, the trigger level can be relaxed to being set to $Q = 0.001$; the trigger can be set so low, compared with the values suggested from the histograms in Fig. 3.10- 3.13, because the algorithm, by working on the vortex cores only, would already reject a large part of data.

3.3.2 Global statistics

As just stated the identification and classification procedure was strongly simplified, but it was found that it allows to extract data of acceptable quality and reliability, which are processed with the statistical tools described in Volume I. In consequence, global quantities (in terms of volume, kinetic energy, etc. etc.) for the population of organized structures were found and the corresponding values are shown in Tab. 3.1. Present statistics here have been computed from about one hundred flow realizations, sampled in time at regular intervals of $\frac{1}{72}^{th}$ of shedding period.

Table 3.1: Cylinder of square cross section: global statistics for measured quantities and comparison between structures and noise(TKE, turbulent kinetic energy; KE, kinetic energy).

	Structures	Noise
$Volume$	4.2859 %	2.9021%
TKE	21.048 %	9.7420%
KE	4.1843 %	2.6511%
$Vorticity$	34.718 %	17.179 %
$Enstrophy_x$	39.480 %	23.688 %
$Enstrophy_y$	39.800 %	15.750 %
$Enstrophy_z$	25.546 %	17.601 %
$Enstrophy$	37.688 %	17.538 %

The noise quoted in Tab. 3.1 is consistent with the definition given in Volume I: it corresponds to nodes which have been detected by the detection algorithm but have been rejected from the identification algorithm. The values of different parameters associated with the structures are bigger than the corresponding ones associated to the noise, but the ratio signal to noise is significantly lower than one previously found for simulations discussed in Volume I; this difference is reasonable, since the difference of adopted procedure in present case could no be expected to lead to similar results.

This stated, it could appear surprising the extremely low presence of structures in terms of volume percentage, comparing with the results of the plane channel (Volume I) and considering Fig. 3.10- 3.13, Fig. 3.1 and Fig. 3.2. However, it can be also remarked that this extremely small volume contains nevertheless $\frac{1}{5}^{th}$ of the whole turbulent kinetic energy, and almost $\frac{2}{5}^{th}$ of total enstrophy. These results show that it is still possible to separate organized turbulence from its un-coherent background.

The ratios between percentages of noise and structures in terms of volume, relative percentage of turbulent kinetic energy and vorticity are similar. This fact does not surprise since noise is expected to cluster all around the identified structures; a better performances of the

identification algorithm, would probably attribute part of noise to the structures themselves.

Therefore, it can be concluded, that present simulation, in spite of its shortcomings. indicates that an very important part of the entire turbulent field lies within very active structures, which cover a very small part of the entire flow field. It can advanced that the characteristics of these structures are the ones which define and control the wake behavior, and their identification could be key of understand and possibly identify and recognize specific wakes.

3.3.3 Structures statistics

It has already brought to the attention that it was very difficult to isolate and define individual structures in current simulation.

While some characteristic entities, like the flapping shear layer or the span-wise rolls are clearly identified, other structures, specially the longitudinal ribs, while shown to exist as put in evidence from flow-visualization techniques, are too small to be properly identified from the current algorithm, in its original shape (Volume I) or in its present revised form § 3.3.1.

Examples of structures whose size was large enough to be identified, are shown in Fig. 3.14, Fig. 3.15 and Fig. 3.16.

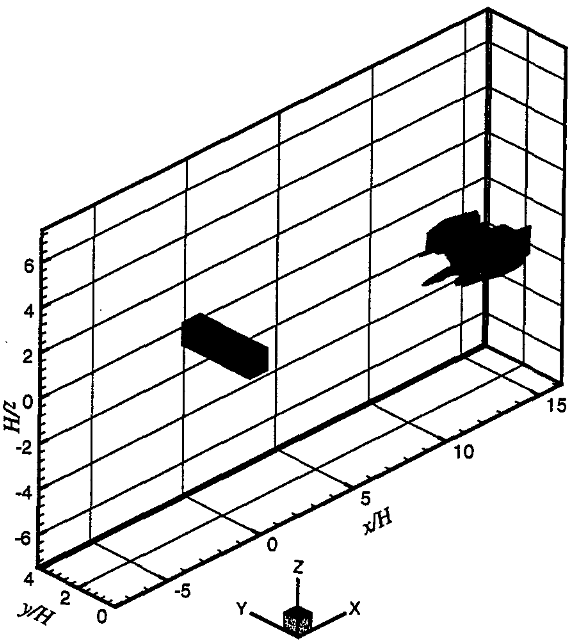

Fig. 3.14: Structure identification: example of identified structures in the wake; last span-wise roll of the domain.

In these figures it is possible to observe the roots of the longitudinal ribs embedded in the

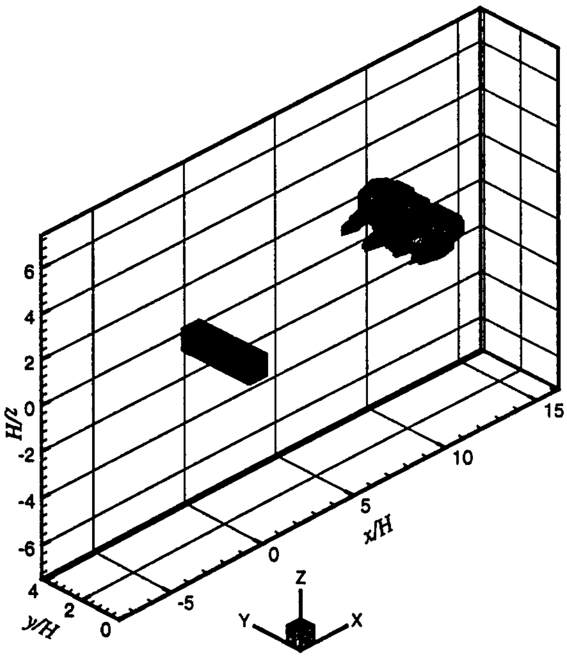

Fig. 3.15: Structure identification: example of identified structures in the wake; last but one span-wise roll of the domain.

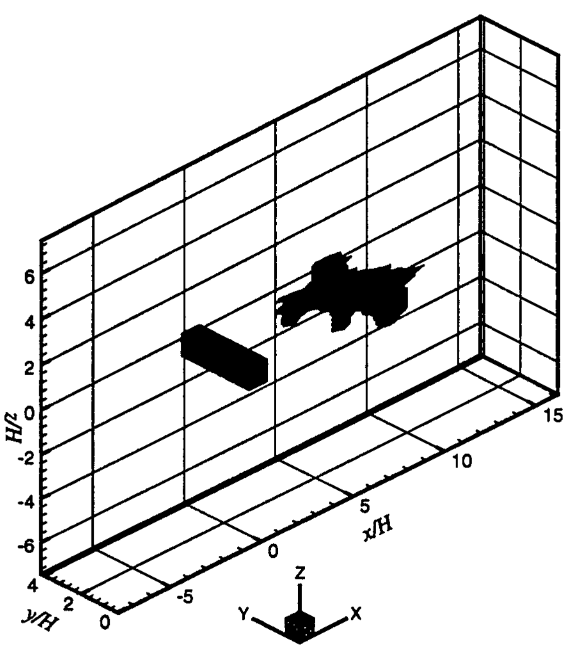

Fig. 3.16: Structure identification: example of identified structures in the wake; last but one span-wise roll of the domain.

span-wise rolls. Due to poor resolution, no more details can be separated. This result again shows that sufficient resolution of the grid is the key parameter for successful simulation.

The PDF for velocity, enstrophy, vorticity, convection velocity and so on, as introduced in Volume I are also presented; these statistics have been performed on about five hundreds identified structures or instantaneous flow field, and since only a few of them can be classified in a well defined category, the results can be expected to present a wide scattering.

In Fig. 3.17 it is interesting to remark the size of the structure in span-wise axis; the upper limit is obviously the whole dimension of the domain. The number of structures having this maximum size is rather small and they correspond to the span-wise rolls and the upper and lower vorticity sheets.

It is also interesting to remark the distribution of mean convection velocity (top-left frame) Fig. 3.18; negative values correspond to structures involved in the various recirculation bubbles generated from the obstacle. Most of the quantities presented in Fig. 3.17 and Fig. 3.18 show a symmetrical behavior respect the zero, as to be expected.

At difference of the case of channel flow (Volume I), no joint PDF are here presented; in previous case those information were needed to further explain the data already collected, but, for the current case, it was found that they do not yield any ulterior information and have been, therefore, neglected altogether.

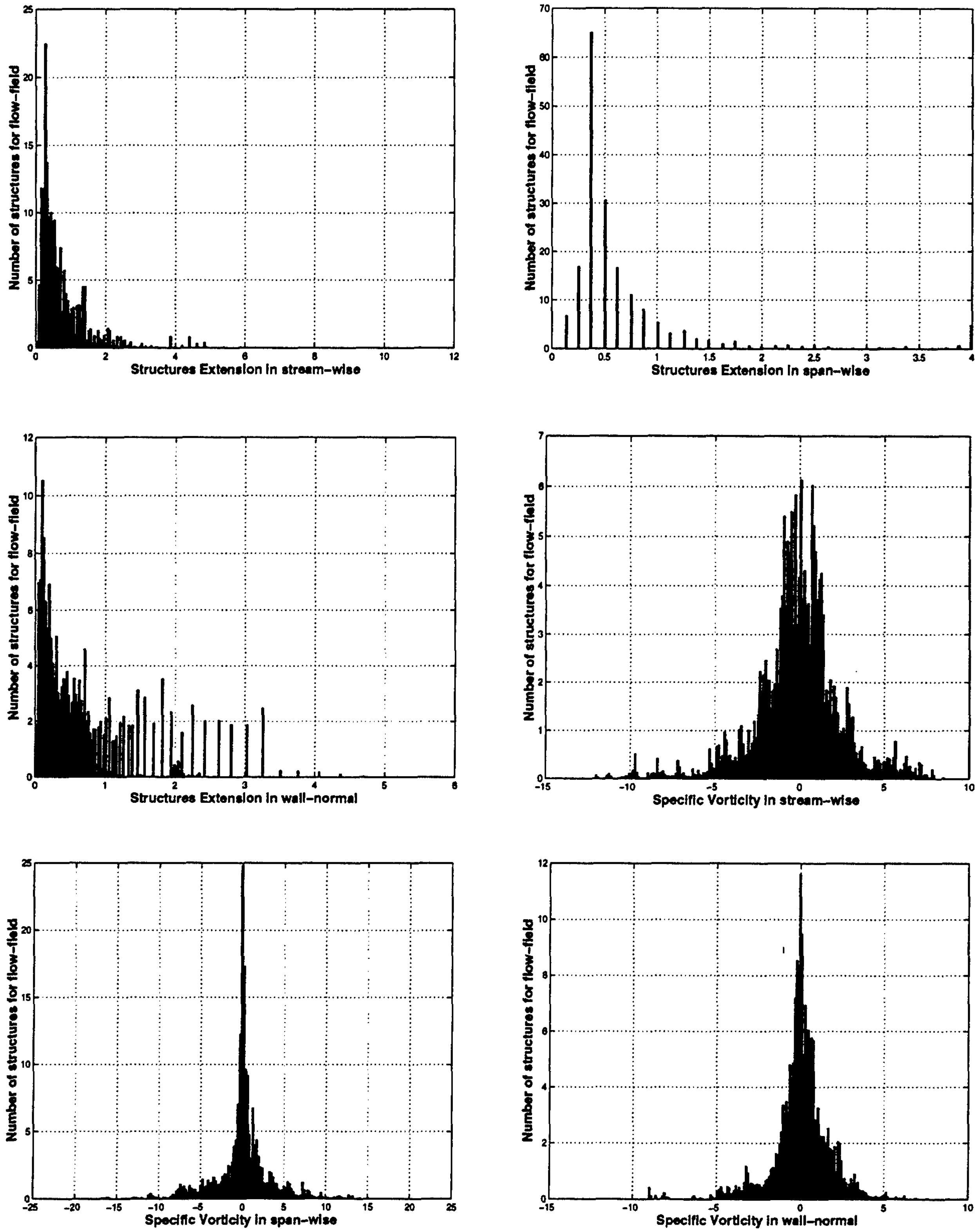

Fig. 3.17: Structures identification: PDF of quantities of interest, like structures dimension and specific vorticity.

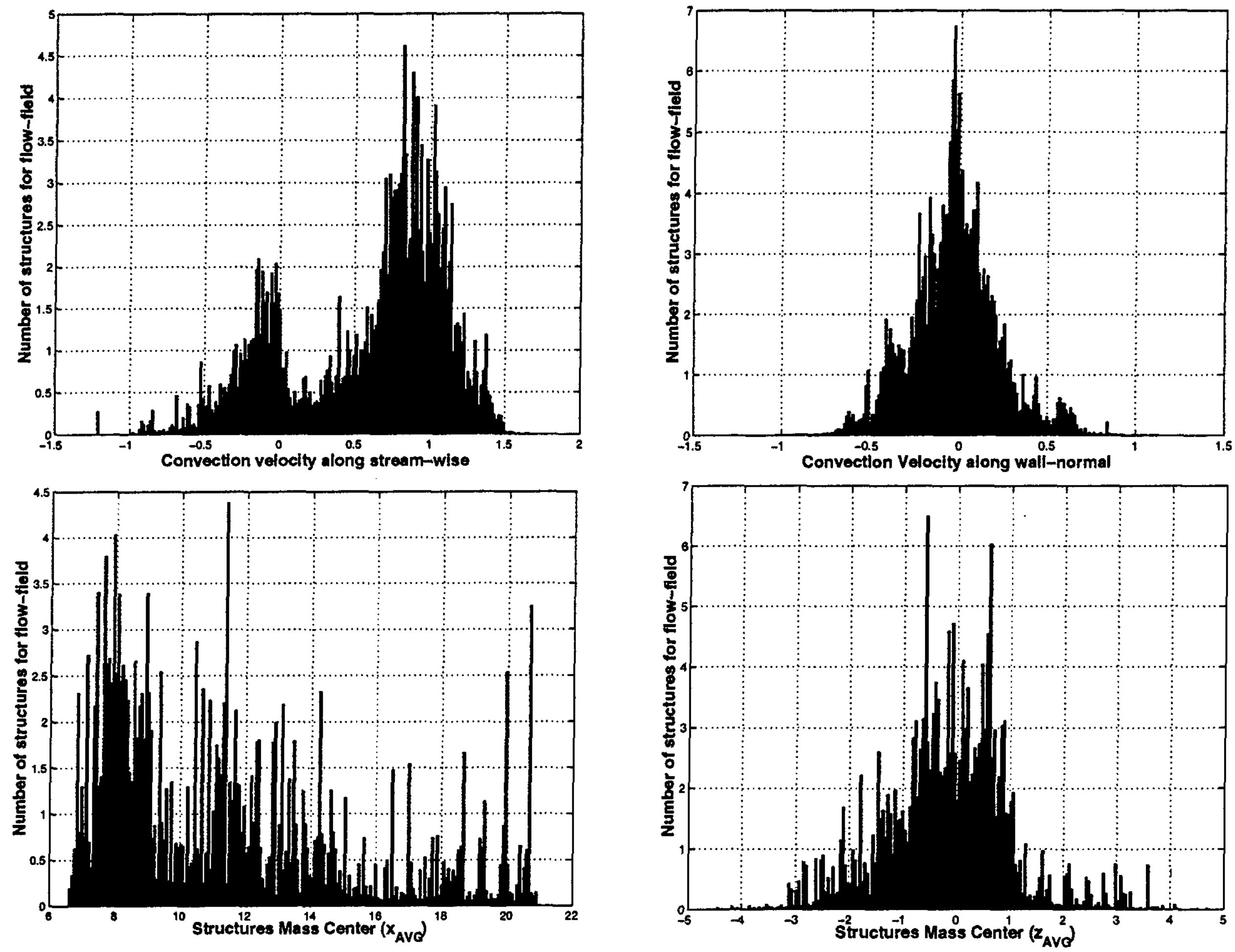

Fig. 3.18: Structures identification: PDF of quantities of interest, convection velocities and mass center position.

4. CONCLUSIONS

Results presented in § 2 have shown that algorithms and models developed for the LES presented in Volume I have the '*theoretical*' capability to simulate complex turbulent flows such the one around a cylinder of square cross section at moderately high Reynolds number.

Most of the defects remarked for present simulation can be attributed to insufficient available computer power, which has limited the size of computational field and the resolution of the grid, primarily along the critical span-wise direction; increasing the size of the computational domain by 50% (L_y=6H against L_y=4H) and doubling the corresponding resolution (96 nodes against 32) are quite likely to yield a full satisfactory simulation of flow field, not only in terms of the eulerian statistics, but most probably terms of detection and identification of the coherent structures. For the second task, assuming that the computational resources would allow the increase of span-wise number of nodes from 32 to 96, an increase in resolution in the wake should also be undertaken.

Continuing increase of computer capabilities on open market allows to assume that the requirements could soon be available for possible future investigations, as more and more inexpensive clustering technology is made available from both software and hardware vendors, operating within area of the GNU/Linux Operating System. At the present moment, available computational resources would allow to compute the configuration proposed above in a massively parallel environment, where the latent parallel capabilities of the code would be exploited.

If, however, assuming that exists the possibility of setting up a simulation in a parallel context, spending necessaries resources in terms of manpower to polish the parallel version of the code, the sped-up that it could be possible to obtain cannot mask the deficiency of the scalar version of the code: explicit treatment of viscous term, absence of an up-to date dynamic SGS model, bottle neck generated by the upwinding procedure, grid conformity between different domains, are all factors that should be faced and solved before planning to use a parallel context to speed-up computations.

Concerning the behavior of dynamic field (§ 3), visualizations with Q criterion (Volume I §4.2.1) have proved the Large Eddy Simulation approach capable of reproducing the principal mechanisms of flow separation over an obstacle and of formation of a wake dominated by large scale, inherently coherent, structures; onset and development of 'Kelvin-Helmholtz' class instability and formation and interaction of rib-roll structure are well put in evidence. Tracking of span-wise vortices trough pressure field[1] has proved the coherent and persistent character of these structures.

[1]The pressure field has been used in order to avoid to compute the gradient of velocity tensor needed by the criteria introduced in Volume I §4.2 . Whenever the pressure field would not be accessible, the detection criteria would produce basically the same result at an higher cost.

Considering the algorithms developed (Volume I, §4) to identify, define, classify all the organized structures in flow-field and extract all relevant statistics of this population, it must admitted that their application to a new class of complex flow has been only partially successful: again this defect can be attributed, in large part, to insufficient grid resolution which has posed unresolvable conflicts to the definition algorithm. Useful global statistics have been obtained relaxing the constraints posed to the procedure, confining the analysis to strongly defined vortex cores and rejecting as numerical noise a large number of the nodes which satisfy the Q criterion. The consequence is, however, to worsen the signal-to-noise ratio with respect the one obtained in simulations of plane channel (Volume I).

However, it can be concluded, as already pointed out in previous chapter, that present simulations,

in spite of their shortcomings, have been able to show that an very important part of the entire turbulent field lies within very active structures, which, by themselves, cover a very small part of the entire flow field. It can advanced that the characteristics of these structures are the ones which define and control the wake behavior, and their identification could be key of understand and possibly identify and recognize specific wakes.

It could be suggested that a general and affordable procedure might pass through the adoption of the afore-mentioned approach (computing only the strongly connected vortex cores), while the full process initially developed and proposed in Volume I might prove itself non-affordable or impossible to apply to complex flow field without introducing ad hoc, case by case, adaptations.

Again, this point could only be proved or confuted by more refined calculations, as the ones proposed above.

It can, however, be concluded that, even in case of complex flows, it is indeed feasible to identify and quantify the contribution of organized turbulence versus non-coherent background trough the Large Eddy Simulation approach; whether the results found are deeply linked to the filtering operator and to the grid dimensions, only a careful campaign of test simulations could provide a definitive answer.

Concerning the eulerian statistics, it is found that even high order ones, such the turbulent kinetic energy budget (defined in Volume I, §2) cannot be used to separate coherent behavior from non-coherent one.

It could be possible, according to some suggestions given in literature, to distinguish structures and un-coherent backgound by the spectral analysis of the two fields, which was found impossible to perform within present frame due to limitations of available time and means.

In this case, it could reveal itself as a further tool able to identify and recognize coherent

structures in wake flows and this application should be investigated.

Bibliography

AGARD (1998). A selection of test cases for the validation of large-eddy simulations of turbulent flows. Agard Advisory Report 345, North Atlantic Treaty Organization, 7 Rue Ancelle, 92200 Neuilly-Sur-Seine, France.

Brown, G. L. and Roshko, A. (1975). On density effects and large structures in turbulent mixing layer. J. Fluid. Mech., 64:775.

Compte, P., Ducros, F., Silvestrini, J., David, E., Lamballais, E., Metais, O., and Lesieur, M. (1994). Simulation de grandes échelles d'écoulements transitionnels. In AGARD, editor, AGARD 74^{th} FDP Symposium, AGARD SERIES.

Compte, P. and Lesieur, M. (1998). Large-eddy simulations of compressible turbulent flows. VKI Lecture Series 5, von Karman Institute for Fluid Dynamics, Chaussée de Waterloo 72,B - 1640 Rhode Saint Genèse - Belgium.

Farge, M., Kevlahan, N., Perrier, V., and Goirand, E. (1996). Wavelets and turbulence. In IEEE 84, page 639.

Germano, M., Piomelli, U., Moin, P., and Cabot, W. H. (1991). A dynamic subgrid-scale eddy viscosity model. Phys. of Fluids, 3(7):1760.

Giammanco, R., Simons, E., Manna, M., and Benocci, C. (2001). Large eddy simulation of turbulent flows over a cylinder of square cross section. In DNS-LES Workshop-IV. University of Twente, Kluwert.

Härtel, C. and Kleiser, L. (1998). Analysis and modeling of subgrid-scale motion in near-wall region of turbulence. J. Fluid. Mech., 356:327.

Hunt, J. C. R., Way, A., and Moin, P. (1988). Eddies, stream, and convergence zones in turbulent flows. Center for Turbulence Research Report CTR-S88, Center for turbulence research, Standford University.

Hussain, F. (1983). Coherent structures-reality and myth. Phys. of Fluids, 26(10):2816–2847.

Hussain, F. (1986). Coherent strucrures and turbulence. J. Fluid. Mech., 173:303–356.

Hussain, F. and Hayakawa, M. (1987). Eduction of large scale organized structures in a turbulent plane wake. J. Fluid. Mech., 180:191.

Lyn, D. A., Einav, S., Rodi, W., and Park, J. H. (1995). A laser-doppler velocimetry study of ensemble-averaged characteristics of the turbulent near wake of square cylinder. J. Fluid. Mech., 304:285.

Moin, P. and Mahesh, K. (1998). Direct numerical simulation: A tool in turbulence research. Annu. Rev. Fluid. Mech., 32:539.

Piomelli, U. (1997). Large-eddy and direct simulation of turbulent flows. VKI Lecture Series 3, von Karman Institute for Fluid Dynamics, Chaussée de Waterloo 72,B - 1640 Rhode Saint Genèse - Belgium.

Pope, S. B. (2000). Turbulent flows. Cambridge University Press.

Robinson, S. K., Kline, S. J., and Spalart, P. R. (1990). Near-Wall Turbulence, chapter Quasi-coherent structures in the turbulent boundary layer: Part II. Verification and new information from a numerically simulated flat-plate layer, page 218. Hemisphere Publishing Corp.

Rodi, W., Ferziger, J., Breuer, M., and Pourquié, M. (1997). Status of large eddy simulation: Results of a workshop. J. Fluids Eng., 119:248.

Scarano, F., Benocci, C., and Riethmuller, M. (1999). Pattern recognition analysis of turbulent flow past a backward facing step. Phys. of Fluids, 11(12):3808.

Simons, E. (2000). An efficient multi-domain approach to large-eddy simulation of incompressible turbulent flows in complex geometries. PhD thesis, von Karman Institute for Fluid Dynamics.

Spalart, P. (1988). Direct simulation of turbulent boundary layer up re_θ =1410. J. Fluid. Mech., 187.

Sungsu, L. (1998). Numerical study of wake structure behind a square cylinder at high reynolds number. Engineering Turbulence Modelling and Experiments, 1(2):127–144.

Tennekes, H. and Lumley, J. L. (1983). A First Course in Turbulence. MIT Press, Cambridge, MA.

van Driest, E. R. (1956). On turbulent flow near a wall. Journal of Aeronautical Sciences, 23(11):1007–1001,1036.

APPENDIX

A. ADDITIONAL SIMULATIONS

The present appendix introduced the supplementary LES simulations performed to evaluate the sensibility of present code to different parameters. No structures analysis is performed and the flow field is computed for comparison to the reference simulation presented in § 2. These new simulations were mainly aimed to assess the effect of the SGS model on the result of the simulation, together with the effect of a grid more refined than the one employed in § 2, in order to also to assess the effect of grid refinement on the computed solution.

The grid has then been refined close to the walls of the obstacle and in the far wake, while it has slightly been coarsened in regions near top bottom boundaries of the computational field. The layout of the simulation has been slightly changed in terms of domain decomposition, as it is possible to observe from Fig. A.1.

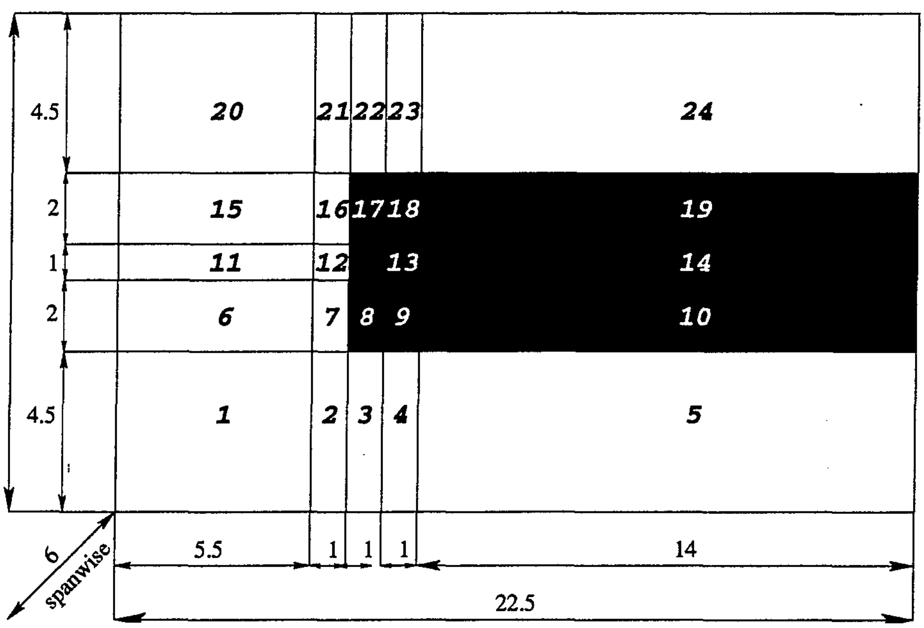

Fig. A.1: Revised multi-domain set-up for computational field. No coloring: 3^{rd} order, upwind treatment of advective term; coloring: 4^{th}order central treatment of advective term.

Present cartesian grid is made of $250 \times 32 \times 184 \cong 1.4 \times 10^6$ points, and the minimum distance of the pressure node from the surface of the obstacle has been decreased from $\cong 0.002H$ in the reference simulation (§ 2), to $\cong 0.001H$. The Multi-domain set-up is described in detail in Tab. A.1, while Fig. A.2 shows a close-up of the grid around the obstacle.

Table A.1: Number of grid points and stretching ratios for individual sub-domains. Number of points in span-wise : 32; L, extension, N number of points, c stretching parameter, x stream-wise, z vertical direction.

Domain	L_x	L_z	N_x	N_z	c_x	c_z
1	5.5	4.5	16	11	1.18	1.162
2	1.0	4.5	48	11	1.075	1.162
3	1.0	4.5	66	11	1.0938	1.162
4	1.0	4.5	48	11	1.075	1.162
5	14.0	4.5	72	11	1.0252545	1.162
6	5.5	2.0	16	48	1.18	1.09385
7	1.0	2.0	48	48	1.075	1.09385
8	1.0	2.0	66	48	1.0938	1.09385
9	1.0	2.0	48	48	1.075	1.09385
10	14.0	2.0	72	48	1.0252545	1.09385
11	5.5	1.0	16	66	1.18	1.0938
12	1.0	1.0	48	66	1.075	1.0938
13	1.0	1.0	48	66	1.075	1.0938
14	14.0	1.0	72	66	1.0252545	1.0938
15	5.5	2.0	16	48	1.18	1.09385
16	1.0	2.0	48	48	1.075	1.09385
17	1.0	2.0	66	48	1.0938	1.09385
18	1.0	2.0	48	48	1.075	1.09385
19	14.0	2.0	72	48	1.0252545	1.09385
20	5.5	4.5	16	11	1.18	1.162
21	1.0	4.5	48	11	1.075	1.162
22	1.0	4.5	66	11	1.0938	1.162
23	1.0	4.5	48	11	1.075	1.162
24	14.0	4.5	72	11	1.0252545	1.162

The practical drawback related to this increase in resolution close to the cylinder lies with the explicit treatment of the viscous term: decreasing the distance of the first pressure node from the wall the stability constraint on the time-step yields smaller and smaller limit values; furthermore, the maximum allowable time-step is found to be extremely dependent on the behavior of the SGS viscosity at the wall.

In this optic, it became necessary to apply SGS models where wall effects are explicitly taken in account, which is the case for the Smagorinsky model with the damping function (van Driest, 1956); this formulation was found to offer better numerical performances than models in the class of filtered structure function model (Compte and Lesieur, 1998), where the

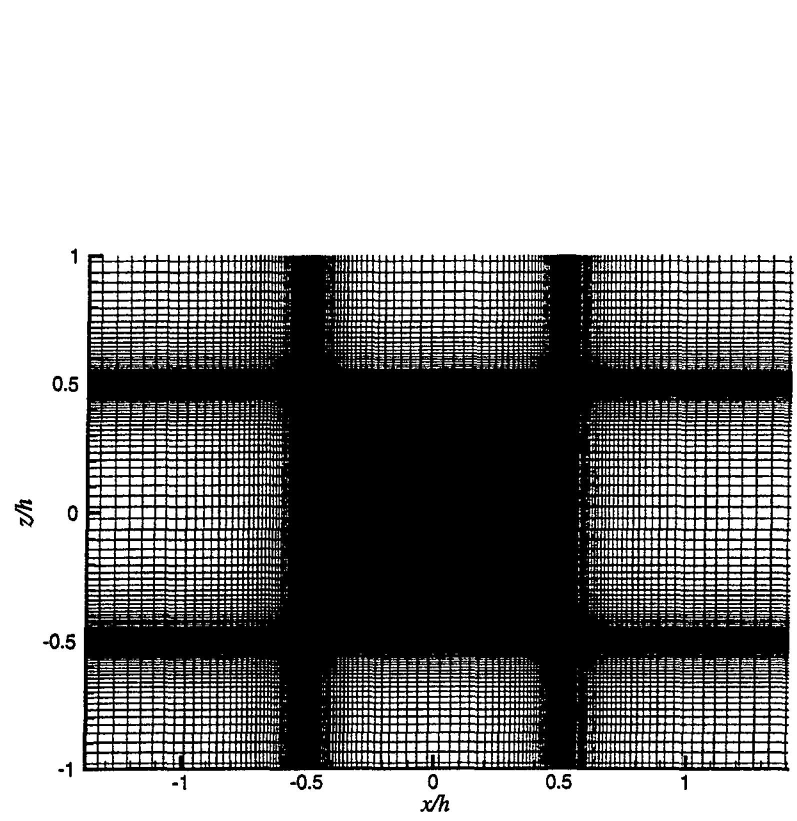

Fig. A.2: Revised grid: Close-up of grid around obstacle.

gradient of decrease of SGS viscosity nearing the wall is not steep enough. In fact, application of FSF model on present grid was found to bring to a time step one order of magnitude smaller than the one employed in the reference computation in § 2 and was, therefore, discarded for the present simulations.

Furthermore, the size of the domain was increased in the span-wise direction, without a corresponding increase of the number of points; the latter would have been extremely costly and not indispensable as long as the objective of the test was limited to find out whether the simple increase of the span-wise dimension would affect the simulation in a significant way.

Finally, different boundary conditions are used for the top and bottom boundaries, which allow flow to leave or to enter the computational domain; even if the flux involved are modest, the resulting streamlines clearly remark a difference between the reference simulation of § 2 and the ones performed hereafter.

While it was not possible to perform a full parametric study, but it was nevertheless possible to extract a series of remarks which might be useful in order to design further simulations devoted to production of more detailed statistics, included, but not limited, to structures analysis and turbulent kinetic budget computation.

This stated, two additional simulations will be presented, chosen between the different other simulations performed; in these two cases, the statistics of the turbulent field were found to be sufficiently converged to be included in present report: both simulations make

use of the Smagorinsky model for two different values of its coefficient, and both do not apply the SGS model outside the wake or the shear layer (see Fig. A.3). They will be named in the following as Case I and Case II respectively.

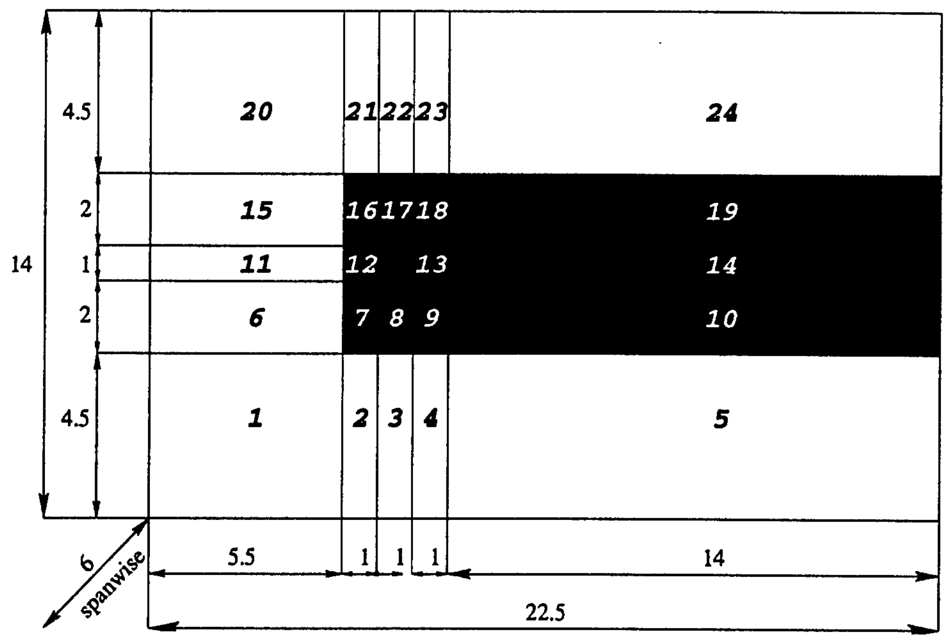

Fig. A.3: Revised multi-domain set-up for Smagorinsky SGS model. No coloring: no SGS model applied; coloring: SGS model applied with uniform constant Cs.

Case I was performed with a Smagorinsky coefficient $Cs = 0.1$. This value already lies in the upper range of values applied for channel flows, turbulent boundary layers and the like; however, since this value corresponds to a parameter (supposedly depending from the flow), its magnitude for a different, new, case cannot be directly taken from the usual range of values established for different and simpler flows. Case II, indeed, applies an higher coefficient, $Cs = 0.2$ and the corresponding results are perfectly reasonable, hinting to some improvements, which led to attempt a third simulation based on a still higher value for the Smagorinsky coefficient; however, limitation of available computer power made it impossible to complete it in time to be included in present report.

The two different simulations also differ by the value chosen for the coefficient of the van Driest damping; in Case II it was increased in order to force a slower decay of the SGS viscosity at the wall. Concerning Case II, it should be noted that, in spite of smaller grid sizes, the permissible time-step was found to be of a size comparable to the one for the reference computation of § 2 due to the use of a different SGS model, while, for Case I, permissible the time-step was three times bigger.

B. ADDITIONAL CASE I

The current simulation is performed on the grid described in Tab. A.1 and with a Smagorinsky coefficient $Cs = 0.1$, applied in the domains marked in Fig. A.3.

An overview of the results of the simulation can be found in Tab. B.1. Fig. B.3 through Fig. B.5 present the c_p distribution around the obstacle for current simulation, together with the recorded history for c_l and c_d. In Fig. B.1 and Fig. B.2 it is possible to see how the new set of boundary conditions influences the flow, and, conversely, how the higher resolution closer to the surface of the obstacle allows a better resolution of the small re-circulation bubble close to the leading edge of the obstacle.

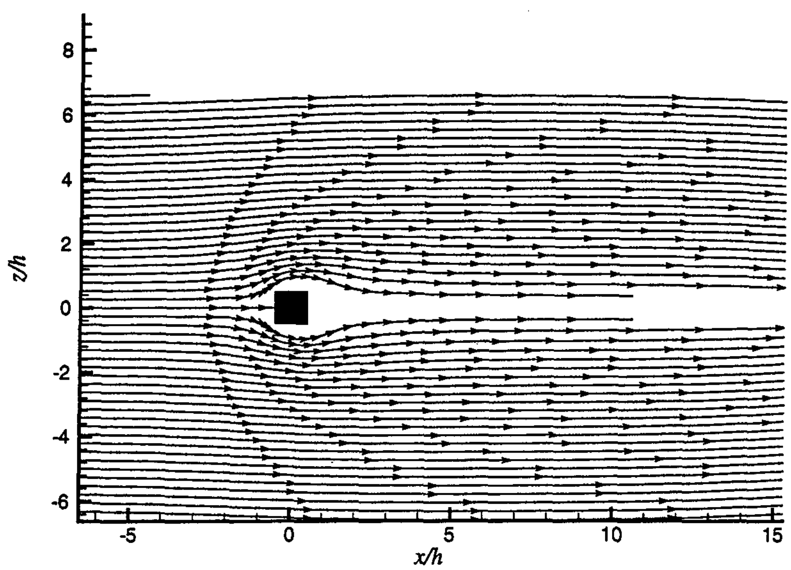

Fig. B.1: Additional simulations, Case I: time averaged stream-lines around square cylinder; LES ($Re = 22,000$)

Table B.1: Additional simulations, Case I: macroscopic quantities of interest: experimental range of admissible values and computed ones.

	St	c_{lrms}	c_d	c_{drms}	lr
EXP	0.133	0.1-1.4	1.9-2.1	0.1-0.23	1.38
LES	0.127	1.41	2.29	0.5382	0.53

It has to be noted the averaging procedure, here applied: an integer number of shedding periods is taken, and, afterward, the average is improved taking advantage of the

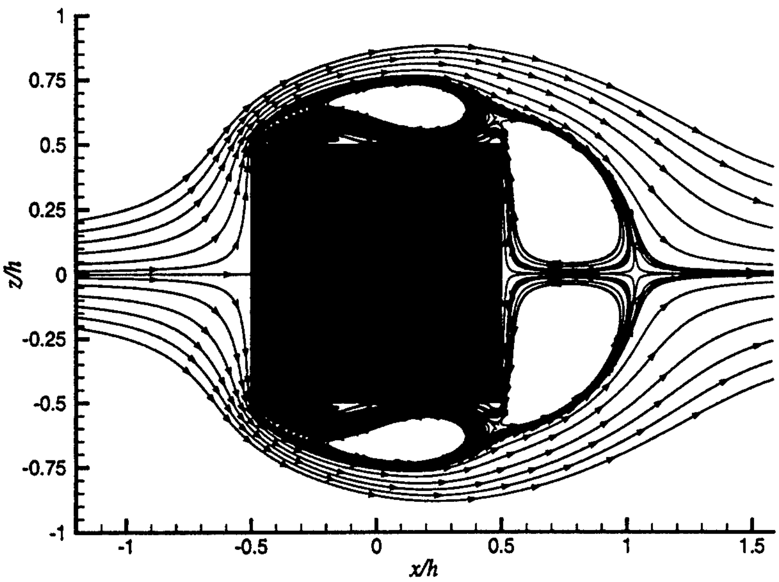

Fig. B.2: Additional simulations, Case I: time averaged stream-lines around square cylinder, close-up; LES ($Re = 22,000$)

symmetry-asymmetry of the flow along the wake centerline. It not directly possible to compare Fig. B.5(b) to with Fig. 2.16(b), since the number of shedding periods used to average the data is different for the two calculations; nevertheless, the number of samples is estimated, for both cases, to be sufficient large to reliably extract macroscopic data such as the mean drag coefficient; comparing with reference simulation, the value of this parameter (see Tab. B.1) decreases and lies closer to the experimental measures, while the c_p distribution on the surface, shown in Fig. B.4 seems to be in good agreement with the lower-valued set of experiments, as opposed to the results shown in Fig. 2.15.

Concerning the plots of average velocities on the obstacle, only minor improvements are visible in the current simulation, by comparison to the reference one (see Fig. B.6 through Fig. B.13 in comparison to Fig. 2.18 through Fig. 2.25).

For what concerns the behavior in the wake, no big difference can be remarked for behavior of the wake centerline, while the combination of Smagorinsky model and new grid appears to offer better results for the simulation of RMS behavior at off-centerline locations. This trend can be remarked, for example, in Fig. B.24 and Fig. 2.36; where the two unphysical prongs of the stream-wise RMS, remarked for the reference simulation disappear and the plot of RMS has the correct shape [1]. Considering the turbulent stress, Fig. 2.47 and Fig. B.35

[1]It must be always kept in mind that true RMS and LES RMS are not directly comparable, but since it is not possible to process the experimental data in order to make it comparable to the computed results, Fig. B.24 is less unsettling in comparison with Fig. 2.36

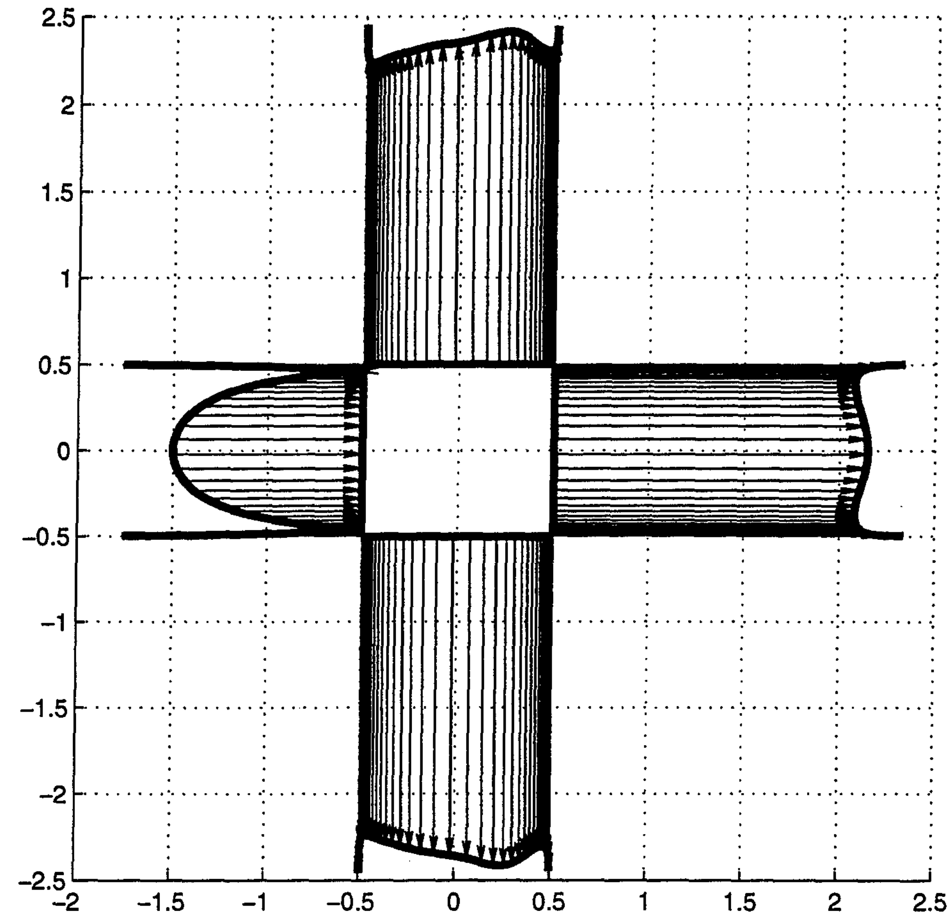

Fig. B.3: Additional simulations, Case I: diagram of averaged c_p distribution around the square cylinder. Average in time and in span-wise direction.

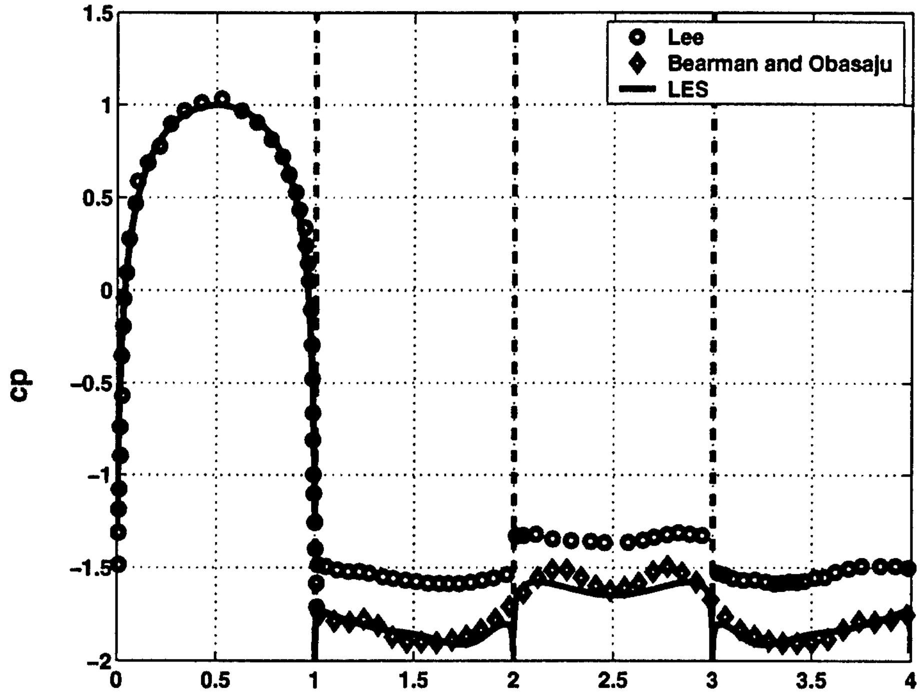

Fig. B.4: Additional simulations, Case I: plot of averaged c_p distribution around the square cylinder. Average in item and in span-wise direction.

show that the current simulation also presents a better behavior in the far wake with respect to the reference simulation.

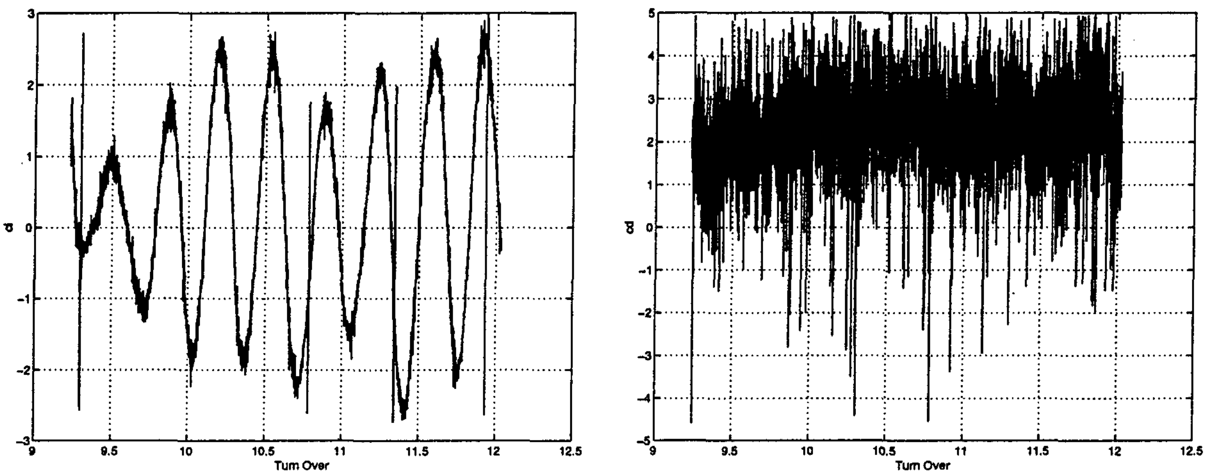

(a) Lift Coefficient (b) Drag Coefficient

Fig. B.5: Additional simulations, Case I: time history of lift and drag coefficients.

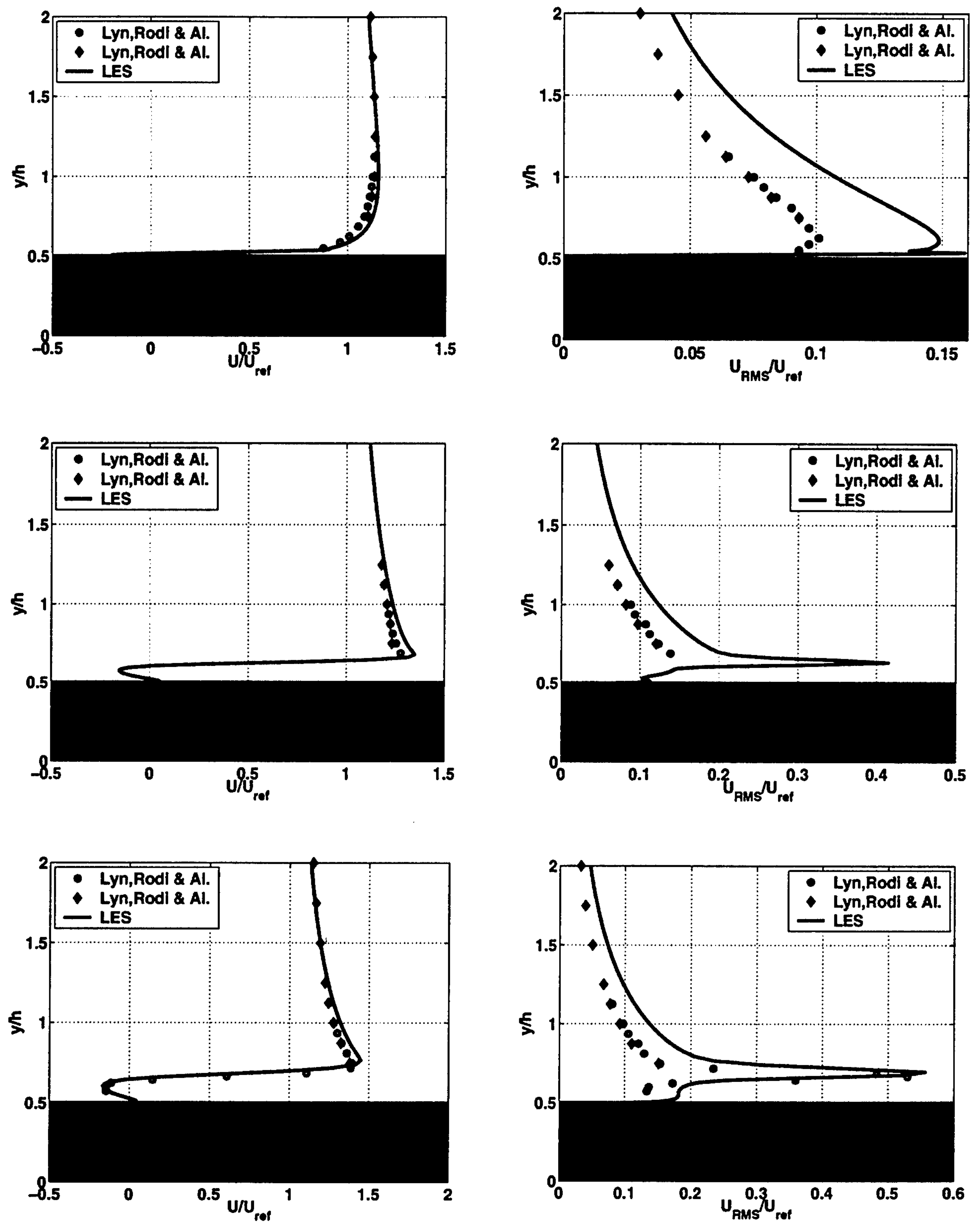

Fig. B.6: Additional simulations, Case I: velocity profiles for stream-wise velocity, left and stream-wise RMS, right, at three stations, from top to bottom: $x = -\frac{1}{2H}$,$x = -\frac{3}{8H}$ and $x = -\frac{1}{4H}$.

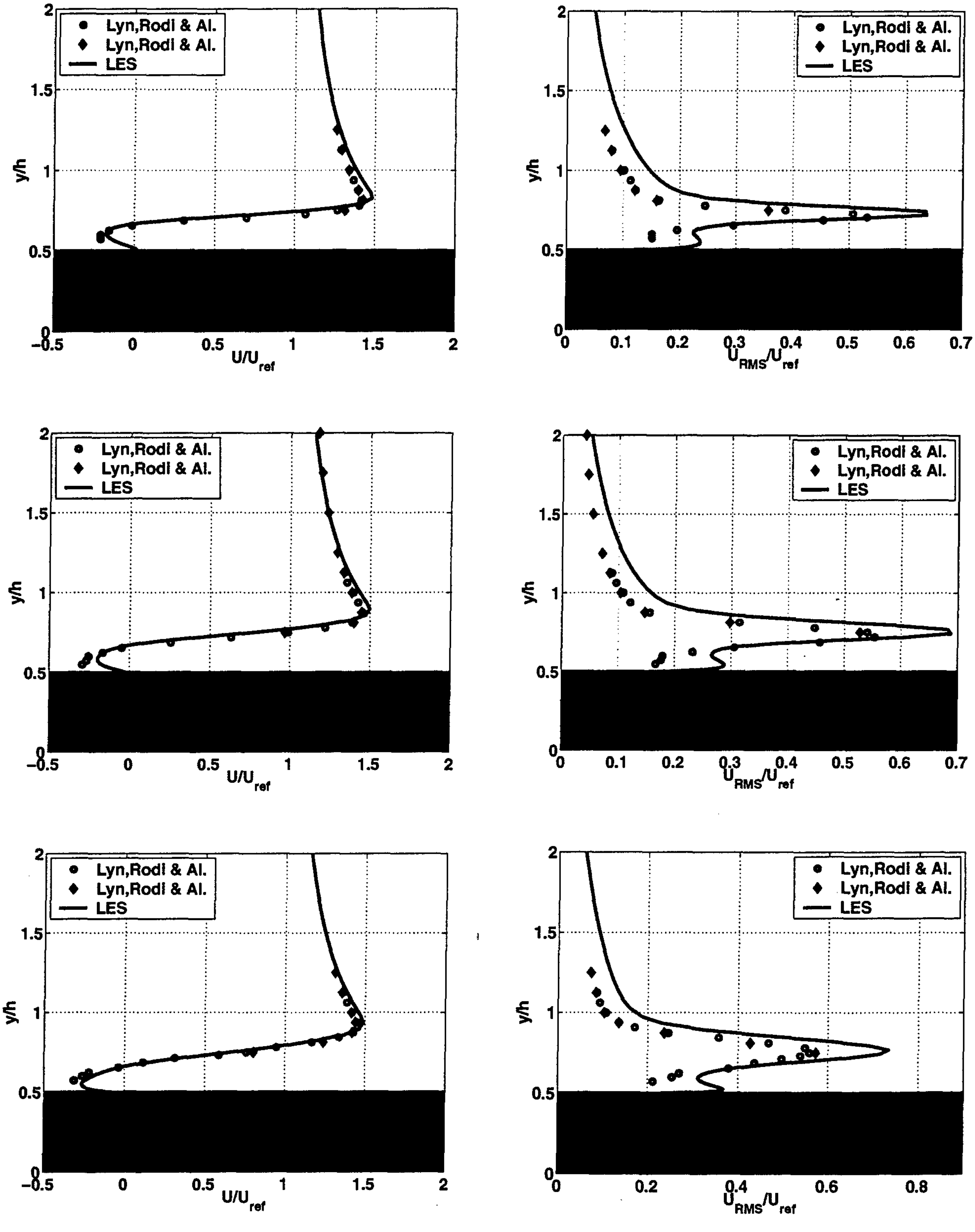

Fig. B.7: Additional simulations, Case I: velocity profiles for stream-wise velocity, left and stream-wise RMS, right, at three stations, from top to bottom: $x = -\frac{1}{8H}$,$x = 0$ and $x = \frac{1}{8H}$.

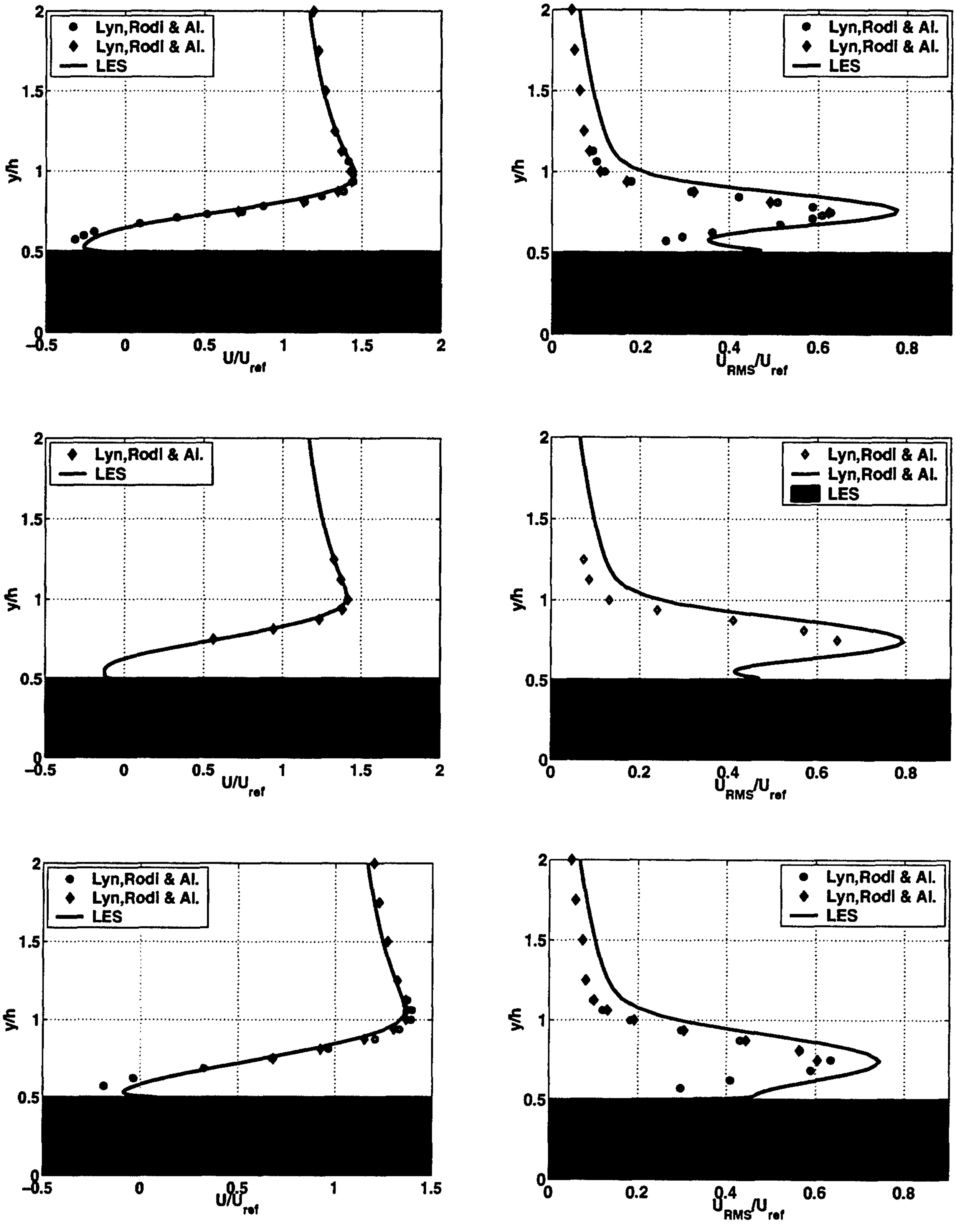

Fig. B.8: Additional simulations, Case I: velocity profiles for stream-wise velocity, left and stream-wise RMS, right, at three stations, from top to bottom: $x = \frac{1}{4H}$,$x = \frac{3}{8H}$ and $x = \frac{1}{2H}$.

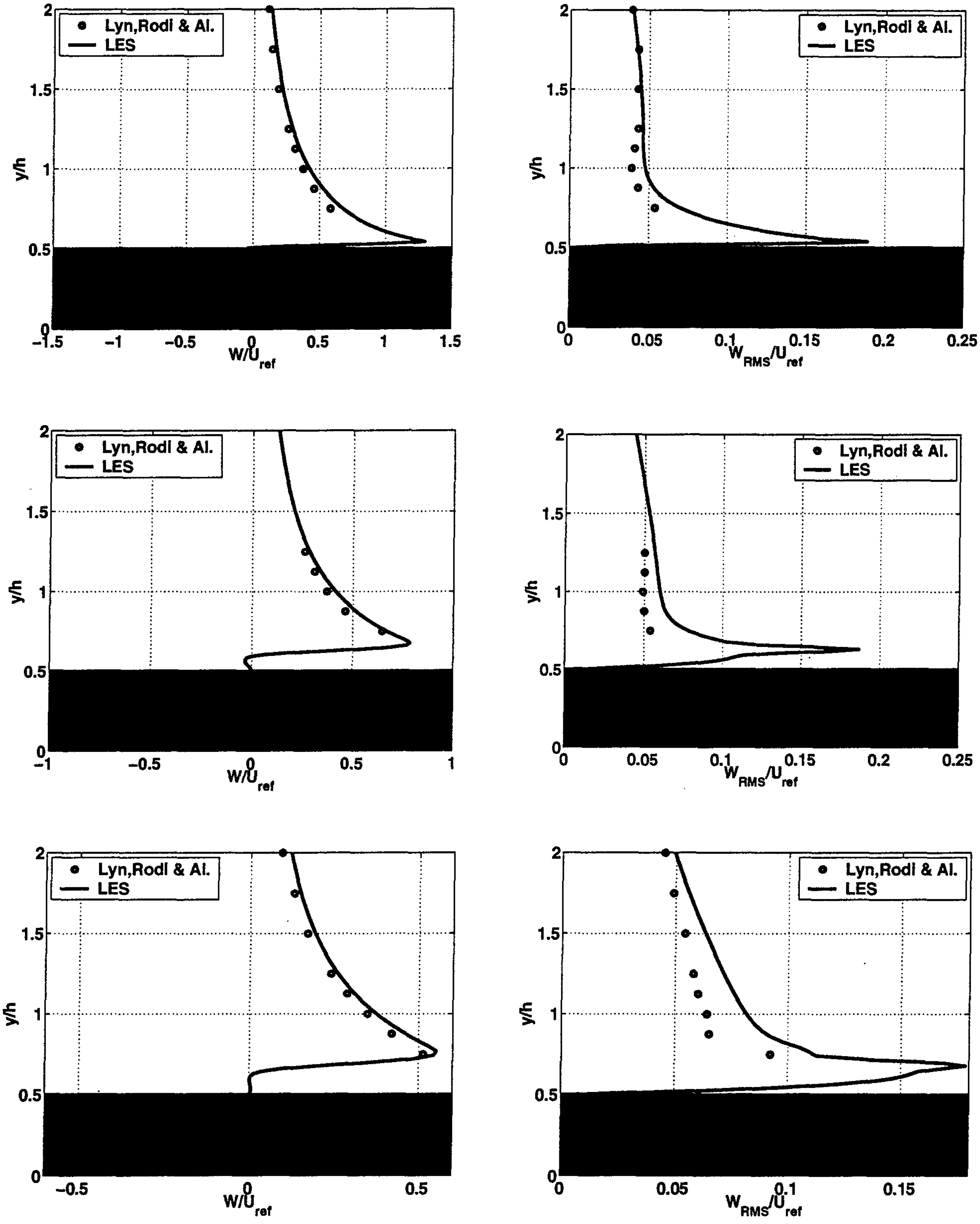

Fig. B.9: Additional simulations, Case I: velocity profiles for vertical velocity, left and vertical RMS, right, at three stations, from top to bottom: $x = -\frac{1}{2H}$,$x = -\frac{3}{8H}$ and $x = -\frac{1}{4H}$.

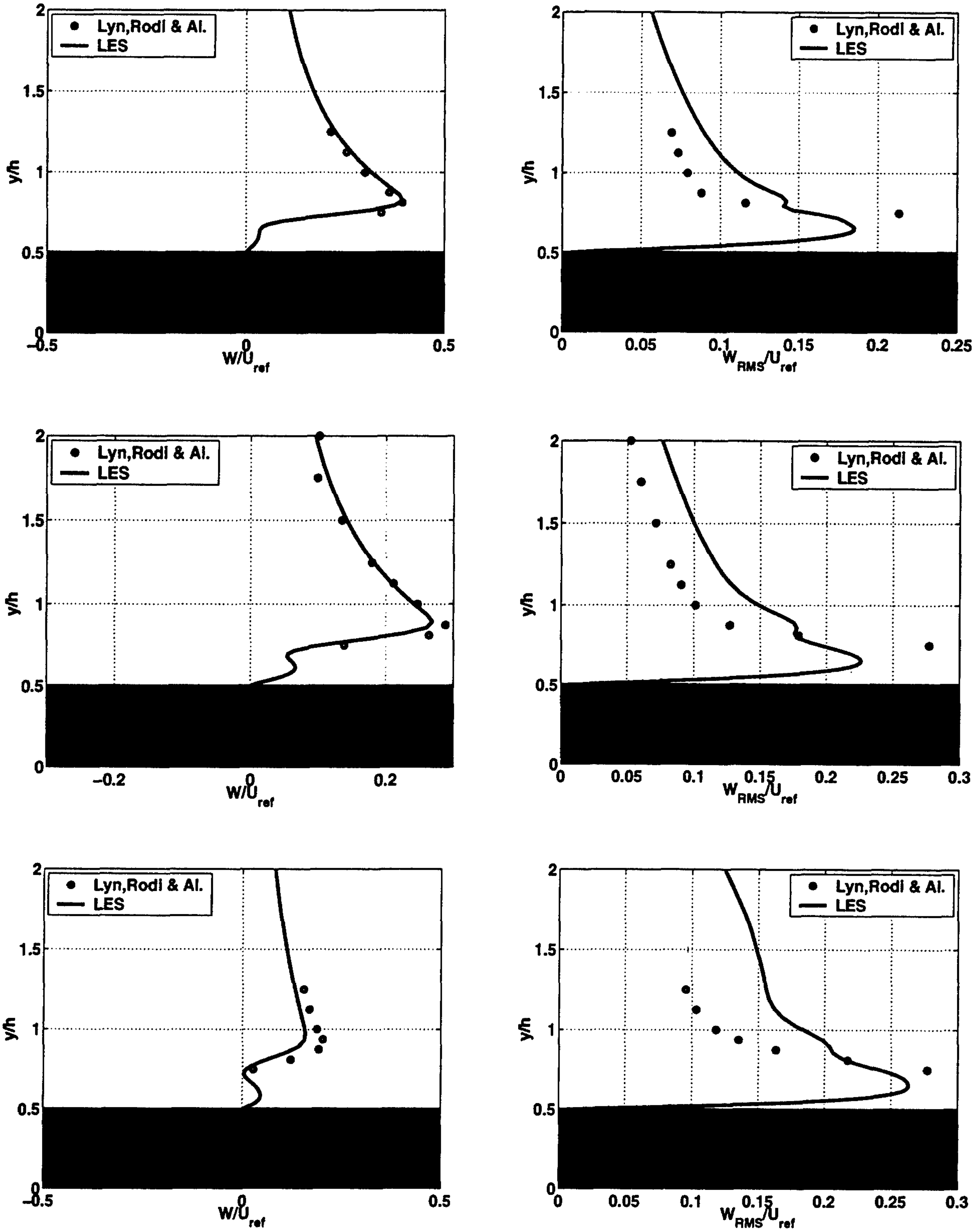

Fig. B.10: Additional simulations, Case I: velocity profiles for vertical velocity, left and vertical RMS, right, at three stations, from top to bottom: $x = -\frac{1}{8H}$,$x = 0$ and $x = \frac{1}{8H}$.

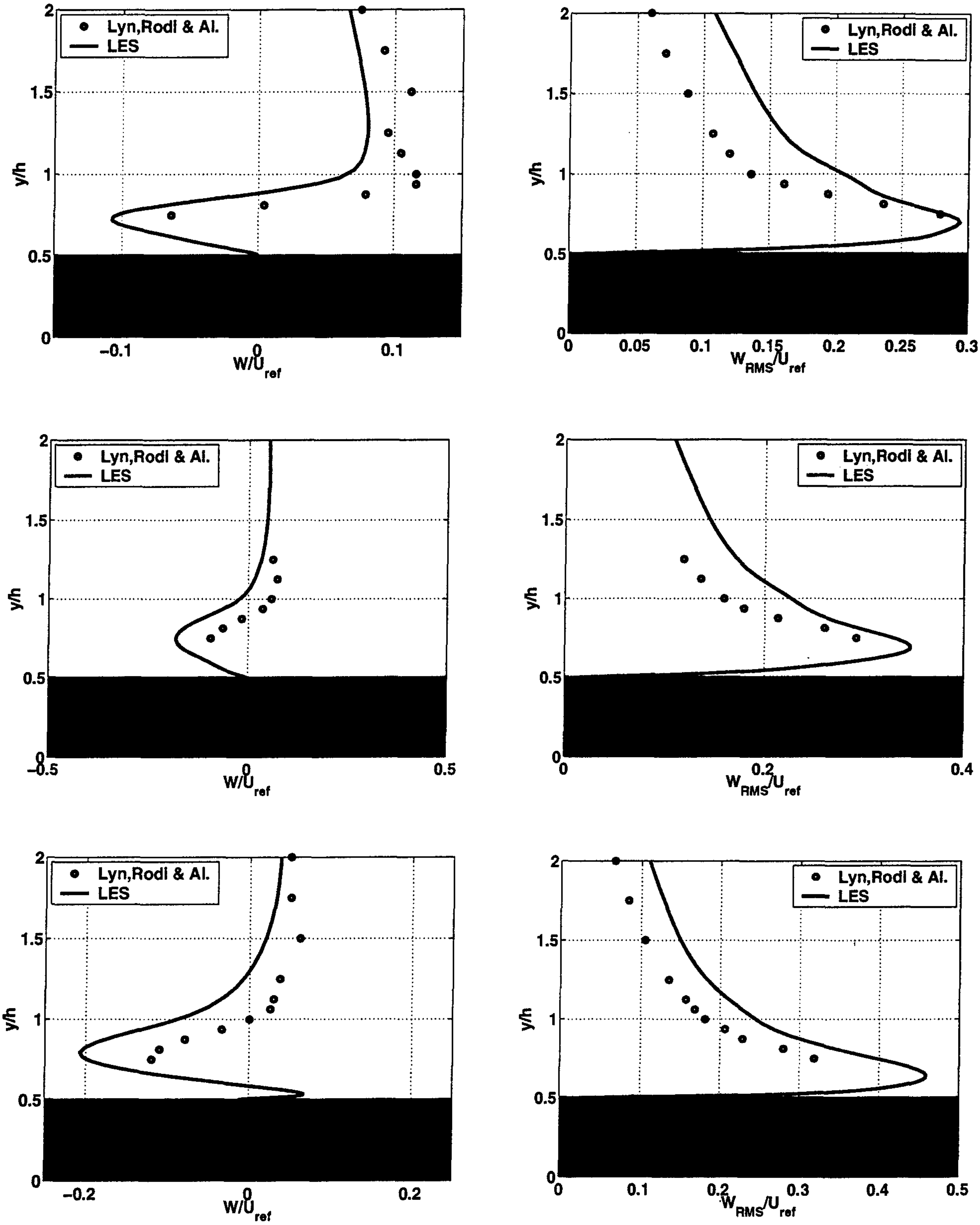

Fig. B.11: Additional simulations, Case I: velocity profiles for vertical velocity, left and vertical RMS, right, at three stations, from top to bottom: $x = \frac{1}{4H}$, $x = \frac{3}{8H}$ and $x = \frac{1}{2H}$.

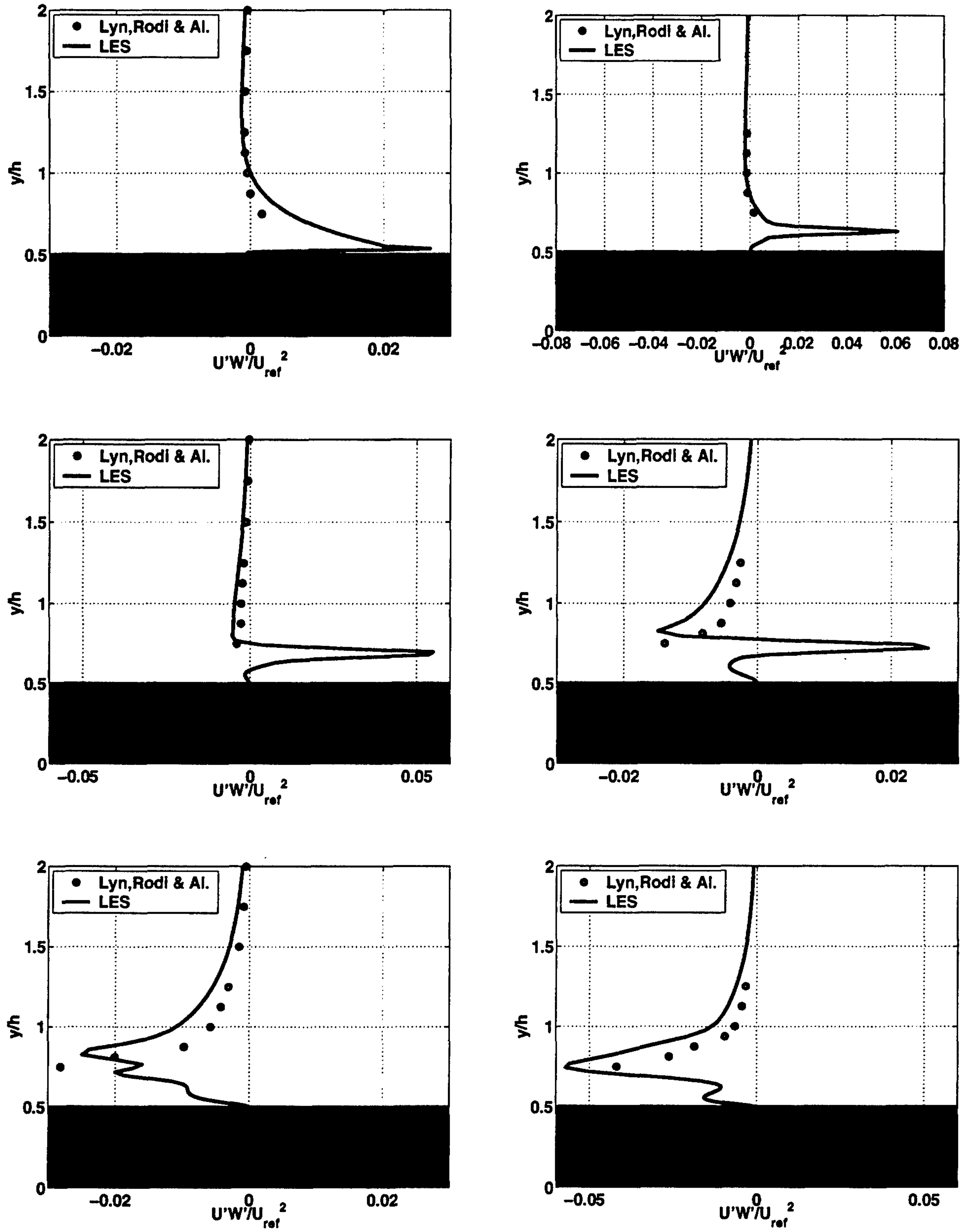

Fig. B.12: Additional simulations, Case I: velocity profiles for turbulent shear stress, from top to bottom and left to right, at the stations: $x = -\frac{1}{2H}$, $x = -\frac{3}{8H}$,$x = -\frac{1}{4H}$,$x = -\frac{1}{8H}$,$x = 0$ and $x = \frac{1}{8H}$

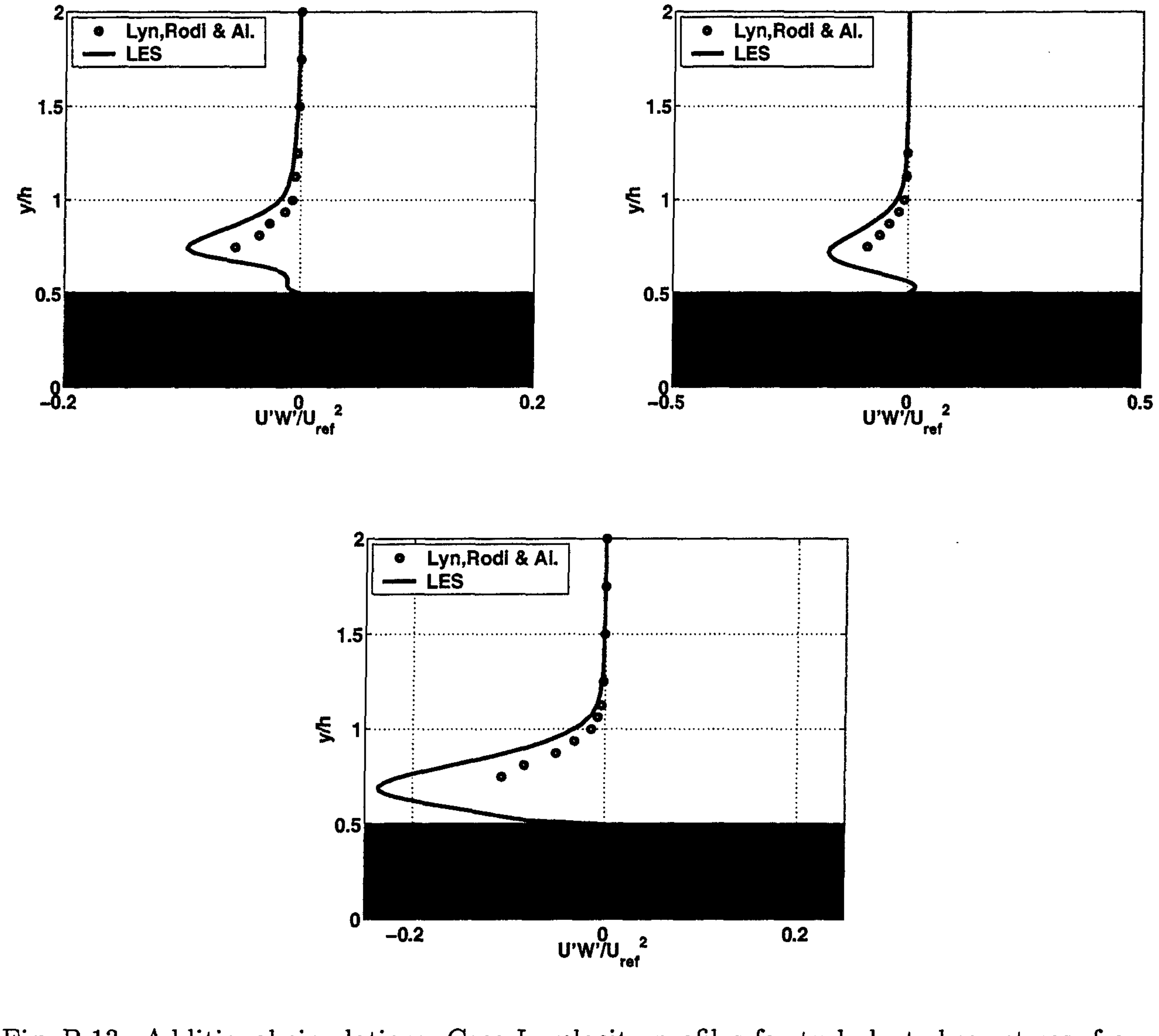

Fig. B.13: Additional simulations, Case I: velocity profiles for turbulent shear stress, from top to bottom and left to right, at the stations: $x = \frac{1}{4H}$, $x = \frac{3}{8H}$ and $x = \frac{1}{2H}$

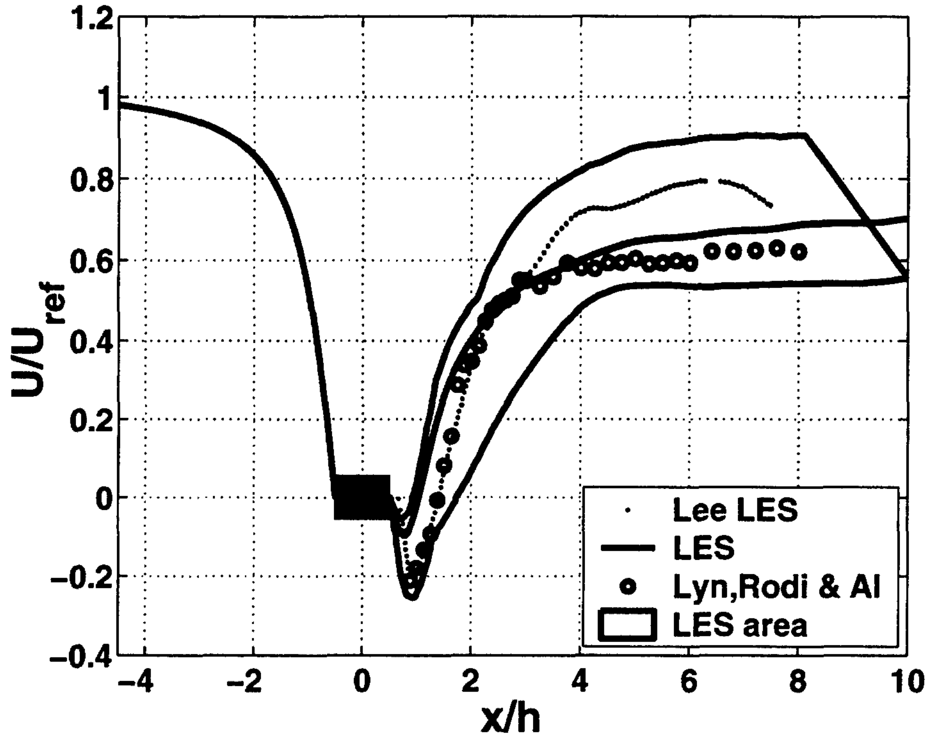

Fig. B.14: Additional simulations, Case I: average stream-wise velocity at wake centerline; present simulation versus experimental data and current LES (Sungsu, 1998)

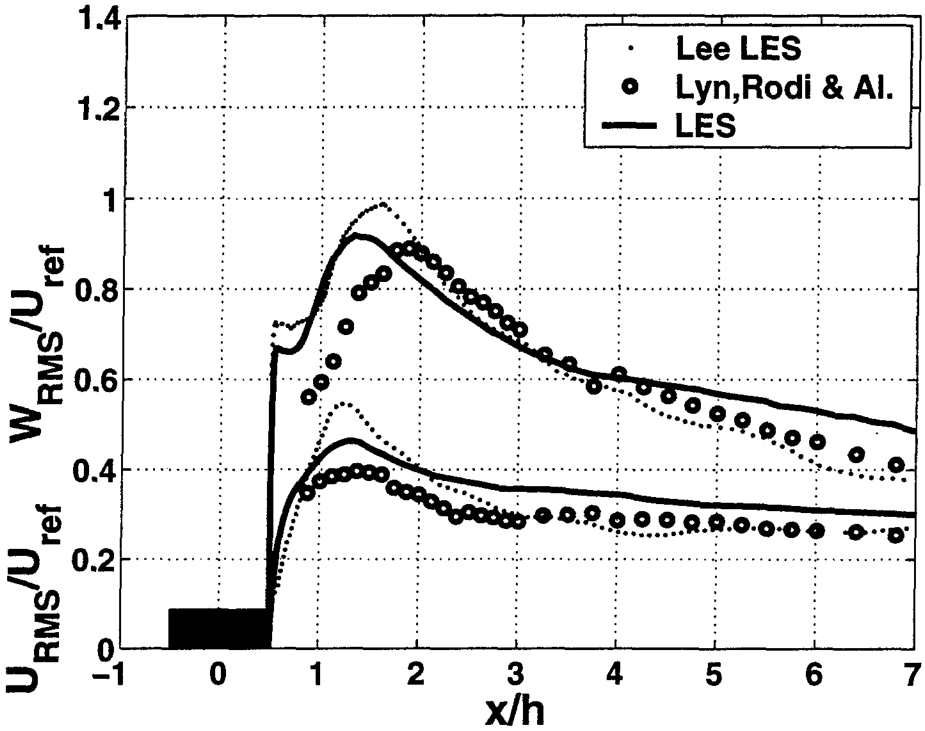

Fig. B.15: Additional simulations, Case I: average stream-wise and vertical velocity RMS at wake centerline; present simulation versus experimental data and current LES (Sungsu, 1998)

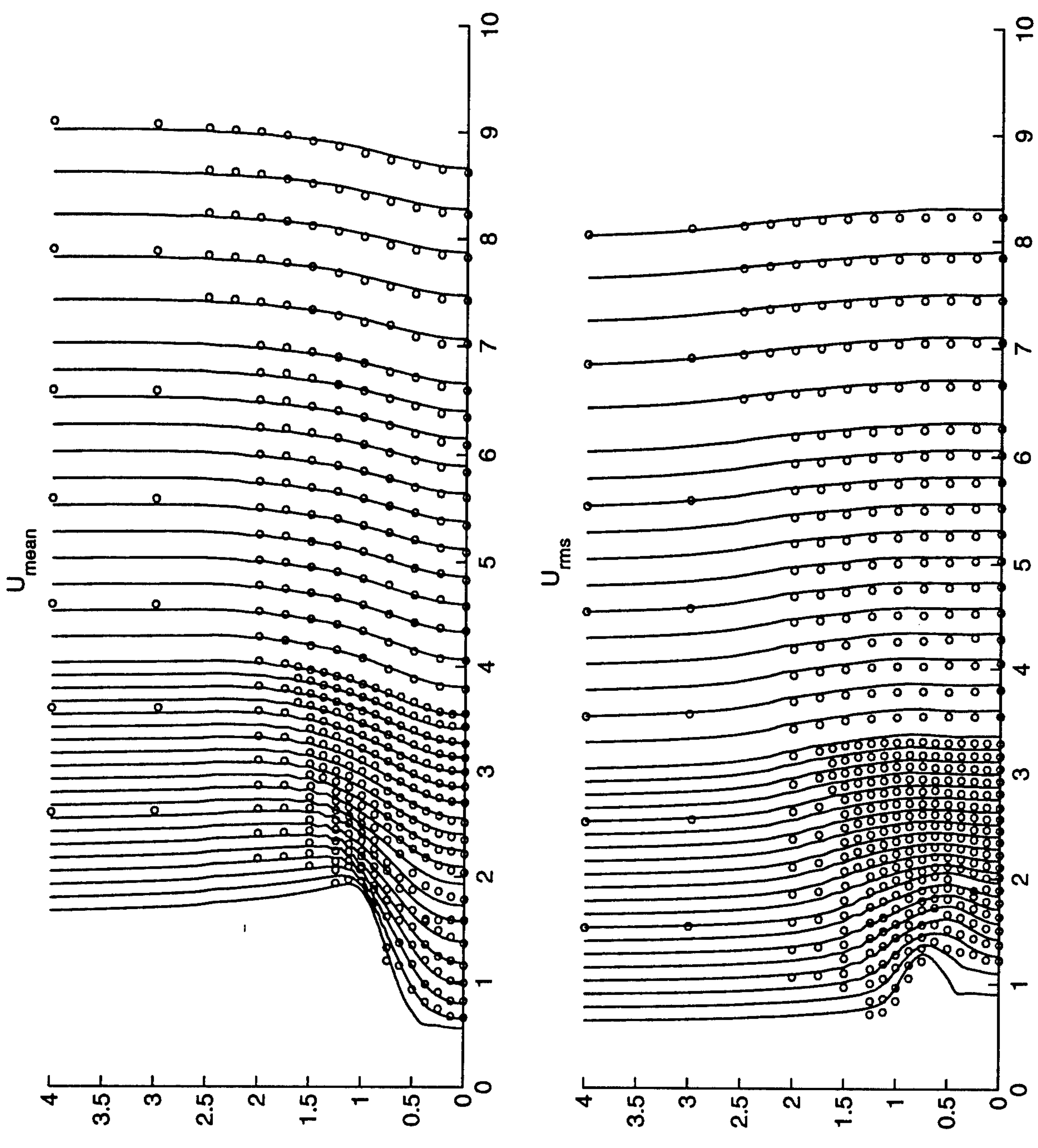

(a) Stream-wise average

(b) Stream-wise RMS

Fig. B.16: Wake overview, stream-wise velocity comparison with experiments.

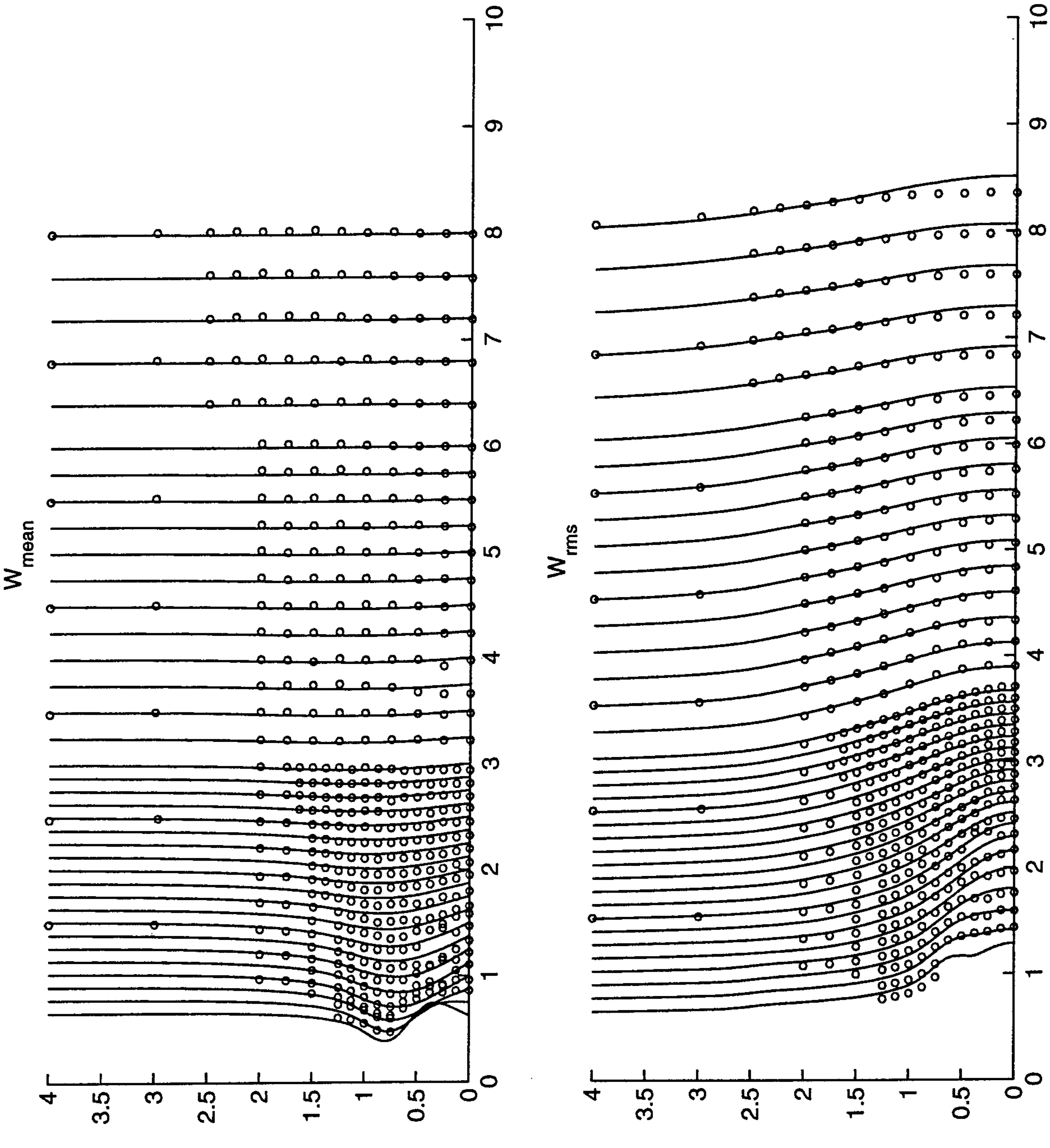

(a) Vertical average

(b) Vertical RMS

Fig. B.17: Wake overview, vertical velocity comparison with experiments.

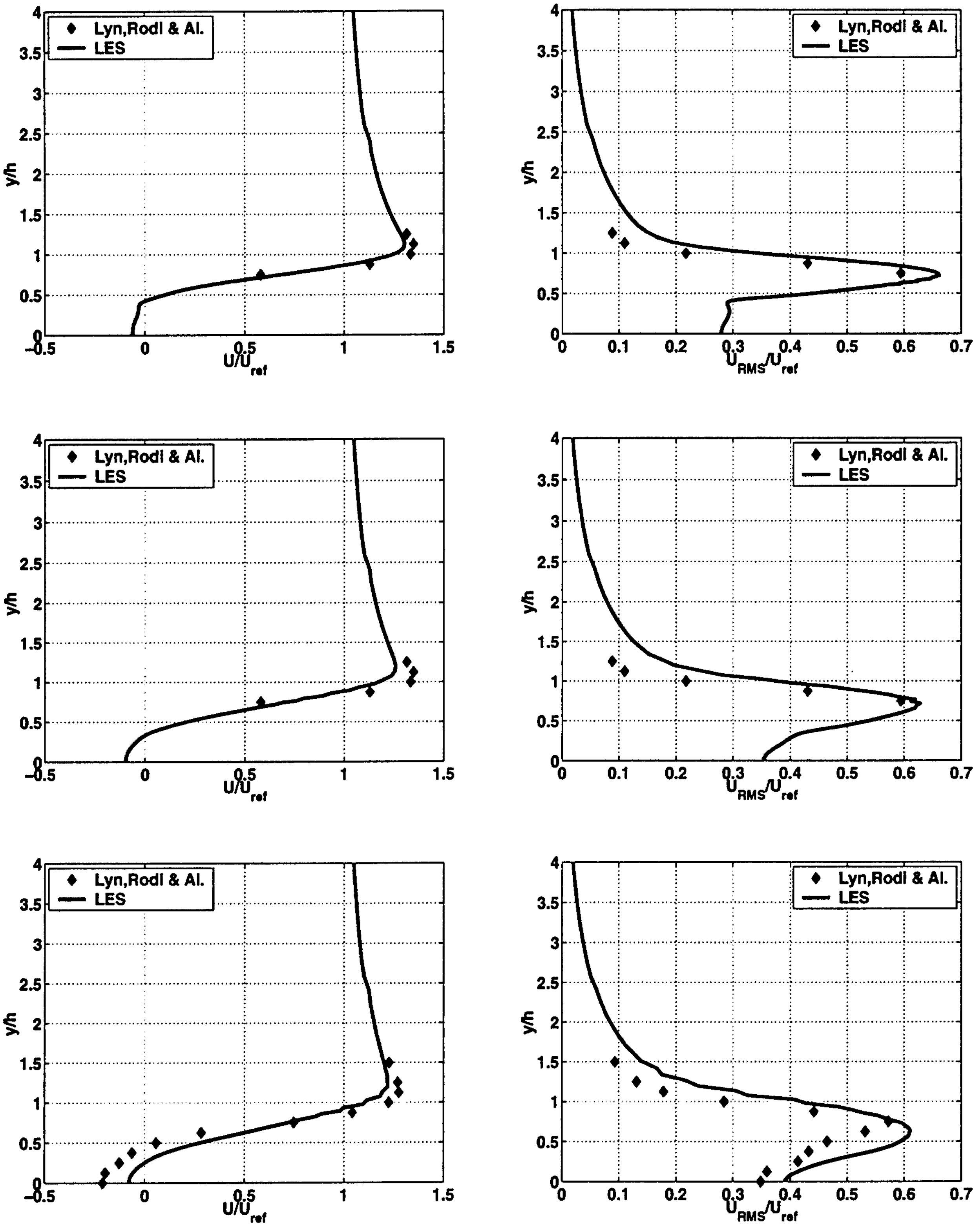

Fig. B.18: Additional simulations, Case I: velocity profiles for stream-wise velocity, left and stream-wise RMS, right, at three stations, from top to bottom: $x = \frac{5}{8H}$,$x = \frac{6}{8H}$ and $x = \frac{7}{8H}$.

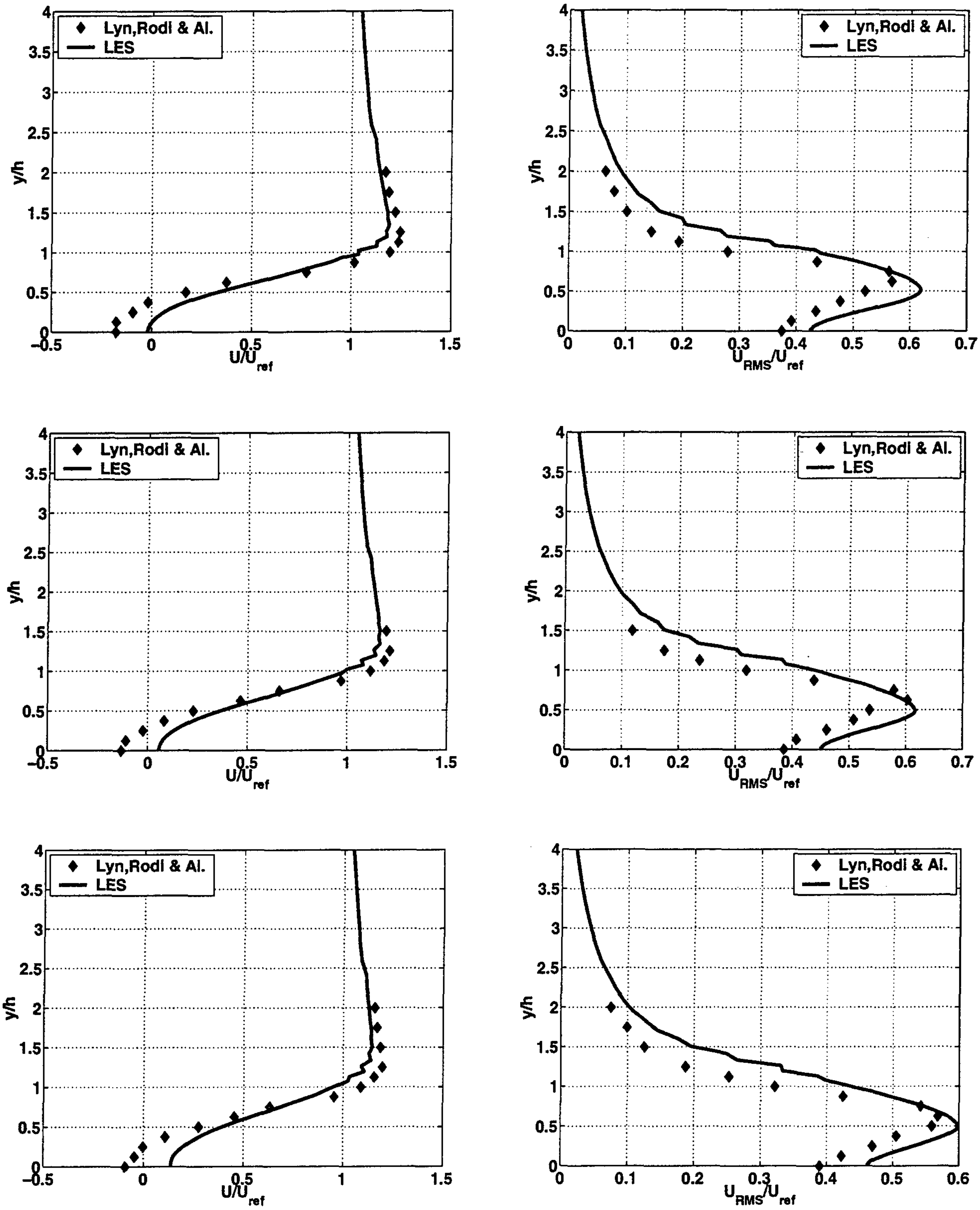

Fig. B.19: Additional simulations, Case I: velocity profiles for stream-wise velocity, left and stream-wise RMS, right, at three stations, from top to bottom: $x = \frac{8}{8H}$,$x = \frac{9}{8H}$ and $x = \frac{10}{8H}$.

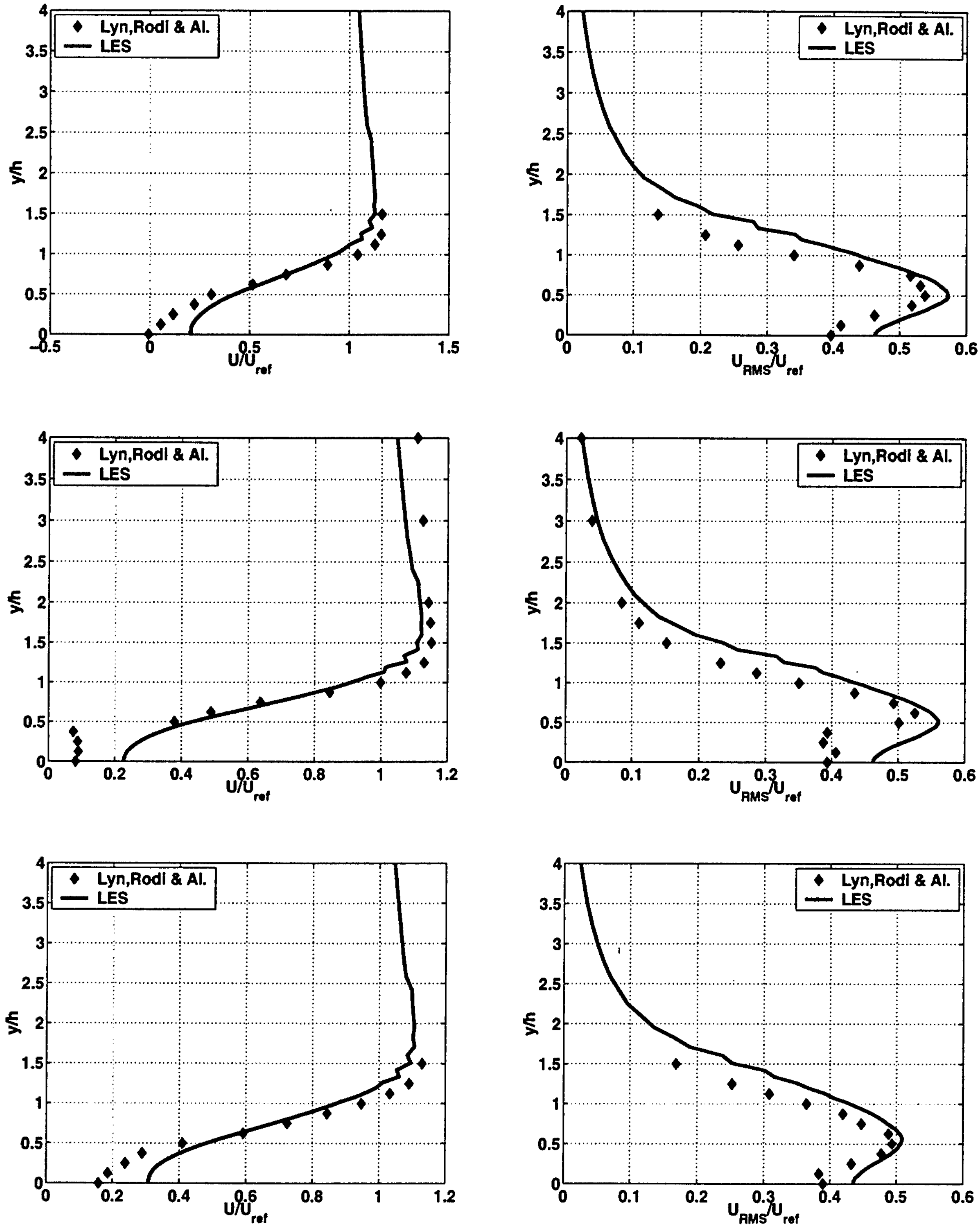

Fig. B.20: Additional simulations, Case I: velocity profiles for stream-wise velocity, left and stream-wise RMS, right, at three stations, from top to bottom: $x = \frac{11}{8H}$,$x = \frac{12}{8H}$ and $x = \frac{13}{8H}$.

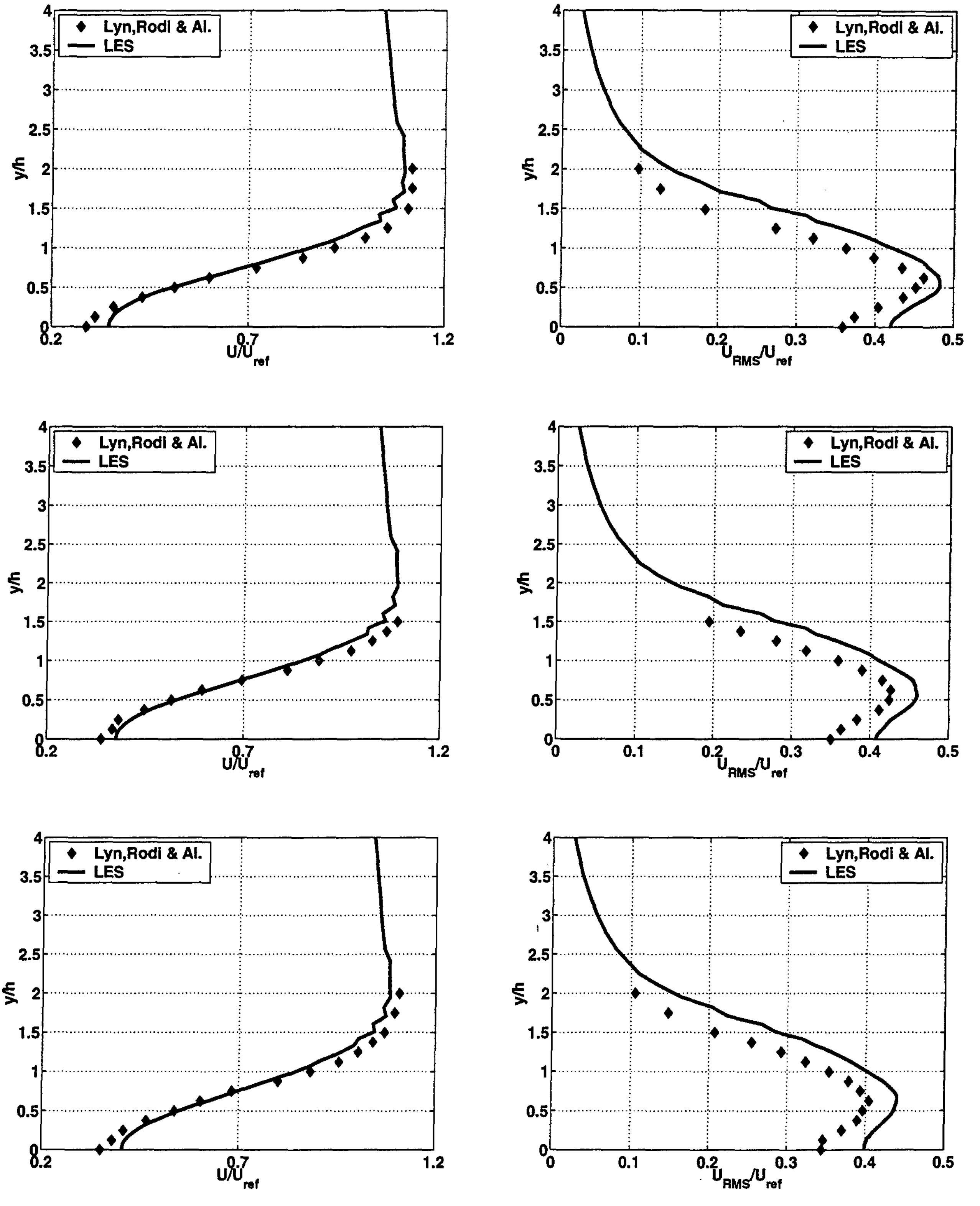

Fig. B.21: Additional simulations, Case I: velocity profiles for stream-wise velocity, left and stream-wise RMS, right, at three stations, from top to bottom: $x = \frac{14}{8H}$,$x = \frac{15}{8H}$ and $x = \frac{16}{8H}$.

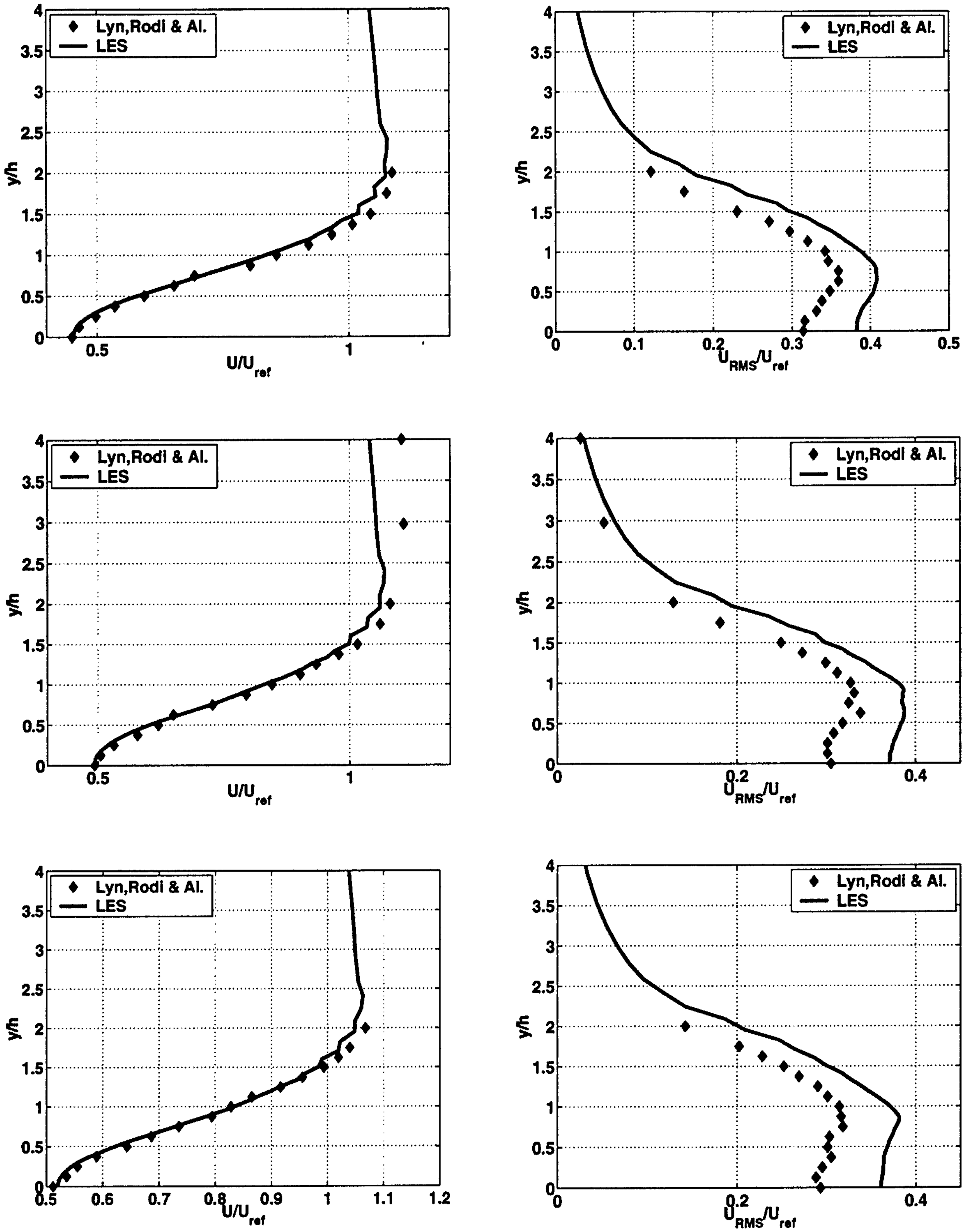

Fig. B.22: Additional simulations, Case I: velocity profiles for stream-wise velocity, left and stream-wise RMS, right, at three stations, from top to bottom: $x = \frac{18}{8H}$,$x = \frac{20}{8H}$ and $x = \frac{22}{8H}$.

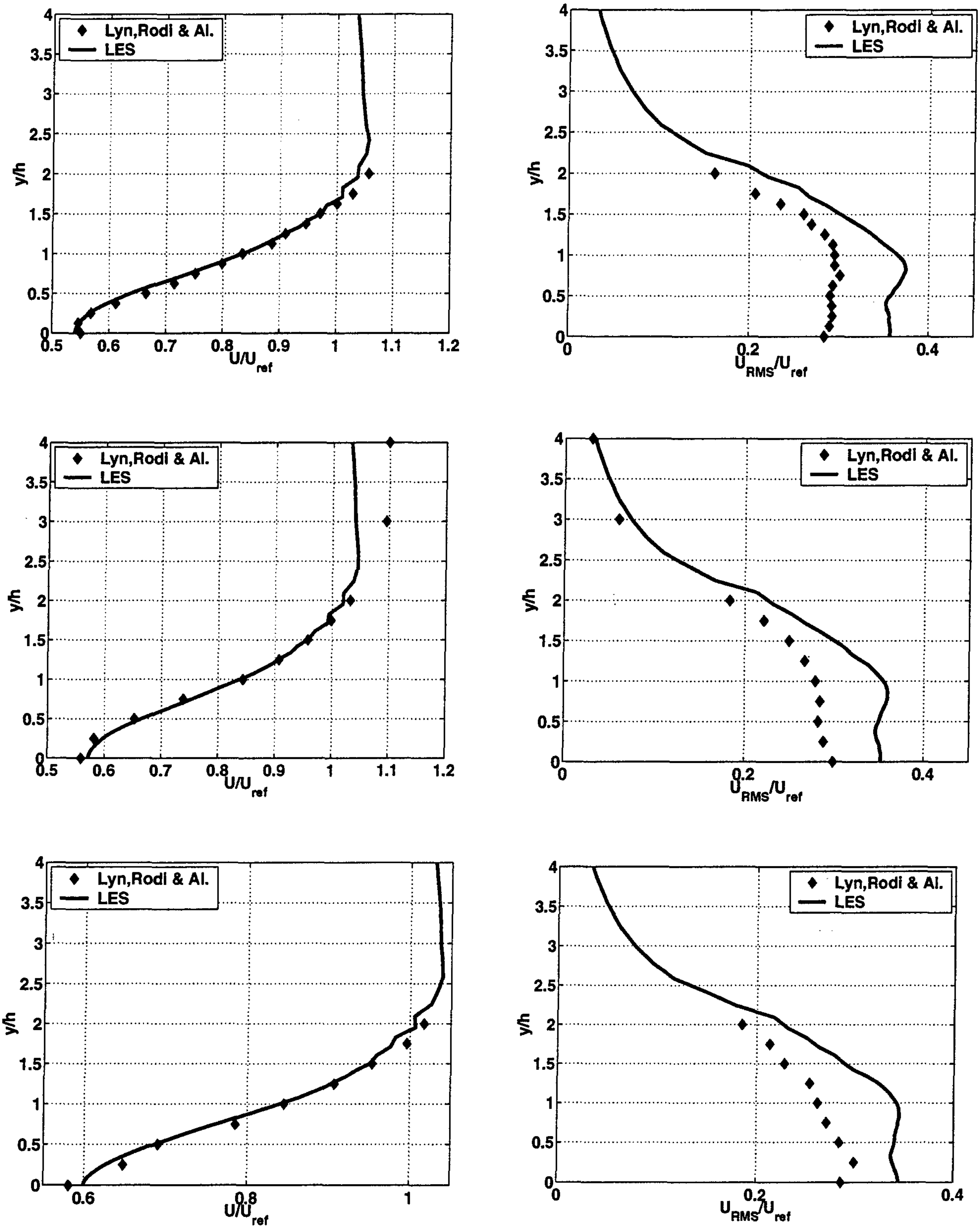

Fig. B.23: Additional simulations, Case I: velocity profiles for stream-wise velocity, left and stream-wise RMS, right, at three stations, from top to bottom: $x = \frac{24}{8H}$,$x = \frac{28}{8H}$ and $x = \frac{32}{8H}$.

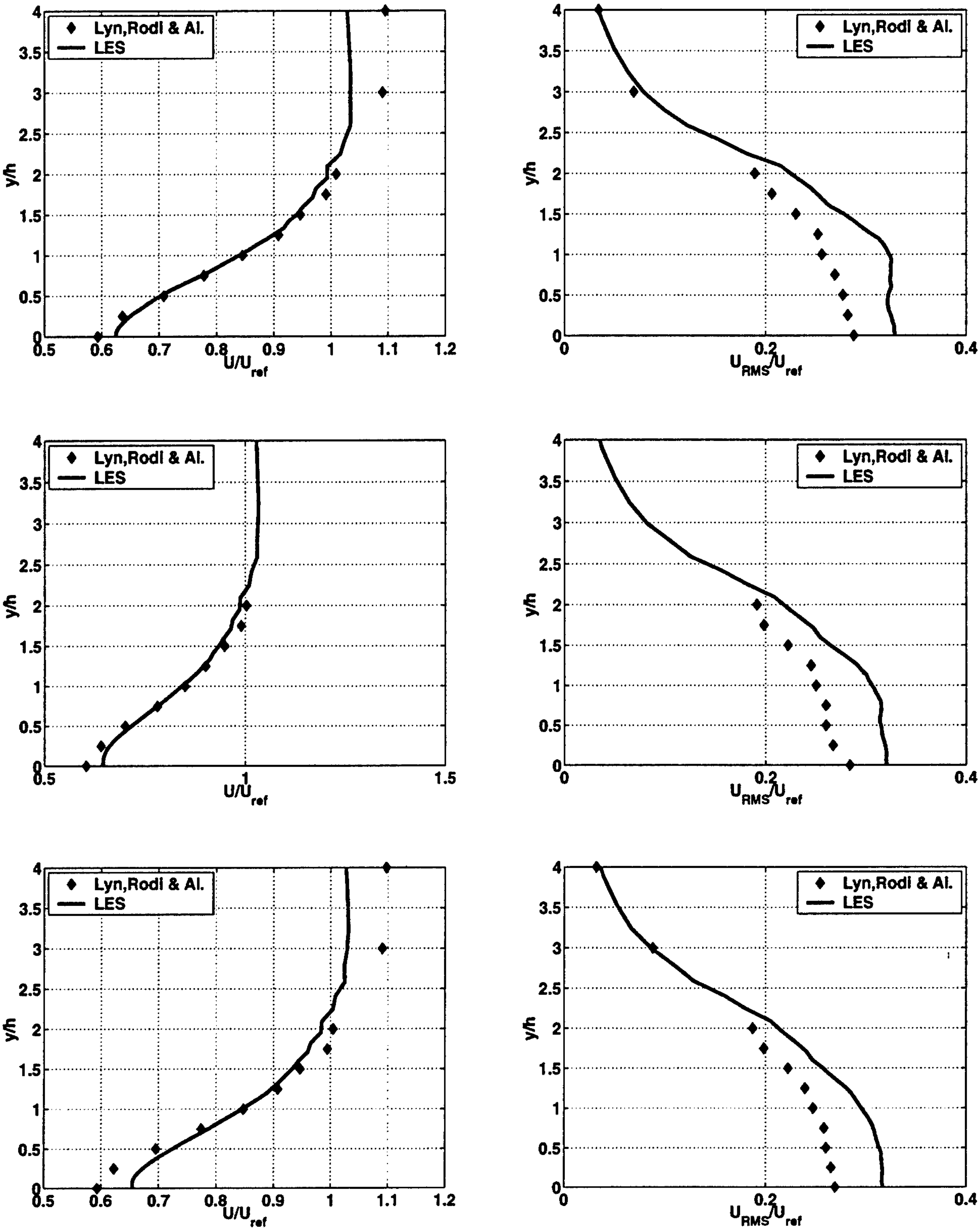

Fig. B.24: Additional simulations, Case I: velocity profiles for stream-wise velocity, left and stream-wise RMS, right, at three stations, from top to bottom: $x = \frac{36}{8H}$,$x = \frac{40}{8H}$ and $x = \frac{44}{8H}$.

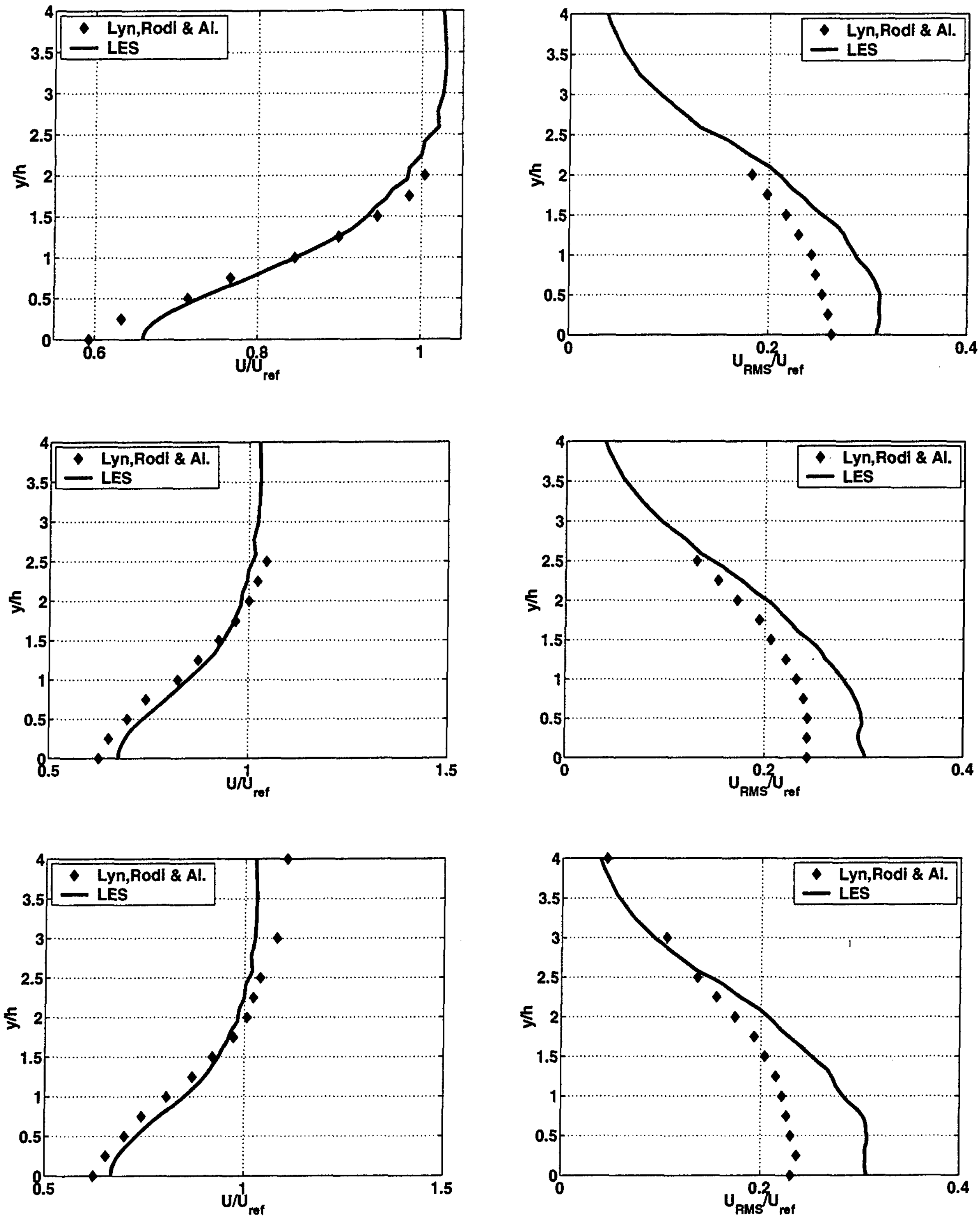

Fig. B.25: Additional simulations, Case I: velocity profiles for stream-wise velocity, left and stream-wise RMS, right, at three stations, from top to bottom: $x = \frac{48}{8H}$,$x = \frac{57.6}{8H}$ and $x = \frac{64}{8H}$.

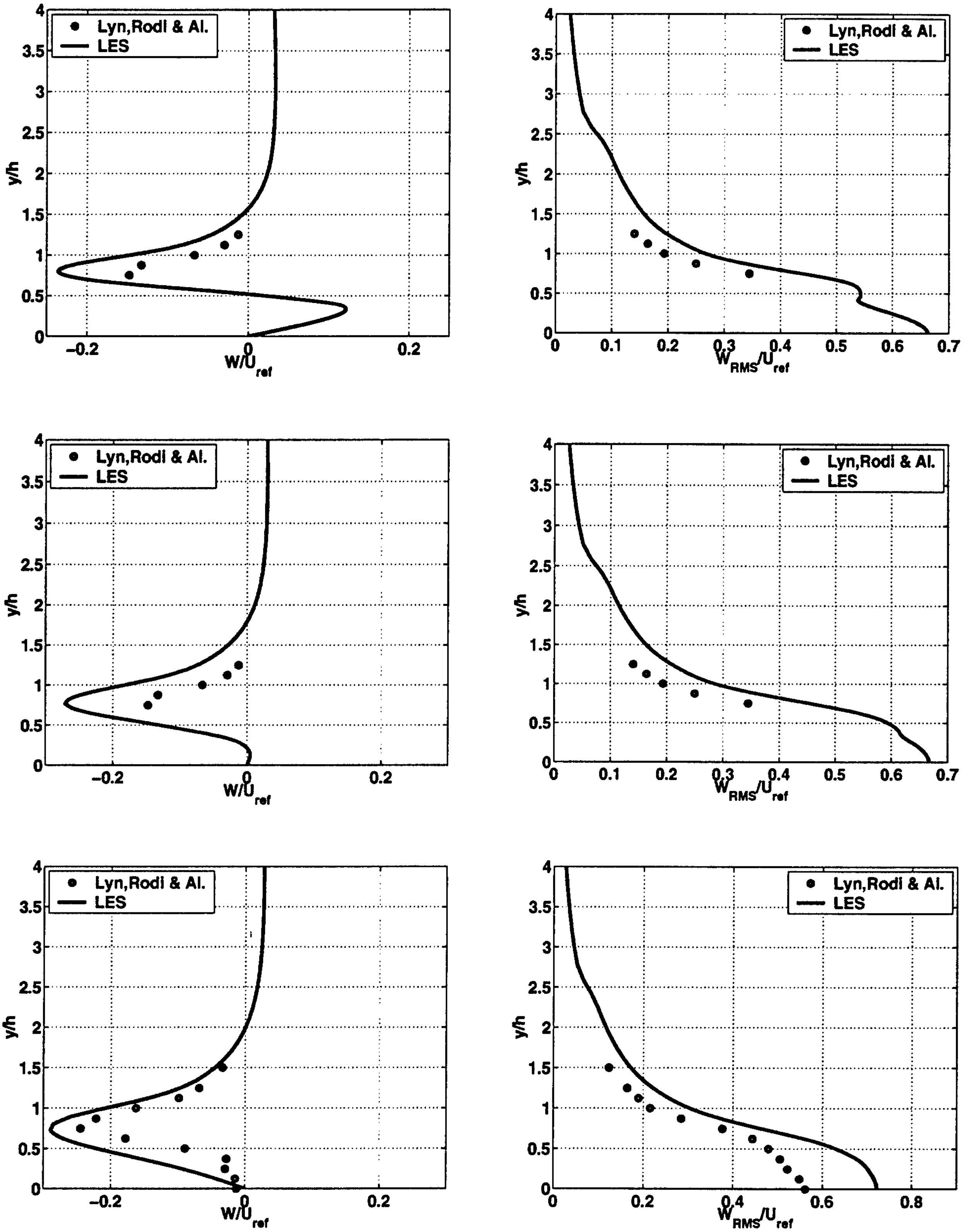

Fig. B.26: Additional simulations, Case I: velocity profiles for vertical velocity, left and vertical RMS, right, at three stations, from top to bottom: $x = \frac{5}{8H}$,$x = \frac{6}{8H}$ and $x = \frac{7}{8H}$.

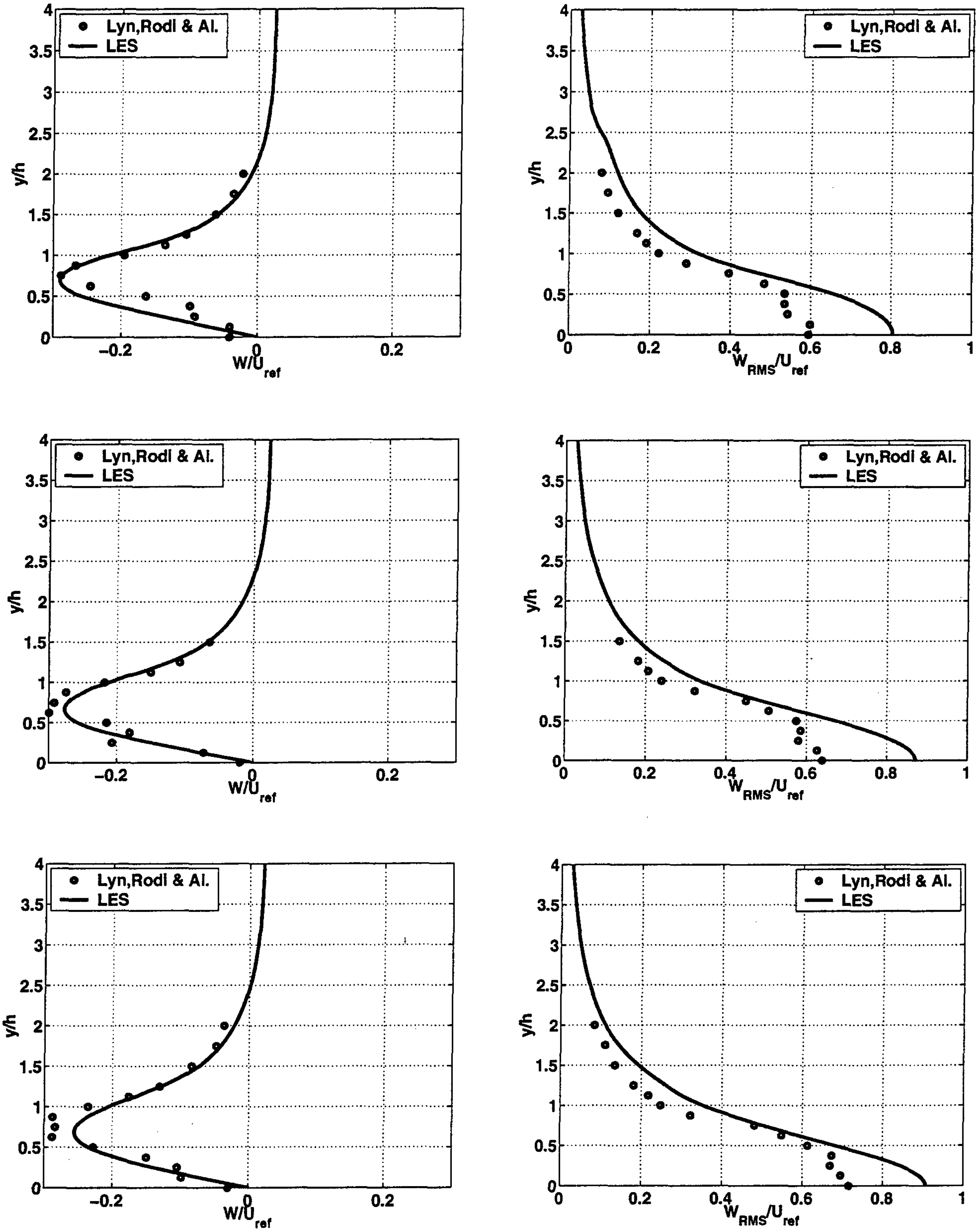

Fig. B.27: Additional simulations, Case I: velocity profiles for vertical velocity, left and vertical RMS, right, at three stations, from top to bottom: $x = \frac{8}{8H}$,$x = \frac{9}{8H}$ and $x = \frac{10}{8H}$.

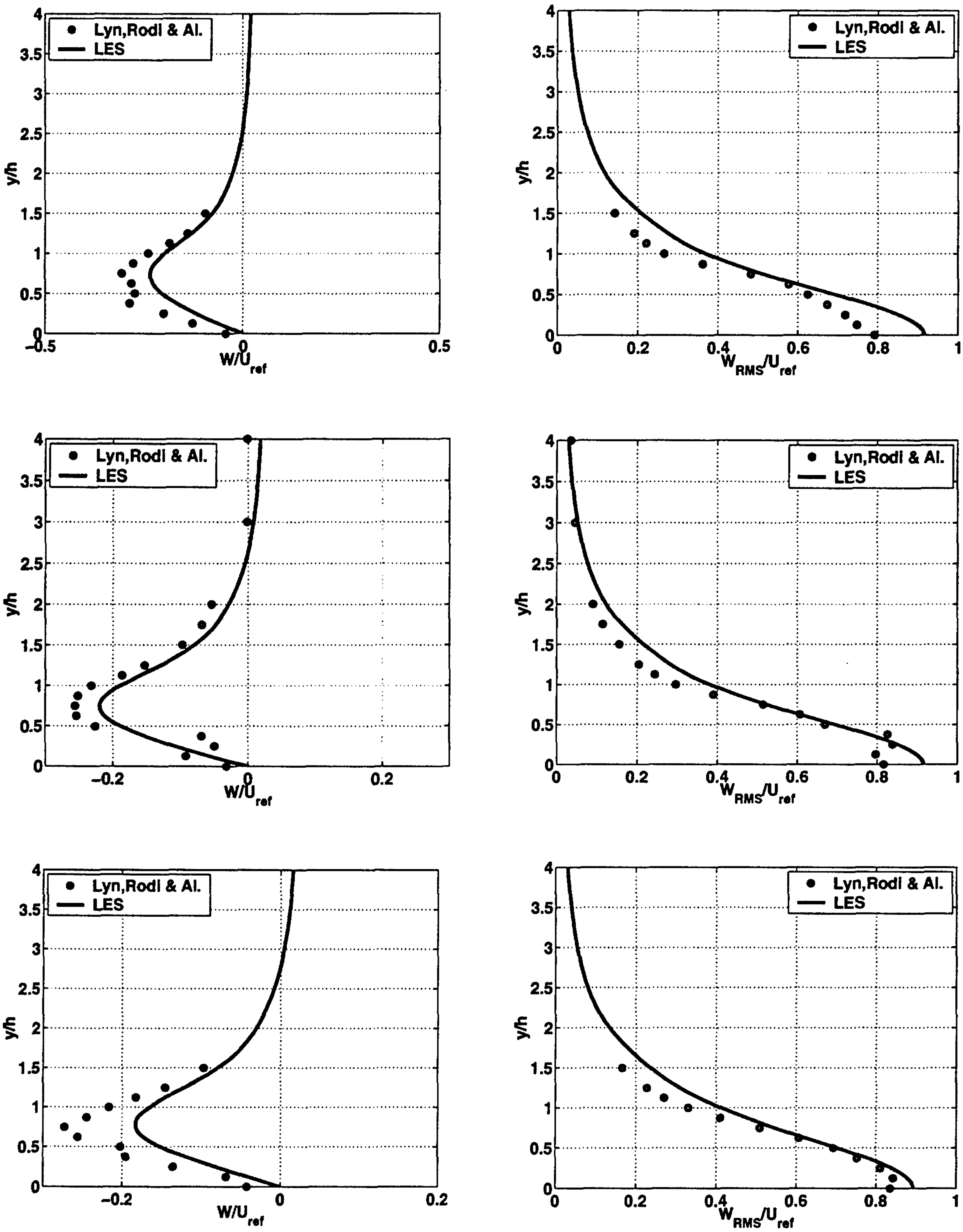

Fig. B.28: Additional simulations, Case I: velocity profiles for vertical velocity, left and vertical RMS, right, at three stations, from top to bottom: $x = \frac{11}{8H}$,$x = \frac{12}{8H}$ and $x = \frac{13}{8H}$.

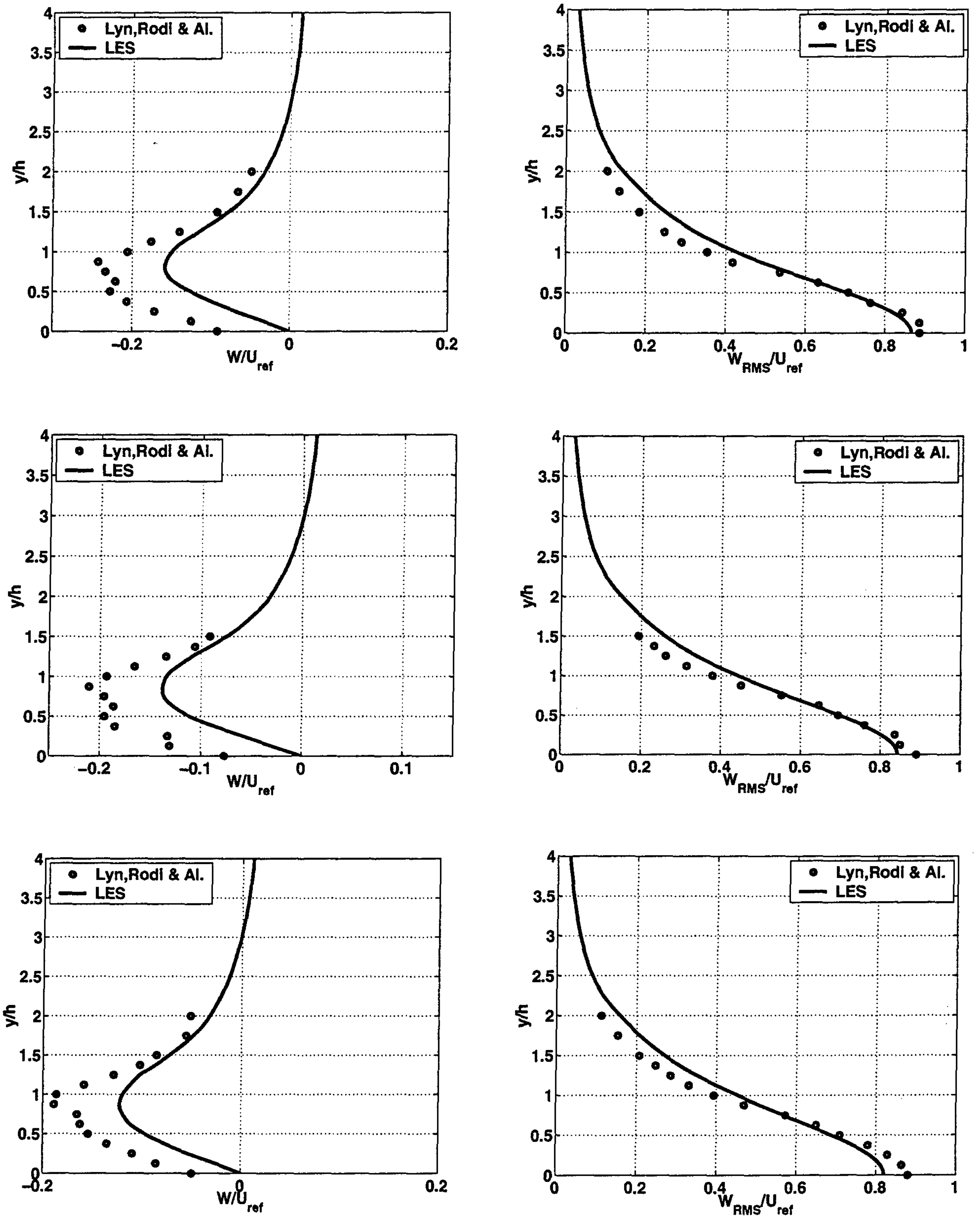

Fig. B.29: Additional simulations, Case I: velocity profiles for vertical velocity, left and vertical RMS, right, at three stations, from top to bottom: $x = \frac{14}{8H}$,$x = \frac{15}{8H}$ and $x = \frac{16}{8H}$.

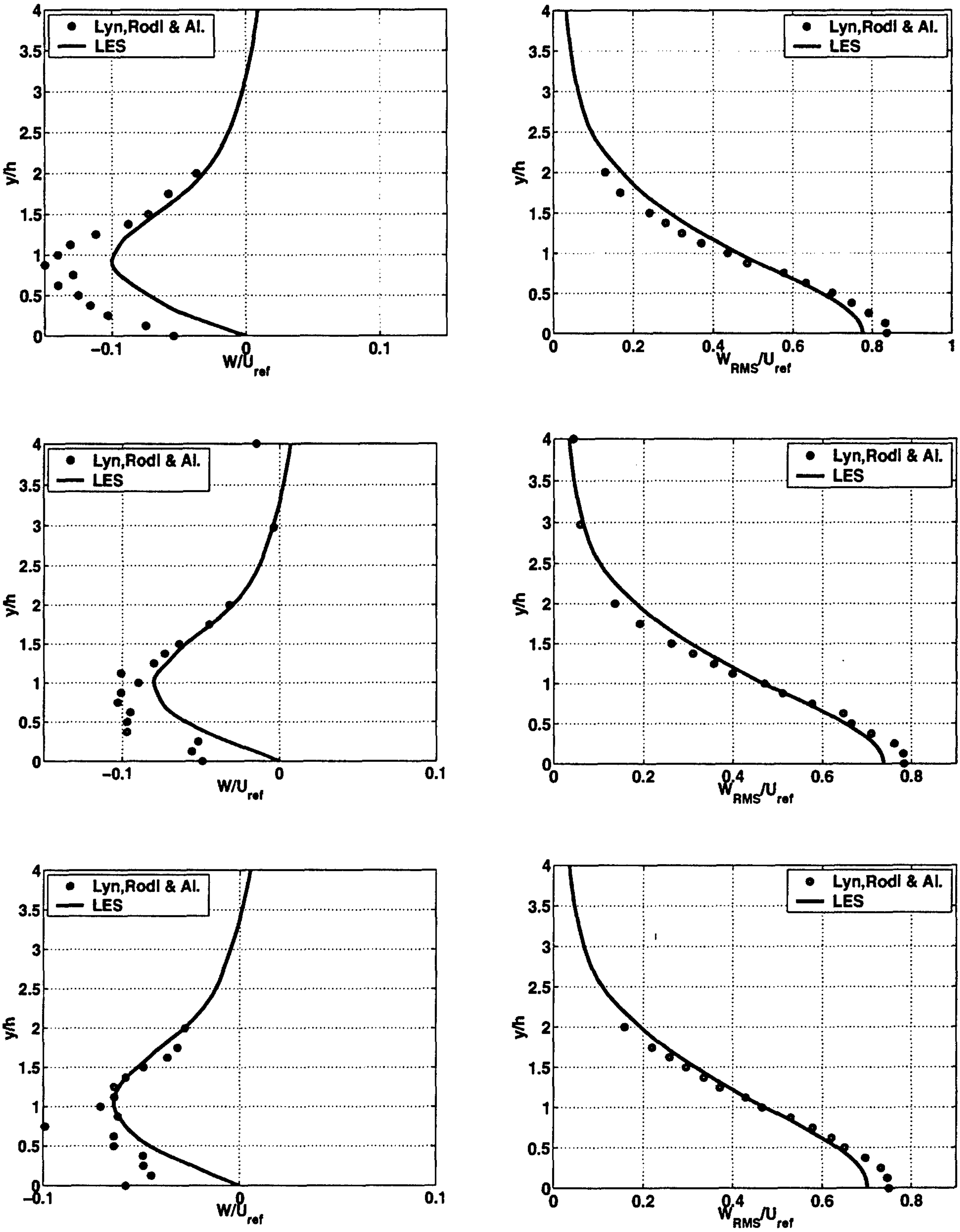

Fig. B.30: Additional simulations, Case I: velocity profiles for vertical velocity, left and vertical RMS, right, at three stations, from top to bottom: $x = \frac{18}{8H}$,$x = \frac{20}{8H}$ and $x = \frac{22}{8H}$.

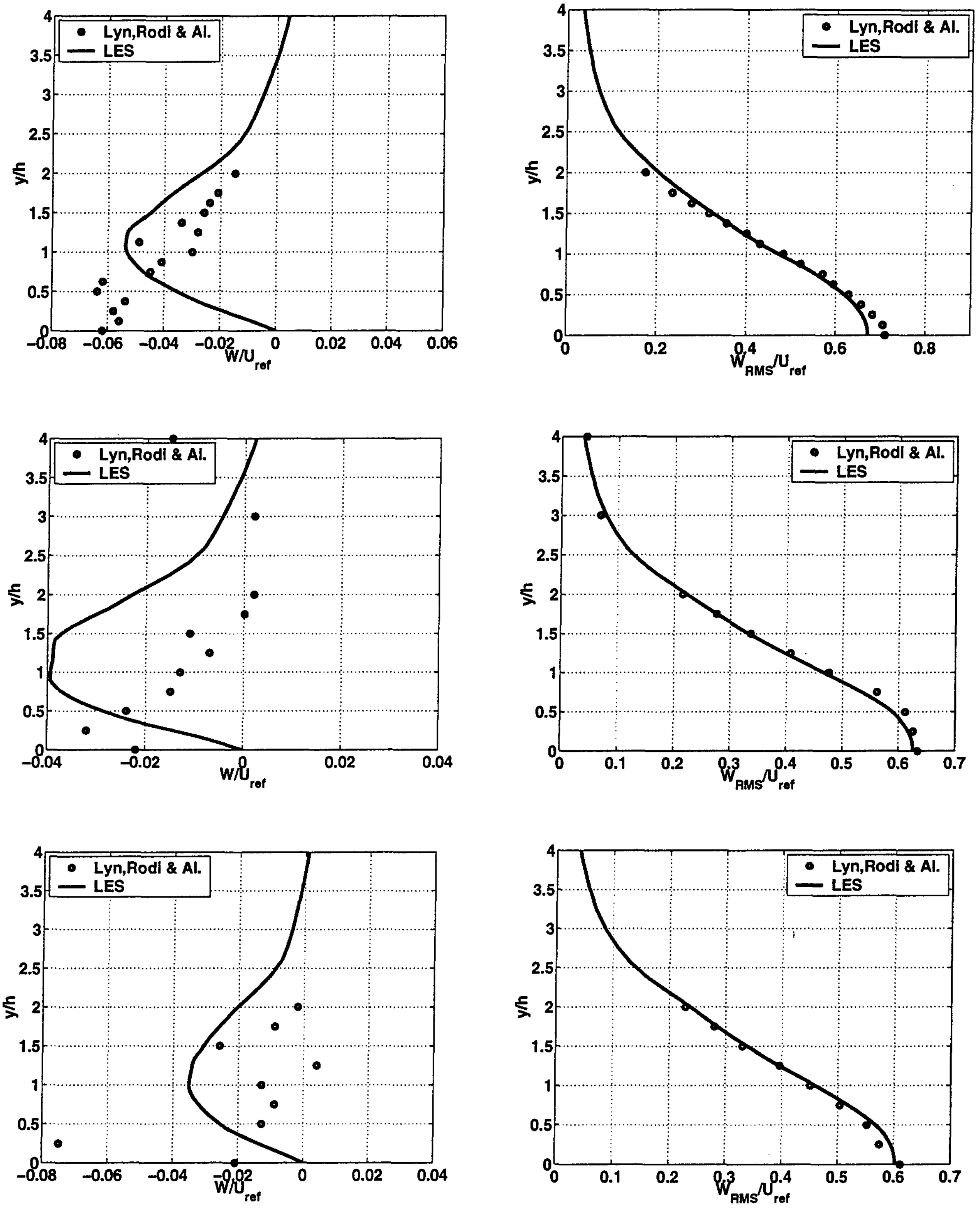

Fig. B.31: Additional simulations, Case I: velocity profiles for vertical velocity, left and vertical RMS, right, at three stations, from top to bottom: $x = \frac{24}{8H}$,$x = \frac{28}{8H}$ and $x = \frac{32}{8H}$.

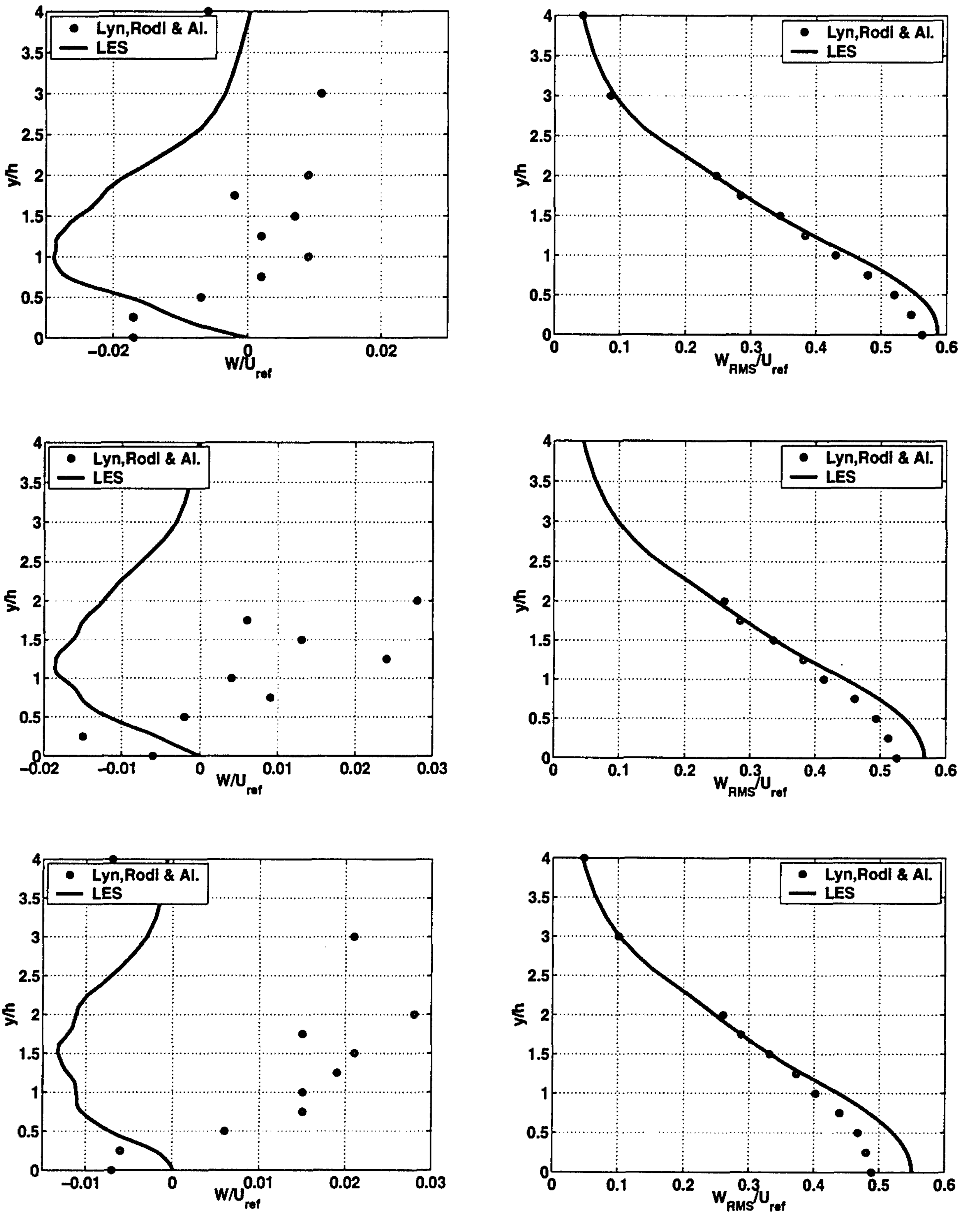

Fig. B.32: Additional simulations, Case I: velocity profiles for vertical velocity, left and vertical RMS, right, at three stations, from top to bottom: $x = \frac{36}{8H}$,$x = \frac{40}{8H}$ and $x = \frac{44}{8H}$.

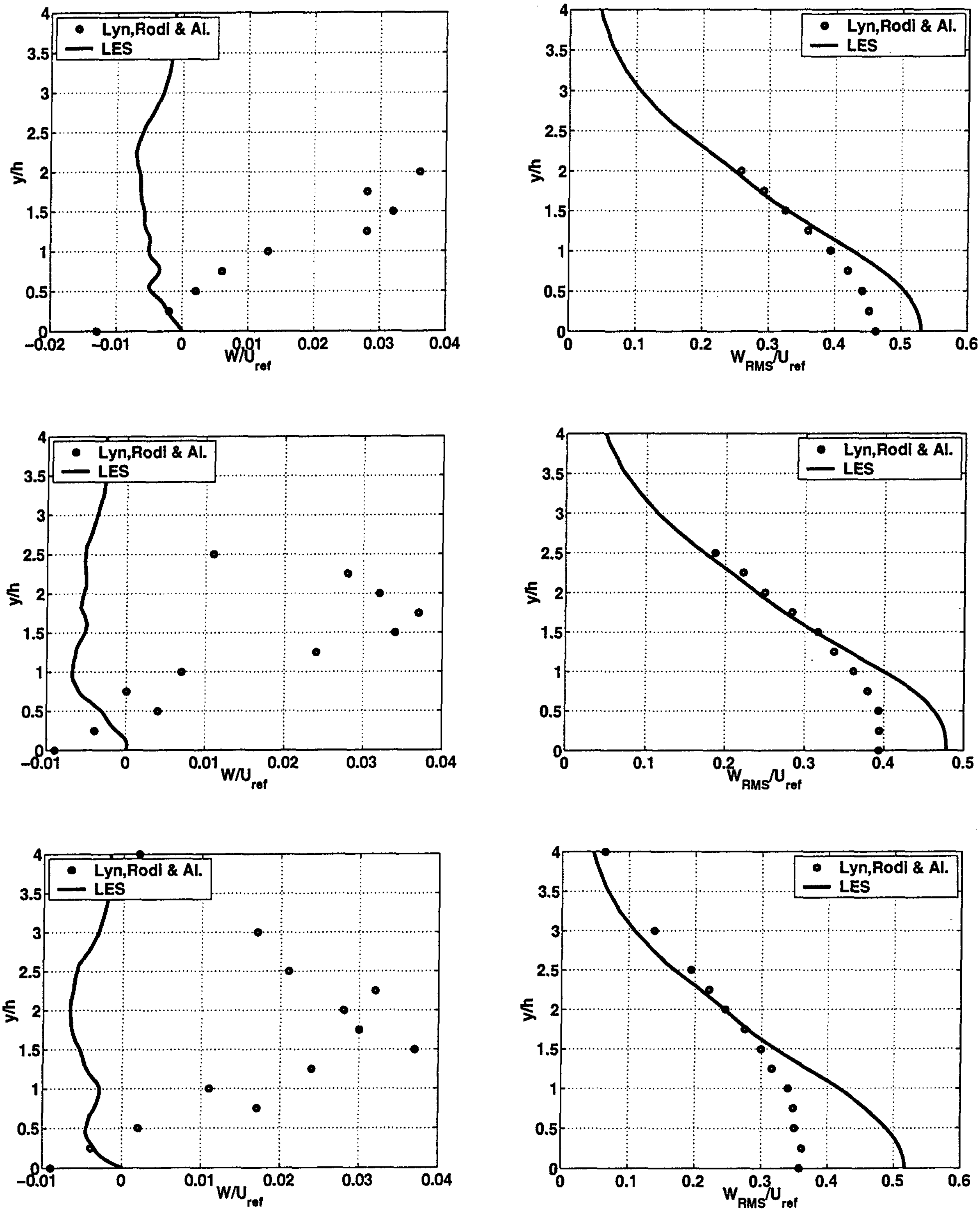

Fig. B.33: Additional simulations, Case I: velocity profiles for vertical velocity, left and vertical RMS, right, at three stations, from top to bottom: $x = \frac{48}{8H}$,$x = \frac{57.6}{8H}$ and $x = \frac{64}{8H}$.

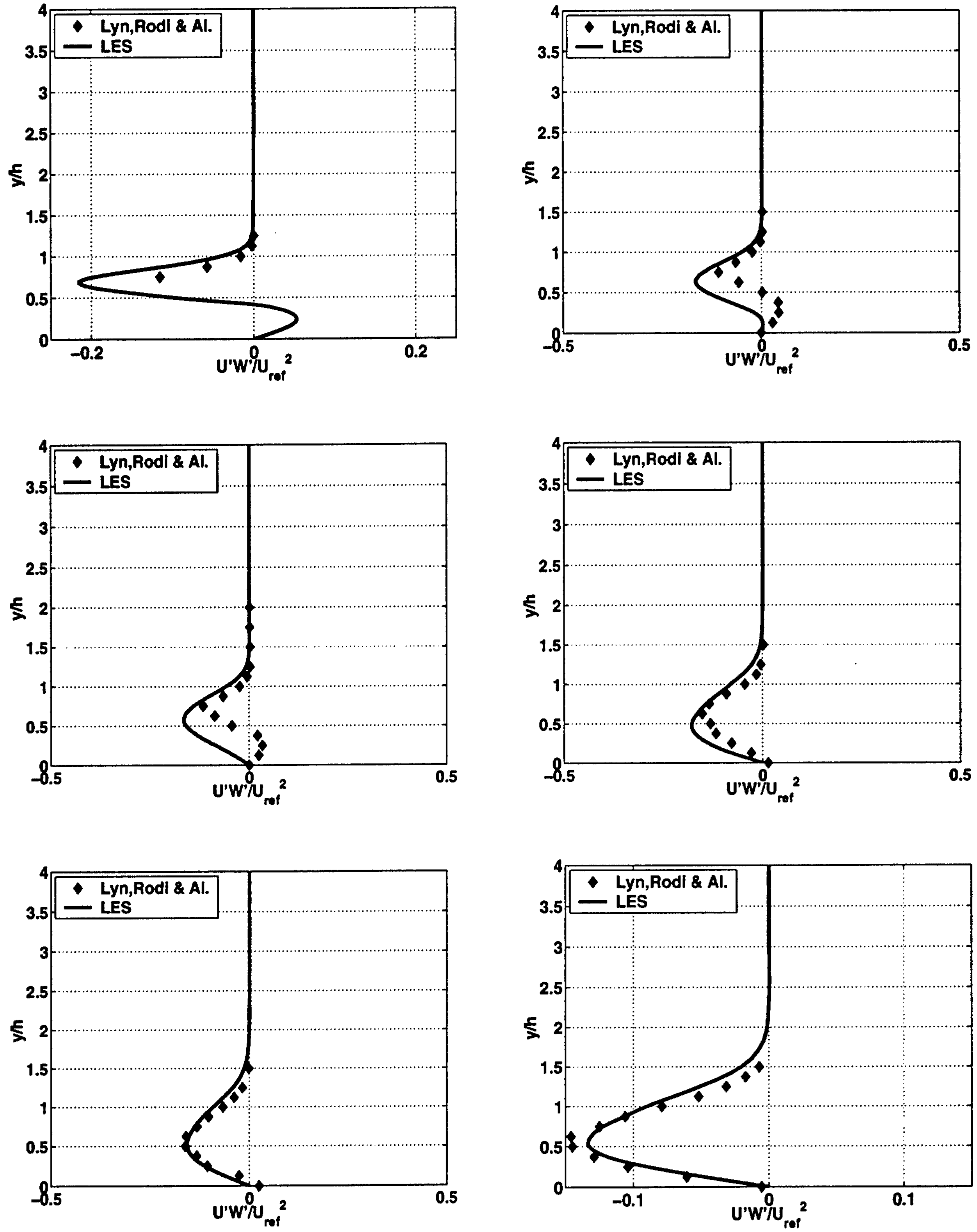

Fig. B.34: Additional simulations, Case I: velocity profiles for turbulent stress from top to bottom and from left to right: $x = \frac{5}{8H}$,$x = \frac{7}{8H}$,$x = \frac{8}{8H}$, $x = \frac{11}{8H}$,$x = \frac{13}{8H}$ and $x = \frac{15}{8H}$.

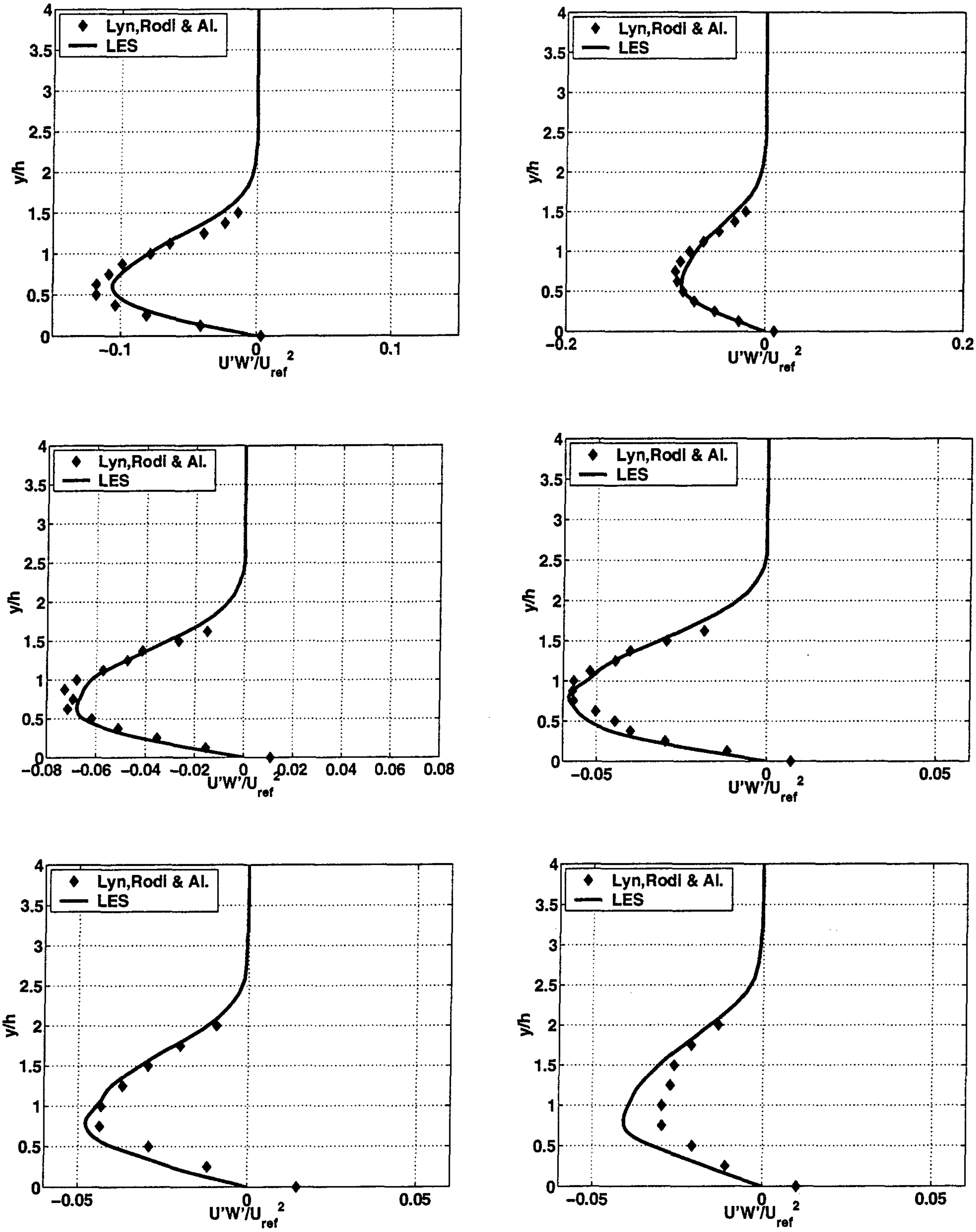

Fig. B.35: Additional simulations, Case I: velocity profiles for turbulent stress from top to bottom and from left to right: $x = \frac{17}{8H}$,$x = \frac{19}{8H}$,$x = \frac{21}{8H}$, $x = \frac{23}{8H}$,$x = \frac{26}{8H}$ and $x = \frac{30}{8H}$.

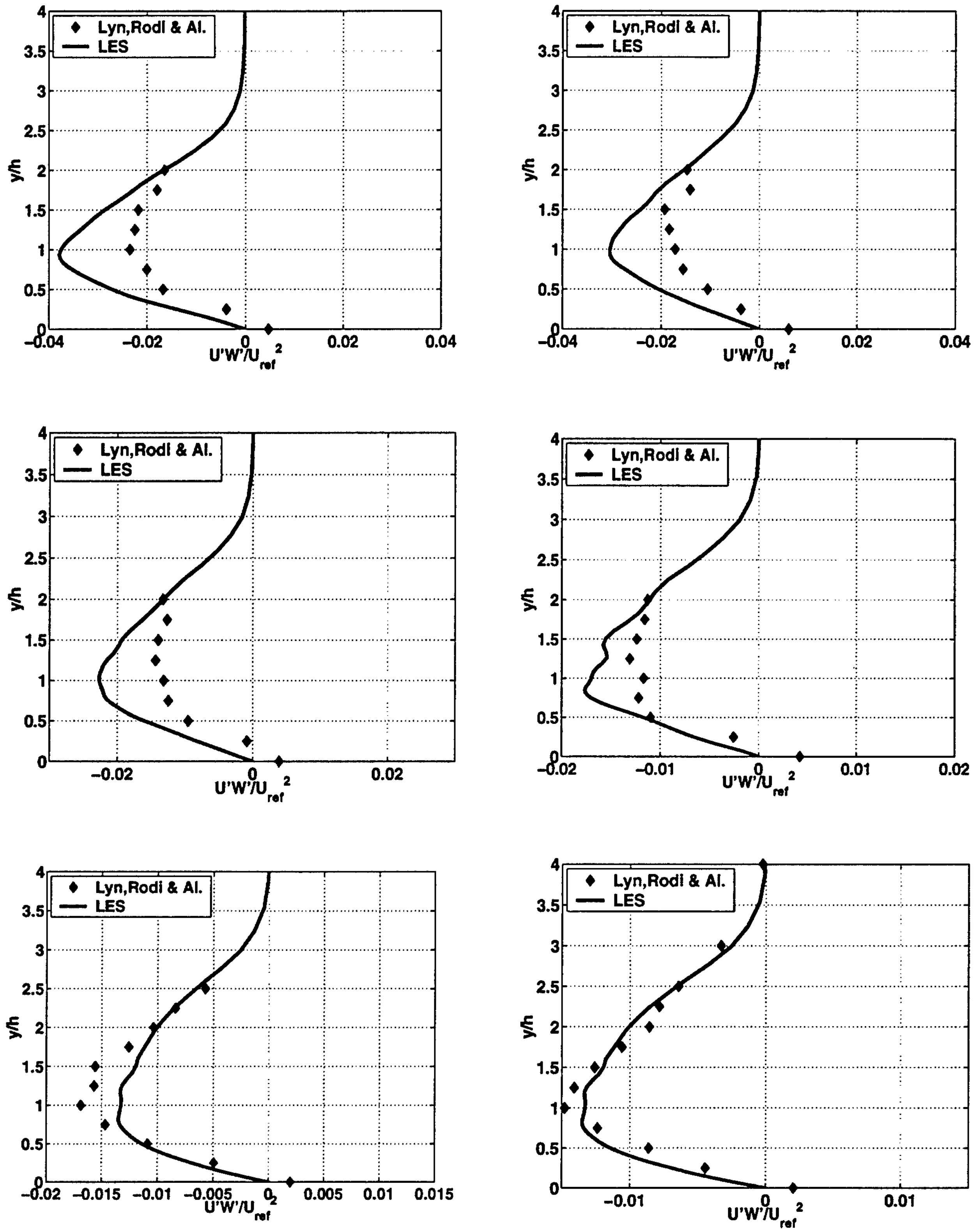

Fig. B.36: Additional simulations, Case I: velocity profiles for turbulent stress from top to bottom and from left to right: $x = \frac{34}{8H}$,$x = \frac{38}{8H}$,$x = \frac{42}{8H}$, $x = \frac{46}{8H}$,$x = \frac{51.2}{8H}$ and $x = \frac{64}{8H}$.

Results of present simulation are of interest in the sense that suggest that a more refined grid (with respect to the one applied for reference simulation) would indeed be necessary; even if a proper comparison between the two SGS model was not performed, the main trends appear to be clear enough.

It was considered that it was not interesting to perform another lengthly and costly simulation on the old grid applying Smagorinsky model; it would have been of much more interest to test FSF model over the new grid, but time-step limitations it would have entail made it impossible.

C. ADDITIONAL CASE II

The present simulation was performed over the grid described in Tab. A.1, using the SGS Smagorinsky model with a coefficient set to $Cs = 0.2$. The multi-domain set-up used is the one presented in Fig. A.3, while the value of van Driest constant was set to three times the one applied for § B.

An overview of the macroscopic results of the simulation are presented in Tab. C.1; the c_p distribution around the obstacle for current simulation, together with the recorded history for c_l and c_d are presented in Fig. C.3 trough Fig. C.5. In Fig. C.1 and Fig. C.2 it is possible to remark how the new set of boundary conditions influence the flow. Resolution of small re-circulation bubble close to the leading edge of the obstacle, which was satisfactory in § B, is, now, worse.

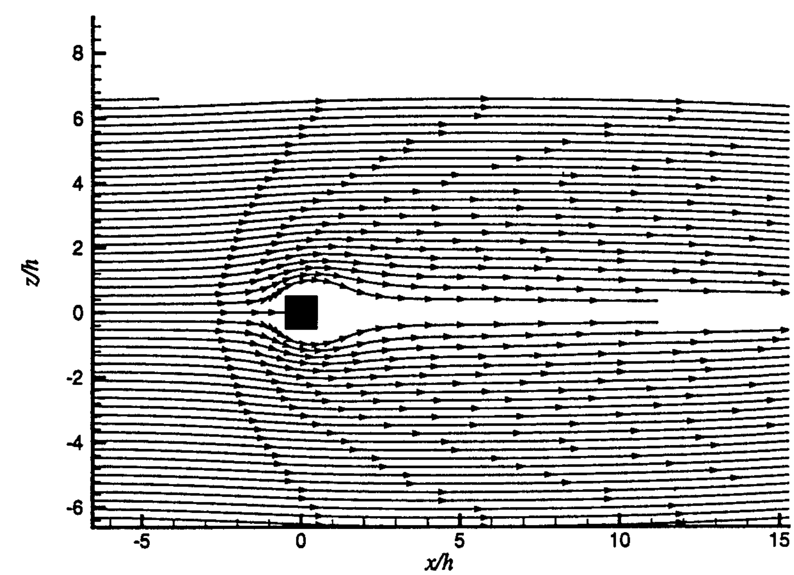

Fig. C.1: Additional simulations, Case II: time averaged stream-lines around square cylinder; LES ($Re = 22,000$)

Table C.1: Additional simulations, Case II: macroscopic quantities of interest: experimental range of admissible values and computed ones.

	St	$c_{l_{rms}}$	c_d	$c_{d_{rms}}$	lr
EXP	0.133	0.1-1.4	1.9-2.1	0.1-0.23	1.38
LES	0.1085	1.36	2.2	0.9119	0.76

For this case, data from only two shedding periods were available at the time of the

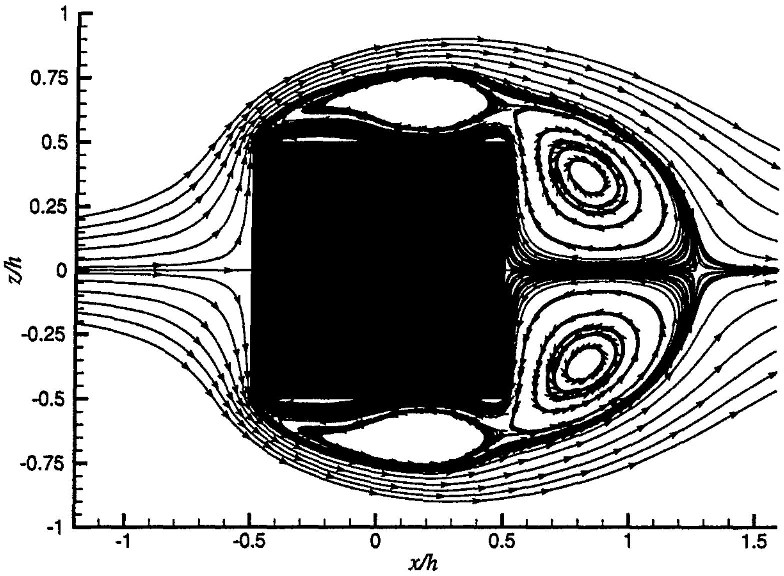

Fig. C.2: Additional simulations, Case II: time averaged stream-lines around square cylinder, close-up; LES ($Re = 22,000$)

writing of this report. However, it was possible to apply the procedure described in § 2, and to extract the statistics relative to the configuration which minimizes the asymmetry of the stream-wise velocity; so it is reasonable to assume that the flow has already reached a state close enough to stationary one, which would allow to extrapolate some tentatively conclusions, subjected to further confirmation, once more samples are gathered. It is possible to observe, in Fig. C.14, that the samples were taken for the far wake were not sufficient, but in the near wake, an apparent improvement is visible in the results.

It is not possible to directly compare Fig. C.5(b) to with Fig. 2.16(b), since the number of shedding periods used for the two averages are different; nevertheless, the number of samples can be estimated sufficient to extract reliable estimations for macroscopic parameters such as the mean drag coefficients; its value (see Tab. C.1) decreases, with respect of previous simulations, moving closer to the experimental measures. Concerning the c_p distribution on the surface, comparison between Fig. C.4 and Fig. 2.15 seems to indicate, now, a better agreement with the set of experimental data by Lee, opposite to the trend observed in Fig. B.4, where the simulation closely matched the ones by Bearman and Obasaju (experimental data extracted from Rodi et al. (1997)).

Considering the plots of velocity profiles on the obstacle, some improvements are visible, in comparison to the reference one (see Fig. C.6 through Fig. C.13 in comparison to Fig. 2.18 through Fig. 2.25).

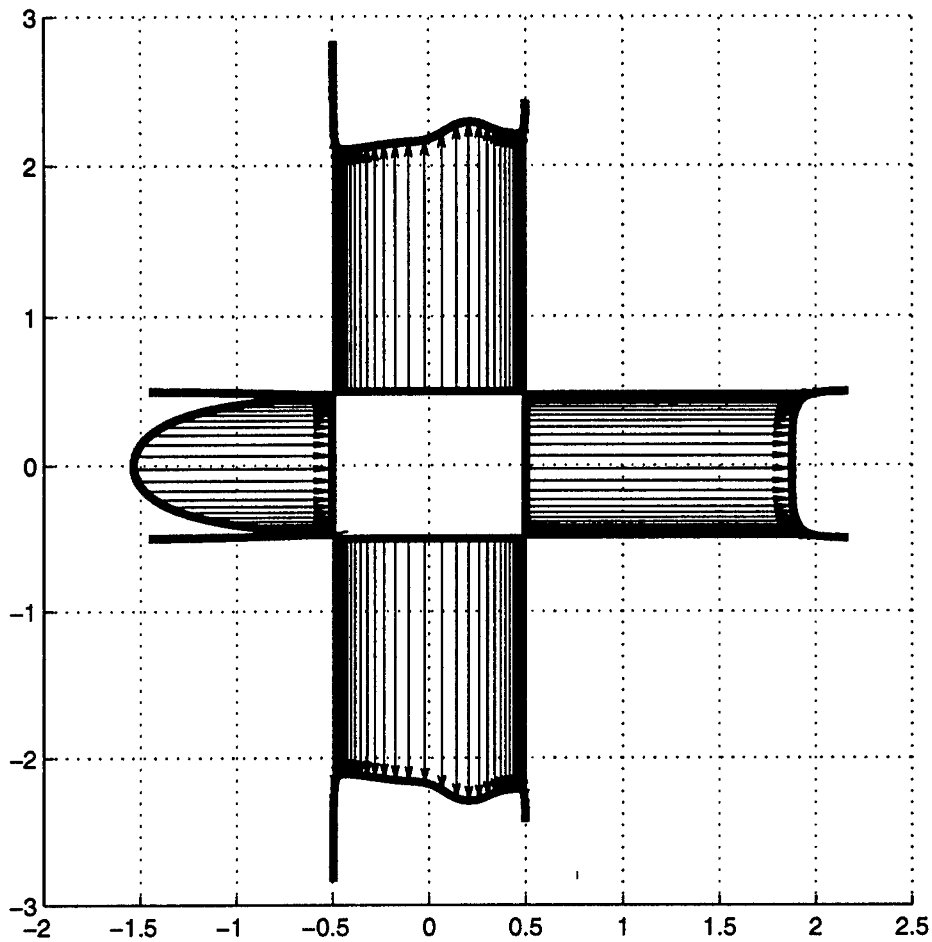

Fig. C.3: Additional simulations, Case II: diagram of averaged c_p distribution around the square cylinder. Average in time and in span-wise direction.

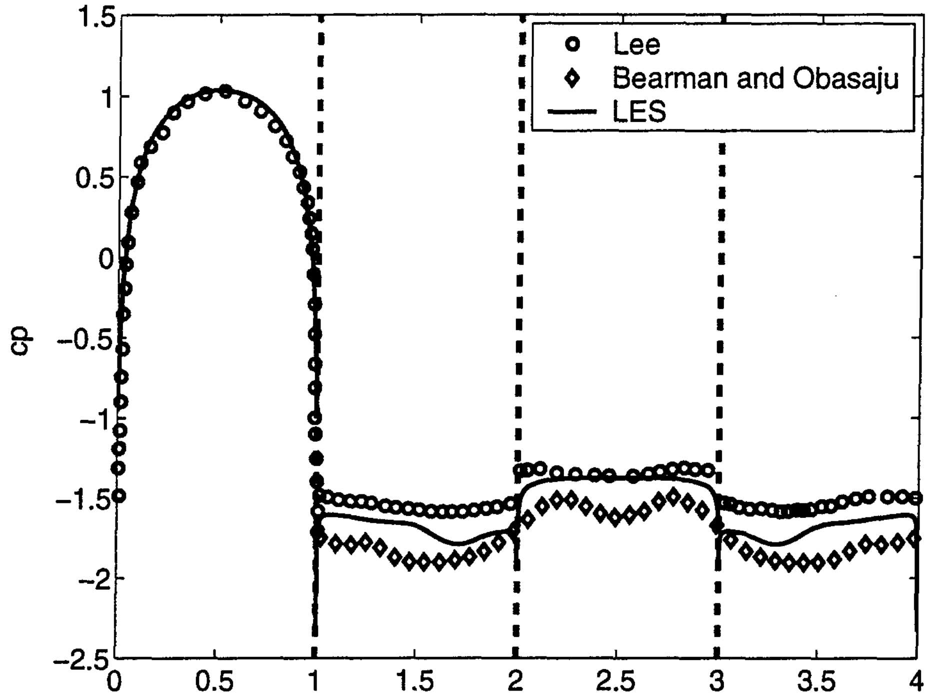

Fig. C.4: Additional simulations, Case II: plot of averaged c_p distribution around the square cylinder. Average in item and in span-wise direction.

Concerning the behavior of simulation in the wake, centerline recirculation length seems in better agreement with experimental data, and the stream-wise velocity along the centerline is also in good agreement with the experiments for the first five and an half diameters behind the obstacle, pending results of further samples. As remarked in § B, present combination of the Smagorinsky model and revised grid appears to yield better results than the ones from reference simulation, in what concerns off-centerline RMS behavior, see for example Fig. C.24 and Fig. 2.36; it can be remarked that the two prongs of the stream-wise RMS disappear and the plot of RMS has the correct shape [1].

For the turbulent stress, observing Fig. 2.47 and Fig. C.35, the current simulation appears to yield better behavior in the far wake respect to the reference case, even if further samples would be needed to be gathered, to ensure full convergence of the statistics in this zone.

[1]It must be again kept in mind that true RMS and LES RMS are not directly comparable, but since it is not possible to process the experimental data in order to make it comparable to the computed results, Fig. C.24 is less unsettling in comparison with Fig. 2.36

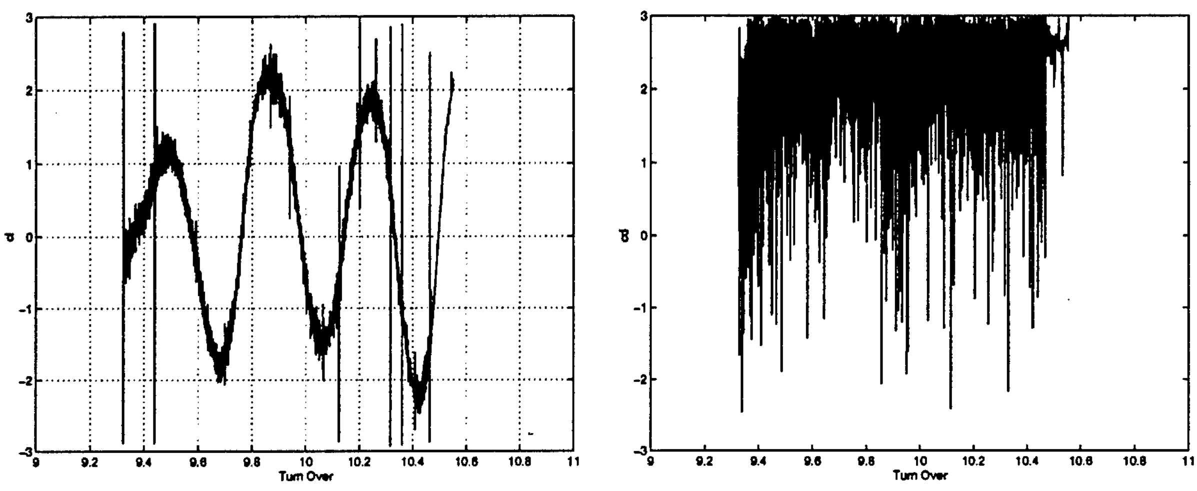

(a) Lift Coefficient

(b) Drag Coefficient

Fig. C.5: Additional simulations, Case II: time history of lift and drag coefficients.

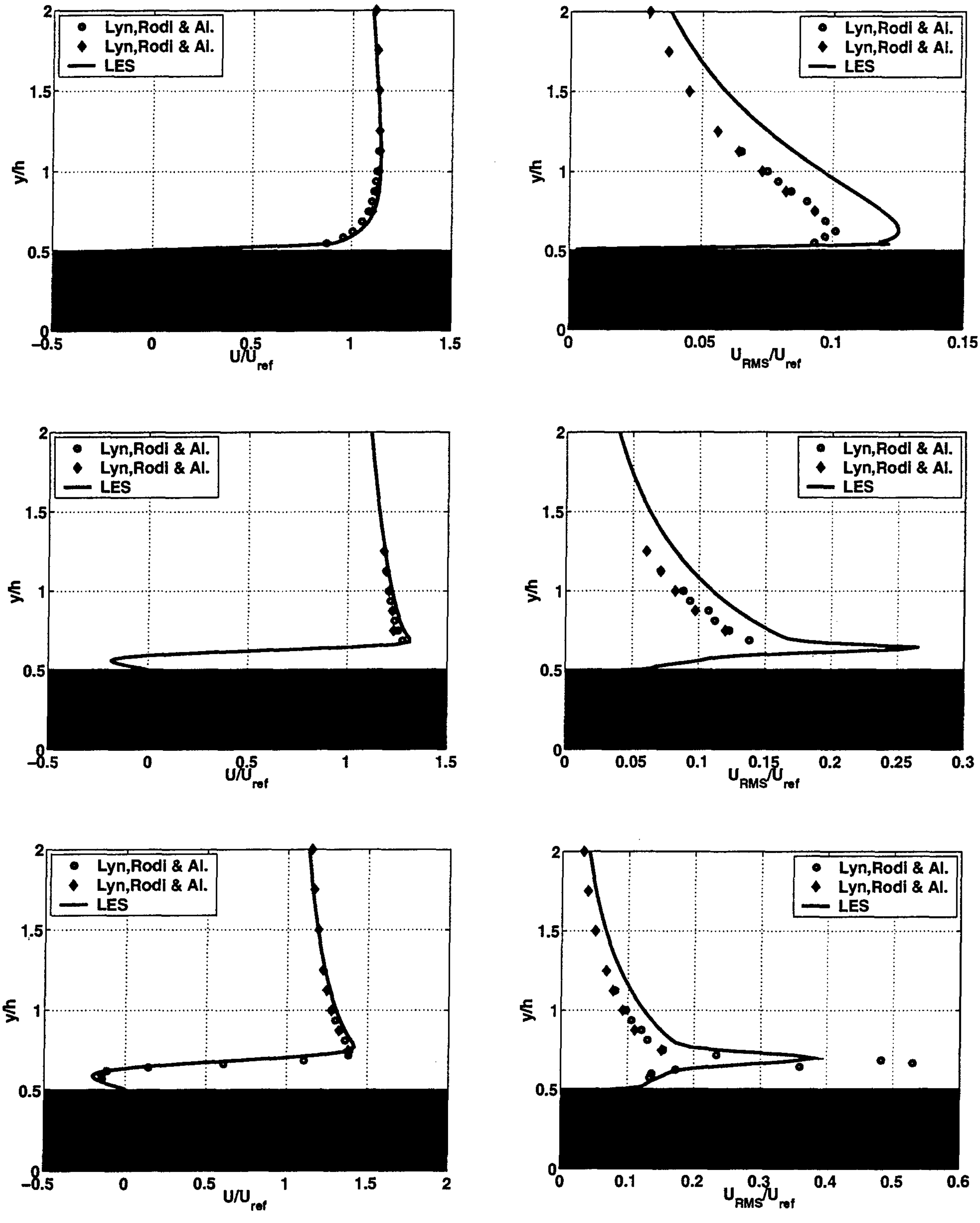

Fig. C.6: Additional simulations, Case II: velocity profiles for stream-wise velocity, left and stream-wise RMS, right, at three stations, from top to bottom: $x = -\frac{1}{2H}$,$x = -\frac{3}{8H}$ and $x = -\frac{1}{4H}$.

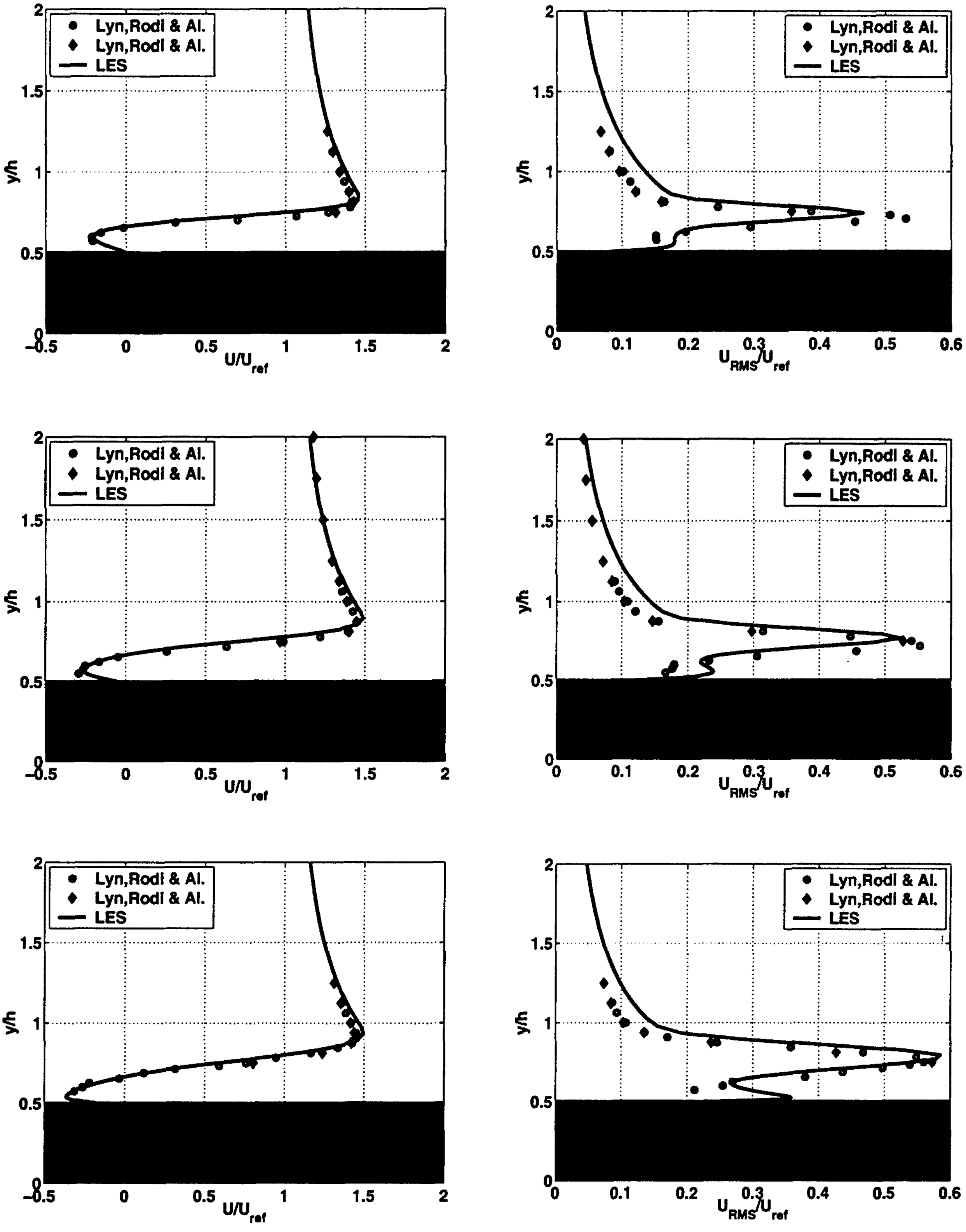

Fig. C.7: Additional simulations, Case II: velocity profiles for stream-wise velocity, left and stream-wise RMS, right, at three stations, from top to bottom: $x = -\frac{1}{8H}$,$x = 0$ and $x = \frac{1}{8H}$.

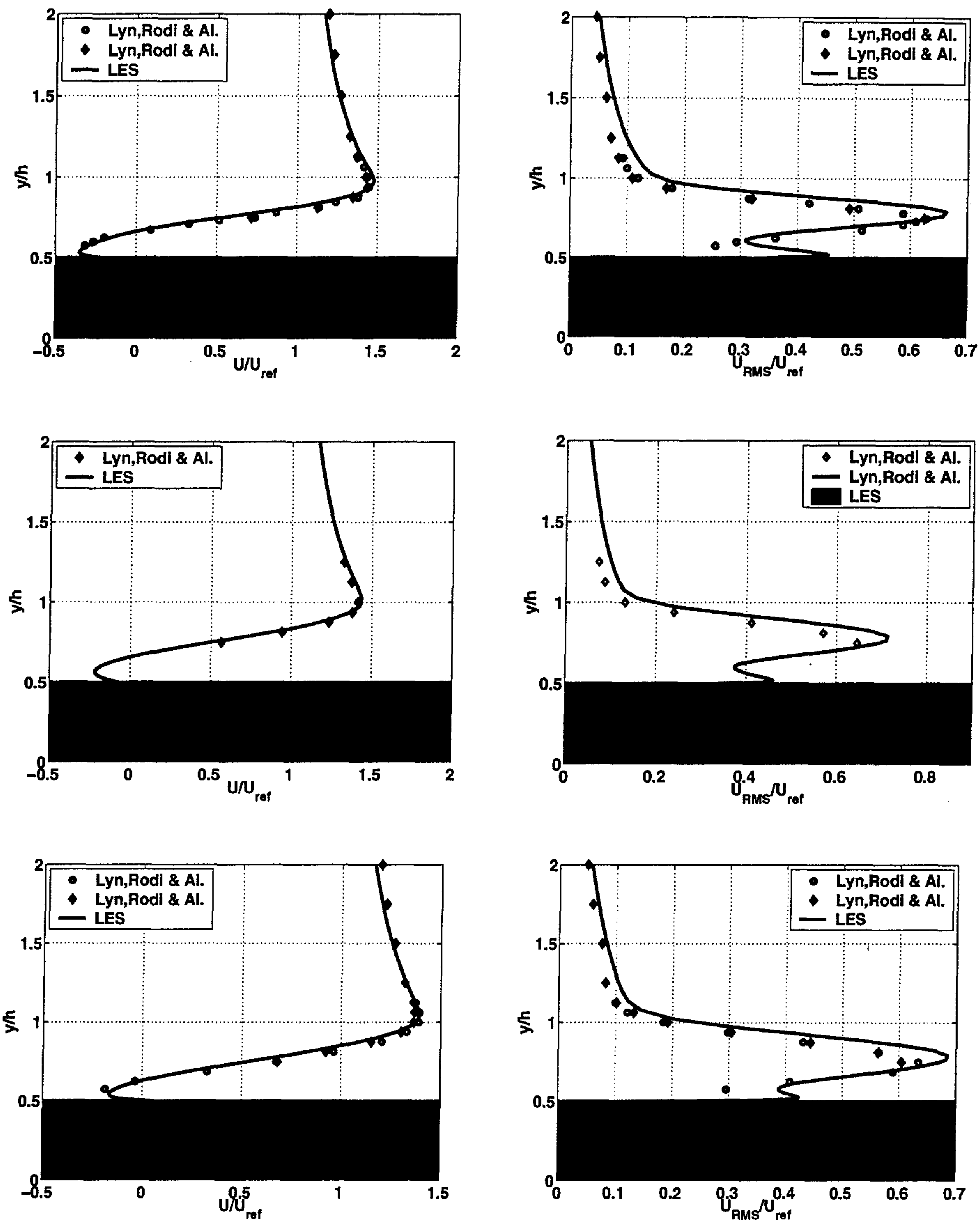

Fig. C.8: Additional simulations, Case II: velocity profiles for stream-wise velocity, left and stream-wise RMS, right, at three stations, from top to bottom: $x = \frac{1}{4H}$,$x = \frac{3}{8H}$ and $x = \frac{1}{2H}$.

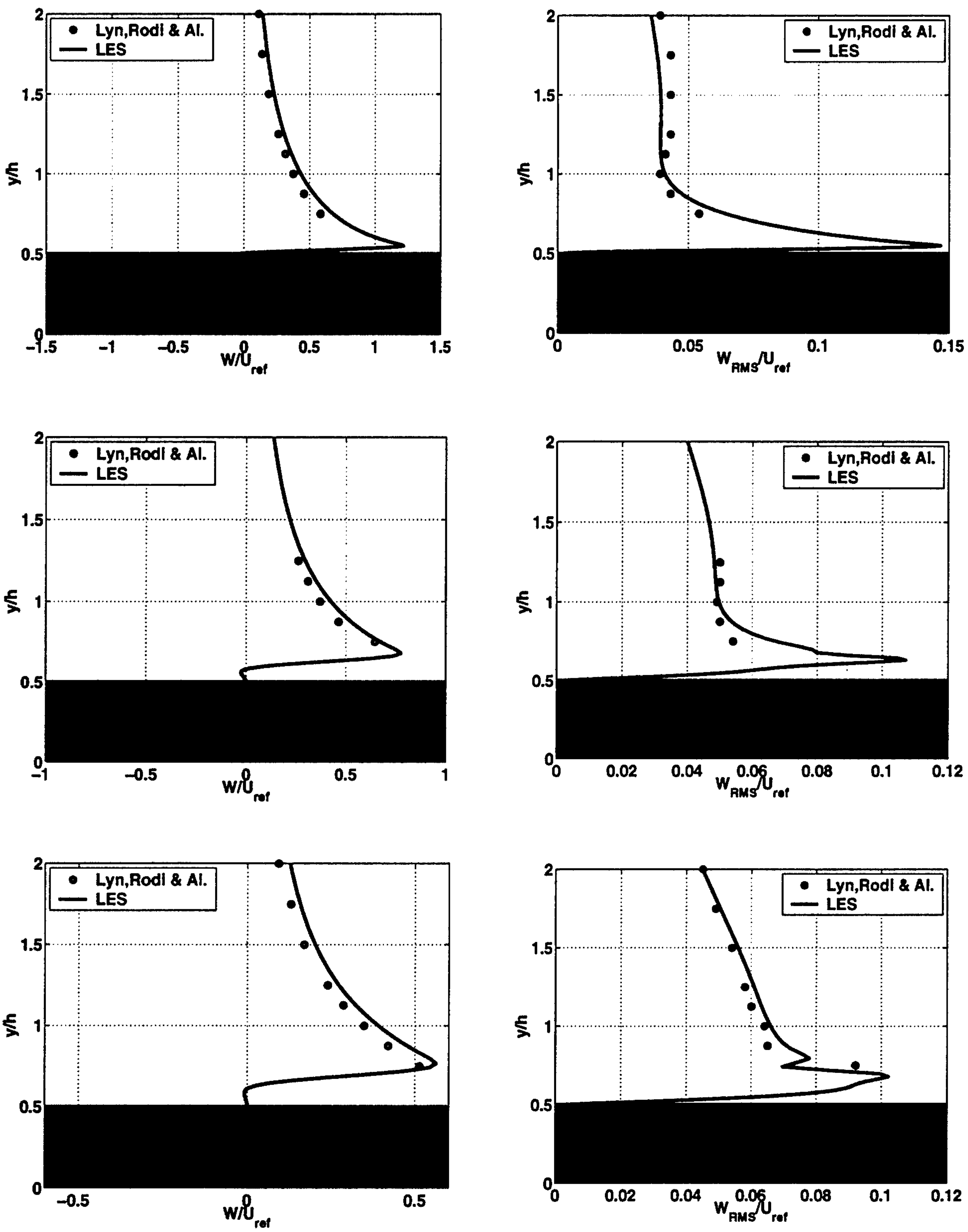

Fig. C.9: Additional simulations, Case II: velocity profiles for vertical velocity, left and vertical RMS, right, at three stations, from top to bottom: $x = -\frac{1}{2H}$,$x = -\frac{3}{8H}$ and $x = -\frac{1}{4H}$.

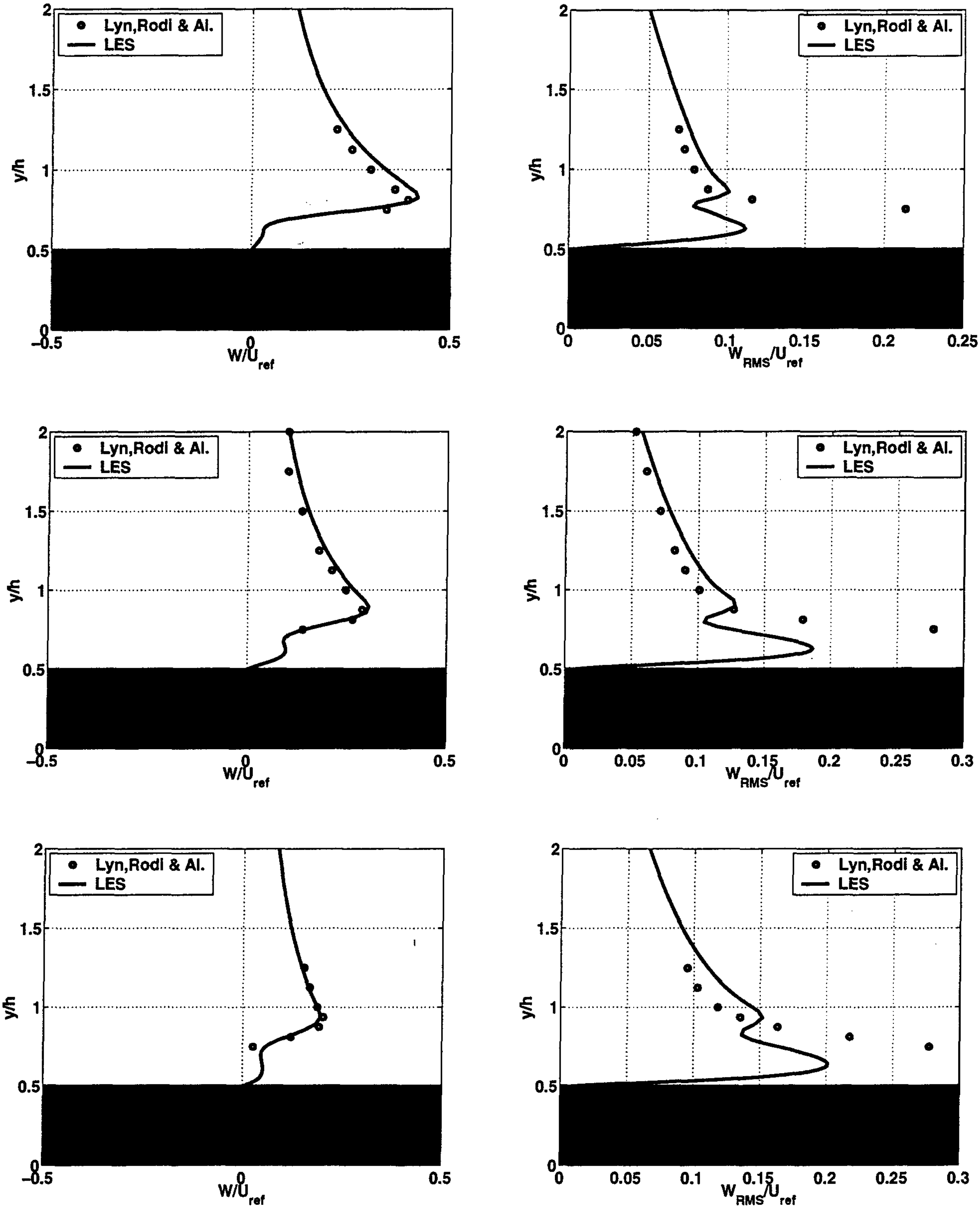

Fig. C.10: Additional simulations, Case II: velocity profiles for vertical velocity, left and vertical RMS, right, at three stations, from top to bottom: $x = -\frac{1}{8H}$,$x = 0$ and $x = \frac{1}{8H}$.

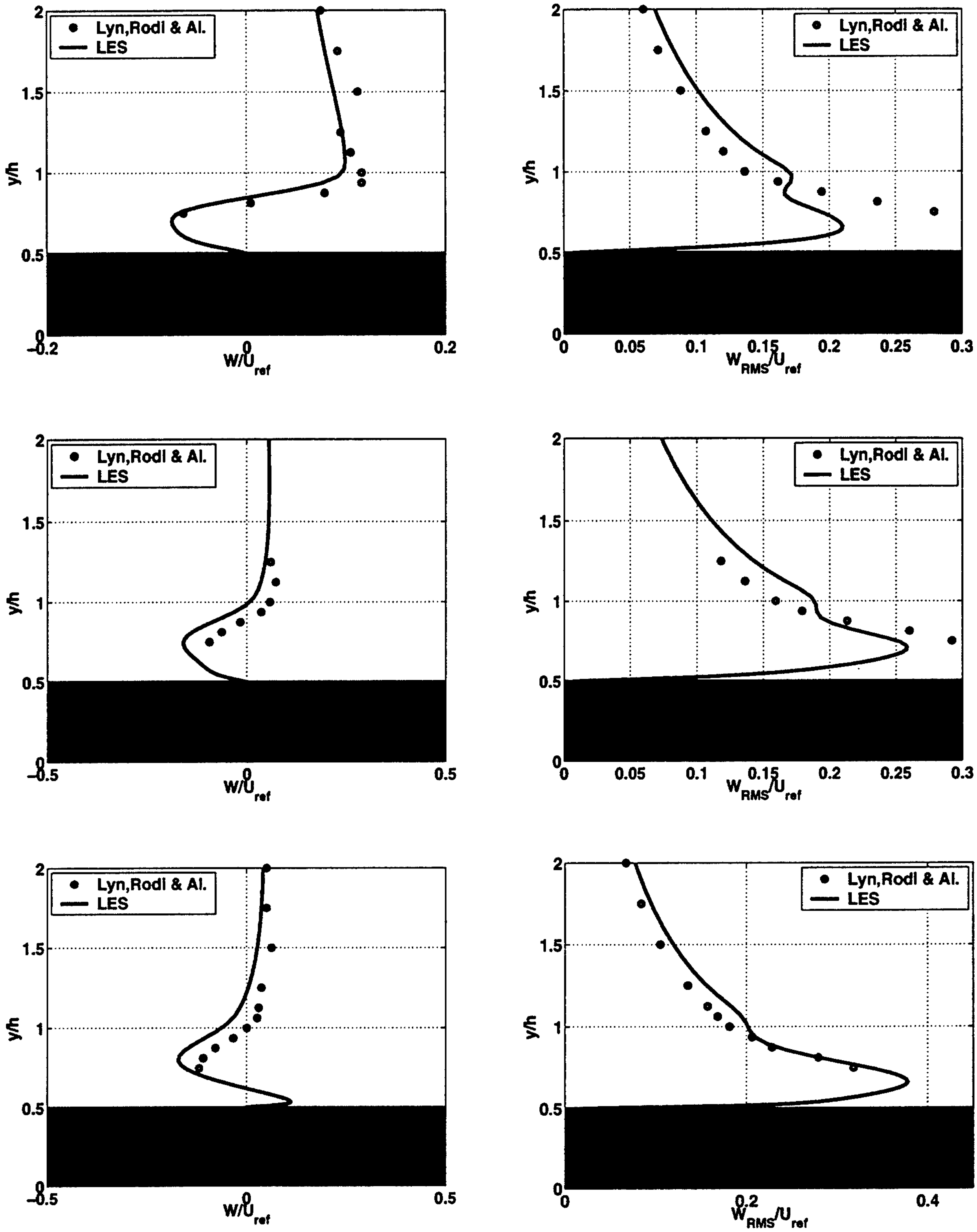

Fig. C.11: Additional simulations, Case II: velocity profiles for vertical velocity, left and vertical RMS, right, at three stations, from top to bottom: $x = \frac{1}{4H}$,$x = \frac{3}{8H}$ and $x = \frac{1}{2H}$.

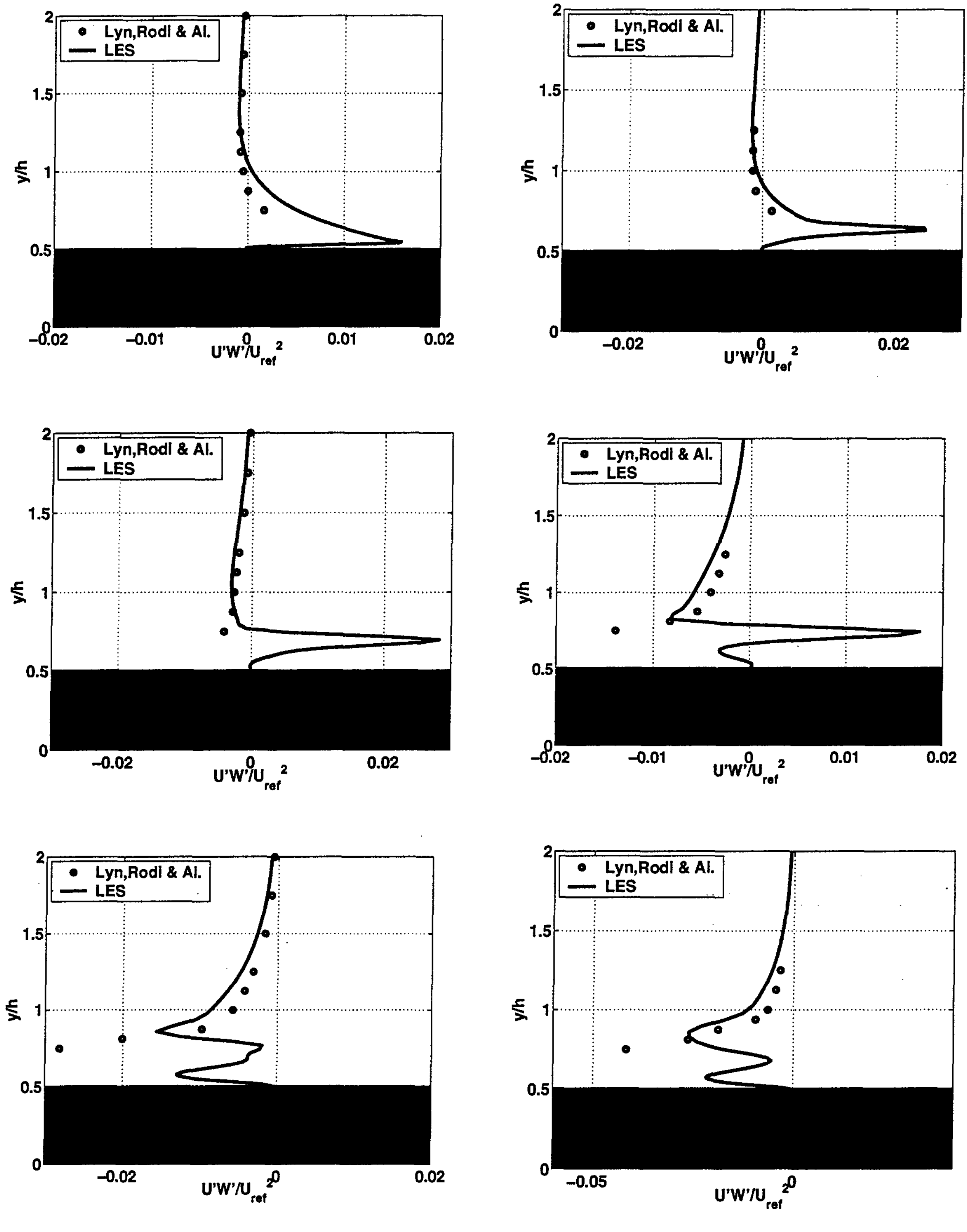

Fig. C.12: Additional simulations, Case II: velocity profiles for turbulent shear stress, from top to bottom and left to right, at the stations: $x = -\frac{1}{2H}$, $x = -\frac{3}{8H}$, $x = -\frac{1}{4H}$, $x = -\frac{1}{8H}$, $x = 0$ and $x = \frac{1}{8H}$

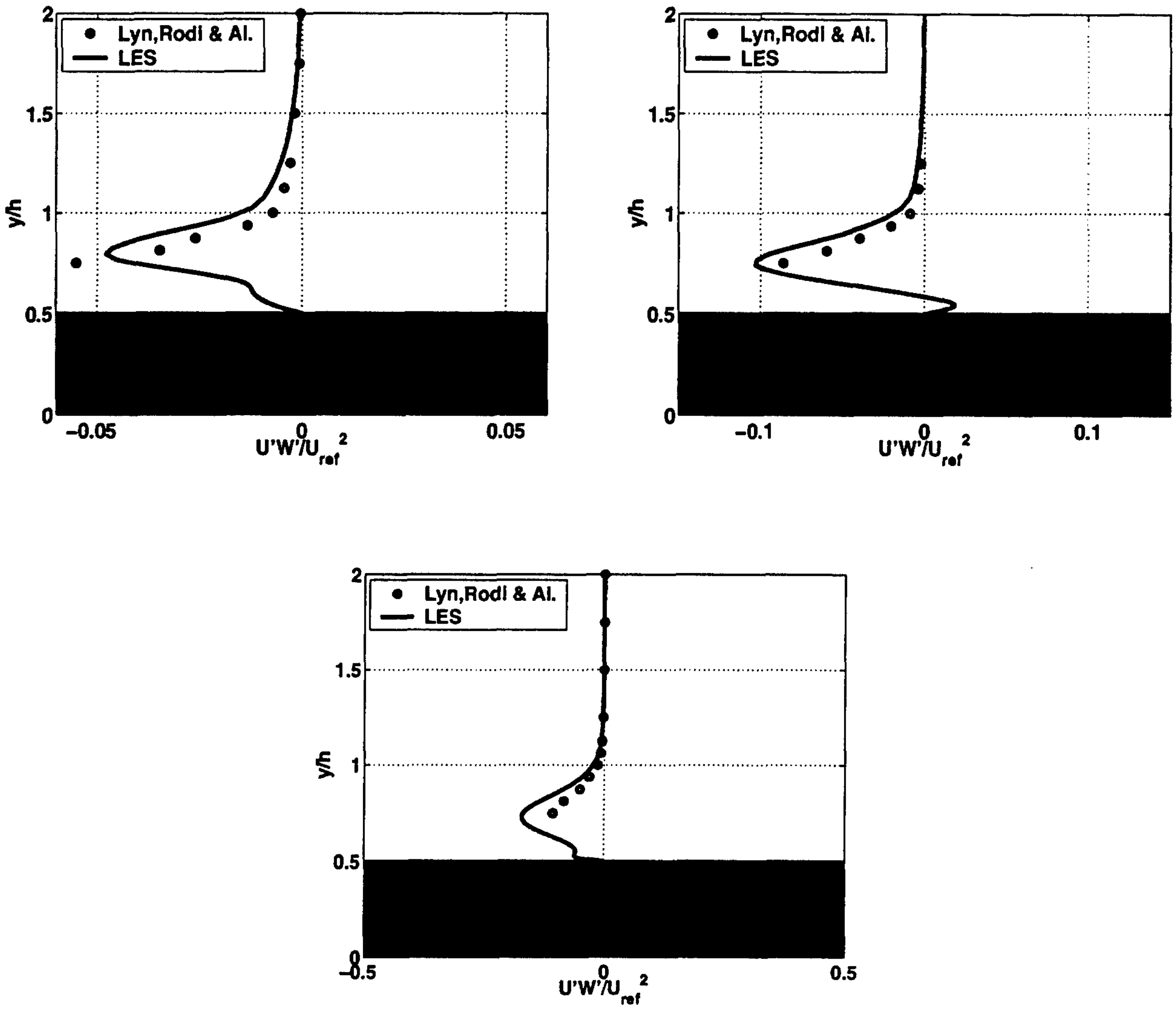

Fig. C.13: Additional simulations, Case II: velocity profiles for turbulent shear stress, from top to bottom and left to right, at the stations: $x = \frac{1}{4H}$, $x = \frac{3}{8H}$ and $x = \frac{1}{2H}$

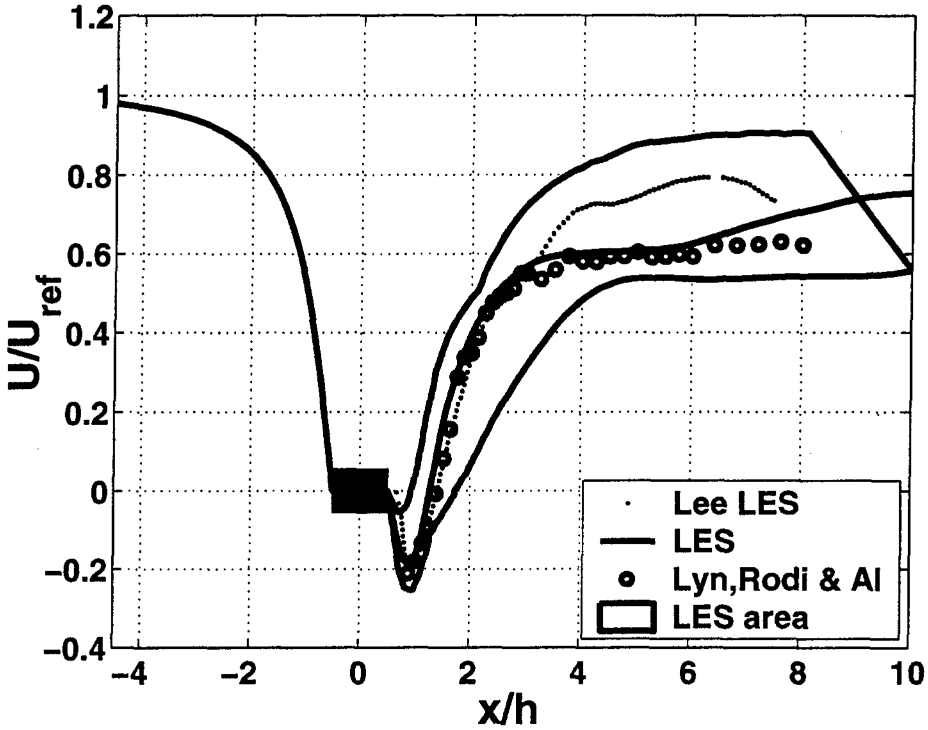

Fig. C.14: Additional simulations, Case II: average stream-wise velocity at wake centerline; present simulation versus experimental data and alternative LES (Sungsu, 1998)

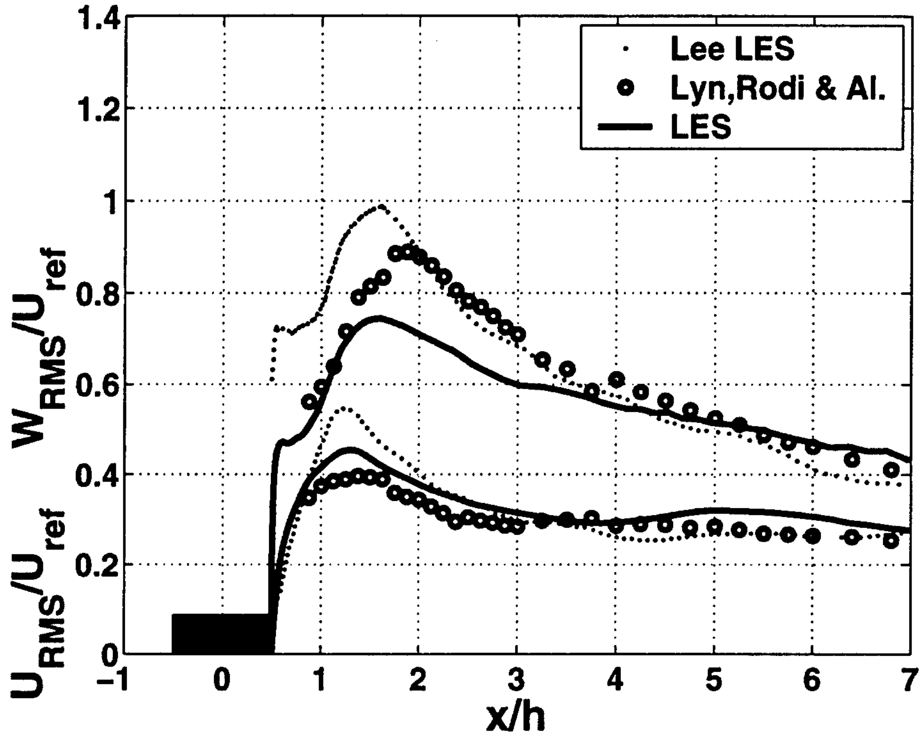

Fig. C.15: Additional simulations, Case II: average stream-wise and vertical velocity RMS at wake centerline; present simulation versus experimental data and alternative LES (Sungsu, 1998)

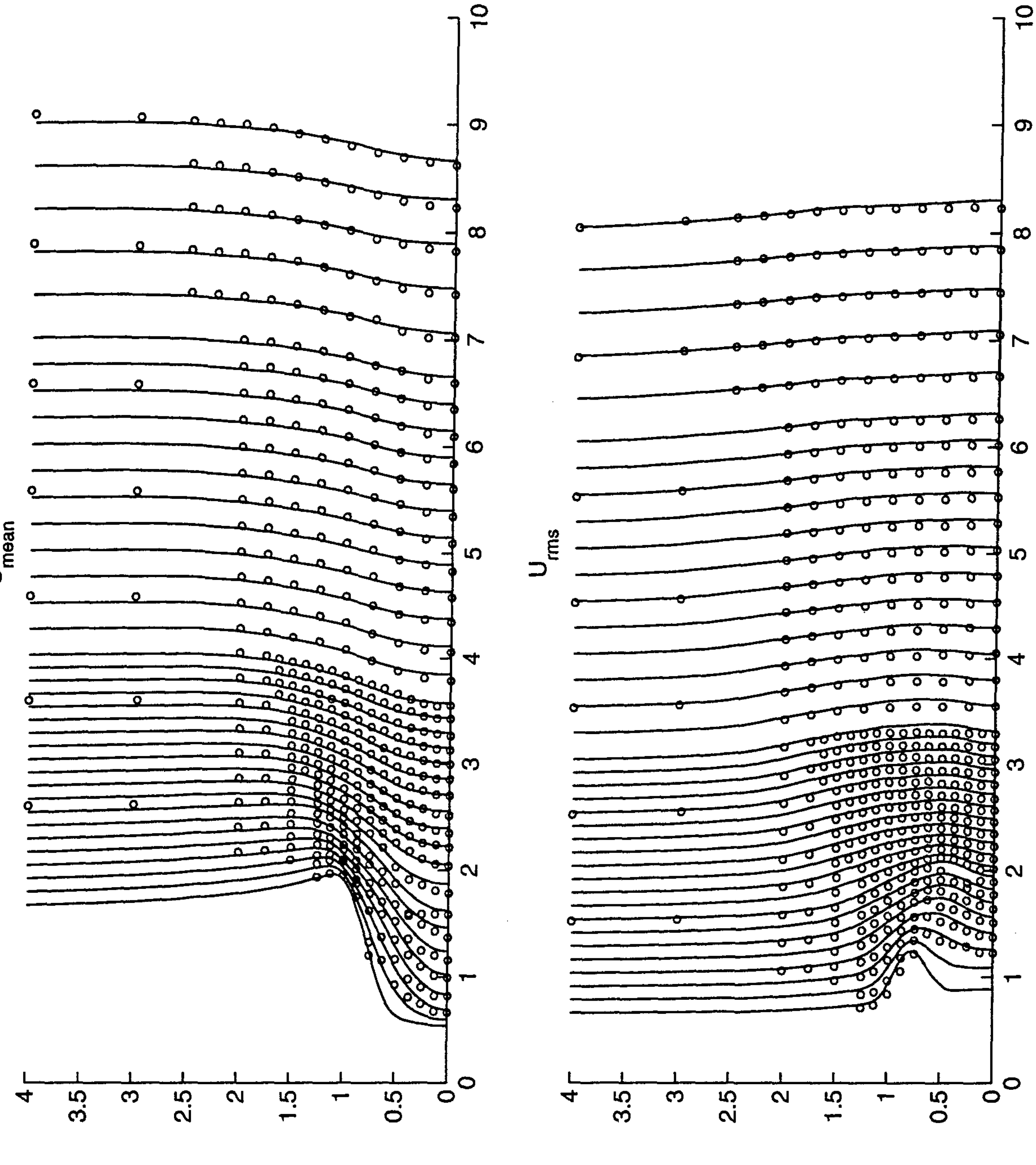

(a) Stream-wise average

(b) Stream-wise RMS

Fig. C.16: Wake overview, stream-wise velocity comparison with experiments.

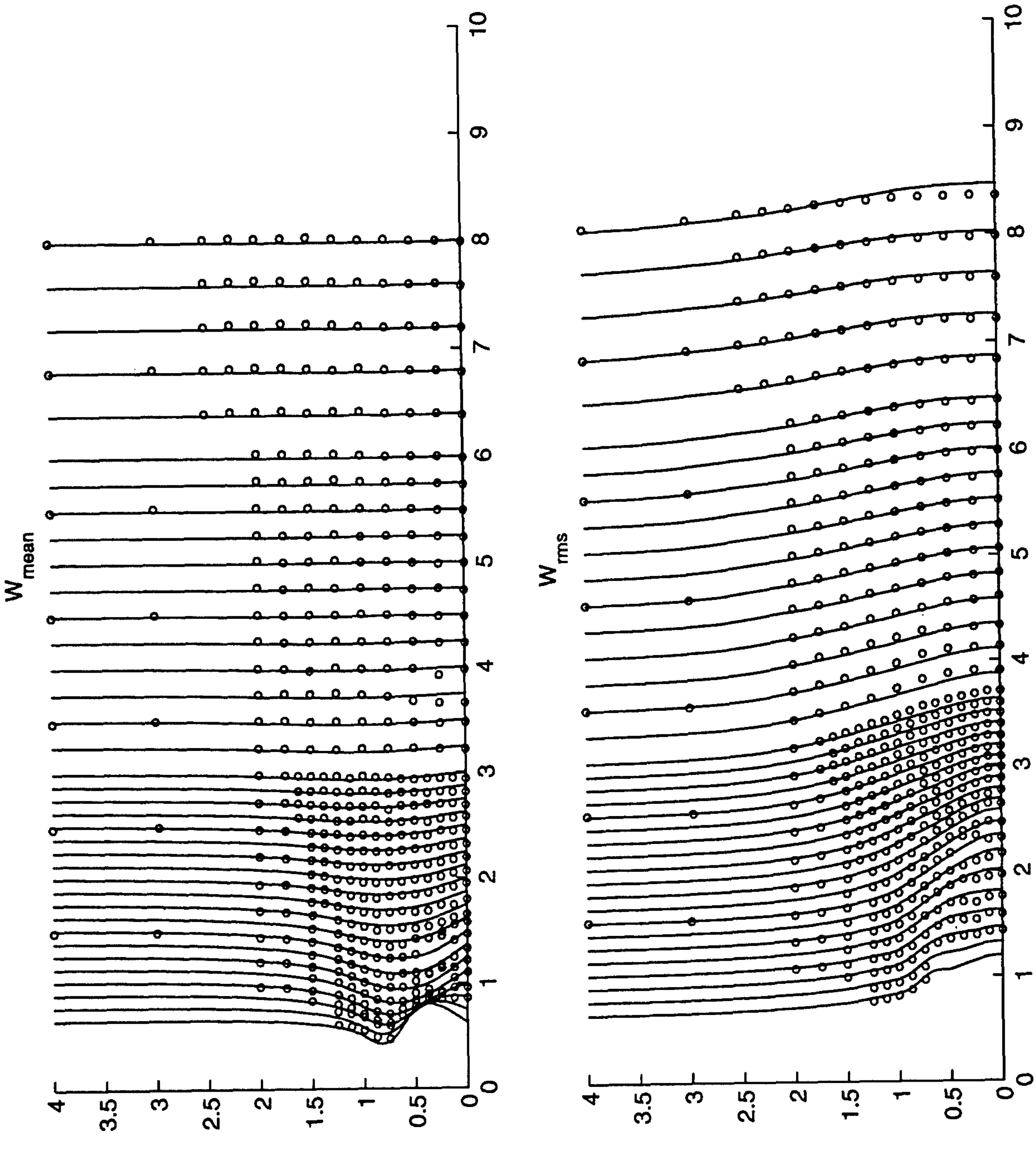

(a) Vertical average

(b) Vertical RMS

Fig. C.17: Wake overview, vertical velocity comparison with experiments.

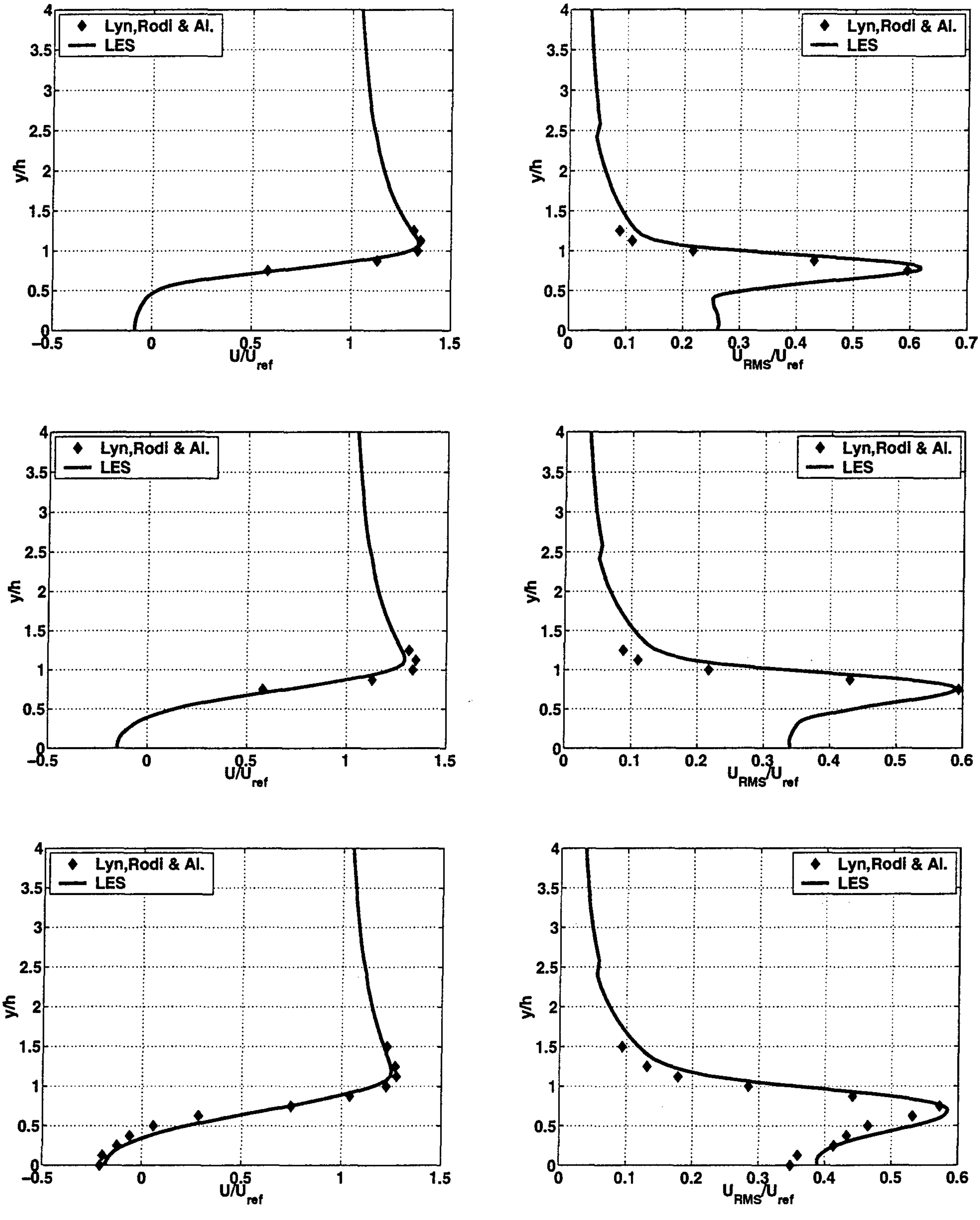

Fig. C.18: Additional simulations, Case II: velocity profiles for stream-wise velocity, left and stream-wise RMS, right, at three stations, from top to bottom: $x = \frac{5}{8H}$,$x = \frac{6}{8H}$ and $x = \frac{7}{8H}$.

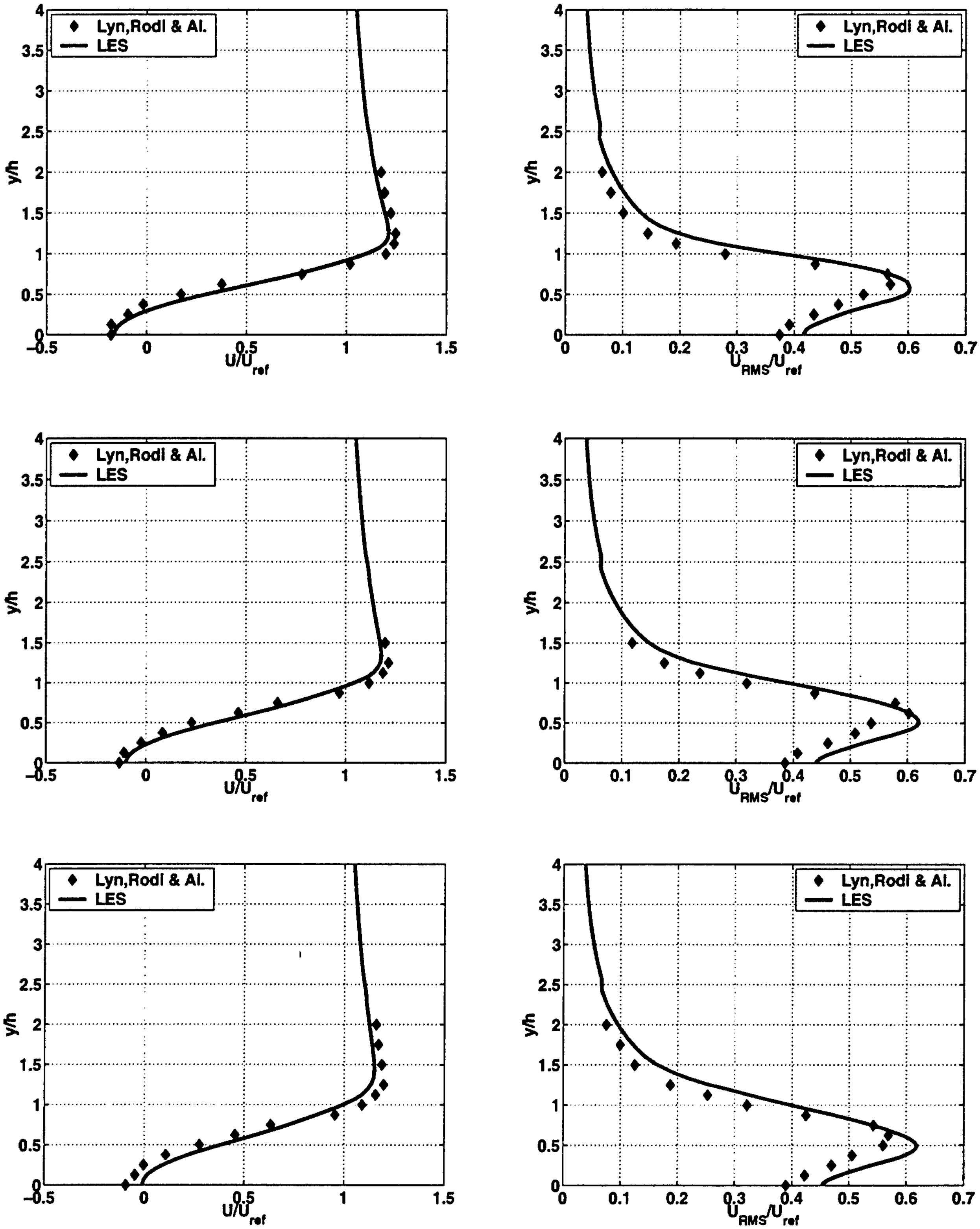

Fig. C.19: Additional simulations, Case II: velocity profiles for stream-wise velocity, left and stream-wise RMS, right, at three stations, from top to bottom: $x = \frac{8}{8H}$,$x = \frac{9}{8H}$ and $x = \frac{10}{8H}$.

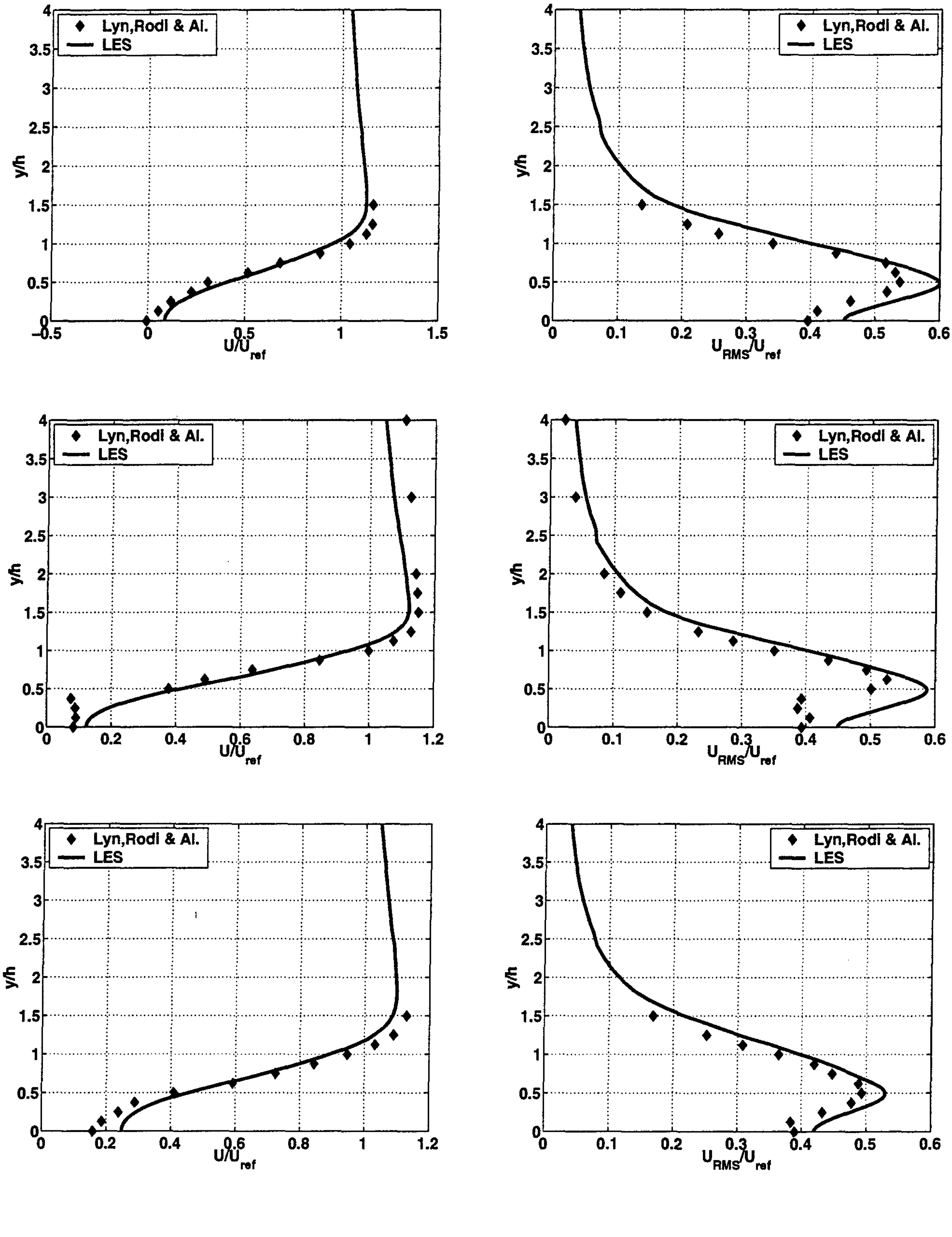

Fig. C.20: Additional simulations, Case II: velocity profiles for stream-wise velocity, left and stream-wise RMS, right, at three stations, from top to bottom: $x = \frac{11}{8H}$,$x = \frac{12}{8H}$ and $x = \frac{13}{8H}$.

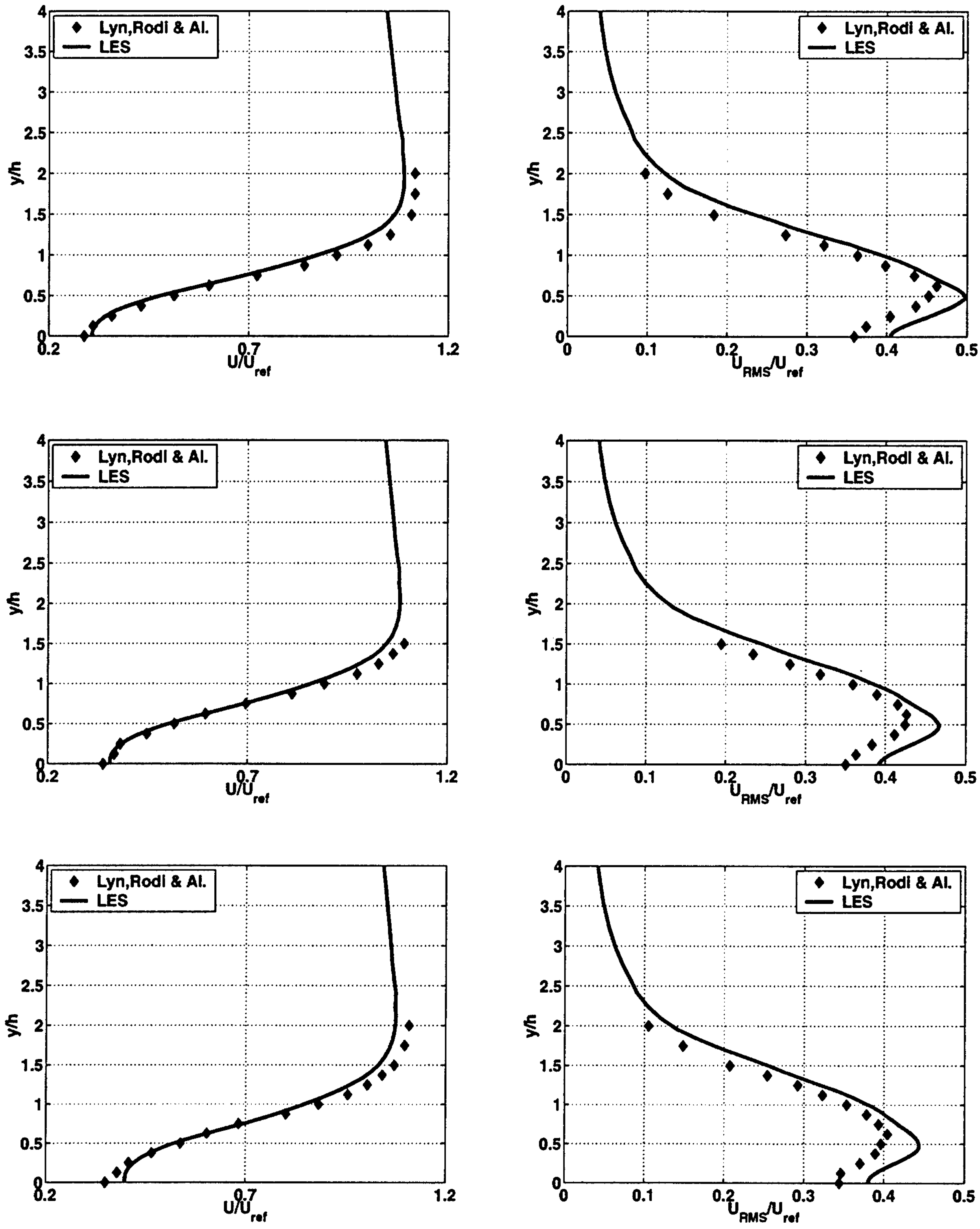

Fig. C.21: Additional simulations, Case II: velocity profiles for stream-wise velocity, left and stream-wise RMS, right, at three stations, from top to bottom: $x = \frac{14}{8H}$,$x = \frac{15}{8H}$ and $x = \frac{16}{8H}$.

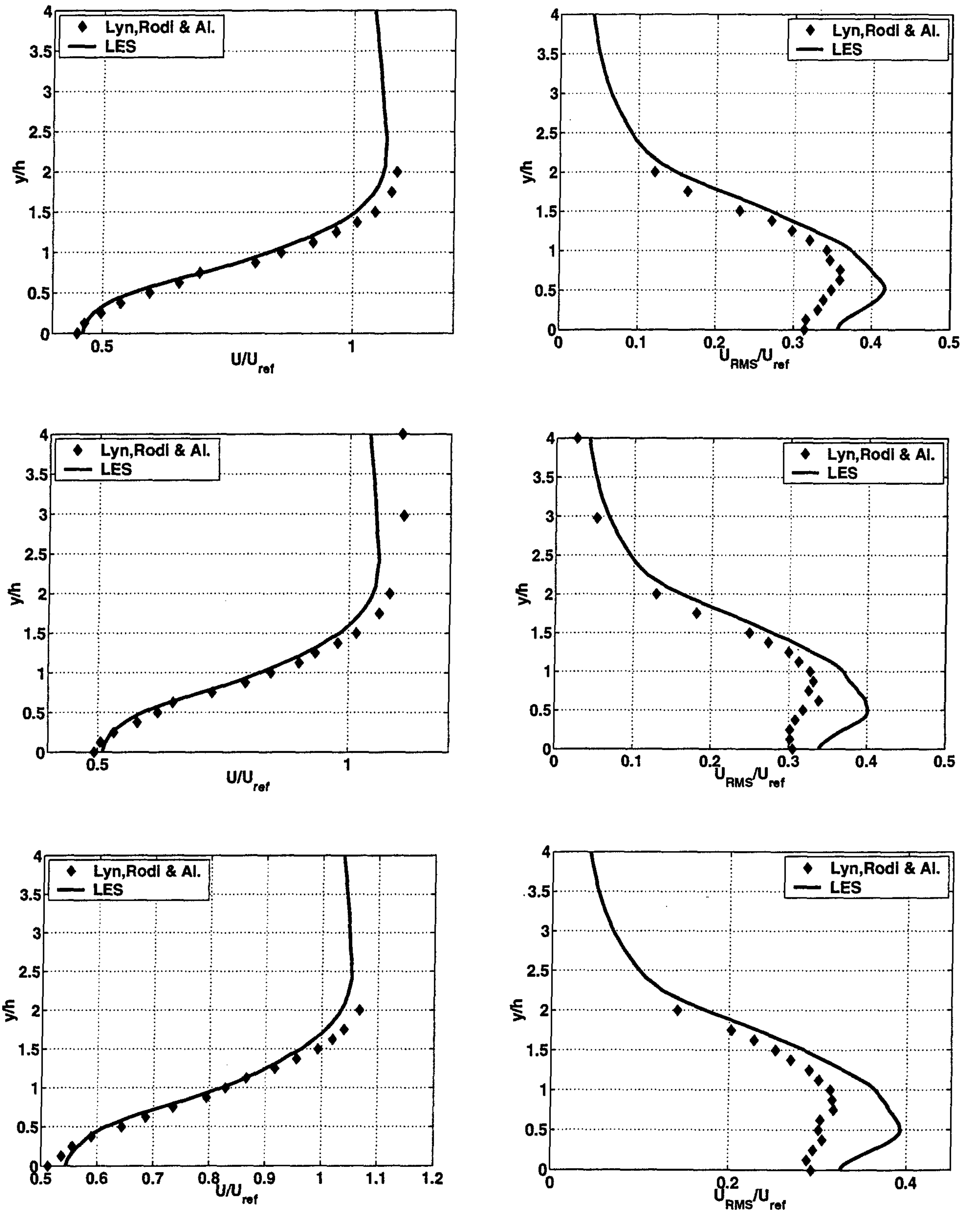

Fig. C.22: Additional simulations, Case II: velocity profiles for stream-wise velocity, left and stream-wise RMS, right, at three stations, from top to bottom: $x = \frac{18}{8H}$,$x = \frac{20}{8H}$ and $x = \frac{22}{8H}$.

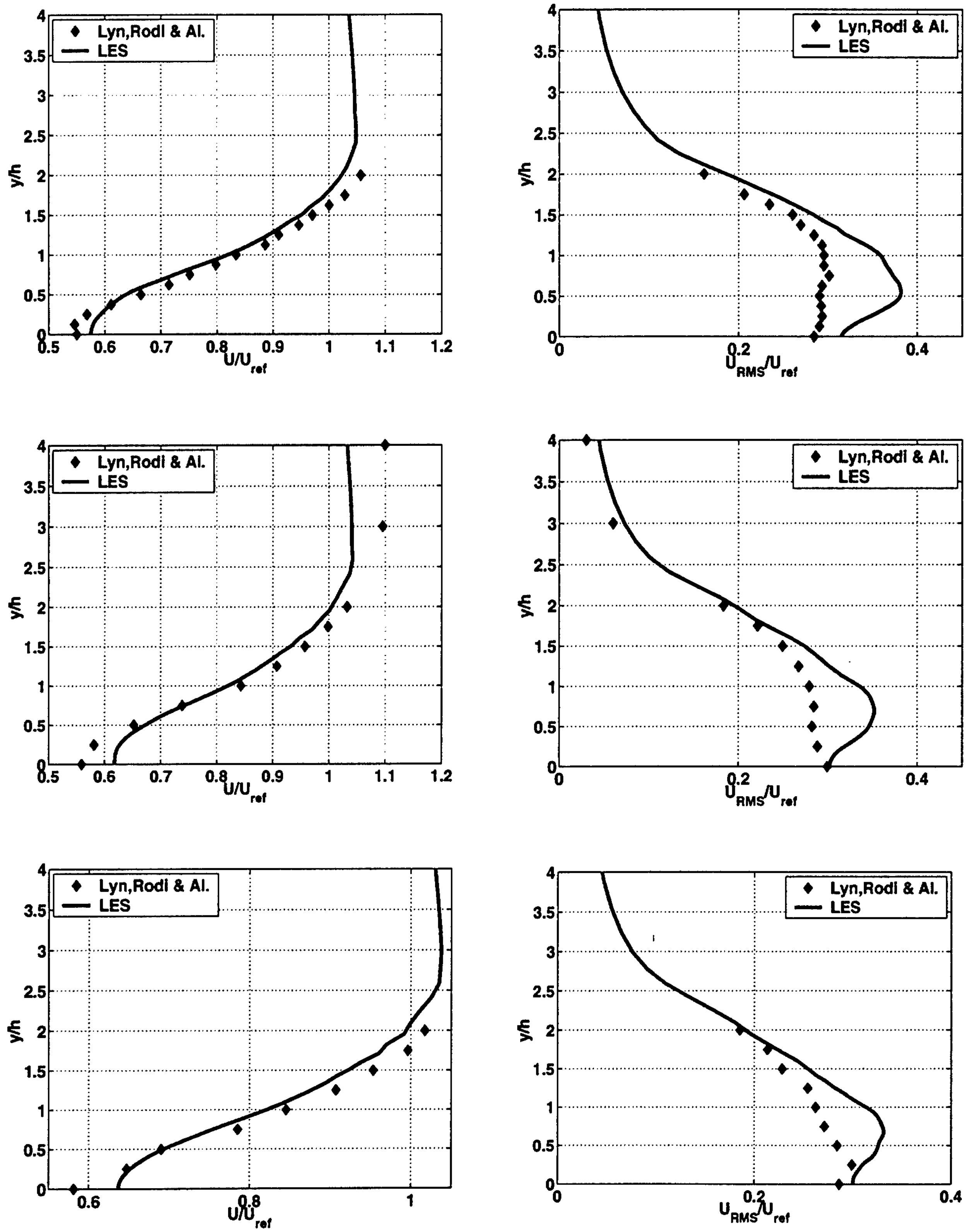

Fig. C.23: Additional simulations, Case II: velocity profiles for stream-wise velocity, left and stream-wise RMS, right, at three stations, from top to bottom: $x = \frac{24}{8H}$,$x = \frac{28}{8H}$ and $x = \frac{32}{8H}$.

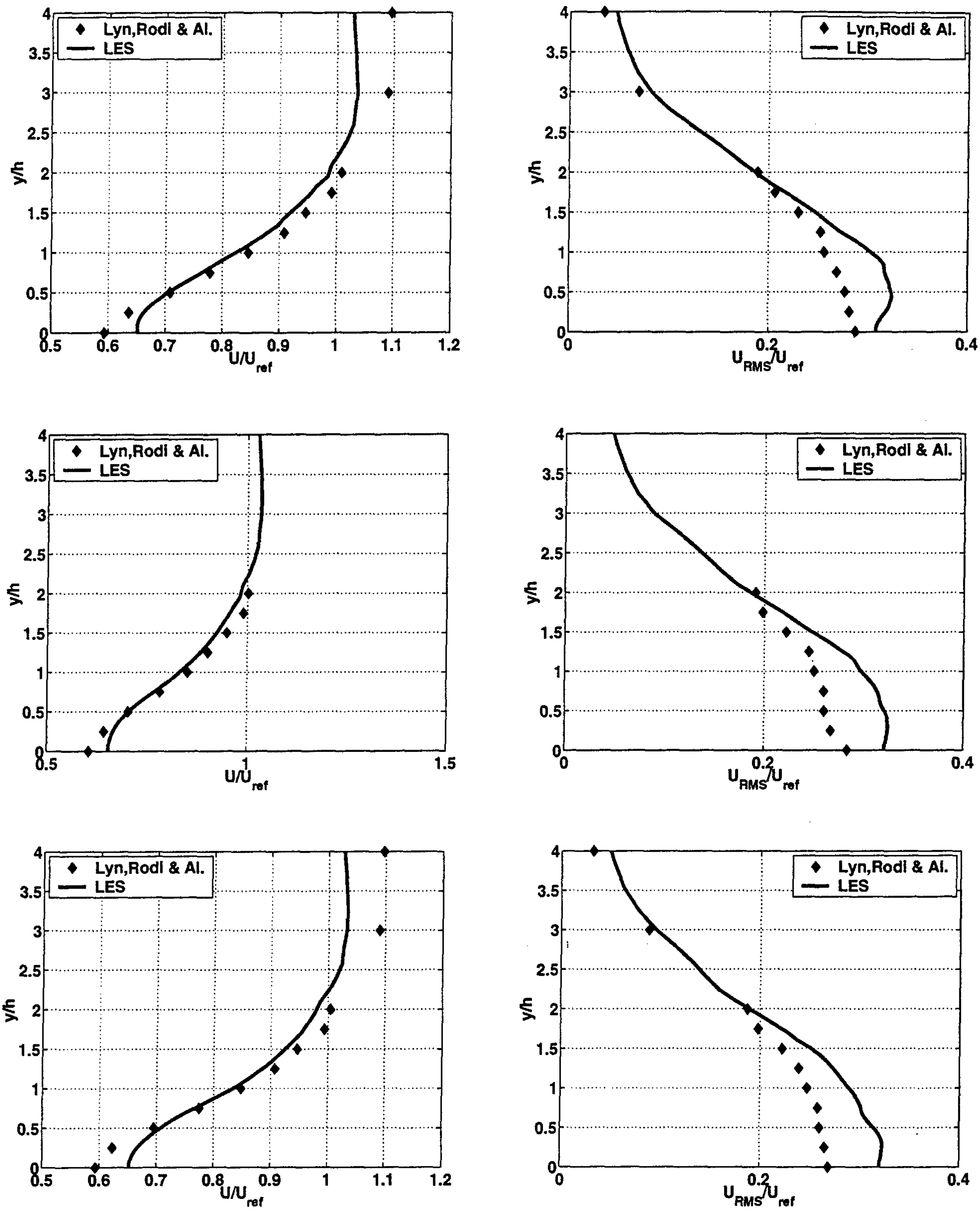

Fig. C.24: Additional simulations, Case II: velocity profiles for stream-wise velocity, left and stream-wise RMS, right, at three stations, from top to bottom: $x = \frac{36}{8H}$,$x = \frac{40}{8H}$ and $x = \frac{44}{8H}$.

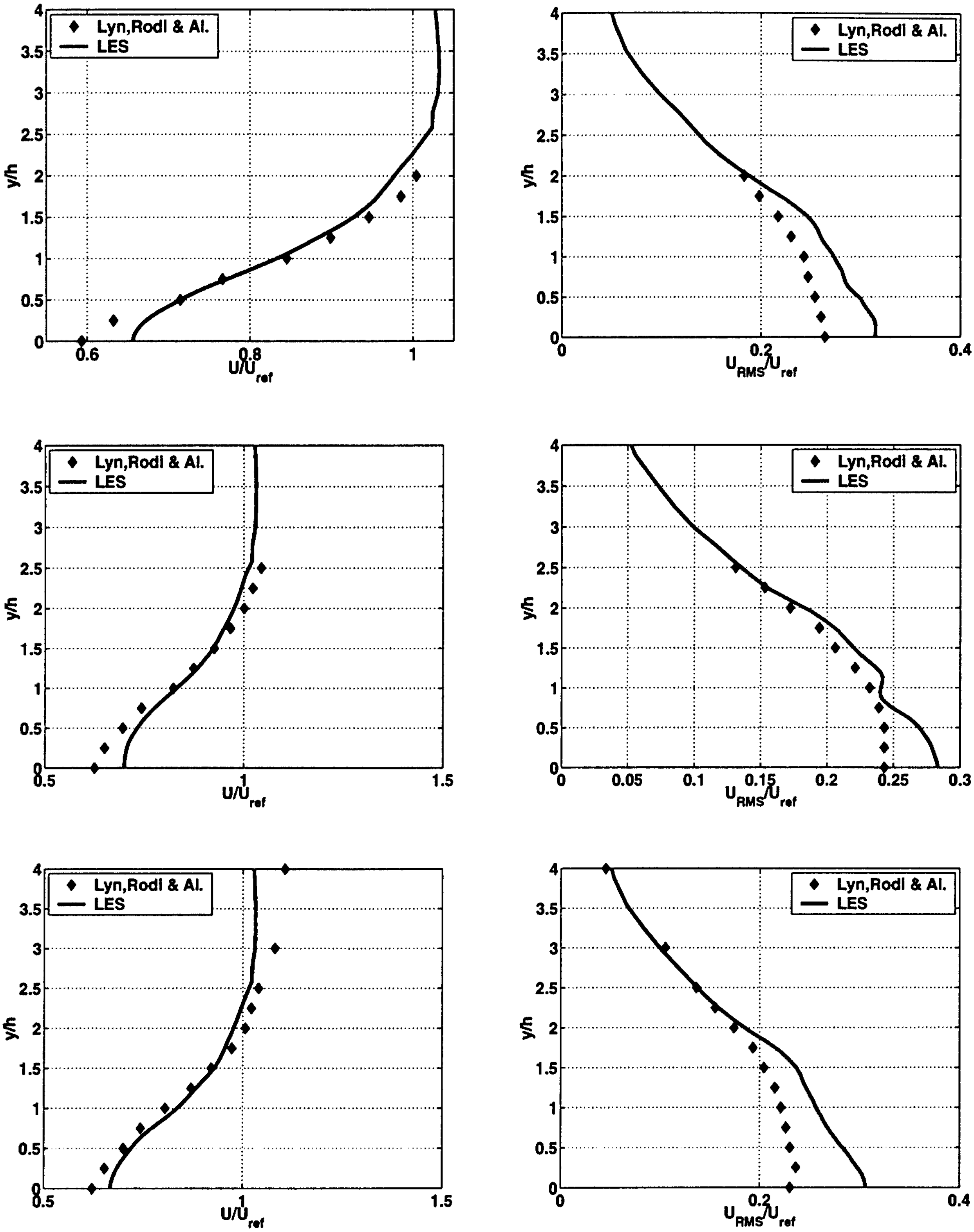

Fig. C.25: Additional simulations, Case II: velocity profiles for stream-wise velocity, left and stream-wise RMS, right, at three stations, from top to bottom: $x = \frac{48}{8H}$,$x = \frac{57.6}{8H}$ and $x = \frac{64}{8H}$.

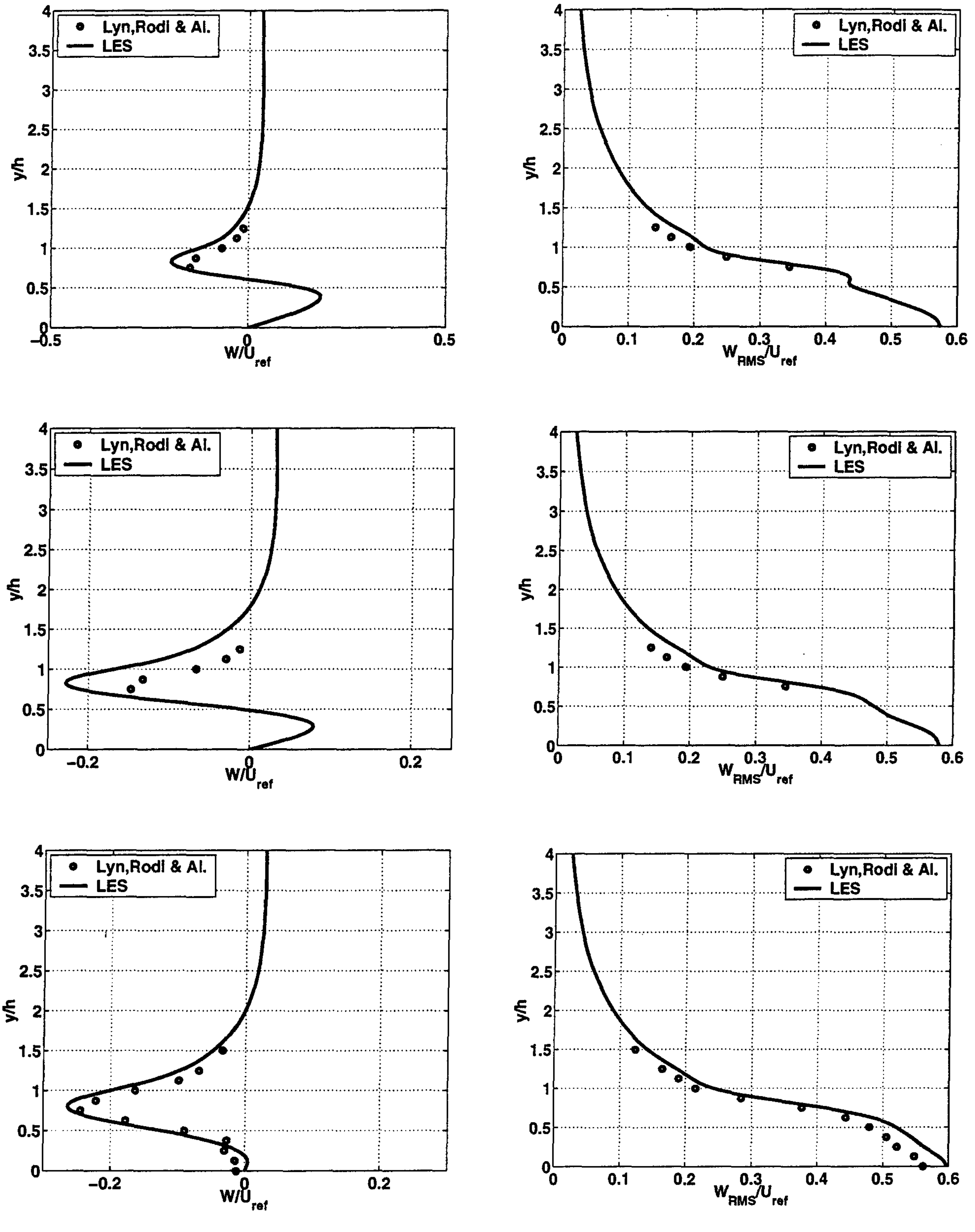

Fig. C.26: Additional simulations, Case II: velocity profiles for vertical velocity, left and vertical RMS, right, at three stations, from top to bottom: $x = \frac{5}{8H}$,$x = \frac{6}{8H}$ and $x = \frac{7}{8H}$.

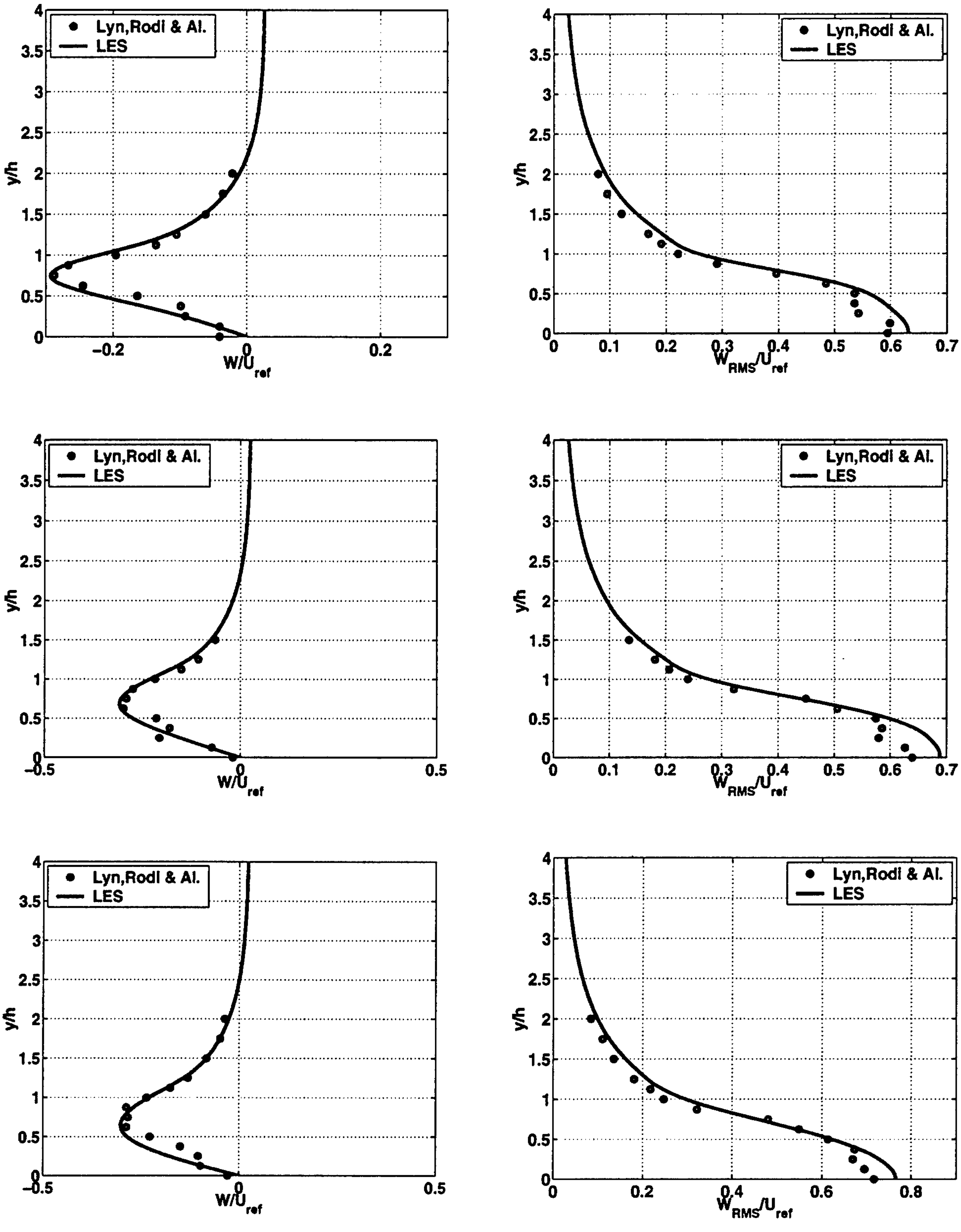

Fig. C.27: Additional simulations, Case II: velocity profiles for vertical velocity, left and vertical RMS, right, at three stations, from top to bottom: $x = \frac{8}{8H}$, $x = \frac{9}{8H}$ and $x = \frac{10}{8H}$.

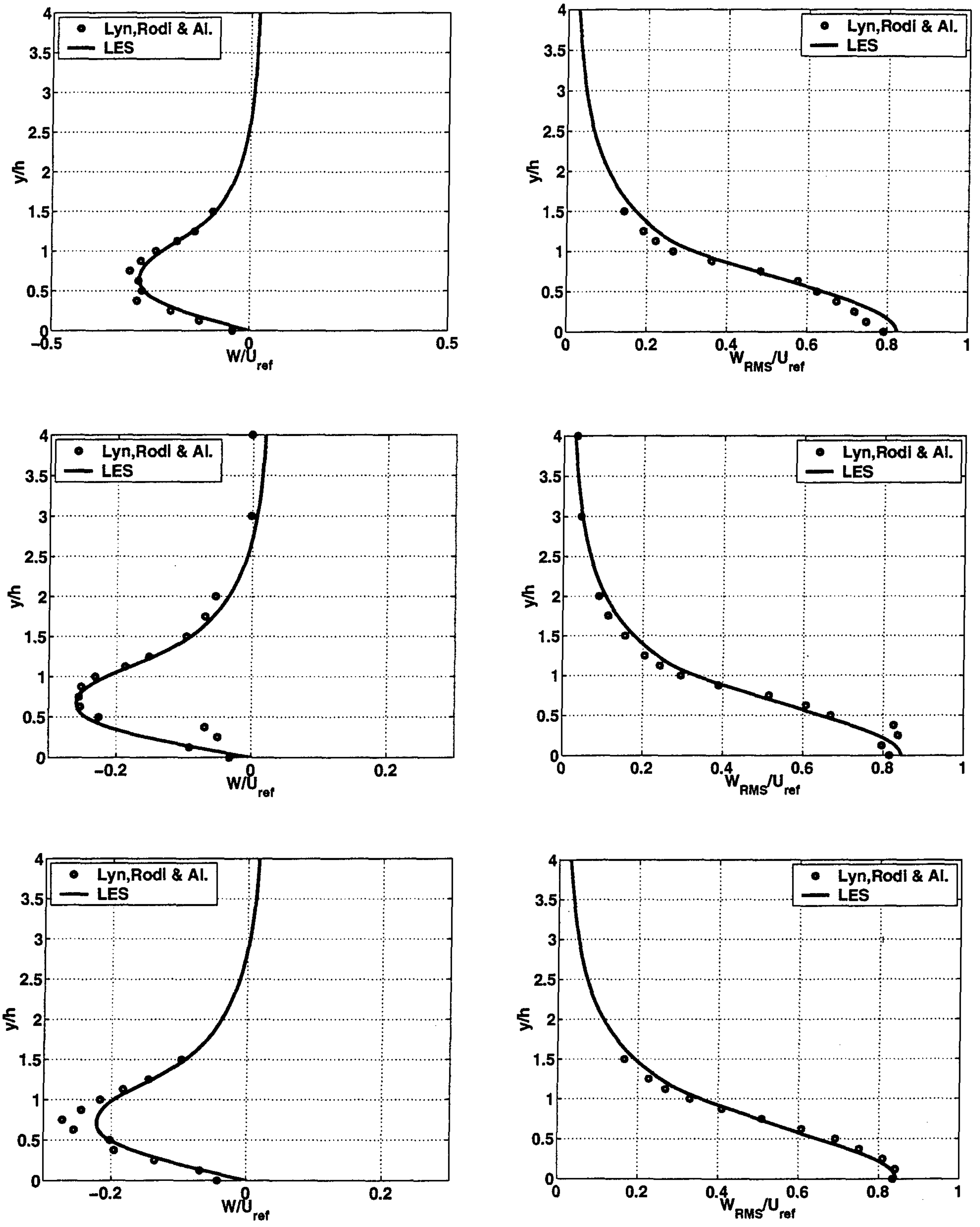

Fig. C.28: Additional simulations, Case II: velocity profiles for vertical velocity, left and vertical RMS, right, at three stations, from top to bottom: $x = \frac{11}{8H}$,$x = \frac{12}{8H}$ and $x = \frac{13}{8H}$.

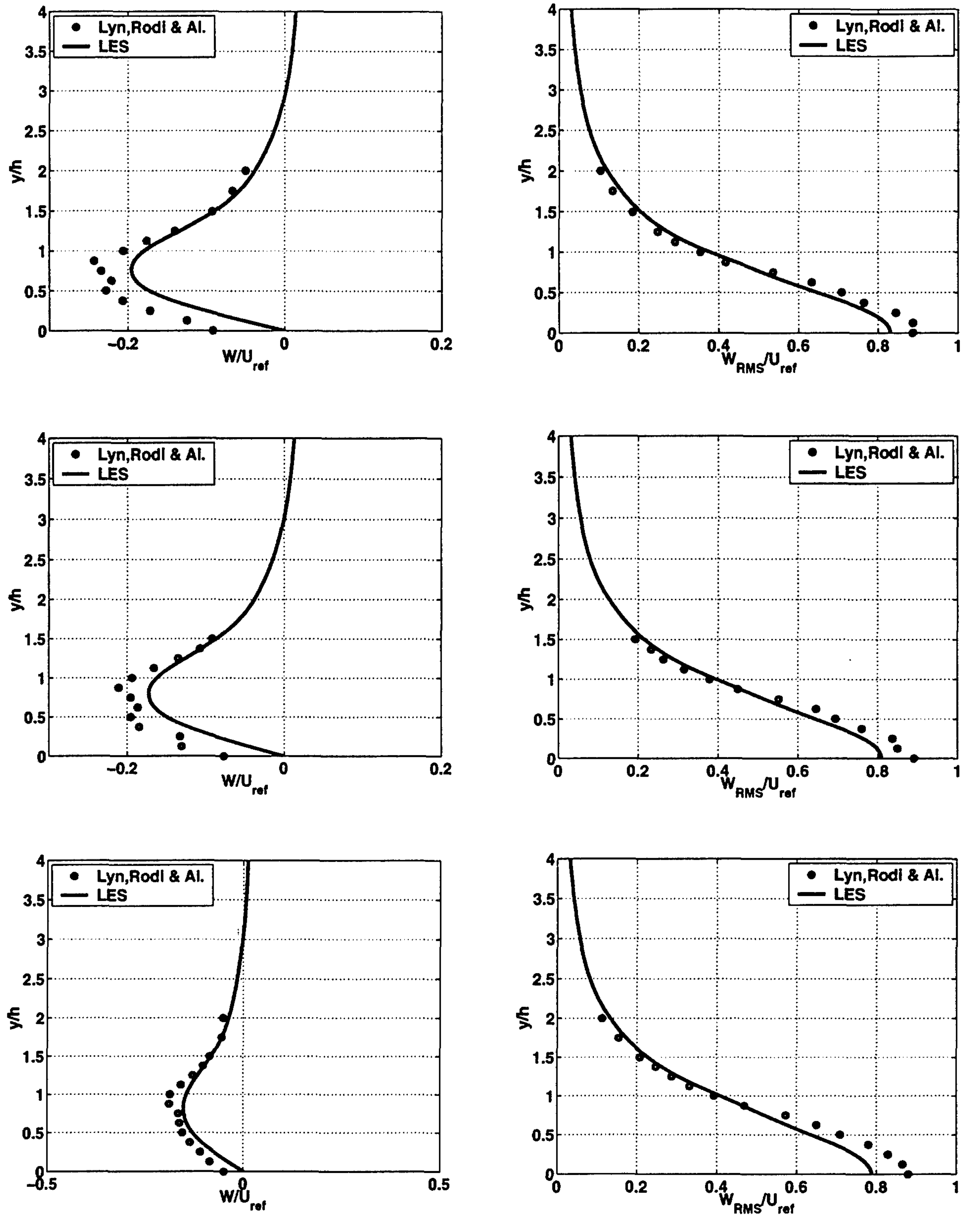

Fig. C.29: Additional simulations, Case II: velocity profiles for vertical velocity, left and vertical RMS, right, at three stations, from top to bottom: $x = \frac{14}{8H}$,$x = \frac{15}{8H}$ and $x = \frac{16}{8H}$.

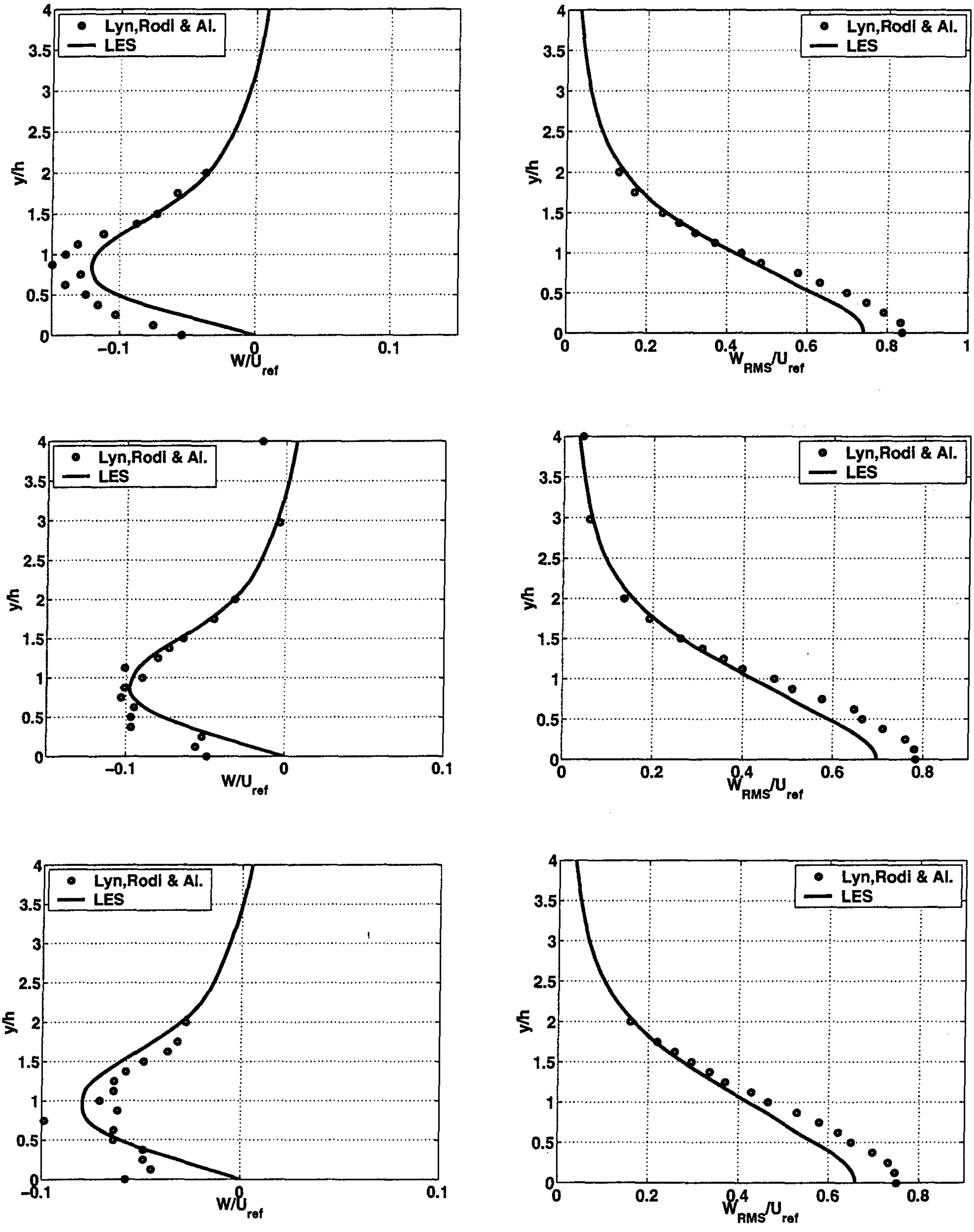

Fig. C.30: Additional simulations, Case II: velocity profiles for vertical velocity, left and vertical RMS, right, at three stations, from top to bottom: $x = \frac{18}{8H}$,$x = \frac{20}{8H}$ and $x = \frac{22}{8H}$.

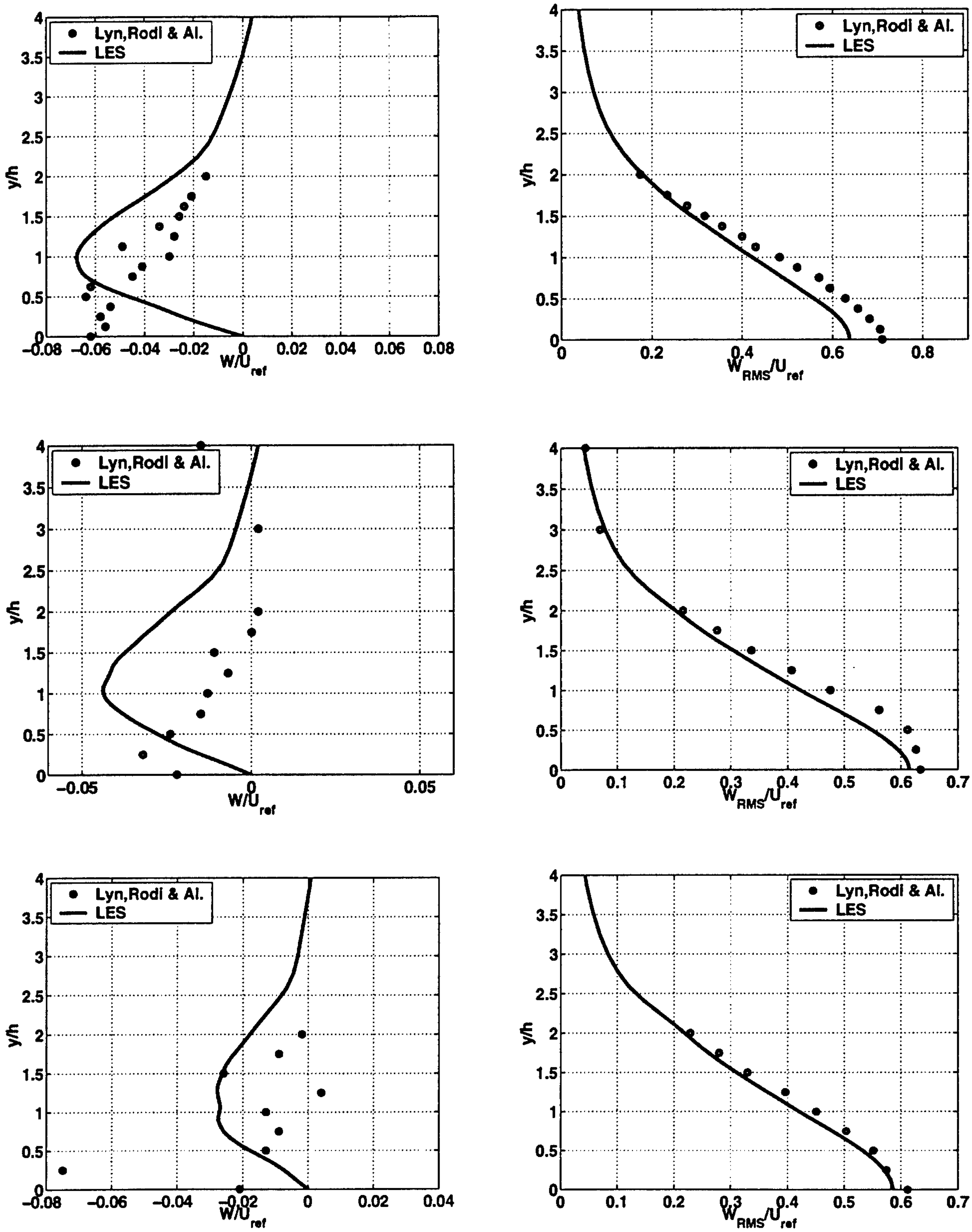

Fig. C.31: Additional simulations, Case II: velocity profiles for vertical velocity, left and vertical RMS, right, at three stations, from top to bottom: $x = \frac{24}{8H}$,$x = \frac{28}{8H}$ and $x = \frac{32}{8H}$.

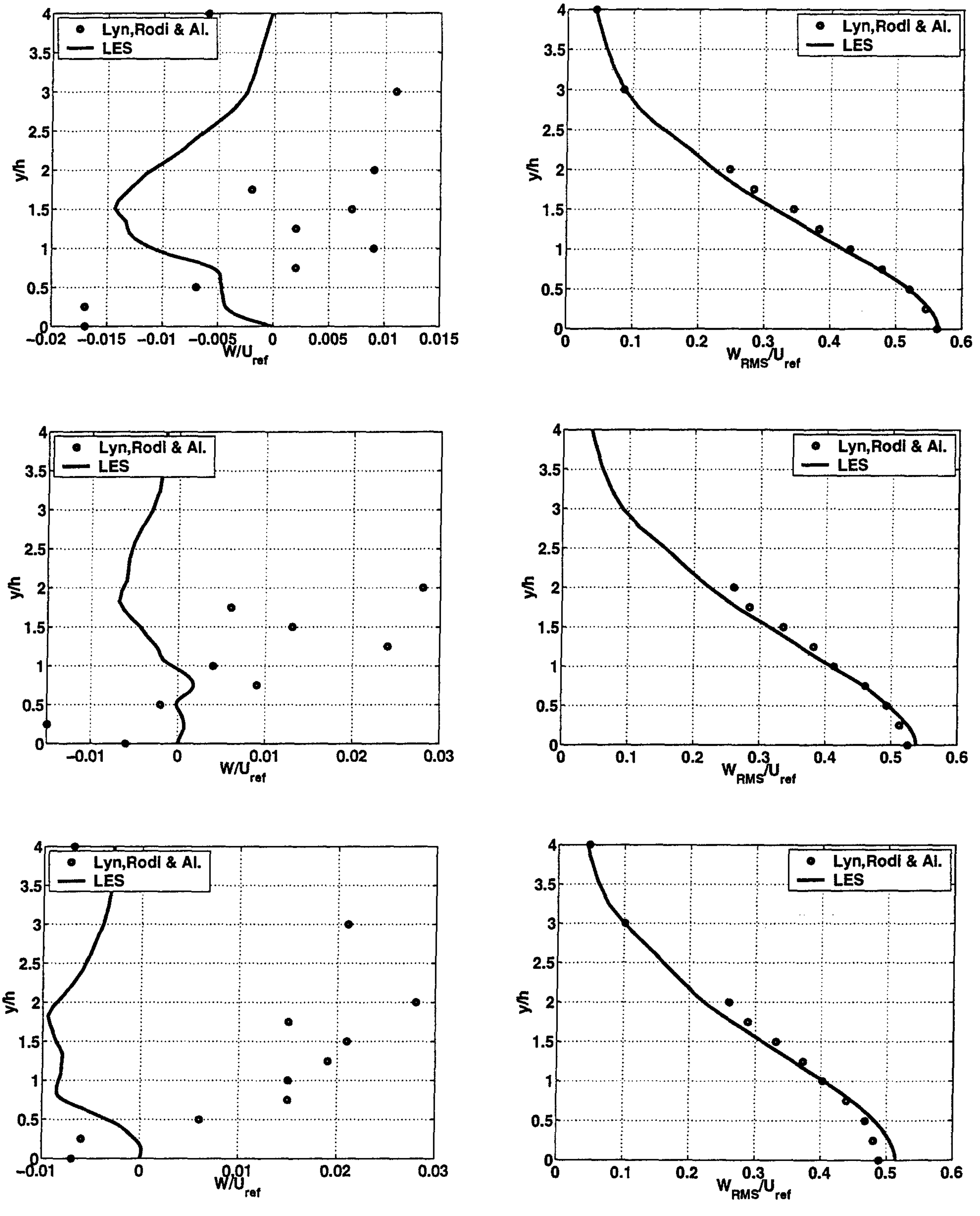

Fig. C.32: Additional simulations, Case II: velocity profiles for vertical velocity, left and vertical RMS, right, at three stations, from top to bottom: $x = \frac{36}{8H}$,$x = \frac{40}{8H}$ and $x = \frac{44}{8H}$.

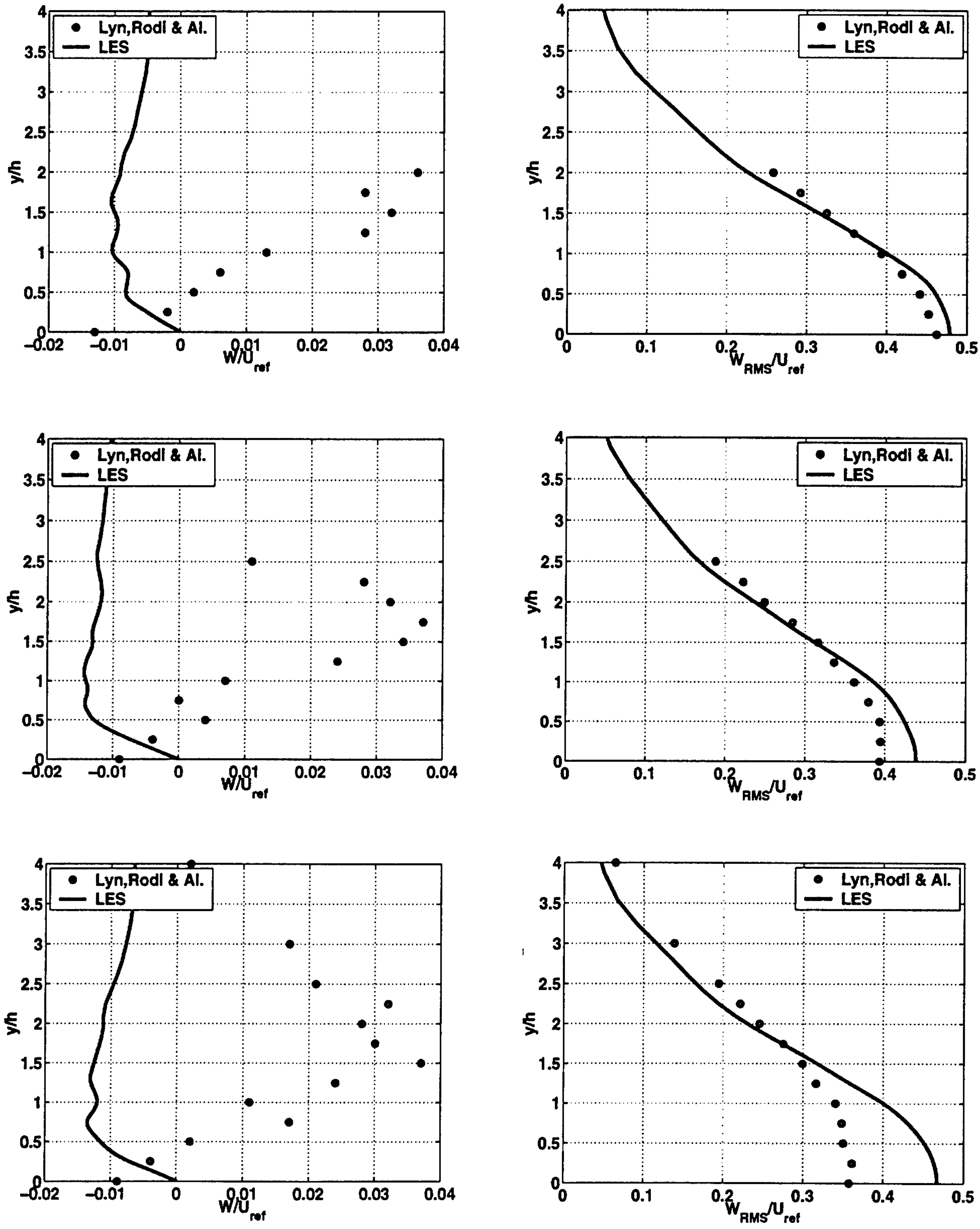

Fig. C.33: Additional simulations, Case II: velocity profiles for vertical velocity, left and vertical RMS, right, at three stations, from top to bottom: $x = \frac{48}{8H}$,$x = \frac{57.6}{8H}$ and $x = \frac{64}{8H}$.

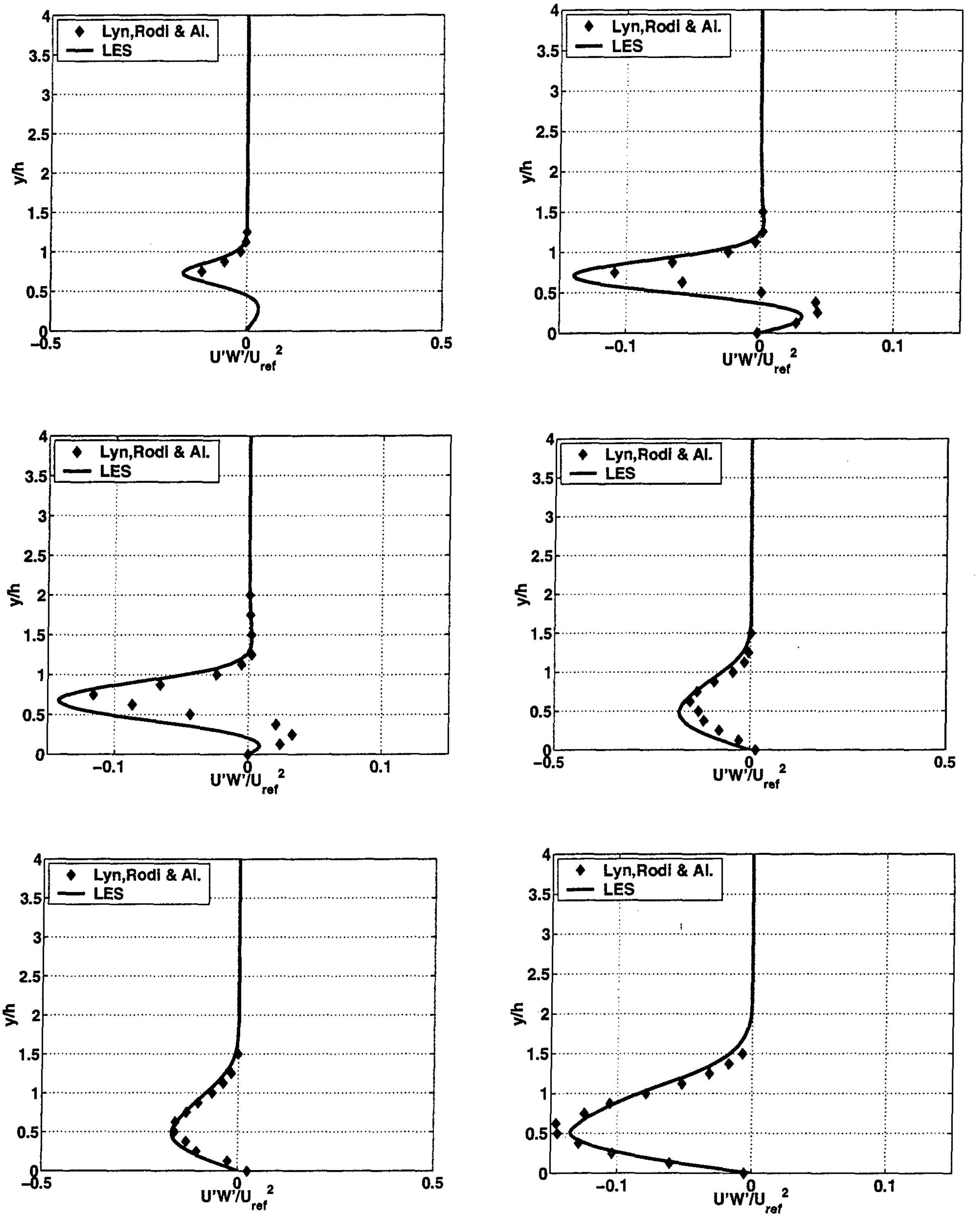

Fig. C.34: Additional simulations, Case II: velocity profiles for turbulent stress from top to bottom and from left to right: $x = \frac{5}{8H}$,$x = \frac{7}{8H}$,$x = \frac{8}{8H}$, $x = \frac{11}{8H}$,$x = \frac{13}{8H}$ and $x = \frac{15}{8H}$.

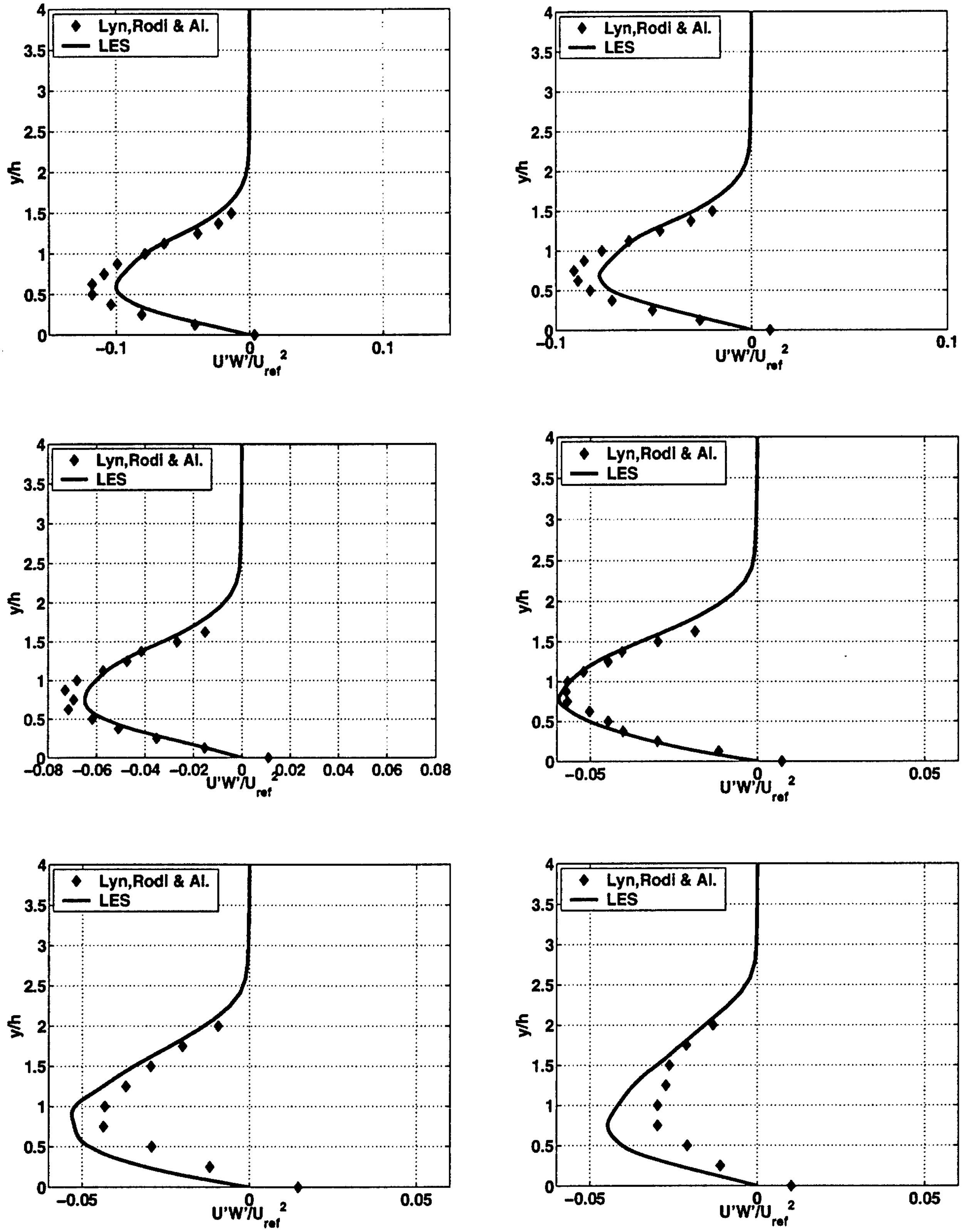

Fig. C.35: Additional simulations, Case II: velocity profiles for turbulent stress from top to bottom and from left to right: $x = \frac{17}{8H}$,$x = \frac{19}{8H}$,$x = \frac{21}{8H}$, $x = \frac{23}{8H}$,$x = \frac{26}{8H}$ and $x = \frac{30}{8H}$.

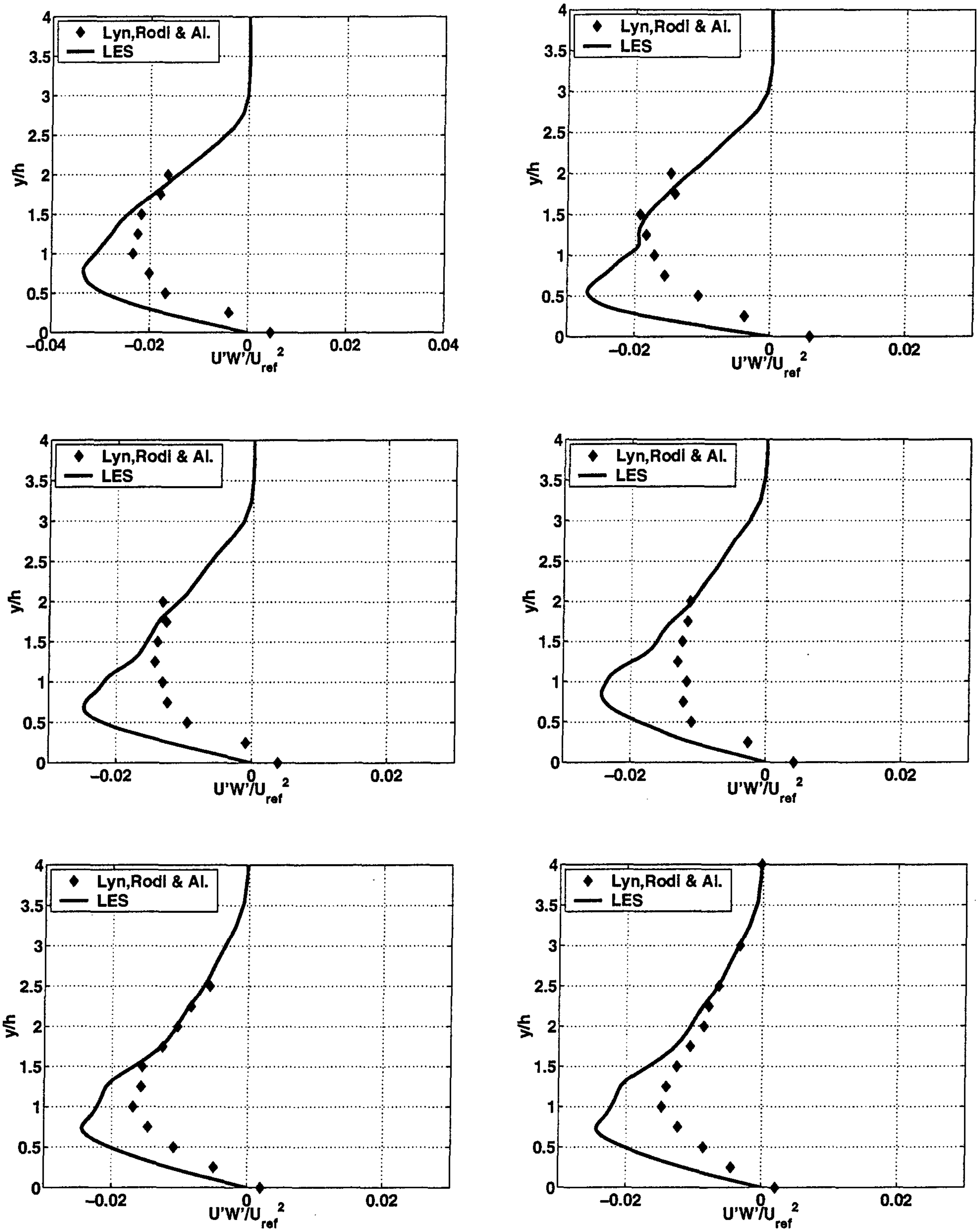

Fig. C.36: Additional simulations, Case II: velocity profiles for turbulent stress from top to bottom and from left to right: $x = \frac{34}{8H}$,$x = \frac{38}{8H}$,$x = \frac{42}{8H}$, $x = \frac{46}{8H}$,$x = \frac{51.2}{8H}$ and $x = \frac{64}{8H}$.

This last simulation confirms that a grid more refined grid than the one for the reference calculation was indeed necessary; to assess whether the improvements in the reproduction of recirculation length and to velocity centerline are really linked to the different choice of the Smagorinsky coefficient the answer would indeed be subjected to two factors: first, that further averaging should confirm the trend outlined here, second, that another simulation, with a different coefficient would confirm this trend.

Whenever it is clear that the simulation is, indeed, strongly affected from the choice of the Smagorinsky coefficient, and, furthermore, that different coefficients yield better results in different portions of the flow. It might be concluded that, for this class of flow, more than for more simpler ones, application of the dynamic procedure (Germano et al., 1991) could indeed be to be preferred in spite of the additional complexity and computer costs which would entail.

REPORT DOCUMENTATION PAGE

Form Approved OMB No. 0704-0188

1. AGENCY USE ONLY (Leave blank)	2. REPORT DATE	3. REPORT TYPE AND DATES COVERED
	December 2002	Final Technical Report

4. TITLE AND SUBTITLE

LES investigation of coherent structures in boundary layers and wakes
Volume II: Wake Around Square Cylinder

5. FUNDING NUMBERS

Grant No. N0014-99-1-0834

6. AUTHOR(S)

R. Giammanco & C. Benocci

7. PERFORMING ORGANIZATION NAME(S) AND ADDRESS(ES)

Institut von Karman de Dynamique des Fluides (Von Karman Institute for Fluid Dynamics)
Chaussee de Waterloo, 72
1640 Rhode-Saint-Genese, BELGIUM

8. Performing Organization Report Number

Grant No. : N00014-99-1-0834

9. SPONSORING/MONITORING AGENCY NAME(S) AND ADDRESS(ES

Office of Naval Research, Ballston Centre Tower, 800 North Quincy Street Arlington, VA 22217-5660

10. SPONSORING/MONITORING AGENCY REPORT NUMBER

EAR9944

11. SUPPLEMENTARY NOTES

This research was sponsored by the Office of Naval Research (ONR Grant Number: N00014-99-1-0834; Contract Report 2003-08). Reproduction in whole or in part is permitted for any purpose of the United States Government. Part of a three volume set -- LES investigation of coherent structures in boundary layers and wakes -- Volume I: Investigation of coherent structure in an attached shear layer (240 pages); **Volume II: Wake Around Square Cylinder (164 pages);** Volume III: Development of a Parallel Unstructured Grid LES Code (173 pages).

12a. DISTRIBUTION/AVAILABILITY STATEMENT	12b. DISTRIBUTION CODE
Approved for public release; distribution is unlimited.	A

ABSTRACT (Maximum 200 words)

Purpose of the present investigation is to assess the feasibility of simulating and studying coherent structures in turbulent shear layers, making use of Large Eddy Simulations (LES).

Volume I of present report has described the general background, the main development and the results obtained for wall bounded turbulent flow, particularly the turbulent channel flow at equilibrium.

The present Volume II is devoted to the study of the flow around an obstacle, in particular a cylinder with square cross section and infinite length in span-wise direction. This test case belongs to a completely different class of flow respect the one analyzed in Volume I, and it is a rather severe test case for the LES code.

Most of the advanced features of the code were exploited, and different simulations were performed, to collect, whenever possible, sufficient data to draw conclusions and remarks.

Differently from the case of channel flow, were the code has been extensively validated and analyzed in detail, down to the level of turbulent kinetic energy budget, the present flow constitutes a still active area of basic research.

The higher complexity of the flow, the absence of a second direction of homogeneity, beside the span-wise direction, the existence of a dominant frequency in the flow, the necessity of employing upwinding discretization for advection terms and other numerical difficulties have led to such complexities of execution that only the very basic set of statistics (statistical moments of first and second order) were obtained. At the same time, limits and draw-backs for current LES code implementation have been outlined.

Most of the efforts were devoted to reach a sufficient similarity in behavior between LES simulation and reference experimental data; this attempt has led to build grids not perfectly suited to analyze structures applying the criteria based on the gradient of velocity tensor introduced in Volume I.

This fact, together with intrinsic difficulty of dealing with a wide range of structures of different sizes and dimensions, has limited the possibility to obtain a through and complete description of vortical behavior for this class of flow.

However, it was possible to find useful global statistics for organized turbulence and to show that a very important part of the entire turbulent field lies within very active structures, which cover a very small part of the entire flow field. It can be moreover suggested that these characteristics of these structures are the ones which define and control the wake behavior, and their identification could be key of understand and possibly identify and recognize specific wakes.

Possible avenues for future investigations starting from present study are also suggested.

14. SUBJECT TERMS

ONR, Belgium, Large-Eddy simulations, SGS models, LES equations, Coherent structure concept, Wall shear layer

15. NUMBER OF PAGES

16. PRICE CODE

17. SECURITY CLASSIFICATION OF REPORT	18. SECURITY CLASSIFICATION OF THIS PAGE	19. SECURITY CLASSIFICATION OF ABSTRACT	20. LIMITATION OF ABSTRACT
UNCLASSIFIED	UNCLASSIFIED	UNCLASSIFIED	UL

298onr 20feb036

von KARMAN INSTITUTE FOR FLUID DYNAMICS INPA
INSTITUT von KARMAN DE DYNAMIQUE DES FLUIDES AISBL
von KARMAN INSTITUUT VOOR STROMINGSDYNAMICA IVZW

REF.

Dr. Patrick Purtell
Office Naval Research
Ballston Center Tower One,
800 North Quincy Street
Arlington VA 22217-5660
U.S.A.

Administrative Office
Office of Naval Research Regional Office Boston
495 Summer Street Room 627
Boston MA 02210-2109
U.S.A

Defense Technical Information Center
8725 John J. Kingman Road Ste 0994
Fort Belvoir VA 22060-6218
U.S.A.

Office of Naval Research
ATTN: ONR 363
Ballston Center Tower One,
800 North Quincy Street
Arlington VA 22217-5660
U.S.A.

Patent Office
Office of Naval Research
ATTN: ONR 00CC
Ballston Center Tower One,
800 North Quincy Street
Arlington VA 22217-5660
U.S.A.